OPTICALLY DETECTED MAGNETIC RESONANCE
OF
RADICAL PAIRS

A thesis submitted for the degree of Doctor of Philosophy

by

Stephen R. Nattrass

Wolfson College,
Oxford.

Michaelmas 1987

CONTENTS

Preparations

CHAPTER 1

INTRODUCTION

1.1 Historical Background

In the liquid phase radical pairs occur widely as reaction intermediates. They are commonly formed by electron or H-atom transfer, may be ionic or neutral and typically their members undergo subsequent reaction at diffusion controlled rates. There are, however, other criteria influencing the overall rate of reaction, aspects of which can be used as tools for probing radical behaviour. It is with these that the following chapters are concerned and, in particular, the effects of external magnetic fields and reaction environment.

Magnetic field effects on chemical reactions have long been a subject of investigation [1]. As a subset of reactions, those involving radicals would be expected to be good candidates for the observation of such effects as they are indeed paramagnetic, offering higher susceptibility than diamagnetic species. From a thermodynamic point of view the interaction energies, at fields of up to 1 T for carbon-centred radicals, amount to only a few Joules mol^{-1}. Kinetic effects by direct modification of the activation energy of a given pathway can also be discounted by considering that RT at room temperature is 2.5 $KJmol^{-1}$. We are left considering the possibility of a magnetic field being able to change the relative importance of pathways open to the reaction and this is in fact the current basis for the explanation of such effects.

The overall spin multiplicity of a pair of doublets (radicals) may be singlet or triplet, the initial state being governed by the total spin of the precursor species. Additionally the multiplicity of any products resulting from the reaction of the pair can only be singlet or triplet, but, importantly, need not be that of the initially produced radical pair. The explanation for the change in spin multiplicity comes in the form of magnetic field sensitive mechanisms which enable rapid intersystem crossing within the radical pair itself.

In the liquid phase the mechanisms were first suggested by Brocklehurst [2] and by workers seeking to explain the phenomena of CIDNP and CIDEP [3]. The latter now provide the key to understanding how external magnetic fields can influence the course of radical reactions and are closely related to the explanation, advanced much earlier by Wigner [4], for the interconversion of ortho and para hydrogen in the presence of paramagnetic centres, and the analogous mechanism proposed by Rushin et al. [5] to explain magnetic field effects upon charge transfer type excitons in organic solids. In the liquid phase positive observation of field effects came from pulse radiolysis work [6] and had been predicted by Lawler and Evans [7].

A natural extension of the theory was to the effect on reaction of static and high frequency magnetic fields applied simultaneously in a manner analogous to the esr experiment. Again first observations were in the solid state [8] with predictions [2,9] and observations [10] in the liquid phase following later. In all cases the effect was employed to achieve a form of optically detected magnetic resonance, essentially revealing spectroscopic information similar to that obtained from conventional esr, but offering potentially greater time resolution.

In summary we have two techniques employing magnetic fields to study doublet - doublet processes in solution, the application of which has been to the relatively specialized areas of photosynthetic reaction centre studies and pulse radiolysis work. Recently, however, magnetic field effect studies have been rejuvenated by the use of restricted diffusion reaction systems employing aqueous surfactant solutions [11]. It is the purpose of the present work to describe the development of equipment, techniques and interpretation for the study of both types of field effects and their application to the 'new media' in addition to homogeneous systems.

The nomenclature adopted to describe the two methods is borrowed from the photosynthetic work [12] in which the use of static fields alone is referred to as MARY (MAgnetic field modulation of Reaction Yield), and that of resonant high frequency fields as RYDMR (Reaction Yield Detected Magnetic Resonance). Details of both techniques may be found in chapter 2, where the theoretical basis for their existence will be discussed.

CHAPTER 2

THEORETICAL BASIS

2.1 Introduction

A radical pair consists of two doublet species and so has, in a coupled electron representation, two possible states of spin multiplicity. Classically, a parallel spin arrangement gives rise to three triplet states, while the anti-parallel possibility establishes a singlet state. This chapter is concerned with the fundamental theoretical aspects of how a liquid phase radical pair system, formed initially in either a singlet or triplet state, evolves in time. The following schematic serves to illustrate the various possibilities open to a single pair :

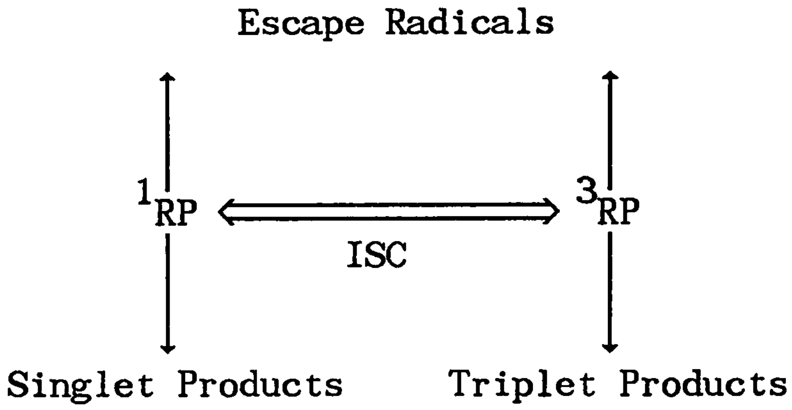

where it may react to give, in general, triplet and singlet products, undergo intersystem crossing (ISC) to a pair of different spin multiplicity, or separate by diffusion such that there is a low probability of the same two radicals returning to a separation at which they could react. As a result of the latter possibility radical reactions are often categorized into two phases. Soon after generation there is a period of reaction dominated by that between radicals born together; the so-called geminate phase. At later times, it is the random encounters between members of different initial pairs that dominate reaction; the homogeneous phase. In general, the diffusive encounters and spin intersystem crossing proceed on comparable timescales and so should be treated simultaneously if the overall system behaviour is required. The diffusive encounters may be pictured as sampling and perturbing the radical pair spin motion. A reasonable level of approximation may be obtained, however, by dealing with spin and spatial motion separately. As an example, the product yield of singlet reactions may be obtained from

$$\varphi_s(t) = \lambda \int_0^t p_s(t)f(t)dt \qquad (1)$$

where $p_s(t)$ gives the time dependence of singlet probability, and f(t) that of the radical pair being at a reactive separation. The inclusion of λ accounts for a less than unity probability of reaction upon singlet encounter.

The following sections examine key features of spin and spatial motion with regard to radical systems in magnetic fields.

2.2 Spin Motion

A radical pair, consisting of two doublet species, has two possible states of electron multiplicity open to it. A convenient classical picture of the possible spin states is shown in figure 2.1, although it has been pointed out that this simple vector model treats the two electrons in an inequivalent manner, inaccurately representing the S and T_0 states [1].

From the classical picture we see that the $T_\pm$ states correspond to parallel arrangements of the two electrons of a radical pair, giving a net spin angular momentum component in the z direction which is absent

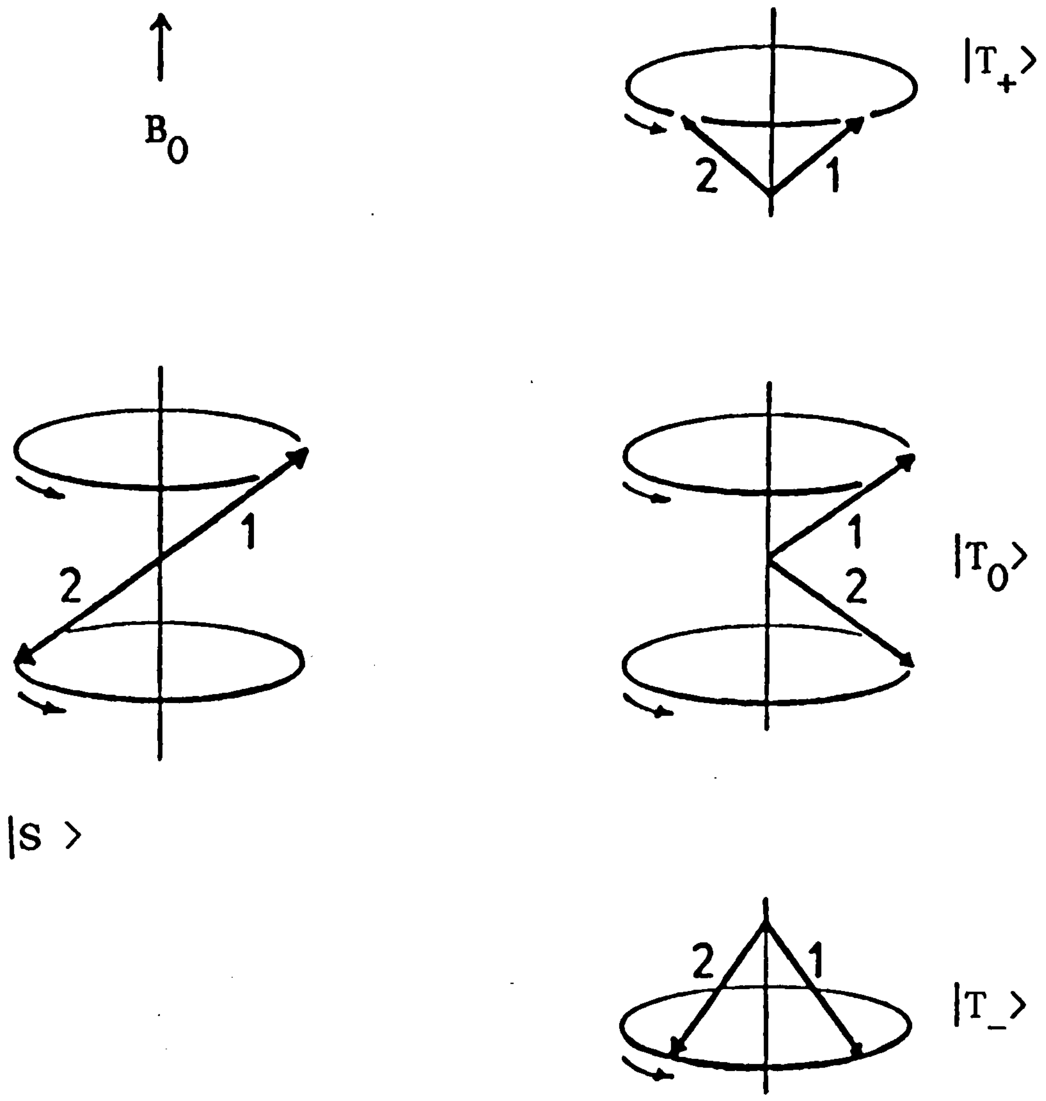

Figure 2.1. Laboratory frame vector model of electron spin states of a radical pair, showing relative energy increasing in the direction of an applied magnetic field, B_0. 1 and 2 designate electrons on individual members of the pair.

in the S and T_0 pairs. The latter two states are nevertheless distinguishable by the presence of a transverse spin component in the T_0 pair. Clearly interconversion of $S, T_0 \longrightarrow T_\pm$ requires a spin flip, whilst the $S \longrightarrow T_0$ interchange may be achieved by a dephasing process.

The coupled basis for the representation of radical pair spins is a convenient one to employ for the treatment of radical pair behaviour from generation through to reaction. It does not necessarily imply any spin-spin interaction. In terms of the products of high field electron-nuclear eigenstates of the component radicals, we have :

$$\begin{array}{llcl} \text{Singlet :} & |S,N\rangle & = & 2^{-\frac{1}{2}}\,(\,|\alpha\beta,N\rangle - |\beta\alpha,N\rangle), \\ & & & \\ \text{Triplet :} & |T_0,N\rangle & = & 2^{-\frac{1}{2}}\,(\,|\alpha\beta,N\rangle + |\beta\alpha,N\rangle), \\ & |T_+,N\rangle & = & |\alpha\alpha,N\rangle, \\ & |T_-,N\rangle & = & |\beta\beta,N\rangle, \end{array} \qquad (2)$$

where $|\sigma_1\sigma_2,N\rangle$ denotes electron spin state $|\sigma_i\rangle$ on radical i and nuclear spin state $|N\rangle$.

Upon formation, a radical pair is considered to acquire the spin state of its immediate precursor, corresponding to a pure state in the coupled basis. Consideration of the radical pair spin Hamiltonian in this basis reveals that it is not an eigenbasis and, in terms of a matrix representation, gives rise to off-diagonal elements coupling the singlet state to the triplet manifold. Consequently the time evolution of the system will involve a degree of $S \rightarrow T$ interconversion.

It is clear that the existence of non-zero matrix elements between antisymmetric singlet and symmetric triplet states requires an antisymmetric coupling operator. For reasons of clarity it is convenient to express the radical pair spin Hamiltonian as a sum of its symmetric and antisymmetric parts with respect to electron spin :

$$\begin{aligned} H_{RP} &= H_{rad1} + H_{rad2} , \\ &= H_{+} + H_{-} , \end{aligned} \qquad (3)$$

where H_{+} and H_{-} represent respectively the symmetric and anti-symmetric components of the pair spin Hamiltonian. In detail we have :

$$H_{+} = 1/2 \left[(g_1 + g_2)\beta B_0 + \left(\sum^{(1)} a_n m_{n,k} + \sum^{(2)} a_n m_{n,k}\right) \right] (S_{1z} + S_{2z}) - J(r)(1/4 - S_1 S_2) , \qquad (4)$$

$$H_{-} = 1/2 \left[(g_1 - g_2)\beta B_0 + \left(\sum^{(1)} a_n m_{n,k} - \sum^{(2)} a_n m_{n,k}\right) \right] (S_{1z} - S_{2z}) + 1/2 \sum a_n (S_1^{+} I_{1n}^{-} + S_1^{-} I_{1n}^{+}) + 1/2 \sum a_n (S_2^{+} I_{2n}^{-} + S_2^{-} I_{2n}^{+}) . \qquad (5)$$

where all symbols have their usual meaning. Anisotropic components of the g and hyperfine tensors are assumed to average to zero as a result of molecular tumbling within the liquid phases in question.

The operator $(S_{1z} - S_{2z})$ acts to rephase S and T_0 states resulting in their interconversion and giving rise to matrix elements of the form

$$2^{-\frac{1}{2}}.\langle\alpha\beta + \beta\alpha|\ (S_{1z} - S_{2z}).2^{-\frac{1}{2}}\ |\alpha\beta - \beta\alpha\rangle \quad = \quad \frac{1}{2}\ . \qquad (6)$$

Hence the first term of H_- (5) effects an S-T_0 interconversion if $\Delta g \neq 0$, whilst the second term produces the same result if the members of the pair have different nuclear hyperfine interactions. In the simple vector model of fig 2.1 these criteria may be seen to amount to the condition that the radical spins have different Larmor precession frequencies.

The final two terms can be seen to depend only on the electron - nuclear states of individual members of the pair, and their effect is embodied in the shift operators encompassing the transverse (x,y) electron - nucleus coupling. The matrix elements of these terms are of the form

$$\langle\beta\beta,m_I{+}1|\ a_n S_1^- I_{1n}^+\ 2^{-\frac{1}{2}}\ |\alpha\beta - \beta\alpha,m_I\rangle \ = \ 2^{-\frac{1}{2}}\ a_n\ [I_n(I_n{+}\ 1) - m_I(m_I\ +\ 1)]^{\frac{1}{2}}, \qquad (7)$$

for a given nuclear configuration m_i and nucleus k. In terms of figure 2.1, such an operator brings about simultaneous electron and nuclear spin flips leading to the interconversion of S,T_0 with $T_\pm$. At this point it is helpful to note that interconversion by this process, often termed the hyperfine mechanism (hfi), is not possible for states such as $\langle\alpha\alpha,m_I = I_n|$ or $\langle\beta\beta,m_I = -I_n|$.

It may be seen that only the first, 'Δg', term in H_- (5) is explicitly dependent upon a longitudinal (z) magnetic field B_0, its value increasing with field. In general, for carbon centred radicals in solution, Δg values are such that contributions to S-T_0 mixing from this term are insignificant below 1 T. Of much greater importance to the system field dependence is the relative magnitude of the $T_\pm$ diagonal Hamiltonian element (4) differences with respect to corresponding off-diagonal quantities (5) described above. This is the criterion for the effectiveness of the state coupling. Thus we are led to compare terms such as $\langle T_+|H_+|T_+\rangle - \langle T_0|H_+|T_0\rangle$ with $\langle T_+|H_-|T_0\rangle$, as a function of field. Figure 2.2 shows the electron-only terms of $H_+(B_0)$. It is clear that increasing B_0 serves to decrease S,$T_0 \rightarrow T_\pm$ coupling, but does not affect that between S $\rightarrow T_0$ (ignoring Δg contributions). When the $T_\pm$-T_0, S energy separation greatly exceeds the magnitude of the off-diagonal elements coupling these states, S,$T_0 \rightarrow T_\pm$ interconversion becomes insignificant.

Clarification of this picture may be gained by considering a two level system with energy separation Δ and time-independent coupling matrix element V. If the system is initially in a pure state, then the probability that it has made a transition to the second state after a time t is given by

$$P(t) = (2V^2/U^2)\ \mathrm{Sin}^2(\tfrac{1}{2}Ut), \qquad (8)$$

where $U^2 = \Delta^2 + 4V^2$. The system oscillates between the two states with increasing frequency and decreasing amplitude as the energy gap between the coupled states increases. Thus interconversion is impeded by increasing state separation.

In general a radical pair ensemble will have many hyperfine states and

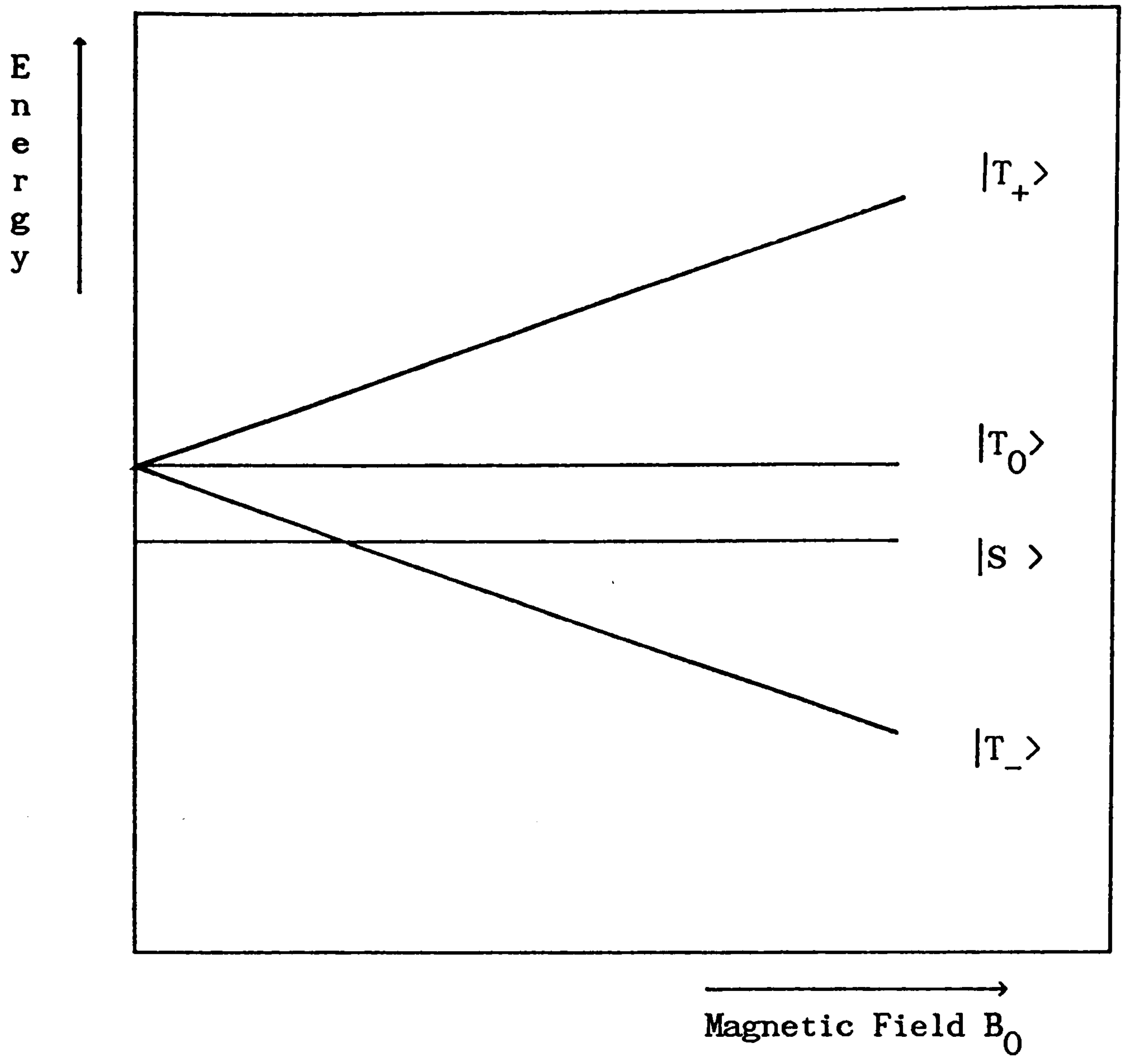

Figure 2.2. Diagrammatic representation of the zeroth-order electron-only energy terms of a radical pair as a function of external magnetic field. The $|S\rangle$ - $|T_0\rangle$ separation determines the magnitude of J, the Heisenberg exchange interaction. Note the $|T_0\rangle$ - $|S\rangle$ crossing at low B_0.

consequently the intersystem crossing will proceed with many frequency components governed by the individual coupling elements, V. The net effect, arising from the interference of all frequency components, is a sigmoidal-type evolution to a statistical distribution over the coupled states, and not an oscillatory behaviour.

In summary, from the point of view of the time evolution of an initial radical pair state, three field regimes may be described:

(1) Zero Field
(2) Low Field
(3) High Field.

2.2.1 Zero Field Case

This case is unique in that B_0-dependent components of H_+ and H_- are completely eliminated, leaving only hyperfine terms. Detailed analysis shows that while most, though not all (see below), states are coupled, many of the resulting eigenstates are degenerate [2,5]. These do not evolve differentially in time and so S →T transitions are precluded. On these grounds, the long time distribution of radical pair population is not expected to become that predicted by the statistical ratio of 3(triplet):1(singlet). Exact theoretical calculations in this regime are virtually intractable for real radical pair systems comprising many electron - nuclear states. Nevertheless excellent approximations are available [3].

2.2.2 Low Field Case

Application of a very low external magnetic field, for example that of the Earth, can serve to lift the many degeneracies found at zero field and so enable further contributions to the S →T transition channels. In consequence, the asymptotic distribution more closely approaches a statistical 3:1. As the field strength is steadily increased, more and more members of the radical pair ensemble are prevented from undergoing intersystem crossing, reducing the overall interconversion rate and bringing the final distribution towards a ratio of 1:1 over the S and T_0 states only (all coupled). Expressions for the field dependence of the 'equilibrium' S-T ratio have been derived [4]. Their complicated appearance conceals the simple sigmoidal form often observed in experimental systems (see below). Again calculations in this regime require much numerical effort.

2.2.3 High Field Case

In this region only S-T_0 interconversion is possible, and exact calculations are greatly simplified. The radical pair Hamiltonian matrix becomes independent of specific nuclear states, assuming a form which is block-diagonal with respect to nuclear configuration and of order 2 in electron states. Singlet-triplet interconversion is independent of field until the Δg term becomes a significant part of H_-. Further field increase then leads to S-T_0 coupling enhancement.

2.2.4 Heisenberg Exchange

A different ISC field dependence is predicted for radical pairs at separations sufficiently small for the existence of significant Heisenberg exchange interaction between the spins. Under such circumstances S-T_0 degeneracy is lifted, the S state falling below T_0 in energy, if a positive J is assumed. Application of a magnetic field now generates the possibility of an S-T_- level crossing resonance as the T_- falls away in energy from T_0, with the result that ISC rates may be enhanced over their values at very low field. Clearly the observation of such resonances can provide data on the magnitude of J.

2.2.5 Additional High Frequency Fields

The important case for consideration here is that of an oscillatory magnetic field, of amplitude B_1, applied perpendicular to a static field B_0. The latter is assumed to be of sufficient magnitude to bring the radical pair system into the high field region, described above. Non-secular nuclear hyperfine terms may then be neglected in the spin Hamiltonian. Again in terms of symmetric and antisymmetric parts we have:

$$H_+ = 1/2\,(g_1 + g_2)\,\beta B_0\,(S_{1z} + S_{2z})$$

$$+ 1/2\,\left(\sum^{(1)} a_n m_{n,k} + \sum^{(2)} a_n m_{n,k}\right)(S_{1z} + S_{2z}) \qquad (9)$$

$$+ J(1/4 - S_1 S_2)$$

$$H_- = 1/2\,(g_1 - g_2)\,\beta B_0\,(S_{1z} - S_{2z})$$

$$+ 1/2\,\left(\sum^{(1)} a_n m_{n,k} - \sum^{(2)} a_n m_{n,k}\right)(S_{1z} - S_{2z}) \qquad (10)$$

$$+ 1/2\,(g_1 + g_2)\,\beta B_1\,[\,(S_{1x} + S_{2x})\cos(\omega t) + (S_{1y} + S_{2y})\sin(\omega t)\,].,$$

where ω is the frequency of the B_1 field.

The Hamiltonian time dependence may be removed by performing a transformation to a reference frame rotating at the frequency of the B_1 field. This is achieved by the operator $\exp(i\omega S_z t)$, yielding

$$\begin{aligned} H_+ \quad = \quad & 1/2[(g_1 + g_2)\beta B_0 - \hbar\omega](S_{1z} + S_{2z}) \\ & + 1/2 \left(\sum^{(1)} a_n m_{n,k} + \sum^{(2)} a_n m_{n,k}\right) (S_{1z} + S_{2z}) \qquad (11) \\ & + J(1/4 - S_1 S_2) \end{aligned}$$

$$\begin{aligned} H_- \quad = \quad & 1/2\ (g_1 - g_2)(S_{1z} - S_{2z}) \\ & + 1/2 \left(\sum^{(1)} a_n m_{n,k} - \sum^{(2)} a_n m_{n,k}\right) (S_{1z} - S_{2z}) \qquad (12) \\ & + 1/2(g_1 + g_2)\beta B_1[(S_{1x} + S_{2x})] . \end{aligned}$$

The effect of the oscillating field is most clearly seen if the S_x operators are expressed by shift operators:

$$S_{1x} + S_{2x} \quad = \quad ½(S_1^+ + S_2^+ + S_1^- + S_2^-). \qquad (13)$$

The appropriate matrix elements are:

$$\begin{aligned} \langle\alpha\alpha,N|\ 1/2\ (S_1^+ + S_2^+ + S_1^- + S_2^-)\ 2^{-½}\ |\alpha\beta + \beta\alpha,N\rangle \quad & = \quad 2^{-½}, \\ & \qquad\qquad (14) \\ \langle\beta\beta,N|\ 1/2\ (S_1^+ + S_2^+ + S_1^- + S_2^-)\ 2^{-½}\ |\alpha\beta + \beta\alpha,N\rangle \quad & = \quad 2^{-½}, \end{aligned}$$

showing that T_0 is mixed with $T_\pm$ but, in contrast to the hyperfine mechanism, the B_1 field does not produce any change of nuclear configuration. As a result, all $T_\pm$ hyperfine states are connected with T_0. In terms of the effectiveness of the mixing, the corresponding differences in the matrix elements are now B_0 and ω dependent. Maximum amplitude of $T_0 \rightarrow T_\pm$ conversion occurs in a **resonant** manner when B_0 and ω achieve the correct balance. Resonance may be thought of as inducing an $S \rightarrow T_\pm$ coupling via T_0. In simple terms system evolution will become more rapid and the triplet:singlet distribution tend towards a statistical 3:1 (but see below for exceptions). The behaviour of a radical pair system, under the influence of perpendicular static and high frequency magnetic fields, will be considered in much greater detail in a later section, where approximate calculations of the system response are described.

2.3 Other ISC Mechanisms

So far attention has been focussed solely on coherent intersystem crossing mechanisms within the radical pair. With regard to the present work, the most important additional contributions come from stochastic relaxational processes familiar in more traditional magnetic resonance work.

For radicals in solution, the important relaxational interactions are brought about by the existence of g value (spin-orbit coupling) and hyperfine tensor (electron-nuclear dipolar terms) anisotropies. Together they provide matrix elements between all four states in the coupled electron representation. Additionally, contributions from electron-electron dipolar terms might be expected when considering radical pairs.

The potential of such mechanisms to lead to field dependent radical pair ISC has been explored previously [5], though their effects have only been observed recently [6].

The interactions responsible for relaxation are not intrinsically field dependent, except when g anisotropy is significant. All relaxation processes depend upon fluctuations of such interactions, longitudinal (T_1) mechanisms requiring the presence of a Fourier component at the relevant field-dependent transition frequency. Pure dephasing (T_2) processes do not show this resonant behaviour.

Assuming an exponential correlation function for molecular tumbling, with time constant τ_c, the relevant power spectrum of fluctuations $J(\omega)$, at angular frequency ω, is given by

$$J(\omega) = \frac{2\tau_c}{1 + \omega^2\tau_c^2} . \qquad (15)$$

Field dependence of this term is carried in ω and 'saturation' clearly occurs only when $\omega > \tau_c^{-1}$. For C-centred radicals in normal solution T_1, T_2 ~1 μs, very close to their minimum expected values for X-band spectroscopy.

Relaxational contributions to magnetic field modulation of reaction will become important when geminate timescales are extended considerably, or when radical species of higher g or hyperfine anisotropies are involved.

2.4 Spatial Motion

Random encounters of radicals during the homogeneous phase of a reaction occur with randomized spin states and so lead to a mixture of singlet and triplet products, without the requirement of an ISC process. The overall effect is to produce a field insensitive background which severely reduces the observable effects of any superposed field modulation [7]. Consequently, for a treatment of external magnetic field effects it is sufficient to consider only the geminate phase of reaction, averaging over the dynamical behaviour of single radical pairs to achieve a result for the ensemble.

2.4.1 Random Walk

Several approaches to determining the averaging function f(t) have been adopted. In an attempt to emphasize the discrete nature of diffusion, Noyes [8] employed a three dimensional random-walk model. He obtained numerical results which could be approximated by :

$$f(N) \quad = \quad 0.24(N + 0.44)^{-3/2} , \qquad (16)$$

giving the probability of a first reencounter of the pair after N diffusive steps. If a mean time between diffusive jumps, τ_D, is introduced, then, with $t = N\tau_D$, the above distribution may be recast to average the spin motion and enable yield determination. For the simple case of an initial singlet radical pair, each member with a single spin-½ interaction of coupling constant A, the time dependence at zero and high field is given by ($\Delta g = 0$) [9]

$$p_T^0 = \frac{3}{16}\sin^2(At) + \frac{3}{4}\sin^2(At/2), \tag{17}$$
$$p_T^\infty = \frac{1}{2}\sin^2(At/2),$$

with the results

$$\bar{\Phi}_T^0 = 0.3\,(A\tau_D)^{1/2}, \tag{19}$$
$$\bar{\Phi}_T^\infty = 0.15\,(A\tau_D)^{1/2},$$

for the respective yields as t → ∞. The square root dependence on the coupling element between the states and τ_D is a characteristic of diffusion models; a result of averaging over $t^{-3/2}$. The dependence on τ_D confirms the notion of an interplay of timescales between RP dynamics and spin motion.

2.4.2 Continuous Diffusion

The alternative continuous view of diffusion commences with an equation of the form [4]

$$\frac{\partial P_d(r,t)}{\partial t} = D\nabla_r^2 P_d(r,t) \ , \tag{19}$$

where P_d is the probability of finding the two radicals at a separation r at a time t. D is taken as the relative diffusion coefficient given by the sum of the coefficients for each radical. When (19) is solved for the probability flux at r = a, with the initial conditions that the radicals are generated at a separation r_0 and an absorbing boundary at a ($a < r_0$), the following expression is obtained:

$$f(t) \quad = \quad \frac{Da(r_0 - a)}{2\pi^{½}} (Dt)^{-3/2} \exp[-(r_0 - a)^2/4Dt] \ , \qquad (20)$$

revealing a $t^{-3/2}$ dependence for large t. Correspondence between this result and that of Noyes is achieved by performing the substitution

$$\tau_D \quad = \quad a^2/6D \qquad \text{(diffusion jump size taken as a).} \qquad (21)$$

Furthermore, if the reaction separation a is replaced by the sum of the radii of the reacting molecules, τ_D becomes approximately the time taken for diffusion across a molecular diameter. For D of the order of 10^{-5} $cm^2\ s^{-1}$, $\tau_D \simeq 10^{-10}$ s.

2.4.3 Exponential Model

The simplest model for f(t) is a static one, neglecting microscopic details of diffusion and essentially assuming unimolecular decay of the radical pair ensemble with a Poisson distribution of lifetimes. Thus we have

$$f(t) \quad = \quad 1/\tau_e \ . \ \exp(-t/\tau_e) \ . \qquad (22)$$

Application of this distribution (22) gives a quite different dependence of yield upon system properties, for the radical pair model adopted earlier [9]:

$$p_T^0 = \frac{3}{8}\left\{\frac{A^2\tau_e^2}{1+4A^2\tau_e^2} + \frac{A^2\tau_e^2}{1+A^2\tau_e^2}\right\}, \qquad (23)$$

$$p_T^\infty = \frac{1}{4}\left\{\frac{A^2\tau_e^2}{1+A^2\tau_e^2}\right\}.$$

In the short diffusional time limit of $A^2\tau_e^2 < 1$ a quadratic dependence of yield on A and τ is to be noted. This contrasts with the much weaker square root dependence of the simple free diffusion model. This can be traced to the enhanced overlap of spin and spatial evolution functions obtained from an exponential model, in comparison with the sharply decaying $t^{-3/2}$ free diffusional form.

The existence of such a marked difference in pair correlation function is of considerable significance to the experimental work of this thesis which relies upon an approach to exponential form under the modified diffusion conditions. These are found in the presence of an inter-radical potential or a diffusional boundary.

The former case applies to the relative motion of radical ion pairs in media of finite dielectric constant and has been illustrated by numerical solution of the relevant diffusional problem in media of several permittivities [7]. The behaviour is close to exponential, even for high dielectric constants, $\epsilon \sim 35$.

Imposing a reflecting boundary on radical pair motion leads to the idea of compartmentalized reaction which, in the limit of one pair per cell, precludes the possibility of random spin encounters and gives pure geminate reaction.

The problem has been addressed in the spherically symmetric case, revealing close approximation to an exponential f(t) [10].

2.4.4 Simultaneous treatment of Spin and Space

When radical pair reaction rates via singlet and triplet channels are not identical, and/or a Heisenberg exchange interaction, J(r), is present, spin and spatial motion are intimately connected. This is, of course, the situation for real radical pair systems and even if such electronic complications did not exist, a changing hyperfine distribution arising from reaction, should also be considered.

The full problem may be treated by solution of a Stochastic Liouville Equation (SLE) describing the motion of a radical pair density matrix in spin (electron-nuclear) and spatial coordinates. In principle it can treat the behaviour of a radical system to the full capabilities of the spin and diffusional models employed, but in practice analytic solutions are only possible after making severe approximations [4]. Even numerical solutions often utilize approximations, beyond those associated with discretization, to render the problem tractable [7].

2.5 Semi-Quantitative Description of Field Effects

As indicated above, a fully quantitative treatment of spin effects on radical reaction is not feasible and so a phenomenological approach, applying a first-order kinetic treatment, is often adopted [11,12]. The designation of a time-independent k_{ISC} becomes a reasonable approximation when dealing with typical radicals comprising many hyperfine states and corresponding component frequencies of spin evolution. Under such circumstances the spin system tends towards an equilibrium singlet-triplet distribution in a manner close to that expected for a stochastic process, unless a dominant hyperfine coupling exists. This behaviour is illustrated in figure 2.3a [3,7].

Consider a singlet radical pair decaying via a field-independent channel with first-order rate constant k_-, and via a field-dependent one involving rate constants, k_{ISC}, k_T to give triplet products. Recognizing the reversible nature of spin interconversion, we have the scheme:

$$\xleftarrow[k_-]{\qquad} {}^{1}\mathrm{RP} \underset{k_{isc}^{-}}{\overset{k_{isc}^{+}}{\rightleftharpoons}} {}^{3}\mathrm{RP} \xrightarrow[k_T]{\qquad} \text{products} \ .$$

A basis for simplifying this scheme has been proposed in which the radical pair is taken to be in a field-dependent, quasi-equilibrium spin state. ISC and diffusion-limited reaction are then represented by one effective rate constant for recombination to the triplet spin state, assuming unit reaction probability on encounter,

$$k_T = \bar{p}_T \, k_d \ , \tag{24}$$

where k_d is an effective first-order rate constant describing

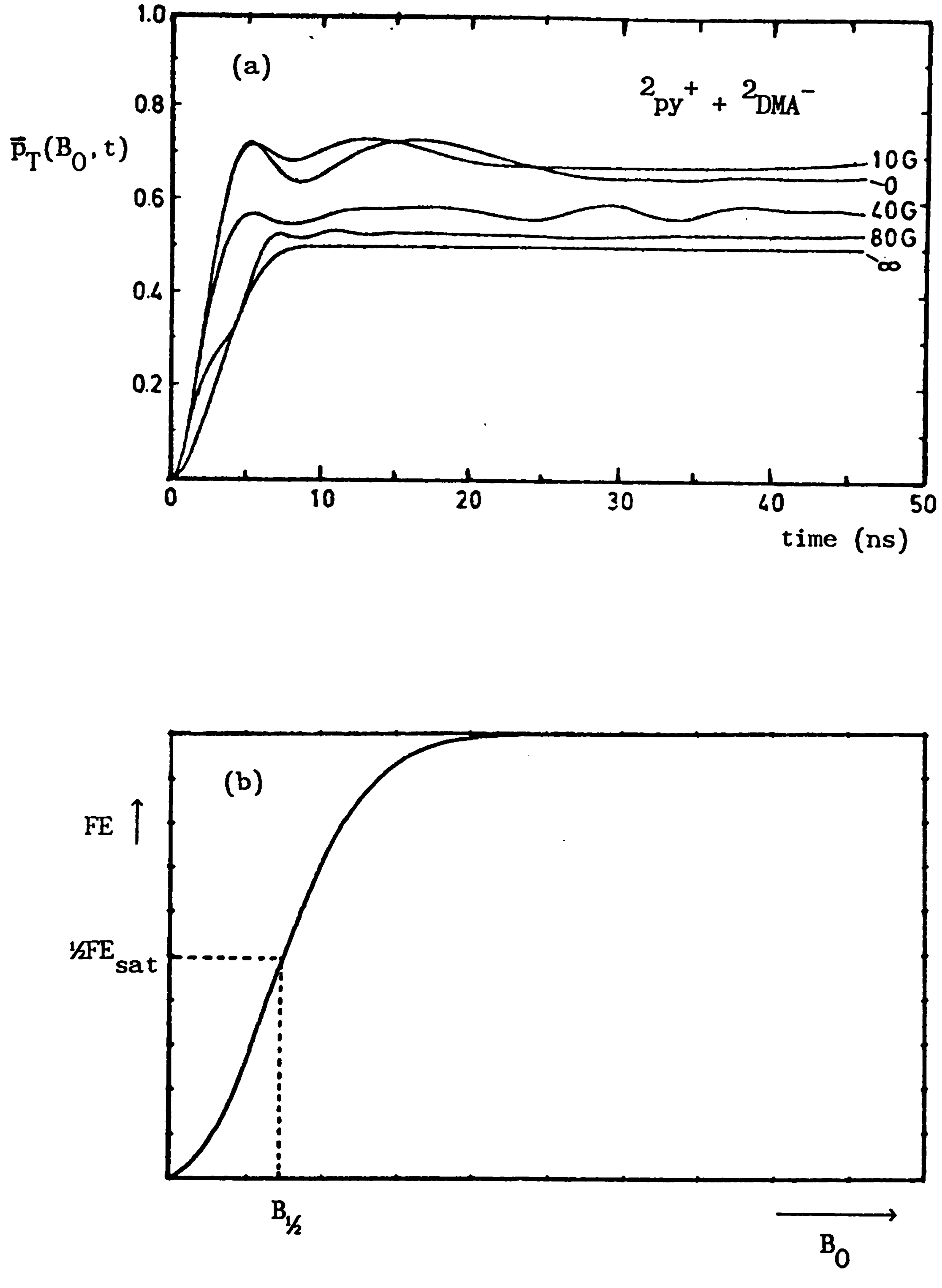

Figure 2.3. Spin system evolution in external magnetic fields.

(a) Calculated evolution of triplet probability, $\bar{p}_T(B_0, t)$, for an initial singlet radical pair in a series of external magnetic fields [7].

(b) Representation of the form of experimentally-observed field effect B_0-dependence, showing determination of $B_{½}$.

diffusional encounters within the pair and $\bar{p}_T = p_T(1/k_d)$ is a mean triplet state probability averaged over the pair lifetime [12]. The value of this approach is in the enabling of a semi-quantitative visualization.

The triplet state product yield is given by

$$\varphi_T = \frac{k_T}{k_T + k_-} , \tag{25}$$

and so the field effect on this product may be written as

$$FE(B_0) = \frac{\varphi_T(B_0)}{\varphi_T(0)} = \frac{k_T(B_0)}{k_T(0)} \cdot \frac{k_T(0) + k_-}{k_T(B_0) + k_-} . \tag{26}$$

In normal solution k_- may well represent a diffusional escape process, in addition to singlet reaction, and $k_- \geq k_T$ often holds, giving

$$FE(B_0) \approx \frac{\bar{p}_T(B)}{\bar{p}_T(0)} . \tag{27}$$

Reference to figure 2.3a reveals that at short sampling times this quantity can have a value greater than that found in the long time limit, due to oscillatory behaviour. In the absence of such phenomena, however, the trend is one of increasing field effect with increasing sampling time until asymptotic values of $\bar{p}_T$ are attained.

The experimentally observed form of the field effect as a function of applied static field, termed a MARY spectrum, is frequently found to be sigmoidal (figure 2.3b) and so can be characterized by a single halfwidth parameter referred to as $B_{½}$ (28):

$$FE(B_{½}) = 1/2\,(FE_{sat} - FE(0)), \tag{28}$$

where $FE_{sat} = FE(\infty)$ for a pure hyperfine ISC mechanism.

Weller et al. have confirmed this form for the triplet yield in a series of radical ion pair systems [13] and have correlated $B_{½}$ with magnetic properties of the radicals. Empirically it was found that if a mean hfi $S \rightarrow T_{\pm}$, matrix coupling element of radical i was represented by

$$B_i = \frac{1}{g\beta}\left(\sum_k a_{ik}^2\, I_k(I_k + 1)\right)^{½} \text{ (G)}, \tag{29}$$

then there was an excellent correlation between observed $B_{½}$ and a weighted sum of B_i's for the radical pair:

$$B_{½} = \frac{B_1}{B} B_1 + \frac{B_2}{B} B_2 = \frac{B_1^2 + B_2^2}{B_1 + B_2}, \tag{30}$$

where $B = B_1 + B_2$. In view of the kinetic dependence, the correlation found by Weller et al. is perhaps surprising, though their results were restricted to a very narrow range of ion pairs in solvents of similar properties.

2.6 RYDMR Spectra

We now turn to the detailed functional dependence on B_0 and B_1 of the modification to radical reaction by simultaneously applied high frequency and static magnetic fields. Recording of the field effect as a matrix, in the coupled electron representation is [14]

$$\begin{array}{c}\left[\begin{array}{cccc} -J - \frac{1}{2}i\hbar k_S & 0 & a_{(k)} & 0 \\ 0 & g\beta B_{z,\mathrm{eff}} - \frac{i}{2}\hbar k_T & 2^{-\frac{1}{2}}g\beta B_1 & 0 \\ a_{(k)} & 2^{-\frac{1}{2}}g\beta B_1 & -\frac{1}{2}i\hbar k_T & 2^{-\frac{1}{2}}g\beta B_1 \\ 0 & 0 & 2^{-\frac{1}{2}}g\beta B_1 & g\beta B_{z,\mathrm{eff}} - \frac{i}{2}\hbar k_T \end{array}\right] \end{array} \begin{array}{c} |S^{\cdot}\rangle \\ |T^{\cdot}_{+}\rangle \\ |T^{\cdot}_{0}\rangle \\ |T^{\cdot}_{-}\rangle \end{array}, \qquad (33)$$

where $B_{z,\mathrm{eff}} = B_0 - \frac{\hbar\omega}{\frac{1}{2}(g_1 + g_2)\beta} + \frac{1}{(g_1 + g_2)\beta}\left[\sum_n^{(1)} a_n m_{n,k} + \sum_n^{(2)} a_n m_{n,k}\right]$,

and $a_{(k)} = \frac{1}{2}(\Delta g\beta B_0 + \sum_n^{(1)} a_n m_{n,k} - \sum_n^{(2)} a_n m_{n,k})$.

Writing the radical pair system wavefunction in the coupled representation as

$$\Psi = \sum_i c_i \varphi_i , \qquad (34)$$

where $\varphi_i = (S^{\cdot}$ or $T^{\cdot}_0$ or $T^{\cdot}_{\pm})$ and c_i are the respective coefficients, we may specify the state by a coefficient vector,

$$\bar{C} = \begin{bmatrix} c_{S^{\cdot}} \\ c_{T^{\cdot}_{+}} \\ c_{T^{\cdot}_{0}} \\ c_{T^{\cdot}_{-}} \end{bmatrix} . \qquad (35)$$

The time evolution of the system is then formally given by

$$\bar{C}(t) = e^{-(i/\hbar)H_R t}\,\bar{C}(0) , \qquad (36)$$

noting that $\Psi(0) = (S, T_0, T_\pm)$ as $\exp(i\omega S_z t) = 1$ at $t = 0$.

The exponential operator may be expressed in the basis which diagonalizes H_R, giving

$$e^{-(i/\hbar)Et} , \qquad (37)$$

where

$$E = \mathrm{diag}(H_R) = B^{-1}\, H_R\, B$$

and B is a matrix whose columns are the eigenvectors of H_R. In the original basis the evolution operator becomes

$$B\, e^{-(i/\hbar)Et}\, B^{-1} , \qquad (38)$$

and so

$$\bar{C}(t) = B\, e^{-(i/\hbar)Et}\, B^{-1}\, \bar{C}(0). \qquad (39)$$

The problem is thus reduced to finding the eigenvalues and eigenvectors of H_R, requiring the solution of a quartic characteristic equation. While analytically possible, the solution is formidable. Perturbation theory can, however, be applied to approximate the required eigenvalues and -vectors [14]. Simplification can be achieved in two ways. Neglect of B_1-dependent off-diagonal elements reduces the problem to order 2 and is a treatment applied to the esr study of radical pairs with significant J interaction, B_1 being included as a perturbation [15]. This is clearly inappropriate if the interplay between B_1 and J is a prime concern, in which case $a_{(k)}$ may be more usefully included in a perturbation expansion, after solution of the 3 x 3 problem resulting from neglect of $a_{(k)}$.

2.6.1 Lineshapes

As indicated above the neglect of $a_{(k)}$ is the more useful approach as regards the functional, or in spectroscopic terms, lineshape dependence on the interplay of B_0, B_1 and J. Such a treatment will be adopted in this section.

In the limit of small $a_{(k)}$ we have the following basis for perturbational expansion:

$|S^{\cdot}\rangle$,

$$|t_+\rangle = \frac{B_1}{\sqrt{2}B_{tot}}|T_0^{\cdot}\rangle + \frac{B_{z,eff} + B_{tot}}{2B_{tot}}|T_+^{\cdot}\rangle - \frac{B_{z,eff} - B_{tot}}{2B_{tot}}|T_-^{\cdot}\rangle,$$

$$|t_0\rangle = \frac{B_{z,eff}}{B_{tot}}|T_0^{\cdot}\rangle + \frac{B_1}{\sqrt{2}B_{tot}}\left[\,|T_+^{\cdot}\rangle + |T_-^{\cdot}\rangle\,\right], \qquad (40)$$

$$|t_-\rangle = -\frac{B_1}{\sqrt{2}B_{tot}}|T_0^{\cdot}\rangle - \frac{B_{z,eff} - B_{tot}}{2B_{tot}}|T_+^{\cdot}\rangle + \frac{B_{z,eff} + B_{tot}}{2B_{tot}}|T_-^{\cdot}\rangle,$$

and eigenvalues

$$\begin{aligned}\epsilon_S &= -J - (i/2)\hbar k_S\,, \\ \epsilon_{t_+} &= -(i/2)\hbar k_T + g\beta B_T\,, \\ \epsilon_{t_0} &= -(i/2)\hbar k_T\,, \\ \epsilon_{t_+} &= -(i/2)\hbar k_T + g\beta B_T\,,\end{aligned} \qquad (41)$$

where $B_{tot} = (B^2_{z,eff} + B^2_1)^{1/2} = \mathcal{B}_T$.

Perturbation theory may be employed to approximate the solutions of the 4 x 4 problem if

$$a_{(k)} \ll |\langle S'|H_R|S'\rangle - \langle T'_0|H_R|T'_0\rangle|,$$

or (42)

$$a_{(k)} \ll \tfrac{1}{2}\{J^2 + \tfrac{1}{4}\hbar^2 (k_T - k_S)^2\}^{1/2},$$

the usual criteria for the validity of the approximation [16]. The results, corrected to first order in the (off-diagonal) perturbation $a_{(k)}$, are given below.

eigenvectors:

$$|S'\rangle = |S\rangle + \sum_{-1}^{1} \frac{\langle t_i|T_0\rangle\, a_{(k)}}{\epsilon_S - \epsilon_i} |t_i\rangle\,,$$

(43)

$$\underset{i\,=\,-1,1,1}{|t'_i\rangle} = |t_i\rangle - \frac{\langle T_0|t_i\rangle\, a_{(k)}}{\epsilon_S - \epsilon_i} |S\rangle\,.$$

eigenvalues:

$$\begin{aligned} \epsilon_{S'} &= \epsilon_{S} , \\ \epsilon_{t_i'} &= \epsilon_{t_i} . \end{aligned} \qquad (44)$$

With these approximations, and implicit assumption $a_{(k)} << \hbar/\tau_{rp}$ (radical pair lifetime), the evolution operator (37) may be evaluated [17] and the spin system time dependence determined. For an initial singlet radical pair, the triplet recombination yield is given by

$$\varphi_T(B_0,B_1) = \qquad (45)$$

$$\frac{a_{(k)}^2 K}{2\hbar B_T^2 k_S} \left[\frac{B_1^2}{(J + g\beta B_T)^2 + (\frac{1}{4}\hbar K)^2} + \frac{B_1^2}{(J - g\beta B_T)^2 + (\frac{1}{4}\hbar K)^2} + \frac{2B_{z,eff}^2}{J^2 + (\frac{1}{4}\hbar K)^2} \right],$$

for a given nuclear configuration, where $K = k_S + k_T$. The dependence upon $a_{(k)}^2$ is to be expected for an exponential model of the radical pair dynamics ((22) above).

The field effect on triplet yield now becomes,

$$FE(B_0,B_1) = \frac{\varphi_T(B_0,B_1)}{\varphi_T(B_0,0)} \qquad (46)$$

$$= \quad 1 + \frac{B_1^2}{2B_T^2} \left[\frac{B_1^2}{(J + g\beta B_T)^2 + (\frac{1}{4} K)^2} + \frac{B_1^2}{(J - g\beta B_T)^2 + (\frac{1}{4} K)^2} - 2 \right],$$

where $\hbar$ has been taken as unity for clarity of representation and comparison with reference [18].

The above expression (46) may be usefully employed to outline the behaviour of the field effect with regard to the variables B_0, B_1, J and K but but its limitations arising out of the requirement for small $a_{(k)}$ must be recognized. Indeed in this first order treatment, the field effect is independent of $a_{(k)}$ and an incorrect 'on resonance' condition of

$$B_{z,eff} = B_0 - \frac{\hbar\omega}{\frac{1}{2}(g_1 + g_2)\beta} + \frac{1}{(g_1 + g_2)\beta} [\sum^{(1)} a_n m_{n,k} + \sum^{(2)} a_n m_{n,k}] = 0. \tag{47}$$

This arises out of the independence of first order energies upon $a_{(k)}$.

From the analytical result for the field effect, FE (46), the following expressions for the extrema of the function may be derived by differentiation with respect to B_0 and B_1 [18]:

B_0 spectrum:

maxima: $$B_{z,eff} = \pm (g\beta)^{-1}[3J^2 - K^2 - (g\beta B_1)^2 - 2|J|(J^2 + K^2)]^{\frac{1}{2}}, \tag{48a}$$

minima: $$B_{z,eff} = \pm (g\beta)^{-1}[3J^2 - K^2 - (g\beta B_1)^2 + 2|J|(J^2 + K^2)]^{\frac{1}{2}}, \tag{48b}$$

maximum or minimum: $B_{z.eff} = 0$,

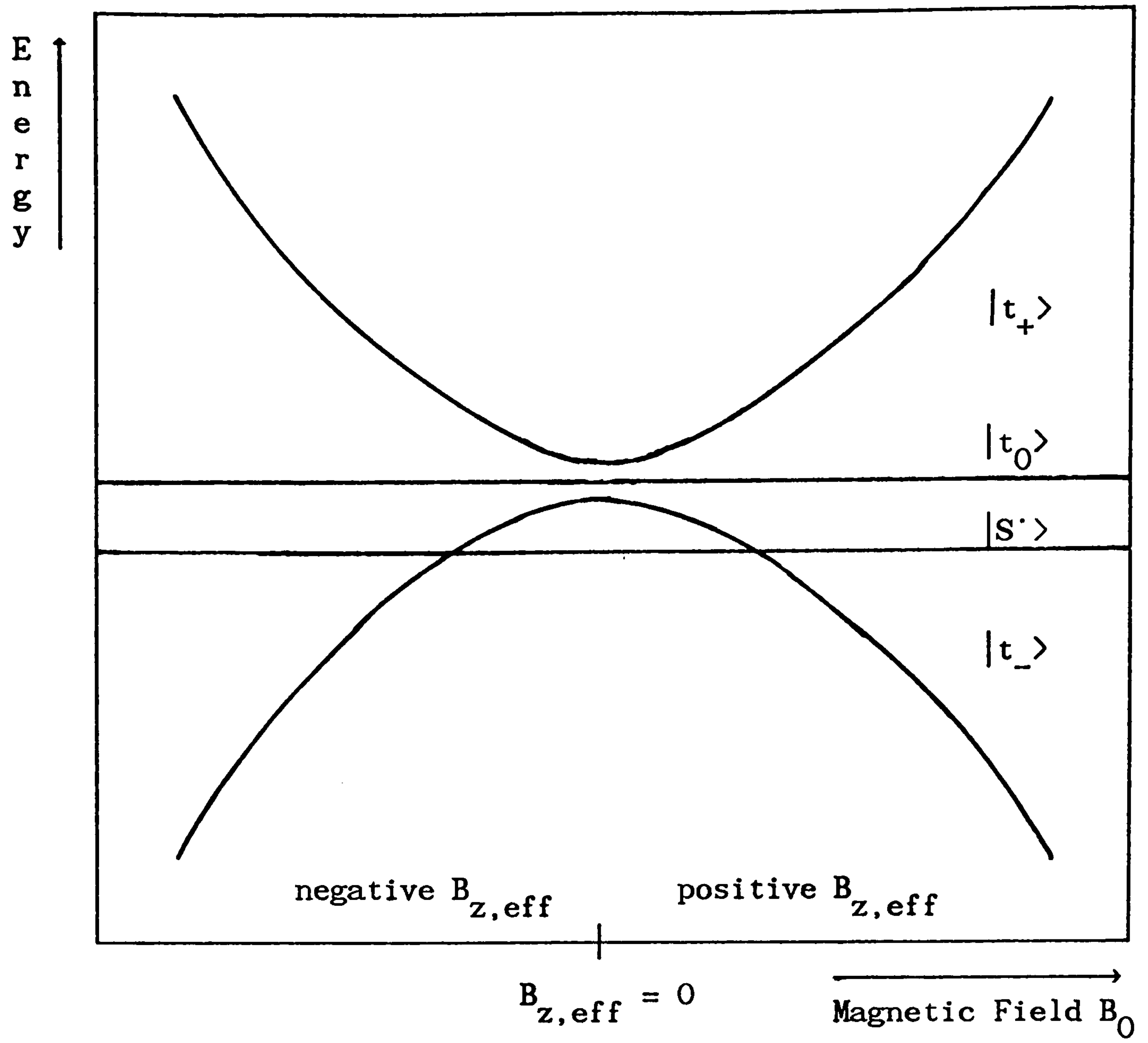

Figure 2.4. Diagramatic representation of the zeroth-order rotating-frame electronic term energies as a function of static field B_0. The $|S'\rangle - |t_0\rangle$ separation is due to a Heisenberg exchange interaction. Note the $|t_-\rangle - |S'\rangle$ crossing close to $B_{z,eff} = 0$.

B_1 spectrum($B_{z,\mathrm{eff}} = 0$):

$$\text{maxima:}\quad B_1 = (g\beta)^{-1}[\, -(J^2 + K^2) + 2|J|(J^2 + K^2)^{1/2}\,]^{1/2},$$

$$\text{maximum or minimum:}\quad B_1 = 0. \tag{49}$$

Interpretation of the above formulae (48,49) is best done in conjunction with figure 2.4 which shows a schematic of the zero order rotating frame eigenstates as a function of B_0. The effect of varying B_0 on S → T intersystem crossing may be viewed by considering two factors:

(1) $\epsilon_{t_i} - \epsilon_S$. ,

(2) $\langle T_0 | t_i \rangle$.

The B_1 field acts to distribute $|T_0\rangle$ character throughout the $|t_i\rangle$ manifold, while $a_{(k)}$ serves to mix $|S\rangle$ and $|T_0\rangle$. If $J \neq 0$, an enhancement in intersystem crossing may be achieved as $|T_0\rangle$ character, mixed into the $|t_-\rangle$ state, is brought closer in energy to the $|S\rangle$ state as $B_{z,\mathrm{eff}}$ approaches zero. The $|S\rangle$, $|t_-\rangle$ crossings in fig 2.4 illustrate how such 'J' resonances occur. More quantitatively the analytical expression for the extrema of a B_0 spectrum (48) reveal symmetrical J resonances at each side of centre field ($B_{z,\mathrm{eff}} = 0$), with each maximum associated with a minimum at a greater offset from the centre position. The occurence of the latter features requires the square root expressions (48) to be real and so

$$B_1 \;>\; (g\beta)^{-1}\,[\, 3J^2 - K^2 + 2|J|(J^2 + K^2)^{1/2}\,]^{1/2}\, , \tag{50}$$

although J maxima disappear at

$$B_1 \quad > \quad (g\beta)^{-1} [\ 3J^2 - K^2 - 2|J|(J^2 + K^2)^{\frac{1}{2}}\ ]^{\frac{1}{2}} . \qquad (51)$$

At $B_{z,eff} = 0$, $|T_0\rangle$ character is equally distributed amongst the $|t_+\rangle$ and $|t_-\rangle$ states. The effect of B_1 is to split the t-state degeneracy, separating $|t_+\rangle$ and $|t_-\rangle$ from $|t_0\rangle$. Thus, in the absence of J, and in the approximation of $a_{(k)} \ll g\beta B_1$, the centre of a B_0 spectrum shows a decrease in intersystem crossing as B_1 moves $|T_0\rangle$ character away from $|S\rangle$. This may be considered as the rotating frame analogue of low field MARY spectra. The parallel may be carried further in that, if $J \neq 0$, a B_1 spectrum will show a J resonance at a position given by (49).

The analytical solution for a singlet initial pair, and triplet reaction, has served to illustrate the origin of RYDMR lineshape. Consideration of an initial triplet pair, together with singlet reaction, introduces one further variable in the form of the relative weighting of ISC contributions from each of the t-states. In turn this is determined by the initial triplet population distribution in the laboratory frame.

Of particular interest is the generation of a radical pair with enhanced $|T_+\rangle$ or $|T_-\rangle$ population relative to $|T_0\rangle$; a situation familiar in CIDEP [19]. Such polarization leads to differential weighting of $t_\pm$ states in the rotating frame.

In the presence of a J interaction, the symmetrical energy relationship of $|t_\pm\rangle$ to $|S'\rangle$ is lost. Under such circumstances polarization effects would be expected to appear at $B_{z,eff} = 0$ and similarly at the J resonance positions.

The hitherto uninvestigated triplet problem has been solved analytically, but the results will not be presented in view of the fact that most features are those revealed by the much simpler singlet expressions. Instead, only the results of calculations for this model will be given.

In order to illustrate the rationale behind the experimental work of chapter 5, calculations were performed to reveal the B_0, B_1, k_S and polarization dependence of RYDMR spectra. All involved a single hypothetical radical pair in the limit of vanishing $a_{(k)}$. Parameters were restricted to those expected and/or observed in the experimental work. Results, in terms of relative singlet yield, are presented in figures 2.5 - 2.9.

The unpolarized B_0 spectra of figure 2.5 show the effect on lineshape of an increasing B_1, ranging above and below J. Both types of resonance predicted by the analytical singlet expression (48) may be seen at low B_1. In the wings, at $B_{z,eff}$ determined by J, B_1 and K, are two J resonances with linewidths governed by K and B_1. At $B_{z,eff} = 0$ (centre field) the second type of resonance is clearly seen.

Increase of B_1 leads to a merging ('power narrowing') and broadening of the J resonances until they cease to be resolved and eventually disappear when expression (48a) gives only imaginary solutions. The outer minima (48b) grow, and also merge, until the RYDMR spectrum is entirely inverted.

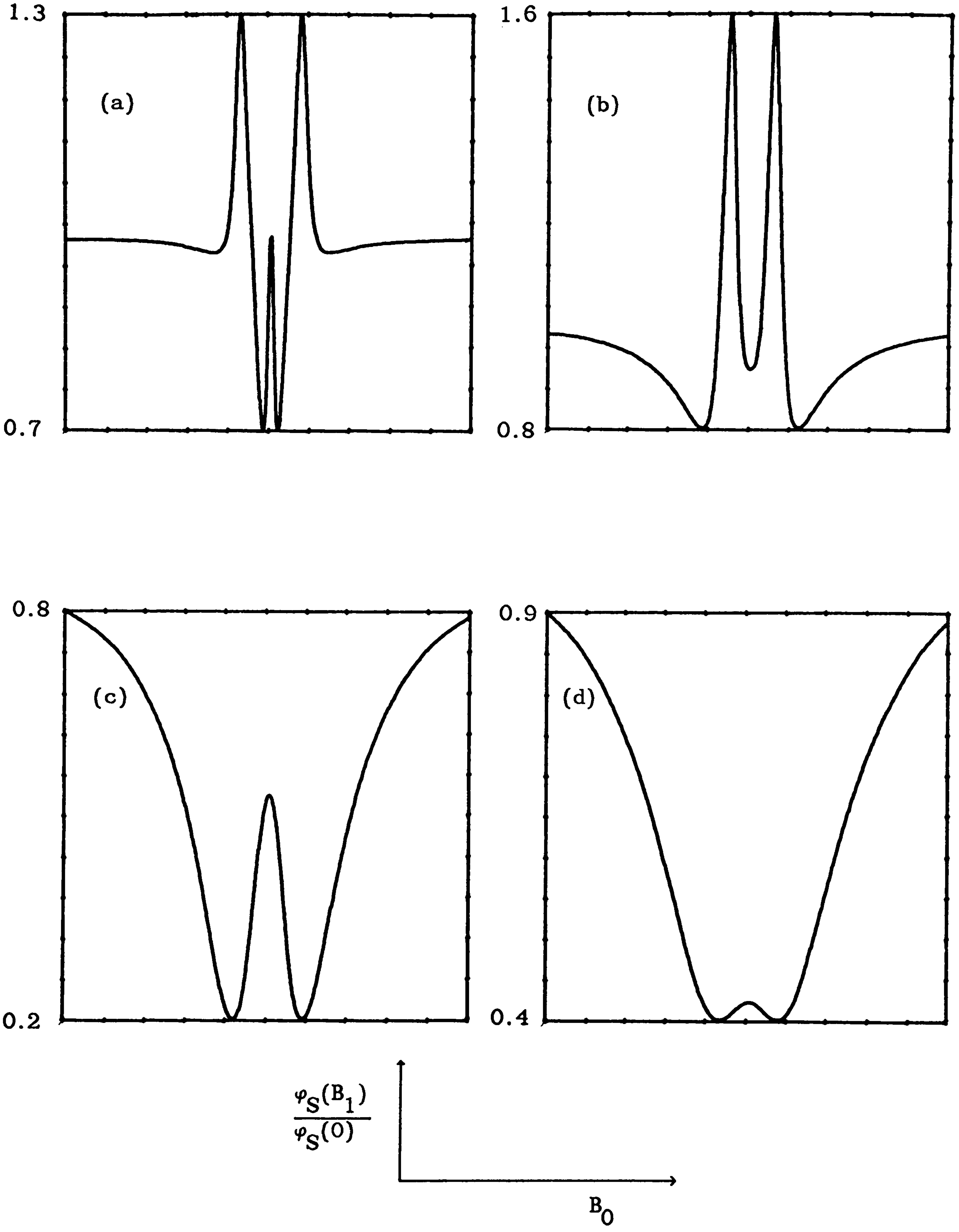

Figure 2.5. Effect of r.f. power. RYDMR B_0 dependence of relative singlet yield, from an initial triplet radical pair, at several values of B_1 and in the limit of vanishing $a_{(k)}$.

Parameters: B_0 sweep = 3425 ± 25 G, r.f. frequency = 9.6 GHz, J = 4 G, $k_S = 5 \times 10^6\ s^{-1}$, $k_T = 1 \times 10^{-3}\ s^{-1}$, uniform initial population.

(a) B_1 = 1 G. (b) B_1 = 3 G. (c) B_1 = 5 G. (d) B_1 = 8 G.

Figure 2.6 illustrates the effect of radical pair lifetime in determining the width and separation of J resonances, and indeed the point at which a spectral inversion is obtained.

The J dependence of B_1 spectra at $B_{z,eff} = 0$ is displayed by the series of simulations in figure 2.7. The absence of a J resonance for the J = 1 G case is accounted for by essentially lifetime broadening effects at a K value equivalent to $\simeq$ 2 G (expression (48b)). The general trend is one of decreasing ISC with increasing B_1, but interestingly maxima may be seen at B_1 values less than those required for J resonance. This is not predicted by expression (48b).

Figures 2.8 and 2.9 repeat the previous B_0 and B_1 spectra but with a polarized triplet pair having an enhanced $|T_+\rangle$ population. B_0 spectra display unsymmetrical behaviour about $B_{z,eff} = 0$, the high field lineshape being inverted with respect to that at low field and that for an unpolarized pair. The converse situation holds for enhanced $|T_-\rangle$ population and so, knowing the form of the initial polarization, the spectral shape is expected to be indicative of the sign of J.

Polarized B_1 spectra show broadly the same features as their unpolarized counterparts except for the presence of a maximum in the J = 1 G case. This would seem to be related to the unexpected maxima observed in the spectra of figure 2.7.

The above simulations have briefly served to illustrate the behaviour expected for vanishing hyperfine interaction and have introduced the further considerations necessary for a triplet initial pair. It must be recognized, however, the treatment was that of simple first-order

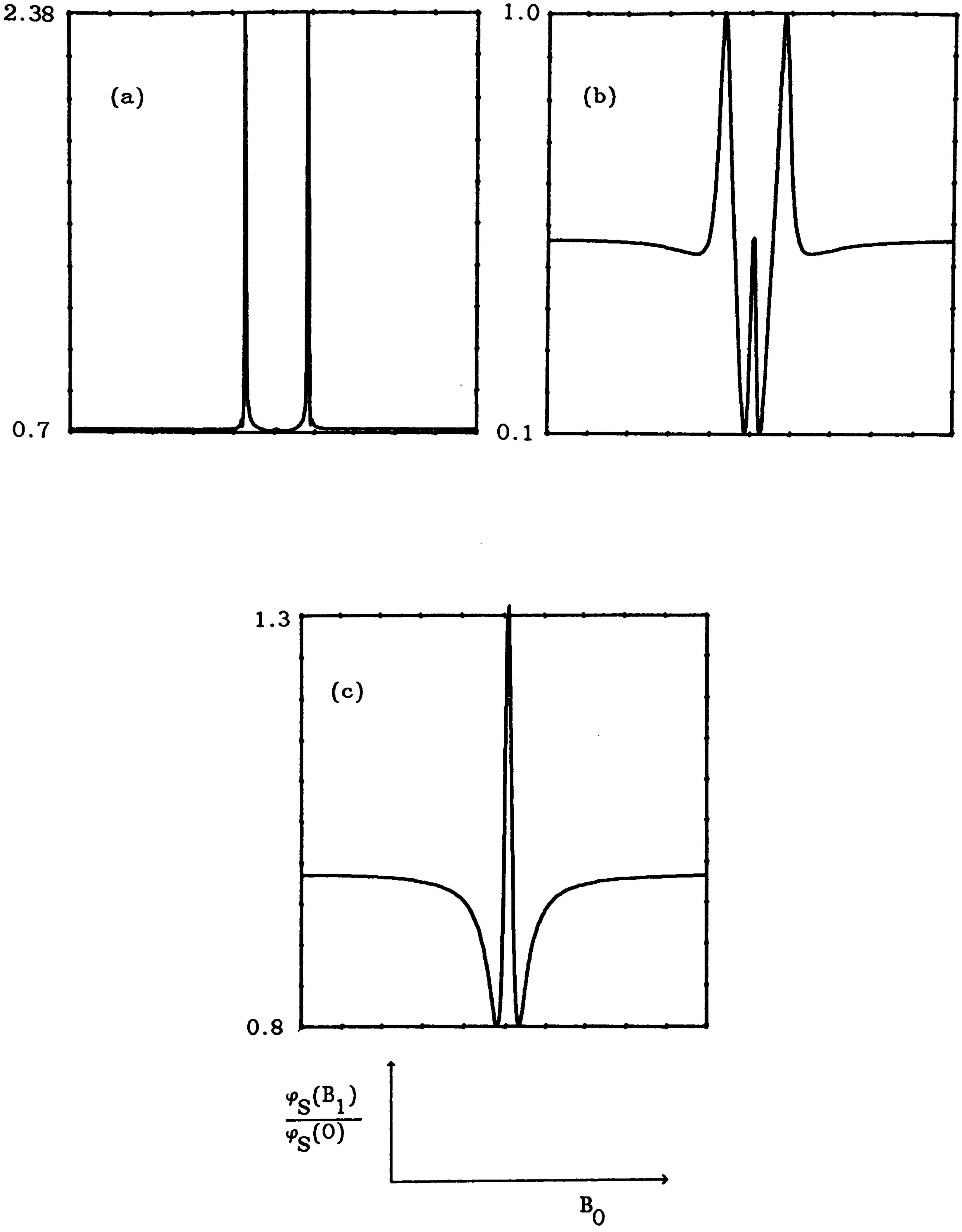

Figure 2.6. Effect of lifetime. RYDMR B_0 dependence of relative singlet yield, from an initial triplet radical pair, at several values of k_S and in the limit of vanishing $a_{(k)}$.

Parameters: B_0 sweep = 3425 ± 25 G, r.f. frequency = 9.6 GHz, B_1 = 1 G, J = 4 G, $k_T = 1 \times 10^3$ s^{-1}, uniform initial population.

(a) $k_S = 5 \times 10^5$ s^{-1}. (b) $k_S = 5 \times 10^6$ s^{-1}. (c) $k_S = 5 \times 10^7$ s^{-1}.

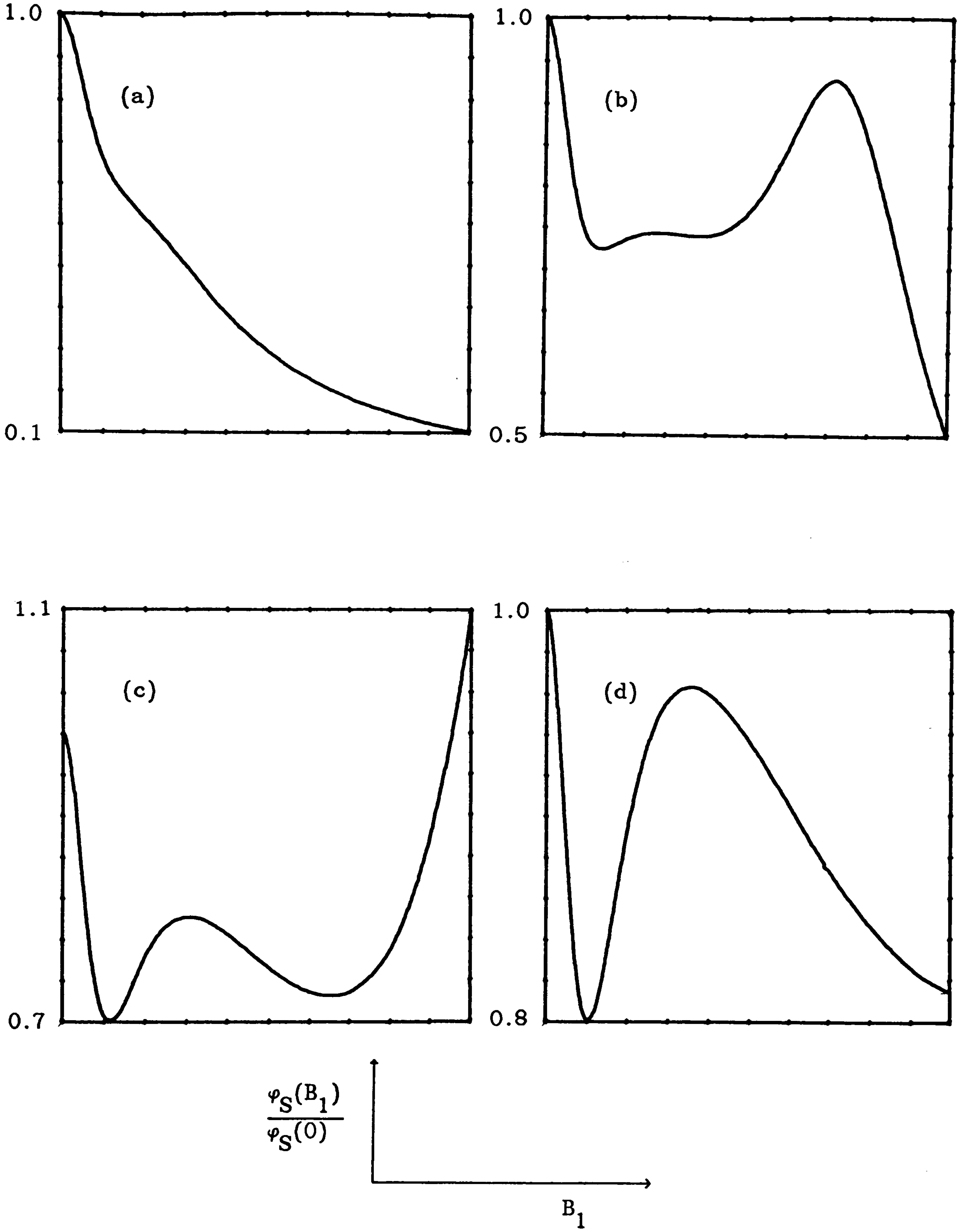

Figure 2.7. Effect of Heisenberg exchange. RYDMR B_1 dependence of relative singlet yield, from an initial triplet radical pair, at several values of J and in the limit of vanishing $a_{(k)}$.

Parameters: B_0 = 3425 G, r.f. frequency = 9.6 GHz, B_1 = 0 - 4 G, k_S = 5 x 10^6 s^{-1}, k_T = 1 x 10^{-3} s^{-1}, uniform initial population.

(a) J = 1 G. (b) J = 3 G. (c) J = 5 G. (d) J = 8 G.

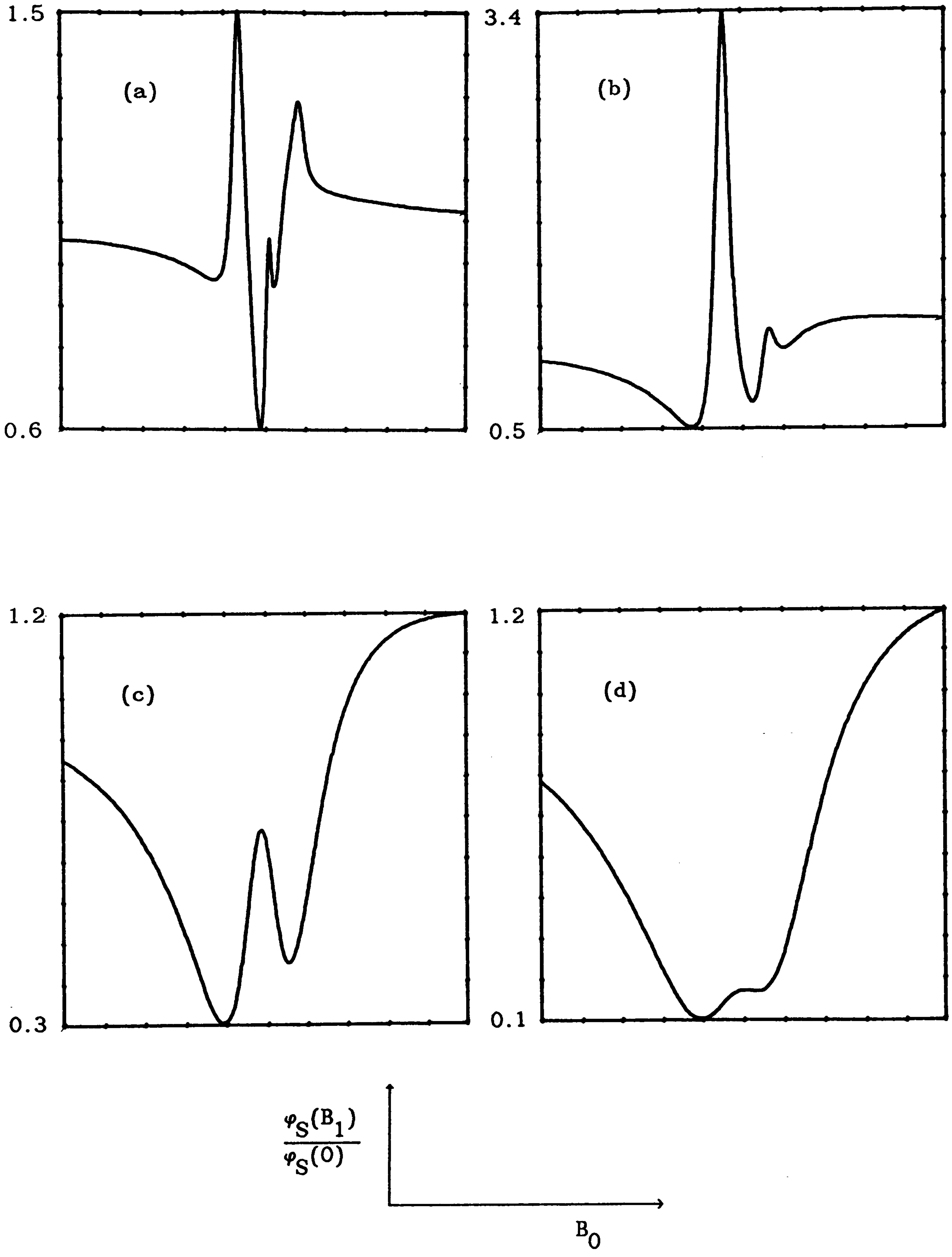

Figure 2.8. Effect of initial pair polarization. RYDMR B_0 dependence of relative singlet yield, from an initial triplet radical pair, at several values of B_1 and in the limit of vanishing $a_{(k)}$.
Parameters: B_0 sweep = 3425 ± 25 G, r.f. frequency = 9.6 GHz, J = 4 G, $k_S = 5 \times 10^6\ s^{-1}$, $k_T = 1 \times 10^{-3}\ s^{-1}$, initial populations: $T_+ : T_0 : T_- = 3 : 2 : 1$.
(a) B_1 = 1 G. (b) B_1 = 3 G. (c) B_1 = 5 G. (d) B_1 = 8 G.

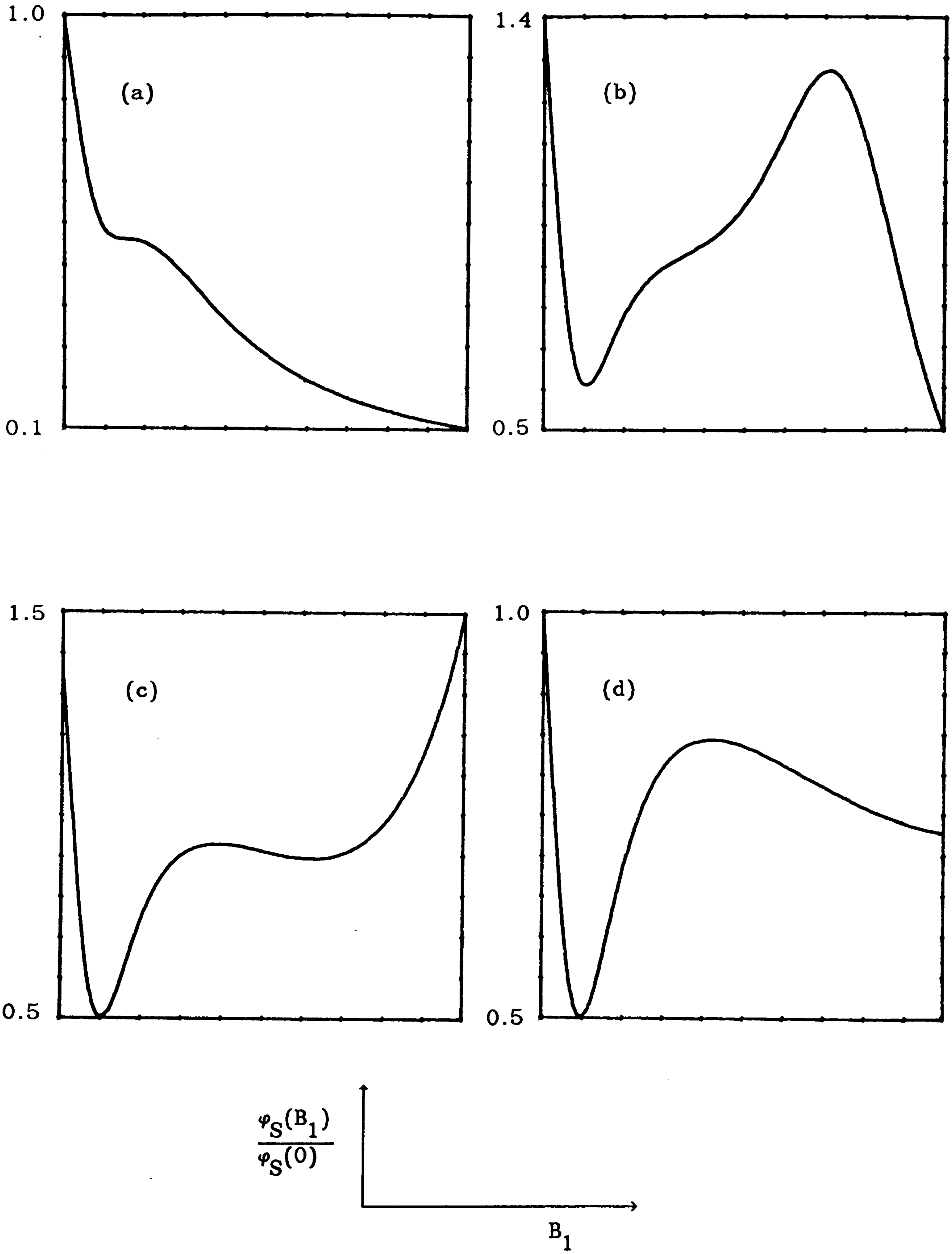

Figure 2.9. Effect of initial pair polarization. RYDMR B_1 dependence of relative singlet yield, from an initial triplet radical pair, at several values of J and in the limit of vanishing $a_{(k)}$.
Parameters: B_0 = 3425 G, r.f. frequency = 9.6 GHz, B_1 = 0 - 4 G, $k_S = 5 \times 10^6\ s^{-1}$, $k_T = 1 \times 10^{-3}\ s^{-1}$, initial poulations: $T_+ : T_0 : T_- = 3 : 2 : 1$.
(a) J = 1 G. (b) J = 3 G. (c) J = 5 G. (d) J = 8 G.

perturbation theory and so its results, especially with regard to RYDMR intensity, are only indicative of the exact values. Consideration of real radical pair systems must also include an averaging over a full ensemble and so predictions, especially as to the points of RYDMR inversion, are not expected to be accurate.

2.6.2 Line Positions

The above discussion has been in the limit of vanishing $a_{(k)}$, focussing purely on a homogeneous lineshape. From the point of view of line positions in a B_0-swept spectrum when the hyperfine interaction is non-vanishing, the problem is best treated in the second limit of vanishing B_1, discussed earlier. The zero-order electronic eigenstates now become [15]:

$$\begin{aligned} |\Psi_1\rangle &= |T_+\rangle\ , \\ |\psi_2\rangle &= \cos\Theta\ |T_0\rangle + \sin\Theta\ |S\rangle, \\ |\psi_3\rangle &= -\sin\Theta\ |T_0\rangle + \cos\Theta\ |S\rangle, \\ |\Psi_4\rangle &= |T_-\rangle\ , \end{aligned} \qquad (52)$$

where

$$\begin{aligned} \cos 2\Theta &= J/2\omega\ , \\ \sin 2\Theta &= a_{(k)}/\omega\ , \\ \omega &= [\ \tfrac{1}{4}J^2 + a^2_{(k)}\ ]^{\frac{1}{2}}\ , \end{aligned}$$

where $(k_T - k_S) \ll |J|$ has been assumed in order that imaginary energy contributions may be neglected.

B_1 induces transitions between the states at energies given by [15]

$$
\begin{aligned}
E(\Psi_2,\Psi_1) &= \tfrac{1}{2}(g_1 + g_2)\beta B_0 + \tfrac{1}{2}\,\Sigma\,(a_{1i}m_{1i} + a_{2i}m_{2i}) - \tfrac{1}{2}J + \omega\ , \\
E(\Psi_3,\Psi_1) &= \tfrac{1}{2}(g_1 + g_2)\beta B_0 + \tfrac{1}{2}\,\Sigma\,(a_{1i}m_{1i} + a_{2i}m_{2i}) - \tfrac{1}{2}J - \omega\ , \\
E(\Psi_4,\Psi_2) &= \tfrac{1}{2}(g_1 + g_2)\beta B_0 + \tfrac{1}{2}\,\Sigma\,(a_{1i}m_{1i} + a_{2i}m_{2i}) + \tfrac{1}{2}J - \omega\ , \\
E(\Psi_4,\Psi_3) &= \tfrac{1}{2}(g_1 + g_2)\beta B_0 + \tfrac{1}{2}\,\Sigma\,(a_{1i}m_{1i} + a_{2i}m_{2i}) + \tfrac{1}{2}J + \omega\ ,
\end{aligned}
\tag{53}
$$

demonstrating that in the limit $J = 0$, the B_0 spectrum becomes that expected from a first-order esr treatment of the individual radicals constituting the pair. If $0 < J \ll a_{(k)}$, the esr lines split into doublets separated by J and whose centres are at the positions expected for non-interacting species.

It is tempting to compose a spectral simulation by convoluting the lineshape and resonance positions from the relevant limiting approaches, but its usefulness would be compromised by neglect of the subtle interplay between the relative magnitudes of $a_{(k)}$ and J. Instead experimental results will be interpreted purely from the standpoint of the two limiting cases.

CHAPTER 3

APPARATUS

3.1 Introduction

This chapter briefly explores what, in principle, may be gained from a study of static and high frequency magnetic field effects on radical reactions. It sets out the experimental requirements and details how these were met in the apparatus constructed by the author. In addition it describes the data manipulation techniques used to enhance the system performance.

The terms MAgnetic Reaction Yield (MARY) and Reaction Yield Detected Magnetic Resonance (RYDMR) [1] have already been introduced and will be utilized here to describe the experiments involving respectively static magnetic fields and resonant high frequency magnetic fields.

Essentially MARY amd RYDMR studies are capable of revealing the same information as to radical pair nature and behaviour, but the latter can offer perhaps the more immediate interpretation. The comparison is really one of a magnetic susceptibility technique versus that of magnetic resonance, capable of selecting out components of the ensemble magnetic behaviour.

From the previous chapter it can be seen that radical pair spin and spatial dynamics are the two factors influencing MARY and RYDMR lineshape behaviour, but that exact calculations, with a view to fitting experimental data, are not feasible for a generalized radical pair. Furthermore, parallels may be drawn between this situation and that of CIDEP, for which models have been shown to be rather insensitive to the microscopic details of diffusional behaviour [2]. We might expect a similar insensitivity in the case of field effects, and so their major application would seem to be in elucidating magnetic properties.

Low field MARY spectra halfwidths serve to provide an estimate of an effective hyperfine coupling constant for a radical pair, allowing discrimination of radicals and an indication of the existence of electron hopping processes [2.3]. Additionally a very low field resonance may be present, permitting the magnitude of $S-T_0$ separation to be determined (see later chapters).

High field MARY spectra, at fields of a few kilogauss or greater, are governed by the Δg mechanism. Saturation behaviour is expected only at extremely high fields of the order of 10^4 kG, and is essentially determined by diffusional behaviour. The saturation condition corresponds to rapid $S-T_0$ interconversion compared to the timescale of diffusional encounters, and shows a sign of field effect opposite to that which is characteristic of low field saturation.

The usefulness of magnetic information gained from MARY experiments is enhanced by the knowledge that it is representative of the species present during a period of time characterized by the 'pair lifetime'. Observations of reaction yield on a timescale long compared to the geminate phase of reaction, but short compared to the much slower homogeneous phase, is thus sufficient to attain geminate time resolution. Indeed any requirement for fast detection is relaxed still further by recognition of the relative insensitivity to magnetic fields of random spin homogeneous reaction. Thus c.w. experiments, involving continuous radical pair generation and yield monitoring, are still able to achieve very high time resolution by virtue of the internal sampling period provided by diffusional motion.

The major drive towards developing the RYDMR technique was one of achieving very high time resolution in an esr experiment, based upon the points outlined above for the MARY experiment. At this juncture it is useful to consider the relationship between conventional esr and RYDMR.

The esr experiment is performed by applying radiation and static fields to a radical system such that their respective magnetic field vectors are in perpendicular planes. In a frame of reference rotating at the radiation field frequency, the behaviour of sample magnetization soon after its generation may be treated by the familiar Bloch equations [3]. A pictorial representation is given in figure 3.1 for the on-resonance situation of the radiation field frequency matching that of the spin Larmor precession in the applied static field. The system evolution consists of a precession of the magnetization in the yz plane about the radiation magnetic field direction, accompanied by exponential decay towards equilibrium of the longitudinal (z) and transverse (x,y) components by T_1 and T_2 processes respectively. Detection of the magnetization component, M_y, in the plane of, and in phase quadrature with, the radiation field corresponds to the absorption mode most usually employed in esr experiments. High time resolution, therefore, requires a significant y component of the magnetization at the time of interest and may be achieved by the application of a high radiation field strength to increase the rate at which the initial longitudinal magnetization is tipped into the observation direction.

As magnetic resonance experiments usually employ a resonant structure to apply the necessary radiation field there are, in general, two means of providing the large field strengths needed for high time resolution. One is to enhance the resonator Q factor, but this also has the effect of

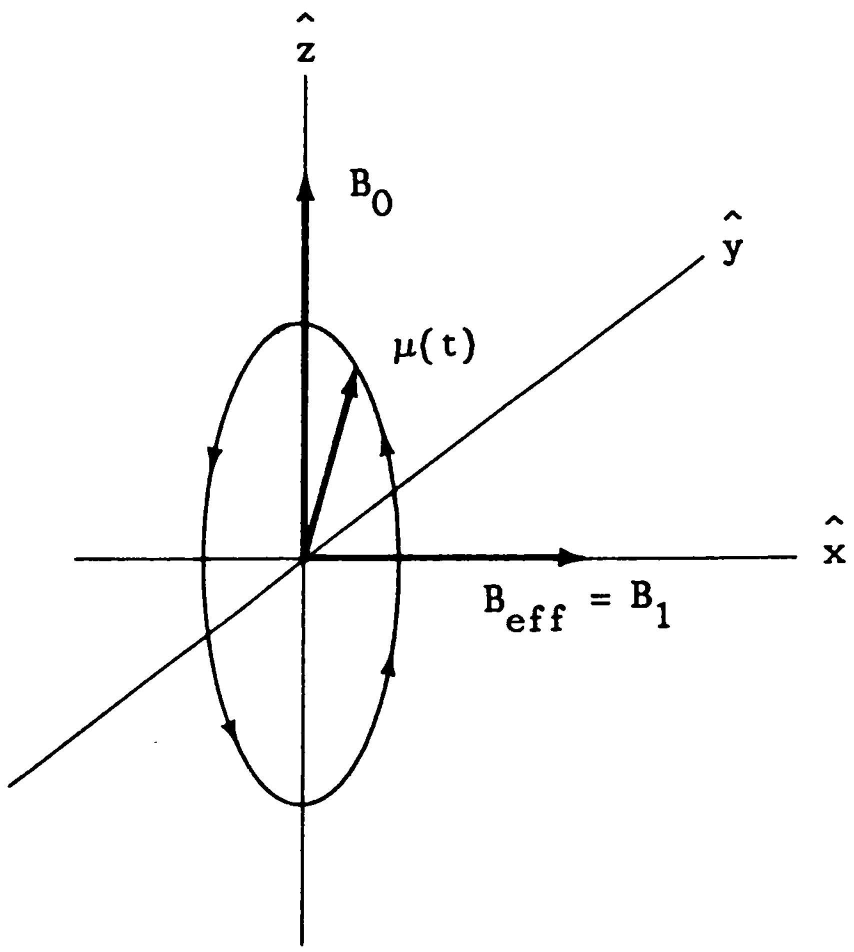

Figure 3.1. Rotating frame Bloch vector representation of coherent transitions in a two-level system. Depicted is the 'on resonance' precession of the magnetization, μ, in the yz plane about the applied radiation-field direction (x).

decreasing the system bandwidth for the esr signal and so tends to negate any improvement in absorption signal magnitude, at short times.

The second option is to increase the radiation power incident on the resonant structure. This, however, introduces technical difficulties associated with maintaining high power levels <u>and</u> monitoring weak absorption signals at an identical frequency and in the same channel. To a certain degree these difficulties may be overcome by the use of pulsed magnetic resonance techniques [4] but nevertheless considerable improvement in the situation might be expected by separating the detected signal frequency from that of the applied (resonant) radiation field, decoupling the conflicting bandwidth requirements outlined above. It is desirable, therefore, to search for a system response, other than the generation of a transverse magnetization, which will enable the resonance condition to be detected. The potential of RYDMR as a magnetic resonance technique of high time resolution now becomes apparent; it is analogous to monitoring the longitudinal magnetization (state population difference) behaviour in terms of the two-level Bloch treatment discussed above.

Depending upon the actual chemical system under study, various possibilities exist for performing the necessary monitoring of state populations required for RYDMR. Perhaps the most direct, and that originally used in solid state work, is the detection of recombination fluorescence. If the emission lifetime is sufficiently short, the time-dependent signal corresponds essentially to the reaction-damped evolution of radical pair ensemble singlet character. This is the basis of the FDMR technique [5] adopted for pulse radiolysis studies.

Less direct methods, though more widely applicable, would involve the detection of reaction yields for either products or reactants. A whole range of physical techniques may be employed, for example making use of optical absorption, fluorescence, scattering or electrical conductivity. Finally, if time resolution within the geminate radical pair lifetime is not a requirement, c.w. methods are quite acceptable, as described for MARY experiments above, and can take advantage of long integration times leading to improved S/N.

The following sections describe how the broad principles, outlined above, were realized in experimental apparatus capable of quantitatively applying MARY and RYDMR to various chemical systems.

3.2 Design Concept

At all stages it was attempted to maintain generality as far as possible, without significantly compromising effectiveness of operation. Consequently a range of time-resolved experiments, in addition to MARY and RYDMR, may be performed. Many of these are essential in providing complementary information needed for a fuller understanding of the MARY and RYDMR work.

The second major element of the design philosophy was to ensure that signal averaging could easily be applied to any mode of apparatus operation. This was based upon the assumption that achieving good S/N would, in general, be a problem as indicated by the inconclusive nature of many reports concerning magnetic field effects on chemical reactions that existed in the literature at the time of design conception.

For descriptive purposes the apparatus may be conveniently divided into five functional elements:

(1) Radical Generation

(2) Signal Detection

(3) Magnetic Field Production

(4) System Control

(5) Signal Capture and Processing.

At this level there is no distinction between MARY and RYDMR experiments.

3.3 Radical Generation

A flash photolysis system, employing a Lamda Physik multi-gas laser, was used to initiate radical production. Previous experience [6] had shown that operation at the 308nm transition of XeCl was satisfactory for the excitation of a wide range of organic species, which subsequently react to give radical pairs. The broadband laser output is quite acceptable for liquid phase applications.

A major limitation of excimer lasers becomes apparent when attempting high time resolution studies in that the pulse width and energy are heavily dependent on the buffer gas (He or Ne) employed in the discharge mixture. To achieve a 20 ns FWHM pulse width, limited essentially by discharge circuitry characteristics, some output energy was sacrificed and a He buffer gas utilized, giving approximately 100 mJ per pulse. Despite this manipulation, the pulse width still remained a major obstacle to some of the attempted work and did not closely approach the desired δ- function excitation, as may be achieved, for example, in pulse radiolysis work.

Use of an N_2 lasing medium, at an output wavelength of 337 nm and energy ~2 mJ per 6 ns FWHM pulse, permitted a useful compromise to be reached for some experiments involving species with high extinctions at this wavelength. The near gaussian temporal structure of the output is also potentially useful for subsequent quantitative data analysis.

A further restriction imposed by the use of multi-gas lasers comes in the form of the low repetition capability. For the particular models used this could not exceed a few tens of Hertz, rendering extensive signal averaging a very time consuming task requiring good long-term stability from other system components. In setting a comparatively low system averaging rate they do, however, ease design requirements on signal processing equipment.

Pulse-pulse reproducibility was optimized with respect to thyratron and discharge voltage settings, achieving, at best, a few percent variability in the output. To maintain these conditions control of photolysis energy was performed by beam attenuation and/or focussing, facilitated by its large area (2.5cm x 1.5cm). In addition a quartz plate beam splitter and silicon photodiode combination served to monitor laser output, allowing compensation for pulse-pulse variation to be accomodated at the signal processing stage; a facility which proved useful for some chemical systems.

The repetitive photolysis of a sample, as encountered when signal averaging, brings with it a need for sample replenishment and this was provided by a flow delivery system. In the interests of sample reproducibility and homogeneity, photolysis volumes were kept small and so enabled high linear to bulk flow rate ratios to be achieved. The choice of 'Spectrosil' rectangular flat cells (2cm x 1cm x 0.5mm) for RYDMR experiments was dictated by the use of aqueous samples, whilst MARY experiments employed rectangular quartz flow cuvettes (1cm x 1cm x 3cm). These proved more convenient from the point of view of coupling to the rest of the optical system.

The whole sample delivery system comprised only 'Teflon' and glass, jacketed, as far as was possible, to allow temperature control by means of a thermostatted fluid (water or N_2). In addition an inert atmosphere (N_2 or Ar) could be maintained around the sample. Flow control was performed by a peristaltic pump on the outflow side.

Further details on the sample containment system may be found in the section covering signal detection.

3.4 Signal Detection

The aim was to detect changes in an aspect of a particular radical pair system, arising as a result of the application of the appropriate magnetic fields. Techniques based upon three observable quantities, all capable of providing high time resolution, were adapted to the needs of MARY/RYDMR experiments, but met with varying degrees of success. Two made use of an optical approach, whilst the third relied on nanosecond conductivity transients arising from the generation of radical ion pairs in an electric field of several hundred volts cm^{-1} and with electrode areas of ~1 cm^2. Major attractions of this technique were its easier adaptation to optically inaccessible areas, its immunity to interfering optical signals arising from photolysis and its direct relationship to radical pair concentration. It is, however, restricted to ion pairs and was found to be excessively susceptible to r.f. noise associated with the photolysis laser discharge. For these reasons the technique was not pursued, but it may warrant further investigation.

Of the two optical methods utilized, that of U.V./visible time-resolved absorption is potentially the most generally applicable in solution, but is limited in its usefulness by several factors. The most fundamental of these is that, by definition, it is an indirect method involving the detection of a change (often small) in a transmission signal. The presence of a large background signal leads to inferior S/N performance compared to a fluorescence technique. Consider, for example, photomultiplier shot noise whose magnitude grows in proportion to the square root of anode current. From the Beer-Lambert law the observed anode current i is related to the optical density, A, of the solution by

$$i = i_0 \exp(-A) \tag{1}$$

where i_0 would be observed for zero optical density. We are interested in a small change, Δi, in anode current resulting from the generation of a transient concentration of absorbing species of optical density A'.

The relevant expression is:

$$\Delta i \quad = \quad i_0\{\exp(-A) - \exp(-[A+A'])\}. \qquad (2)$$

The term in braces cannot exceed unity and is typically << 1. Writing it as a constant C, for a particular radical concentration, we have,

$$\Delta i \quad = \quad Ci_0, \qquad (3)$$

and for the rms noise amplitude,

$$N \quad = \quad k\sqrt{i_0}, \qquad (4)$$

giving, for the signal to noise ratio,

$$S/N \quad = \quad \frac{\Delta i}{N} \quad = \quad \frac{Ci_0}{k\sqrt{i_0}} \quad = \quad \frac{C}{k}\sqrt{i_0}, \qquad (5)$$

where k is a detection system constant which includes the bandwidth. This should be compared to the direct-detection situation where the required signal is the primary observable,

$$S/N \quad = \quad \frac{i}{k\sqrt{i}} \quad = \quad \frac{\sqrt{i}}{k}. \qquad (6)$$

Clearly a direct technique is to be preferred on the grounds of signal to noise for a given detection bandwidth. Considering photomultiplier shot noise alone,

$$k = (2eG\Delta f)^{\frac{1}{2}} \qquad (7)$$

where e is the electronic charge, G the photomultiplier gain and Δf the system bandwidth. Thus this simple expression (7) serves to illustrate the requirement of high photon flux for wide bandwidth (high time resolution) experiments, and that fluorescence detection can offer potential S/N enhancements over an absorption technique.

Before describing the details of the detection apparatus it should be made clear that neither optical method was considered ideal for use in the liquid phase as a consequence of the generally poor species discrimination, arising from broad absorption/emission spectra.

Figures 3.2 and 3.3 show typical designs for MARY and RYDMR sample cells together with optical arrangements for application of the fluorescence and absorption techniques.

A key feature of the RYDMR cell design is the use of light guides for conveying light into, and out of, the flat cell, which is itself situated in a rectangular microwave resonant cavity. Despite large coupling losses associated with the use of light guide structures, they were seen as the most efficient means of incorporating the inaccessible sample area into the optical system and maintaining a signal path transverse to that of the photolysis beam. In the case of absorption detection, the resulting path length is much greater than would be achieved by the use of co-linear analyzing and photolysis inputs.

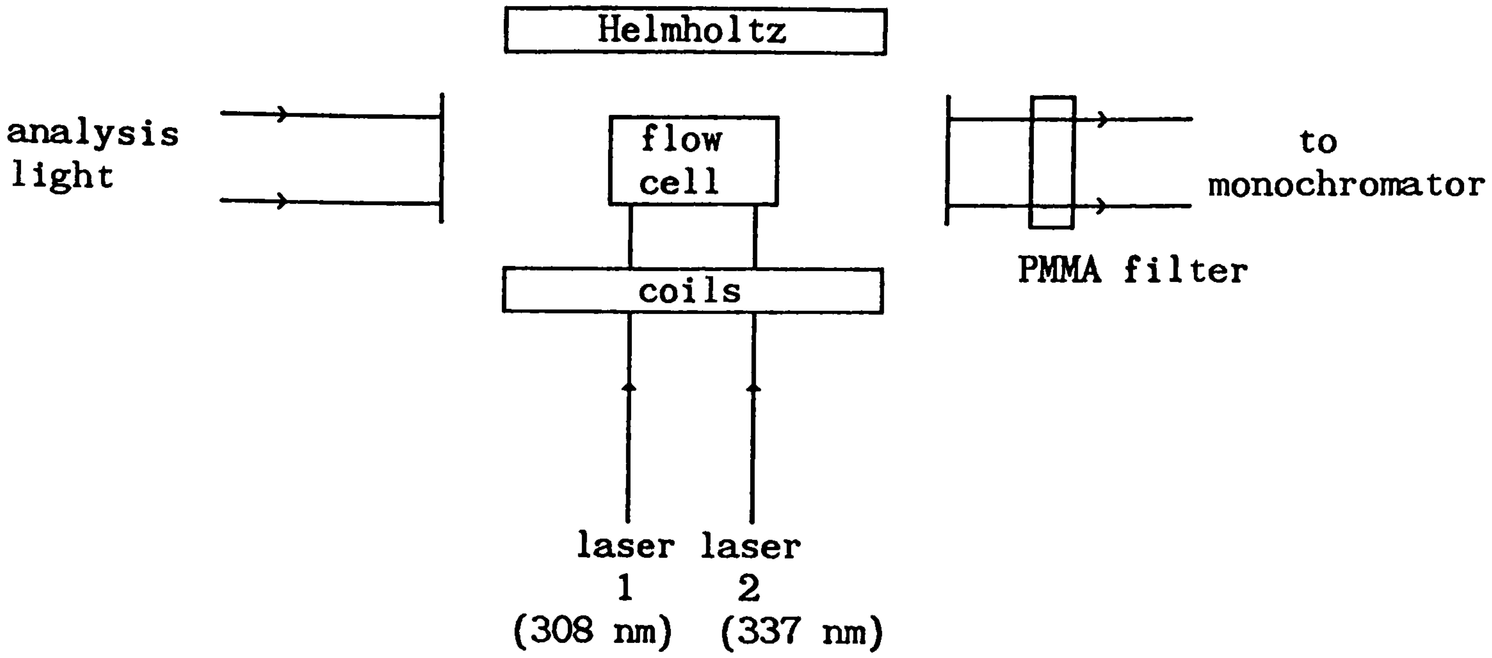

Figure 3.2. Schematic showing optical arrangement for fluorescence and absorption detection.

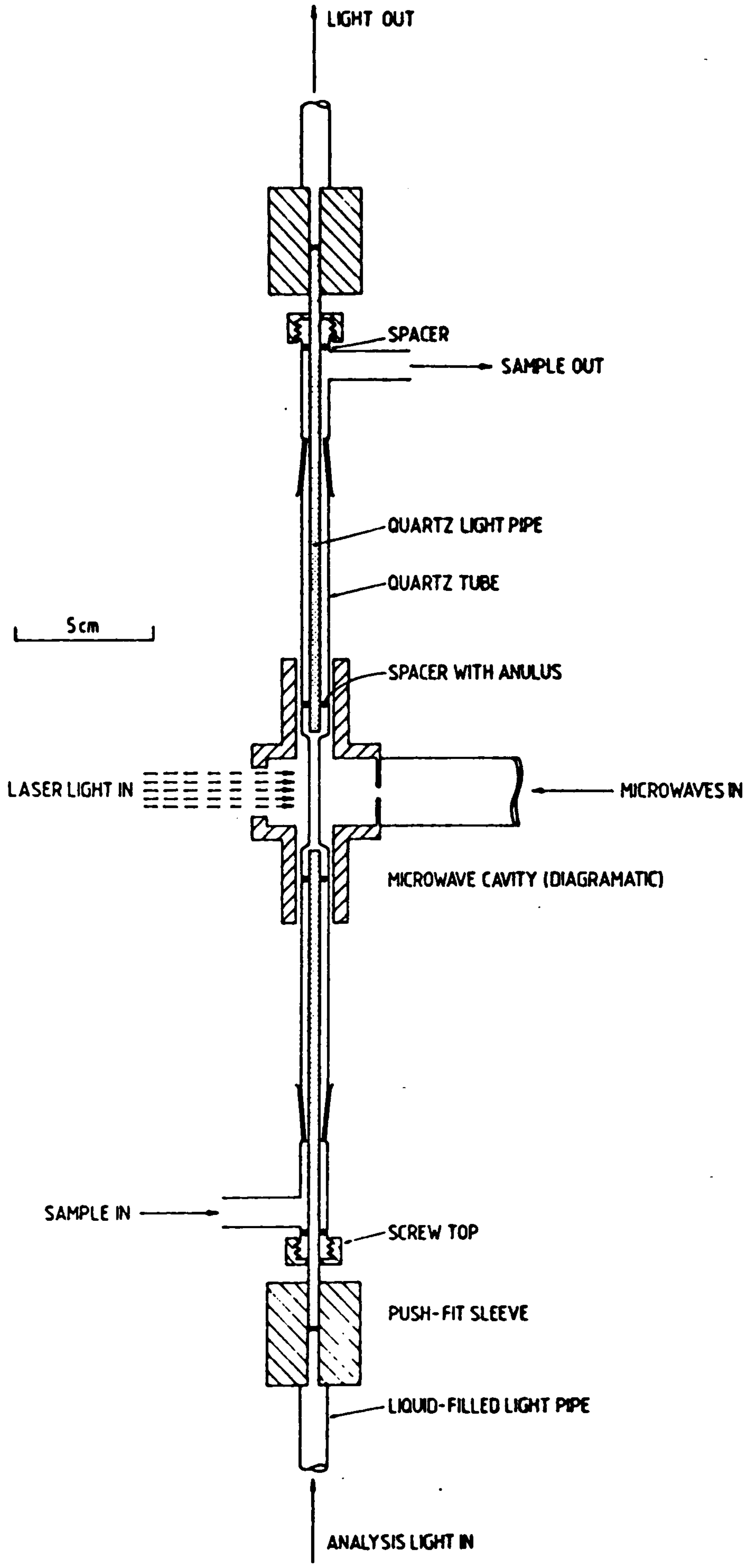

Figure 3.3. Diagrammatic representation of the RYDMR sample cell, showing optical arrangements for fluorescence and absorption detection techniques.

The arrangement for MARY experiments was much more conventional, utilizing fast lenses to efficiently focus light into and out of the rectangular flow cuvette. This permitted high light fluxes and correspondingly enhanced S/N in detection.

Wavelength selection was achieved by a fast, f3.5 manually driven monochromator with a choice of diffraction gratings blazed at either 300 nm or 500 nm. Most experiments demanded maximum light throughput and so entrance and exit slit widths were adjusted to give a wide optical bandwidth of typically 10 nm.

All optical elements were capable of adequate transmission into the near U.V., allowing a wide range of species to be studied. For visible applications, however, problems were encountered with higher order diffraction images of intense laser scatter from the solution (308 nm and 337 nm). To eliminate these a U.V.-absorbing PMMA filter was constructed for insertion into the optical path at a point immediately preceeding the monochromator.

In all cases the final stage in the optical detection system was a photomultiplier tube, the exact nature of which was determined by the application. Further details of specific modifications to this element of the apparatus can be found in separate sections dealing with absorption
and fluorescence detection techniques.

3.4.1 Absorption Detection

At first sight a technique based upon the observation of a small transient change in a much larger optical transmission signal, places severe demands on the dynamic range of the recording equipment. The traditional approach to this requirement is to precede the recording device with a high pass, frequency selective element in the electronic circuit. This has the effect of separating out the transient signal and enables it to be recorded at the full dynamic range of the equipment. If the analyzing light source is operating in a c.w. mode, the filter element can take the form of a simple d.c. blocking capacitor. Alternatively, if the light source is pulsed, an r.f. reversing transformer would be the appropriate element to use, acting to subtract the background light pulse from the higher frequency transmission transient. Both approaches, however, are something of a compromise, leading to a distortion of the transient signal.

Even when precise temporal profiles were not crucial to the application in question, it was found that the use of a d.c. blocking capacitor led to unacceptable baseline instability when performing repetitive signal averaging experiments. The problem was solved by extending the system bandwidth down to d.c. and applying electronic sampling techniques to eliminate the background transmission signal. A schematic of the device constructed to achieve this, and to generate a ratiometric output, can be found in figure 3.4. In essence the procedure may be termed a time-multiplexed double beam spectrometry technique and was successfully employed within the limits of the 1 MHz electronic bandwidth set by the analogue division circuit. Analyzing light was provided by a c.w. white light continuum, emitted by a stabilized 150 W high pressure Xenon short arc lamp.

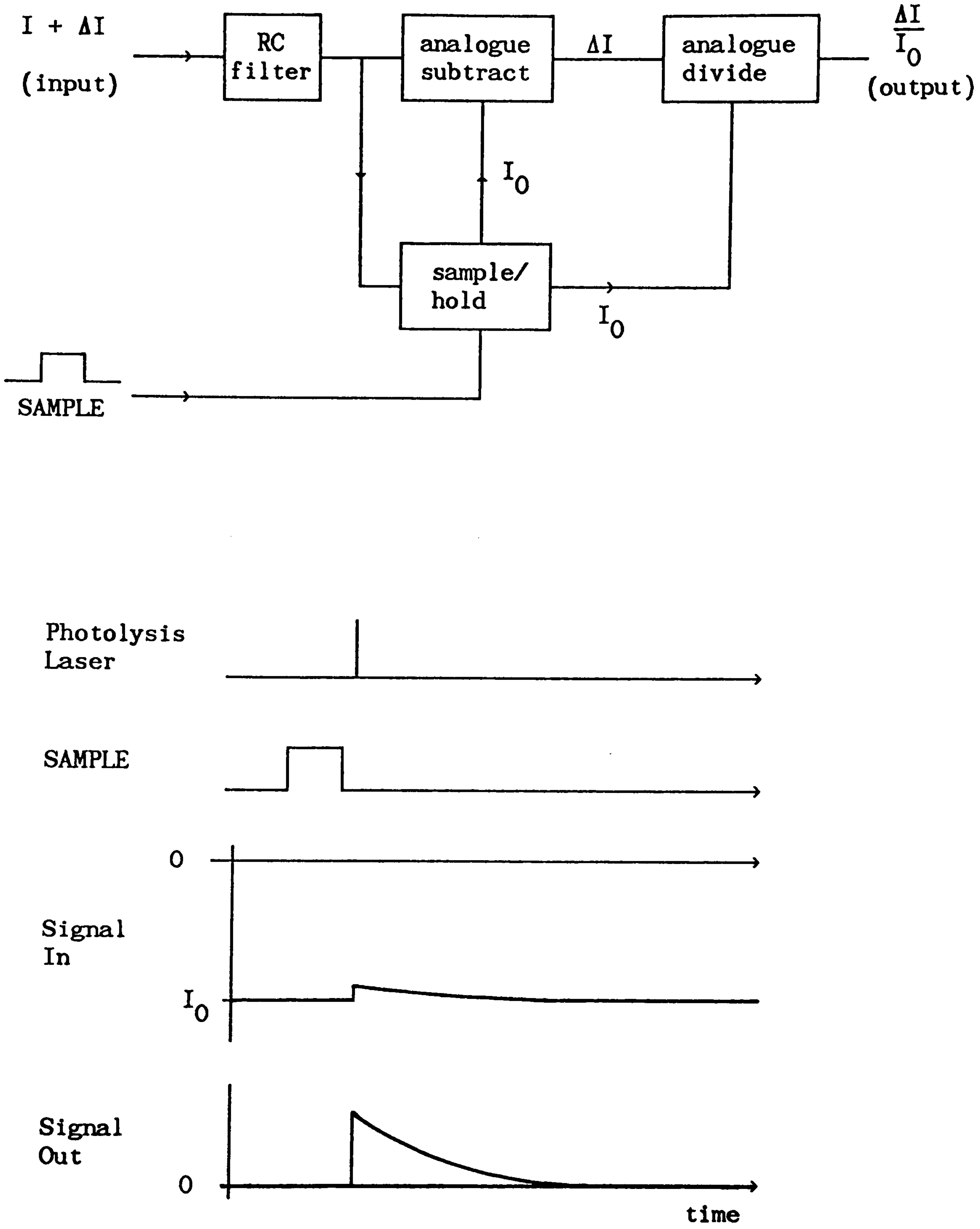

Figure 3.4. Functional schematic and timing relationships for the Time-Multiplexed Double Beam Spectrometry facility.

Operation at the low bandwidth of 1 MHz did not place any stringent requirements on photomultiplier dynode design and so a side-on 1P28 with S5 photocathode and U.V. glass envelope was employed, with all 9 dynode stages in use, together with a 10 kΩ anode load. For convenience of operation, however, first and last gain stages were clamped to a p.d. of 100 V to allow variation of overall gain, without loss of linearity or response speed, simply by adjusting the p.m. tube supply voltage. In addition, a 50 Ω driver enabled long signal cable lengths to be handled at low impedance with concomitant increase in immunity to r.f. noise pickup.

Extension of the absorption technique to higher bandwidth, and so shorter times after radical generation, is fraught with problems. As well as the need for reduction in detector response times and the associated S/N degradation (6,7), there is often a problem arising from strong fluorescence excited by the photolysis laser. In many cases this can completely mask any transmission signal from a c.w. analyzing light source. The solution to this problem, and that of poor S/N, is to provide a very intense analyzing beam, but for reasons of sample stability it is obviously unwise to utilize a high power c.w. white light source. The use of a pulsed source is, however, more strongly indicated by consideration of photomultiplier characteristics. Operation of such devices in a pulsed mode allows the generation of high peak anode currents without the saturation and linearity problems which would ensue for identical continuous currents. The benefits in terms of shot-noise limited performance, and indeed for signal magnitude into a 50 Ω anode load, are clear. Details of photomultiplier dynode bias chain design will be described under fluorescence detection.

With the apparatus available at the time, a convenient pulsed analyzing light source was formed by excitation of a suitable dye solution with an N_2 laser pulse following closely after photolysis; the dye being chosen for emission in the range of interest. Unfortunately at such high bandwidths, and with dye fluorescence lifetimes short compared to the transient radical events being monitored, it was not possible to apply the full dynamic range of the recording device to the change in transmission resulting from photolysis. Instead only the full transmitted intensity of the dye flash could be measured. For these reasons S/N values for changes in transmitted intensity due to magnetic field modulation were poor and so this technique was not further pursued.

3.4.2 Fluorescence Detection

Detection of fluorescence from two types of processes was attempted. One relied on luminescent emission accompanying ion pair recombination and the other upon emission observed subsequent to excitation of a transient species. This was achieved by a secondary laser pulse following shortly after photolysis input to the sample. Typical emission lifetimes were 20 ns or less, requiring a fast photomultiplier arrangement, particularly when a true representation of temporal profile was important as, for example, in luminescent recombination studies.

The photomultiplier chosen was a Hamamatsu R928 side-on tube with a multialkali photocathode, and U.V. glass envelope, capable of good spectral response throughout the visible region. Only five out of a total of nine dynodes were connected in a manner which employed r.f. techniques for divider chain design in order to minimize stray capacitance and inductance in the output circuitry. Details of the design were similar to those published by Beck [7] who achieved subnanosecond response from a 1P28 tube. Such performance was obtained by running the tube at non-uniform interdynode potentials which exceeded the maximum manufacturer's specifications; a technique which proved equally applicable to the R928 tube. Problems with resonances at ~100 MHz were, however, encountered on using a dynode as an anode in the reduced gain configuration. They were manifested as spurious afterpulses in the electrical of the photomultiplier and their cause traced to resonant elements formed by the dynode inductance and the bypass capacitors employed in the dynode chain. A solution to the problem was found to be the inclusion of damping resistors (~50 Ω) in series with the last few (high current) dynode stages. Other artifacts were eliminated by careful impedance matching of the electrical system, from the p.m. tube to the recording device, by means of 50 Ω cable and termination.

Overall system performance was assessed by recording an N_2-laser pulse profile of FWHM 6 ns, the form of which was expected to be a symmetrical gaussian. Results, figure 3.5, showed the absence of afterpulses, serious distortion and time broadening. Linearity was checked by repeating the experiment over a range of incident light intensities confirming linear operation up to peak anode currents of 8 mA.

3.5 Magnetic Field Production

As has been described, the key feature of experimental design is the comparison of reaction yields under field on and field off conditions with consecutive observations in a signal averaging regime. Such a

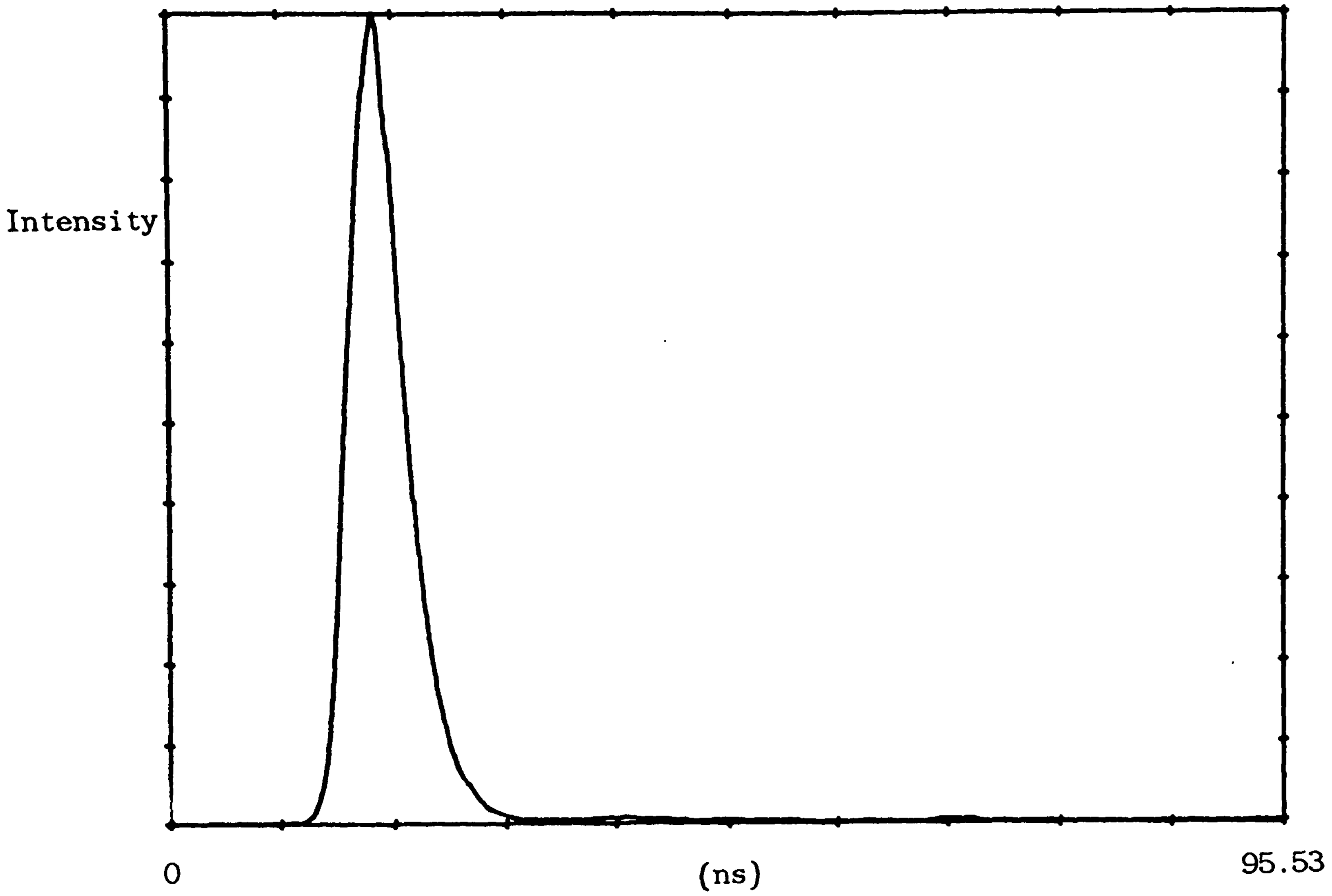

Figure 3.5. N_2-laser pulse profile recorded at 337 nm.

technique implies the provision of pulsed magnetic fields and consequently obviates the need for the equipment design to handle high thermal loads associated with continuous provision of static and high power microwave fields. Particular field requirements of MARY and RYDMR are detailed separately below.

3.5.1 MARY Requirements

A Helmholtz pair of coils (air core) each of 200 turns and radius 4 cm, utilized for all MARY experiments, were mounted on brass plates at a separation of 4 cm as indicated in figure 3.6. In this way serious thermal effects upon the sample were eliminated and a certain degree of heat sinking provided for the magnet coils. Operation was at frequencies no higher than 20 Hz and so skin depth effects of the brass plates (~2 mm gauge) could be safely ignored.

Peak fields of 200 G were readily achieved by a purpose-built switched current supply whose output could be programmed digitally, with 8 bit resolution. The power supply frequency response was rolled off to give a field-time profile free from superposed oscillations, the resulting risetime being quite adequate at ~ 1 ms.

To enable MARY field sweeps to be calibrated, a field probe, designed for placement at the sample cell position, was constructed and calibrated with reference to a commercial Bell 310 static field gaussmeter. The probe relied for its operation on the output of a linear Hall effect device capable of operating at up to 400G and several hundred Hertz.

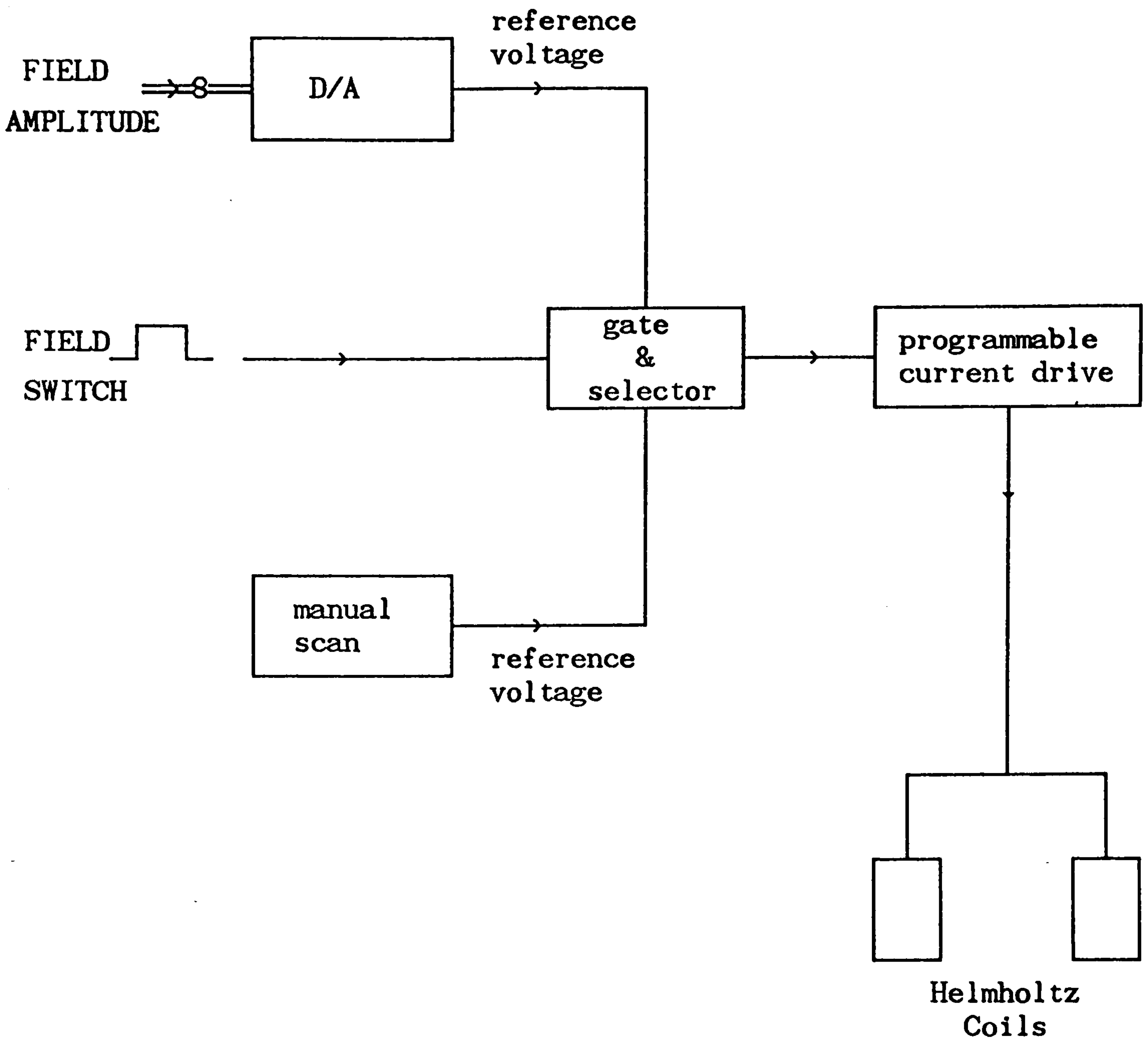

Figure 3.6. Functional schematic of the MARY pulsed-field apparatus.

3.5.2 RYDMR Requirements

The magnetic field requirements of a RYDMR experiment are very similar to those of conventional esr. To ensure close correspondence between the two experiments, the static magnetic field was chosen to be in the region of 3500 G ,setting the high frequency field at a frequency of around 10 GHz in order to satisfy the electron resonance condition.

Departure from conventional spectrometer design comes in the need for very short microwave pulses at power levels several orders of magnitude greater than those to be found in basic esr equipment.

A commercial water-cooled 9" electromagnet requiring a current of ~60 A to give the necessary static field, was driven by a 100 A power supply constructed for the purpose. The design included the provision of a servo system to stabilize the magnetic field generated, but the silicon Hall element utilized as a field sensor proved to be excessively temperature sensitive, leading to undesirable fluctations in the field. To overcome this problem, the magnet power supply was modified to rely purely on a current control mode of operation, giving rise to field scan hysteresis difficulties. The impact of the latter could be reduced by performing only narrow scans and by conditioning the magnet, prior to use, by field cycling close to the desired range.

Measurement of the static field was performed by a commercial proton magnetometer which sensed the field at the sample to a resolution of .001 G at 3500 G.

A microwave magnetic field perpendicular to the static field was ensured by the standing wave configuration of a rectangular TE_{102} resonant cavity situated between the electromagnet pole faces and containing the sample. This arrangement is entirely equivalent to that found in conventional esr. The actual cavity was indeed a modified low power commercial esr component, fitted with an irradiation port.

Vital to the microwave system design was the facility for continuously tuning the cavity resonance frequency, over a range of 9.3 GHz to 9.9 GHz by varying the degree of insertion of four quartz dielectric tunning rods. This avoided the need for a tuneable microwave source in order to accomodate a wide range of sample cells within the cavity.

Major modifications for adaption to the needs of RYDMR involved the sides of the cavity and its impedance-matching iris. The original gold-coated ceramic plates, constituting the cavity sides, were replaced with copper slabs to enhance durability under high incident laser intensity, whilst the nylon carrier for iris adjustment was duplicated in teflon, and the copper iris-adjusting mask was replaced with one of higher thermal mass.

Figure 3.7 is a schematic of the microwave system clearly showing the manipulation of the microwave radiation at low power, amplification being performed only at the final stage.

The microwave source comprises a mechanically-tuned, temperature-compensated (tempco 50 KHz/°C) Gunn oscillator giving a nominal 20 dBm at 9.6 GHz. A regulated 12 V, 1 A d.c. supply ensures minimal f.m. noise, there being no requirement for frequency pushing by

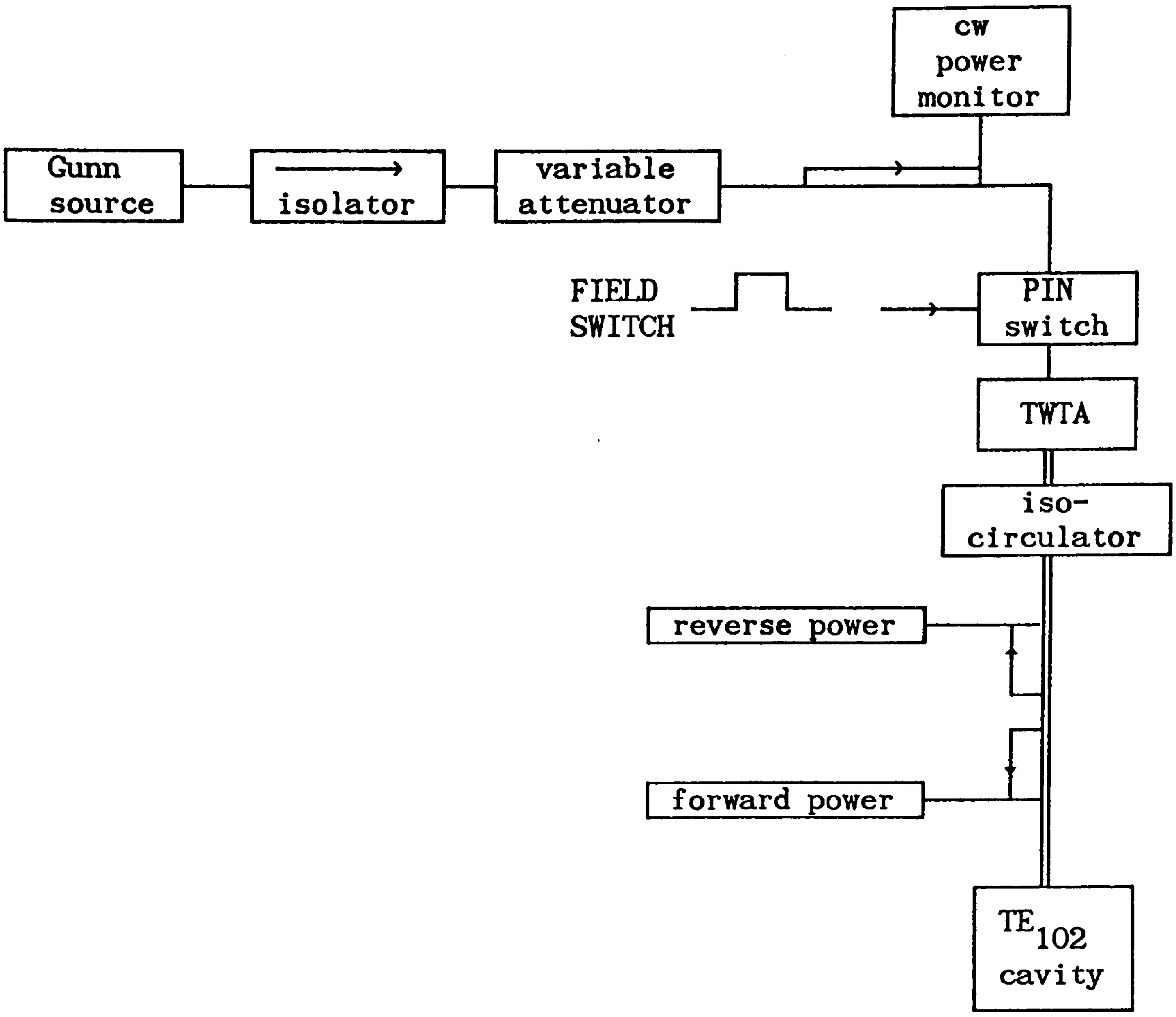

Figure 3.7. Microwave circuit schematic. The high-power circuit is denoted by ═══.

drive voltage variation. Output stability is further enhanced by the use of an isolator at the oscillator output to present a high return loss and so eliminate frequency pulling effects when the source is operating into imperfectly matched loads.

The determination of B_1 spectra requires a variable microwave power incident on the resonant cavity and to this end there exists a manually operated, rotary vane attenuator, calibrated at 1 dB intervals over a range of 30 dB. Reproducibility of the setting is assisted by a digital power readout obtained by monitoring the c.w. power output of the attenuator via a 30 dB coupler.

Following the attenuator, full depth square wave modulation is performed by a reactive switch composed of a TTL driven, PIN diode waveguide device. It achieves rise and fall times of approximately 5 ns, enabling the generation of very short microwave pulses from the stable c.w. source.

From the switch, the microwave pulse is applied to a wideband Travelling Wave Tube Amplifier (TWTA) operating at a fixed gain and rated at a nominal 200 W. At 9.6 GHz its output saturates at approximately 270 W when driven by the full Gunn oscillator output. This presents an upper limit to the power which may be delivered to the resonant cavity. Reverse power protection for the amplifier is in the form of a high-power isolator formed from a 3-port circulator and load, the temperature of which is monitored as part of an amplifier over-temperature interlock circuit.

The system described provides a more stable frequency and power output, and much more convenient control, than could be obtained from an inherently pulsed magnetron generator system.

Forward and reverse power are measured via 30 dB couplers and detectors in the interface region between the power drive system and its cavity load. The detectors operate into 100 Ω loads and are interfaced to a 50 Ω coaxial signal system by wide bandwidth buffers, all employed to attain a detector response time comparable with that of the PIN modulator. Absolute detector calibration was performed in a c.w. manner with reference to a commercial bolometer head.

The microwave pulse monitoring system serves two main purposes. One is to allow tuning and matching of the resonant cavity by iterative adjustment of tuning rods and coupling iris such that the reverse pulse amplitude is minimized for any particular sample system. The second application is in the characterization of the power being delivered to the cavity, in terms of pulse shape, amplitude and relative timing with respect to radical pair generation. Knowledge of these parameters then permits the estimation of the B_1 field experienced by the radical pair system generated within the cavity.

In practice the determination of B_1 presents several problems. The approach centres on ascertaining the laboratory frame r.f. field amplitude at the sample position within the cavity. With the equipment described above, this is most easily achieved by relating the desired field strength to that in the waveguide feeding the cavity and so to the incident power. Although this method is adopted here, it should be stressed that great care must be taken in order that inaccuracies in the result are kept to an acceptable level. Major problems arise in the assessment of coupling losses and introduction to the cavity of a dielectric inhomogeneity in the form of a sample cell and its contents.

The case in question involves a TE_{102} rectangular cavity containing a quartz flat cell and, in general, an aqueous sample. Coupling losses are assumed negligible when the iris is correctly adjusted and the cavity optimally tuned. Within the cavity the relevant spatial magnetic field dependencies are [8]

$$B_x = \frac{B_p}{[1 + (d/2a)^2]^{1/2}} \sin(\Pi x/a) \cos(2\Pi z/d) \ ,$$

$$B_z = - \frac{B_p}{[1 + (d/2a)^2]^{1/2}} \cos(\Pi x/a) \sin(2\Pi z/d) \ , \qquad (8)$$

$$B_y = 0 \ ,$$

where the x direction is taken along the sample tube, z along the cavity length d and a is the width of the cavity in the x direction.

It is clear that the r.f. field amplitude exhibits a sinusoidal variation across the sample tube in the x and z directions, but is uniform along the y. Field amplitudes are thus conveniently represented by their spatial rms values $(\langle B^2 \rangle)^{1/2}$.

The mean square field in the plane perpendicular to that of the applied static field (y direction) is given by

$$\langle B^2 \rangle_c = \langle B_x^2 + B_z^2 \rangle_c \ . \qquad (9)$$

This may be related to the rms value of the field at the sample by the definition of a filling factor η

$$\eta = \frac{V_s}{V_c} \frac{\langle B^2 \rangle_s}{\langle B^2 \rangle_c} , \tag{10}$$

where V_s, V_c are respectively the cavity and sample volumes. Clearly the mean r.f. field depends on the sample and cavity geometries.

The mean field in the cavity may be related to that in the feed waveguide and the loaded cavity Q factor, Q_L, by

$$\langle B^2 \rangle_c = Q_L \, (V_w/V_c) \, \langle B^2 \rangle_w \tag{11}$$

where V_w is the volume of a waveguide section whose length is one guide wavelength. $\langle B^2 \rangle_w$ is itself related to the power being transmitted by the waveguide, P_w, and if this is expressed in Watts, with field strength in Gauss [8],

$$\langle B^2 \rangle_w = 2 \times 10^{-3} \, P_w \, . \tag{12}$$

Combining all the above relations gives

$$\langle B^2 \rangle_s = 2 \times 10^{-3} \, P_w Q_L \eta \, (V_w/V_s) \, . \tag{13}$$

For the present case of a flat cell, the filling factor is given by [8]

$$\eta = V_s/V_w \tag{14}$$

and so

$$\langle B^2\rangle_s \quad = \quad 2 \times 10^{-3} P_w Q_L \; V_w / V_c \; . \tag{15}$$

Further simplification results when the resonant cavity has the same cross-section as that of the waveguide whereupon $V_w/V_c = 1$. Thus we arrive at

$$\langle B^2\rangle_s^{1/2} \quad = \quad (2 \times 10^{-3} P_w Q_L)^{1/2} \; , \tag{16}$$

for the case under consideration.

It is important to realize that $\langle B^2\rangle_s^{1/2}$ is the spatially averaged rms amplitude corresponding to a laboratory frame linearly polarized r.f. field. For magnetic resonance considerations the requirement is a value for B_1, the amplitude in a rotating frame of reference corresponding to cicularly polarized radiation. The two quantities may be linked by resolving the linearly polarized radiation into two counter-rotating circularly polarized waves and applying the rotating wave approximation which regards only one of the waves as effective in inducing transitions. Thus B_1 may be estimated,

$$\begin{aligned} \langle B^2\rangle_s^{1/2} \cos\omega t \quad &= \quad B_1 \, (e^{-i\omega t} + e^{i\omega t}) \\ &= \quad 2B_1 \cos\omega t, \end{aligned} \tag{17}$$

where ω is the radiation angular frequency. Hence

$$\begin{aligned} B_1 &= \tfrac{1}{2} \langle B^2 \rangle_s^{1/2} \\ &= \tfrac{1}{2} (2 \times 10^{-3} P_W Q_L) \ , \end{aligned} \tag{18}$$

showing that knowledge of the power incident on the cavity and the Q factor are sufficient to determine the r.f magnetic field amplitude in the rotating frame. Of these, the latter presents the most difficulty with regard to its experimental determination. The method adopted in the present work relies on the relationship between Q and the time domain step response of a resonant cavity as the microwave drive is switched on. In terms of power:

$$P(t) \quad \alpha \quad \exp(-2\omega_0 t/Q) \ , \tag{19}$$

where ω_0 is resonant frequency in angular units. The effective time constant for the power decay is thus

$$\tau_c^P = Q/2\omega_0 \ , \tag{20}$$

or, in terms of the radiation field intensity (α $P^{1/2}$)

$$\tau_c^E = Q/\omega_0 \ . \tag{21}$$

Figure 3.8 shows the reverse power response obtained from a microwave pulse trailing edge input to the cavity, as indicated. It is clear that the cavity time constant is comparable to the switch response time, both of which are close to that of the detector. Obviously the situation is far from ideal and, indeed, the matter is further complicated by the

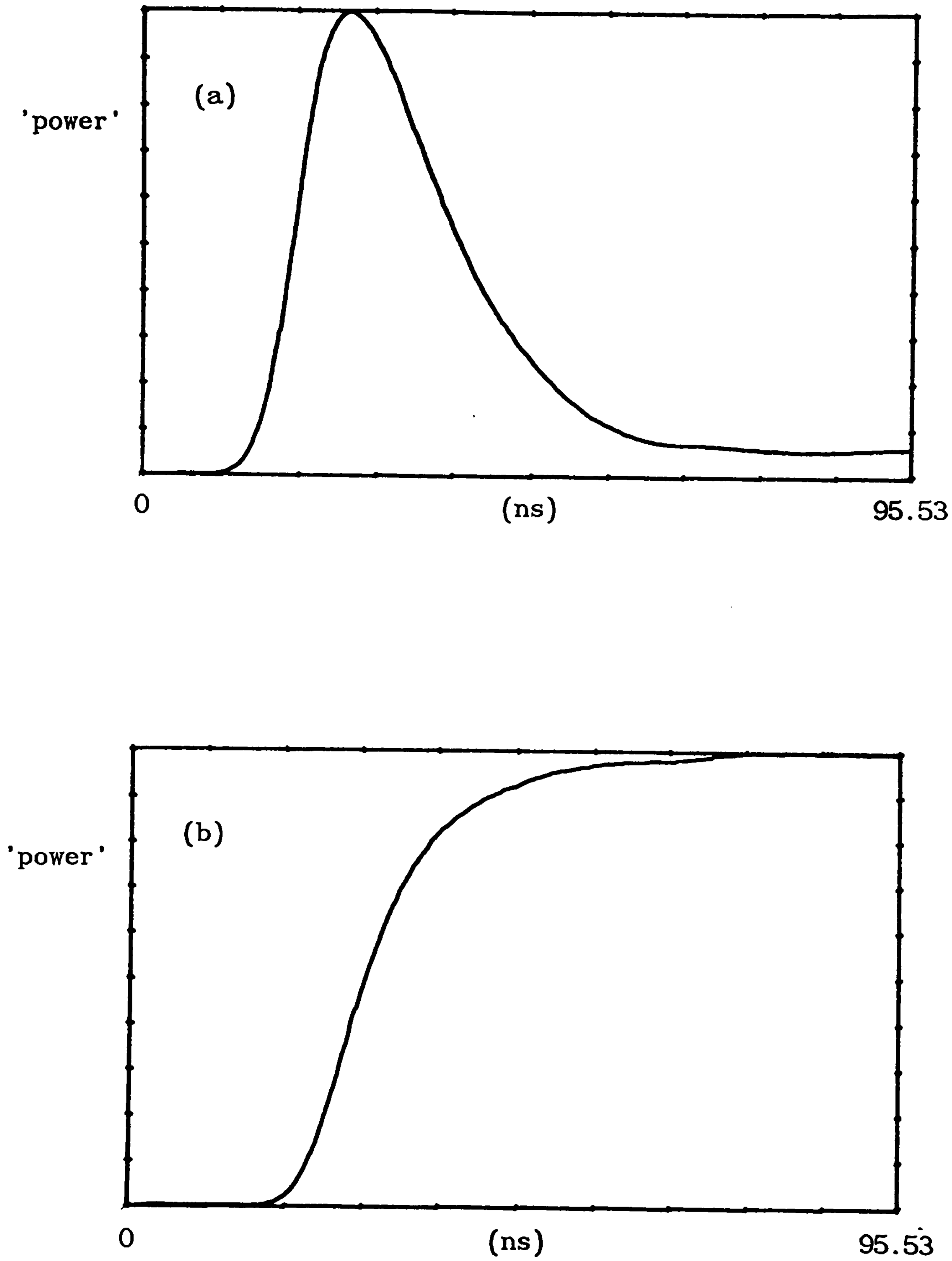

Figure 3.8. Microwave cavity response to a step function.
(a) Reflected 'power' response subject to
(b) microwave switch stimulus.

highly non-linear behaviour of the unbiased silicon 'crystal' detectors. At low powers the response follows approximately a square law in r.f. electric field intensity (α power) but makes the transition to a linear detector, with respect to the field intensity, at higher incident power levels (α power$^{1/2}$). Attempts were made, using Fourier transform techniques (see below), to reduce the effects of finite switching time of the PIN modulator by deconvolving the measured responses of figure 3.8. No significant improvement could be obtained, however, without severe deterioration in S/N. Non-linear least squares curve fitting of a single exponential to the cavity response of figure 3.8 gave a time constant of 5 ns for the trailing edge of the curve, and a value of 18 ns (poor fit) for the region close to the peak, offering albeit not unequivocal, evidence of the square/linear-law changeover at increasing powers. Assuming the former value to be the more representative of the required response, an estimate of the loaded Q at 9.6 GHz may be obtained as ~600.

Measurement of forward power pulse amplitude as a function of rotary vane attenuator setting was necessary to eliminate non-linear behaviour of the TWT amplifier at high output power before the relationship between attenuator setting and rotating frame field strength B_1 could be established.

The maximum power measured was 290 W, setting a ceiling of 9.3 G for B_1, though coupling losses were uncertain. Further correction to this figure is needed for dielectric enhancements dependent upon the sample cell and the particular solvent employed. Unfortunately the correction factors are heavily dependent upon the cell dimensions but nevertheless have been tabulated for a similar experimental arrangement [8]. For aqueous systems a value of ~1.4 might be expected for the enhancement factor, leading to an effective maximum B_1 of ~13 G.

Any requirement for an increase in B_1 could be met by improving the cavity Q, a value of 600 being very low for such a rectangular cavity. A figure of 2000 should be achievable and would lead to an approximate doubling of the rotating-frame B_1. The price paid for such an increase would be loss of the ability to produce very short microwave pulses within the cavity and to perform some of the time-resolved experiments to be described below.

Alternatively, smaller volume resonant structures would enhance B_1 with an increase in η, whilst still maintaining low Q and consequently large microwave bandwidth. Such structures are exemplified by loop-gap (split ring) or slotted tube resonators [9]. Additionally coupling efficiency can be improved by replacing the traditional reactive adjustment with a variable length waveguide section operating below the cutoff wavelength for the TE_{10} mode. This is the so-called Gordon coupler arrangement [13].

Attempts were made to make use of the improvements suggested above but technical difficulties associated with their incorporation into the system rendered them unjustified for an initial exploration of the RYDMR technique.

3.6 System Control

The system control function was implemented in software, for the most part, in order to maintain versatility. Hardware was only employed where a particular function was clearly fundamental to system operation, or where speed of response was critical. Figure 3.9 presents a schematic of the system control function capable of supporting all experiments to be described.

The figure clearly shows the basic design philosophy entailing a free running experiment generating data which may be optionally captured by the software subsystem. By having laser and sample systems operating at a steady rate in this way, irrespective of a possibly variable software function, benefits may be obtained in terms of data reproducibility.

The software-hardware interface contains an unique start control signal, labelled CAPTURE REQUEST, and a group of signals determining experimental condition outputs. In the current design the latter category contains only two signals; one, the FIELD FLAG, to determine the on/off state of the appropriate magnetic field, and the other, FIELD AMPLITUDE, to permit magnetic field scanning. Clearly there is much scope for extension of this class of signals without disrupting the system concept. Thus software control of pulse timings and widths, monochromator wavelength scanning and laser ouput selection would all fit easily into the scheme.

Vital to the control operation is the synchronization of the CAPTURE REQUEST signal to the start of a data generation cycle in order that signal capture is enabled only under determinate conditions.

Data generation cycles are driven by a master clock at a frequency variable up to approximately 30 Hz. The laser trigger outputs derived from this clock are capable of being delayed with respect to it, and to each other, enabling slow response control functions, such as the Helmholtz drive, to attain their required state before laser firing.

The final output of the hardware control unit is a variable-width TTL pulse drive for the microwave PIN modulator and pulsed current supply for the Helmholtz coils. The width range was designed to be switchable, accomodating the differing requirements of MARY and RYDMR experiments.

When capturing fast signals of a few tens of nanoseconds duration, using signal averaging techniques, there is a need for precise registration of consecutive signals through a reproducible time reference. This requirement was met by detecting laser emission with a fast response (200 MHz) silicon photodiode-amplifier system driving a 50 Ω link to the signal capture device.

Further details of the software, and modes of operation for particular types of experiment, will be discussed in the following section.

3.7 Signal Capture

The signal capture or recording device, referenced above, actually encompasses two very different components acting as transient recording equipment, but appearing to all higher software levels as identical items. For relatively low speed applications there is a Datalab 920 transient recorder capable of capturing 2K data points at up to a 20 MHz sampling rate with 8 bit resolution. Operation is as a stand alone device communicating data values to the controlling computer via a 8 bit parallel interface operating at a bandwidth of 1MHz. Experiments not requiring sampling rates in excess of 20 MHz can take advantage of the

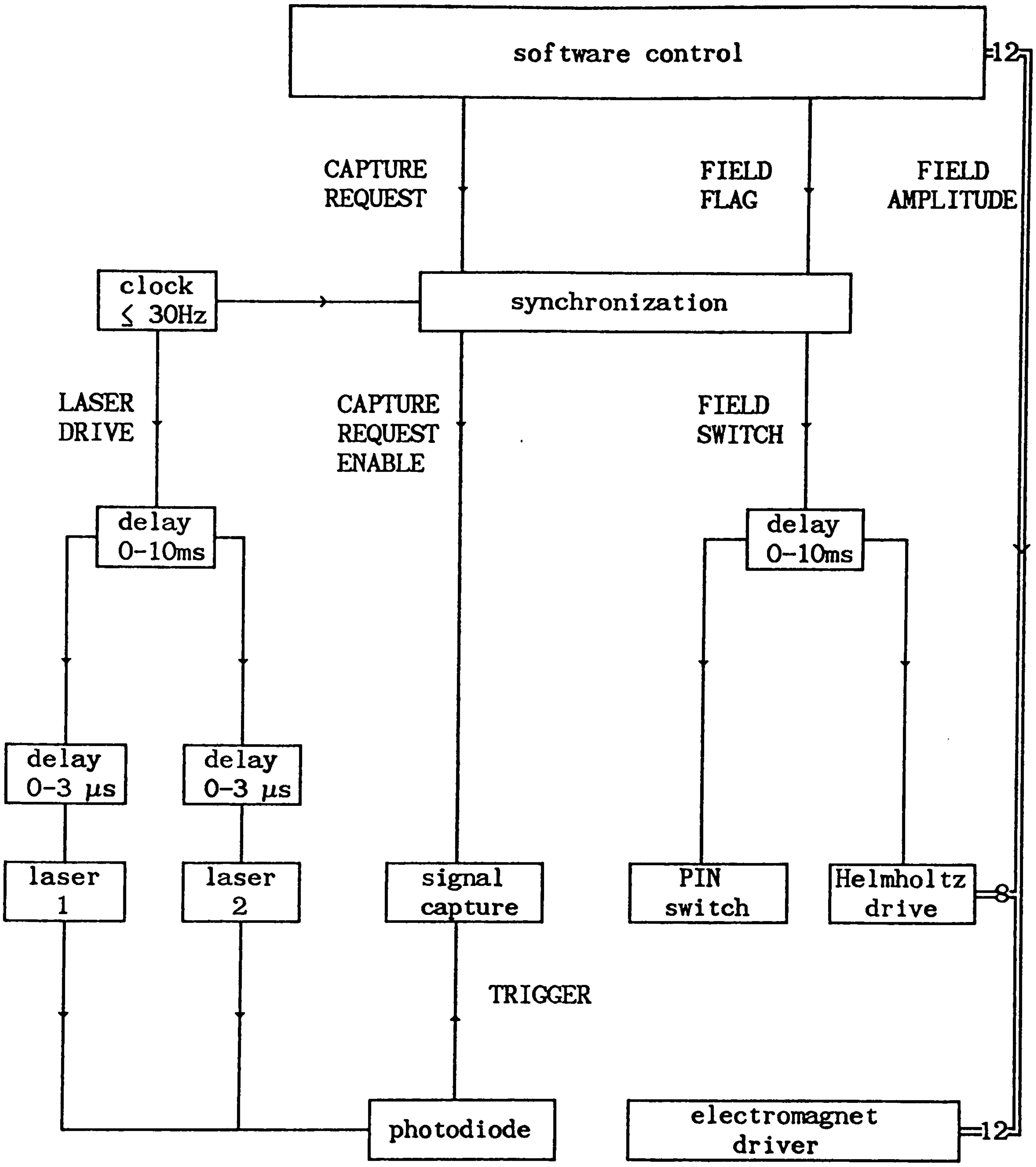

Figure 3.9. System control schematic showing control signals of the software-hardware interface.

minimum software intervention necessary for this recording device; an example being that of capturing millisecond timescale transient absorption signals.

The second signal capture facility offers an effective sampling rate of up to 20 GHz but an analogue bandwidth restricted to 250 MHz and can be used in parallel with the Datalab device. It is an instrument designed specifically for the purpose and unavailable commercially.

Currently the only practical way to record at digital sampling rates of 1 GHz or greater is to utilize an analogue technique which accurately retains a representation of the desired waveform for a length of time sufficient to allow subsequent digitization. The device in question was constructed around an existing 250 MHz analogue oscilloscope and relies on the crt phosphor acting as the intermediate store for the trace. The typical phosphorescence lifetime is of the order of 20 ms allowing the trace image to be read by a video camera at the comparatively low standard frame rate of 50 Hz and simultaneously digitized.

In detail the oscilloscope trace image is intensified via a photon - electron multiplication - photon process in an image intensifier module prior to falling on a ccd solid state light sensor array containing 384 x 491 pixels. An overall photon gain of some 85000 ensures reliable capture in the cases of very low trace intensity associated with high crt writing speeds and low signal repetition rates. Assisting in this respect is the rather higher sensitivity of the solid state image sensor and its improved contrast capabilities compared with those of a standard 'vidicon' tube. Immunity to image 'burn-in' was also a major factor considered when choosing the ccd sensor array.

In operation a video monitor is used to display continuously an image of the oscilloscope crt, allowing initial set up of an experiment. When signal capture is enabled, digitization of the camera video output is initiated on receipt of a trigger signal, and continues for exactly one whole video frame irrespective of the particular image line on which it started. One peculiarity of the ccd sensor, however, is that frame information is output whilst recording the succeeding frame and so the information relevant to the oscilloscope trace image is available only after a 20 ms delay. This is accomodated within the trigger handling hardware.

The composite video signal from the camera is stripped of sync. information, digitized by a flash 4 bit converter, compared to a software programmable 4 bit threshold level and the outcome stored as one bit in a video RAM via a 16 bit shift register (figure 3.10). The comparator itself comprises a 4 bit half-adder, the inputs of which are the digitized video signal and the preset threshold; the output is taken from the carry line. A direct mapping of the video frame to the video RAM is maintained by driving the camera in an external sync mode with signals derived from the same master clock used to provide the RAM addressing. The overall effect is to produce a two tone (1 bit) representation, in memory, of a given video frame at a particular black/white level chosen by the preset threshold.

Completion of a signal capture cycle is indicated by a signal issued from an address comparator, one input of which is the memory location being addressed at the trigger arrival time. Consequently on cycling through the memory and returning to the start address a full frame is signalled, further signal capture disabled and a microprocessor interrupt request generated.

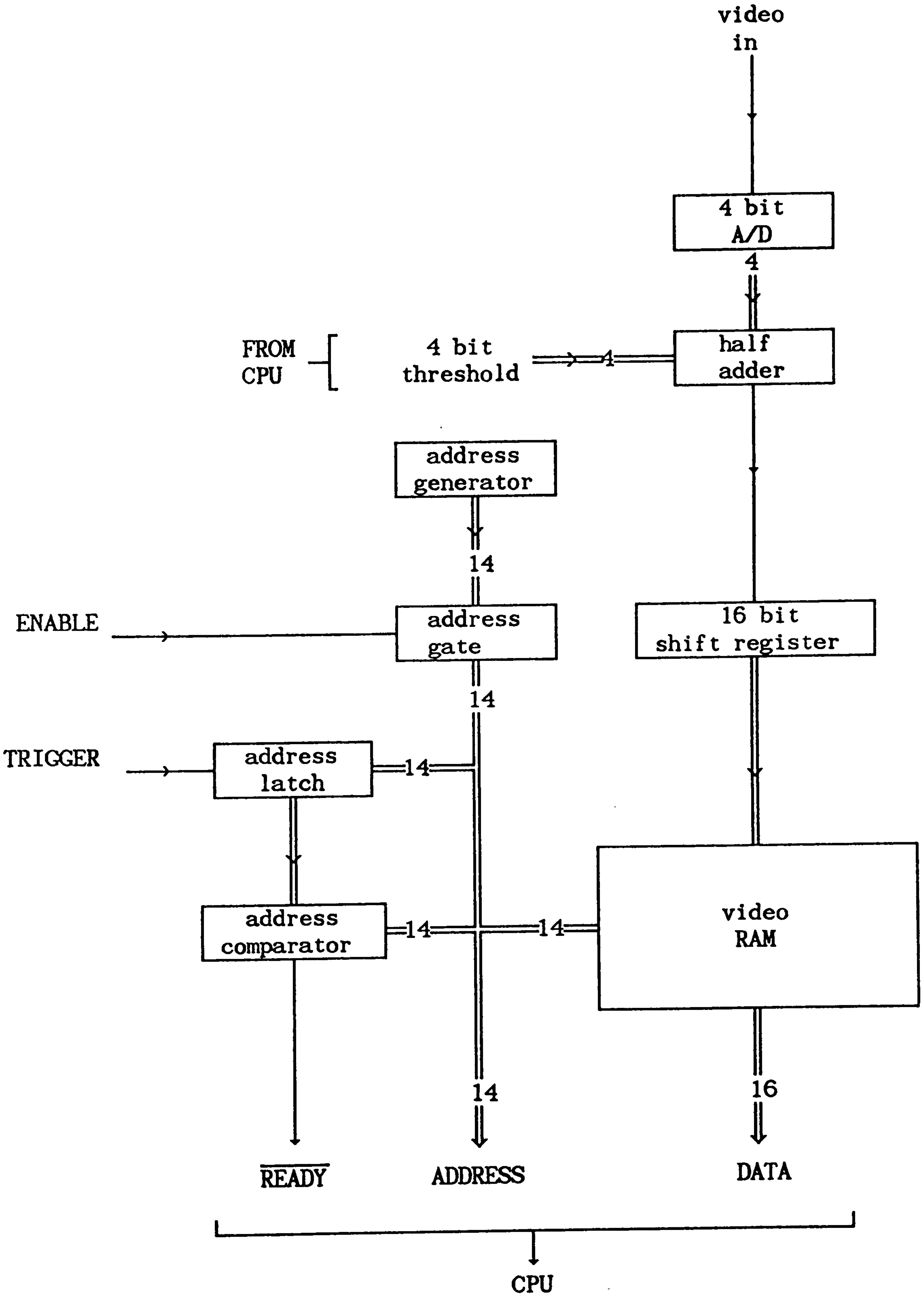

Figure 3.10. Schematic showing key operating details of the scan digitization facility.

Servicing of the interrupt consists of the activation of software routines designed to extract the mean coordinates of the trace image contained within the video RAM. Formally this requires the processing of around 65000 pixels in a 208 x 312 array. Assumptions about the image can, however, be applied to greatly reduce the time taken for completion of this task, bearing in mind that the scan digitizer was required to operate in a signal-averaging environment at up to 20 Hz repetition rates. As the trace image is expected to occupy only a very small fraction of the video frame, the algorithm actually utilized for searching the frame could be optimized for speed by assuming that most of the video RAM would be clear.

Implementation of the image processing algorithm was performed on a 10 MHz MC 68000 processor chosen for its capability to handle, with ease, variable data sizes from single bits to 32 bit long words. Scanning of the RAM is performed in a 16 bit wide column mode; a compromise between the increased speed which would result from 32 bit scans and the extra processing arising from the higher probability of detecting a non-zero element. For each set pixel detected the row number, together with a pixel count, is accumulated in a 16 x 32 bit buffer; each element corresponding to a single pixel column. On completion of a 16 bit column scan, the buffer contents are multiplied by 4 prior to undergoing integer division by the pixel count. In this manner the mean y coordinate of the oscilloscope trace, for each pixel channel, is determined to an effective resolution which exceeds that set by the ccd sensor array dimensions. The overall result is approximately 10 bit single shot vertical resolution over 208 channels.

As an option, it is possible to specify only part of the image for digitization, allowing only a fraction of the trace to be sampled and offering a concomitant decrease in the processing time required. This is particularly useful in a digital boxcar mode of operation where the requirement is for a represenation of an integral under part of a waveform.

In operation, image intensifier gain was set such that the video camera produced a clipped output signal ensuring that variations in camera sensitivity, or phosphor output, had a minimal effect; a clear distinction between black and white levels was apparent. The programmable video slicing threshold was then set to the highest possible value whilst still maintaining reliable trace representation. Phosphor image-lag effects could thus be reduced to insignificant levels, even at averaging rates of 20 Hz, and the total frame processing time reduced in accordance with the smaller white frame fraction. When followed, this setup procedure produced a very reliable and efficient scan digitization system, offering extreme ease of use on a wide range of signals.

Calibration of the scan digitizer timescale was achieved by reference to sinusoidal signals, of known frequency, recorded under a range of oscilloscope sweep conditions; time per channel figures were obtained by curve fitting to several periods of each recorded sinusoid.

3.8 Signal Processing and Apparatus Modes.

It now remains to describe how data from the two signal capture devices was manipulated to meet the requirements of the range of experiments undertaken. Many experiment-specific details, however, are best reserved until the applications chapters of this thesis where the context will be much clearer.

A need for two distinct modes of operation was apparent. In one, temporal information was of the utmost importance and was to be acquired under constant conditions with respect to the other experimental variables. The alternative mode had temporal dependence as a secondary factor, uppermost being the need to obtain the mean value of a sample property as a function of another variable. This latter mode essentially corresponds to that of a digital integrator.

Both modes, and their subcategories, were implemented in a 'C'-language program which also undertook the control of all signal capture and field production devices. Signal averaging was achieved by 'in memory' accumulation; the final result, together with details of the particular experimental conditions, could then be transferred to permanent storage on floppy disk where it was available for further processing by purpose-written utility programs.

The simplest operating mode (1) enabled accumulation of up to 2^{16} single shot waveforms in 32 bit buffers, offering a dynamic range sufficient to obviate the need for rescaling during the averaging process. Optionally, any interval of the waveform could be chosen by an interactive cursor facility and used as a mean baseline reference to be subtracted before the accumulation of each single shot event. This was helpful when low frequency signal components produced a drifting baseline. Precise triggering eliminated any horizontal drift.

The second operating mode embraced two submodes, both of which had the effect of averaging a sum of channel contents over a given interval and under a sequence of experimental conditions. They therefore comprised the spectrum gathering modes of the apparatus.

The first submode (2a) made use of programmed baseline and summation intervals to integrate digitally a sample of a recorded single transient waveform. Successive integrals were then accumulated in floating point format to provide a running sample mean and variance for the data set. All statistical information was displayed as the averaging process was underway providing clear, quantitative insight into the significance of the result and the quality of the data being generated from any particular experimental configuration. The latter point proved particularly invaluable in providing a criterion for the optimal adjustment of the many experimental variables such as sample flow rate, laser conditions and optical alignment.

After accumulation of the required number of samples, experimental conditions were changed (e.g field advanced, monochromator wavelength stepped), another set of averages taken and the process repeated for a preset number of points to form a spectral sweep. On completion of such a sweep, both mean values and associated variances were stored in a floppy disk file.

The second submode (2b) performed an operation similar to that of 2a but in a pairwise manner involving the ratioing of consecutive pairs of single shot integrals. The ratio was then treated as the quantity to be averaged for each spectral point. Provision of this mode was to perform MARY and RYDMR experiments in the manner discussed above whereby data is gathered with the microwave or static field alternately in an and off state. Field switching was performed by the program, ensuring that the correct sequencing was maintained. Results were presented in terms of the field-on integral divided by that obtained with the field off. Subtraction of unity from the quotient converted the result to a signed fractional field effect. A positive value indicated an enhancement in the measured quantity when the magnetic field was present.

To increase averaging efficiency, certain refinements were made to the mode 2b procedure. Short term system drift, arising from laser pulse-pulse variation, was eliminated by sampling the laser intensity for each signal captured so that the corresponding integrals could be normalized to laser output. The effectiveness of this addition was evidenced in a lower field-effect variance and consequently a higher S/N for a given averaging period.

Much lower frequency noise in the form of long-term system drift, whose major source was found to be contamination of the sample cell by the deposition of photoproducts, was compensated by the designation of a reference field point to which the apparent mean field effect was regularly corrected throughout a spectrum-gathering sequence. In use this option proved valuable in determining when cell deposition rates were excessive, indicating a need for adjustment in laser intensity or sample flow rate.

Backing up the signal processing performed during data collection were a series of utility programs operating on the stored data files. They will be briefly described here and their use assumed for much of the work presented in the application sections of this thesis.

Transfer of data and error information to hard copy devices, either graphically or numerically, was handled by two programs driving a flatbed plotter or a printer. Similarly data files could be sent to other devices supporting a serial channel. The transfer to other computer systems for numerically intensive data processing is easily achieved.

On many occasions, particularly when working under mode 1 conditions, single shot transient signals were contaminated with a noise waveform which did not average out but accumulated coherently to give an unwanted background contribution to the final result. The main offender in this respect was found to be residual pickup of electrical noise generated by the laser discharge despite careful shielding of the signal channel. Elimination of this problem was one of the reasons for the writing of a file-editing program capable of combining several files in varying proportions. A pure background file could then be easily subtracted from one containing the desired signal contaminated with this background. Other applications were to the elongation or truncation of a data set in preparation for further processing, for example by Fourier transform techniques.

Some waveforms obtained from mode 1 experiments were distorted by convolution with another signal which could be recorded separately. A prime example of this occurs when studying short-lived fluorescence elicited by a laser pulse of a comparable timescale. By recording the laser pulse waveform separately it is possible, in principle, to remove its effects from the desired signal revealing the form of response that would be observed for δ-function excitation.

Two general approaches to this problem exist, relying either on the operation of deconvolution becoming that of division upon Fourier transformation, or on the assumption of a particular parameterized analytical form for the desired signal.

Obviously the transform technique is the most general and often the least processor-intensive if combined with Fast Fourier Transform routines. It is, however, fraught with problems arising from the emphasis of higher frequency components, as well as their generation by numerical truncation and rounding errors [10] on performing complex divisions with operands close to zero. In essence:

$$\text{Time domain} \quad f = g * h \quad \text{(convolution)}, \qquad (22)$$

$$\text{Fourier domain} \quad \bar{f} = \bar{g} \times \bar{h} \quad \text{(multiplication)},$$

$$\text{or} \quad \bar{h} = \bar{f} / \bar{g}, \qquad (23)$$

where f is the observed response function, g the excitation function incorporating the instrumental impulse response, h is the desired sample impulse response and $\bar{f}$ etc. represent transformed functions. A practical solution to the generation of spurious high frequency components is to re-convolute with a synthesized excitation pulse of reduced width (time domain) compared to the actual laser profile. In the transform domain this is equivalent to multiplication with a low pass filter function. Application of the technique then involves a compromise between obtaining the true δ-function response and keeping spurious frequency content to an acceptable level. The performance of a 'C'-language implementation of this algorithm, utilizing an FFT function, may be judged by its application to data displayed in the applications chapters of this thesis.

Deconvolution methods based on curve-fitting a convoluted trial function obviate the need for re-convolution and may be exemplified by that of Ware et al. [11] who noted that, in general, response functions encountered in photophysics can be expressed as a sum or difference of exponentials. They employed a generalized trial function of the form

$$h = \sum_{k=1}^{n} a_k \exp(-t/\tau_k) \ , \tag{24}$$

and found it to be a reasonable approximation to a range of experimental decays provided the τ_k's were chosen correctly and were sufficient in number. When convoluted with a measured excitation response, the deconvolution problem reduces to a solution of n linear equations in a_k.

This particular algorithm was again implemented in 'C', employing gaussian elimination to solve the linear set of equations. In use, however, it was found to be inconveniently sensitive to the particular choice of the basis τ_k's, especially for multi-exponential decays.

A further utility program was written to perform multi-parameter non-linear least squares fitting of generalized functions to floppy disk data files. The algorithm used was that of Marquardt, interpreted by Bevington [12], providing rapid and reliable convergence for a wide range of fitting functions and initial trial parameters. An option allowing fitting accompanied by convolution with a designated data file was also included but found to be of limited applicability as a result of the excessive numerical effort required. All curve fitting referenced in the following chapters was performed with this utility.

APPLICATIONS

The original experimental concept had within it the aim of developing MARY and RYDMR techniques for application to a very wide range of radical pair systems. These included, of course, freely diffusing, uncharged species in solvents of 'normal' viscosity (~1 cP) but as yet this is a category which has eluded all refinements of the techniques.

Chemical systems successfully studied all exhibit restricted relative motion within the radical pair and may be categorized by the manner in which this is achieved. Thus there are two major categories, employing, on the one hand, the restricting influences of coulombic forces between radical ion pairs whilst, on the other, the control of radical motion is exercised by the presence of a phase interface provided by surfactant aggregates dispersed in a host solvent. To a large degree such systems may be considered to comprise a collection of microreactors, at least on the short timescales of interest.

Although, at first sight, the reaction systems may appear to be excessively specialized, they do in many ways approach those to be found in nature where the use of a structured reaction medium in aiding a particular reaction is of fundamental importance and universal; I refer, of course to, enzymes and membranes. In this light the systems described in the following chapters may be seen as of greater significance than the somewhat artificial conditions of free diffusion in a homogeneous medium, though studies of the latter clearly have a role to play in attempting to simplify the problem of determining the fundamental behavioural components found in natural systems.

CHAPTER 4

ION PAIRS

4.1 Exciplexes and Ion Pairs

For many years attempts have been made at unravelling the processes resulting in the dissipation of energy from an electronically excited species in solution. Of particular interest in the present case are those involving aromatic π-systems and their intermolecular interactions. Experimentally, for many systems, it was found that as concentrations rise there are accompanying changes in the fluorescence spectra, leading to the appearance of a red-shifted broad, structureless band. No corresponding changes can be observed in the absorption spectrum, showing that the phenomenon is a property of an excited state. Explanation of these observations was advanced in terms of the formation of excited state-ground state complexes [1]. Furthermore the frequency maximum of the new emission is found to be related linearly to the differences in the oxidation and reduction potentials of the appropriate interacting molecules, pointing towards charge-transfer character in the species produced.

Most commonly the complexes result from bimolecular interaction and are referred to as excimers (excited dimers) when the components are identical, and exciplexes (excited complexes) when they are not. The latter will clearly have the greater charge transfer character and it is their importance to the photolytic generation of radical ion pairs that forms the content of this chapter.

An example of an exciplex is that formed by the interaction of the strong electron acceptor 1,4 dicyanobenzene (1,4 DCB) with electronically excited pyrene (Py^*) molecules. The effect on the system fluorescence upon increasing the concentration of 1,4 DCB in a toluene solution of Py is shown in figure 4.1 [1]. The pyrene (S_1-S_0) monomer emission is replaced by a broad exciplex band peaked at longer wavelength. Both bands show Stern-Volmer intensity variation with 1,4 DCB quencher concentration fitting the process,

$$\begin{tikzcd}
{}^1\mathrm{Py}^* + \mathrm{DCB} \arrow[r] \arrow[d] & {}^1(\mathrm{Py}^{\delta+}\ldots\mathrm{DCB}^{\delta-})^*. \arrow[d] \\
\text{monomer emission} & \text{exciplex emission}
\end{tikzcd}$$

Formation in a singlet state is to be expected from consideration of the very low S-T molecular ISC rate of ~ $10^5 s^{-1}$ for pyrene [1].

With the advent of laser techniques, further studies were performed on charge transfer systems, especially with a view to elucidating the fate of exciplexes in media covering a range of dielectric constants [2]. Absorption transients, coinciding with the decay of exciplex emission, were detected and their spectra assigned to those of the molecular complexes. Their similarity to the spectra of the appropriate radical ions, prepared by non-photolytic techniques, provided further support for exciplex charge transfer nature.

As the solvent polarity is increased it is found that the exciplex fluorescence lifetime and intensity both decrease until, for example, in acetonitrile (ϵ = 38) it is no longer detectable [3]. Flash photolysis and absorption studies revealed that the loss of exciplex emission is associated with the formation of radical ions [4,5] but a crucial observation, however, was that exciplex fluorescence quantum yield decreased more rapidly than the corresponding lifetime, as distinct from the parallel changes expected in these quantities for a single

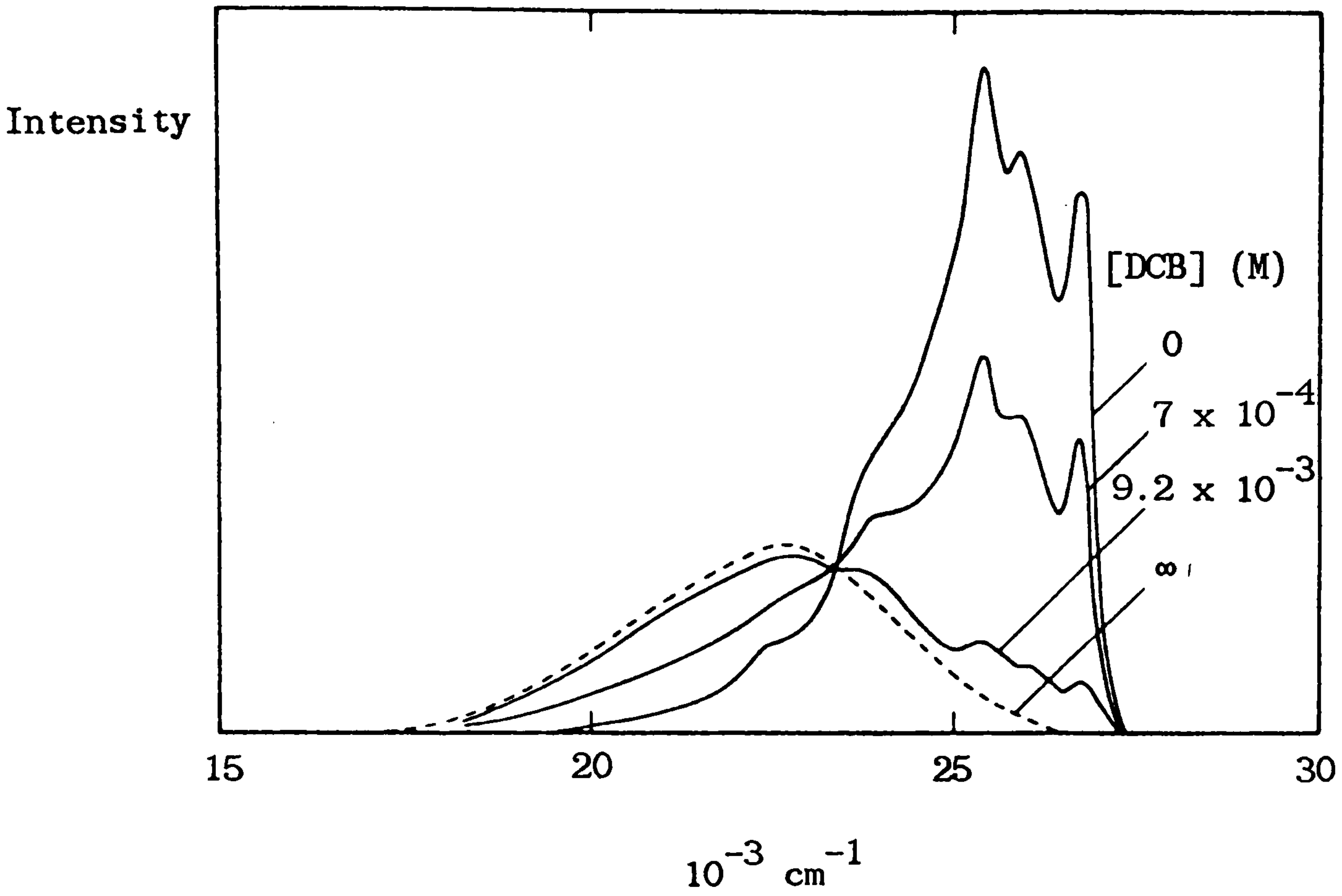

Figure 4.1. Fluorescence spectra recorded in toluene of 5.1 x 10^{-5} M pyrene alone and with increasing amounts of added 1,4 dicyanobenzene. Excitation was at 313 nm [1].

exponential decay. Two contradicting explanations were forwarded by early workers to account for this effect but neither resolved the problem satisfactorily.

Mataga et al. [3] proposed an exciplex structural change was associated with increasing solvent polarity, resulting in changes to exciplex radiative and non-radiative probabilities. This explanation was disfavoured by theoretical considerations which indicated that such changes would be insignificant [1].

Weller et al. [4] provided an alternative explanantion by introducing an alternative kinetic pathway to radical ions which bypassed the exciplex state and gained in importance with increasing polarity. The reaction scheme becomes,

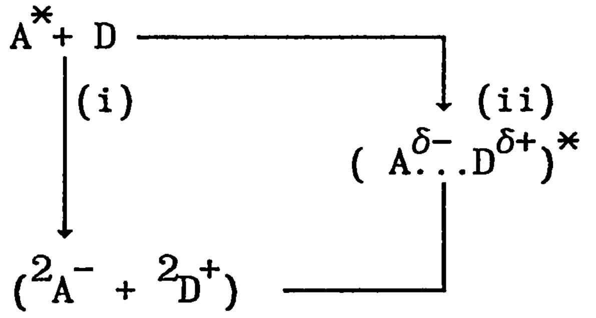

where A and D respectively represent generalized acceptors and donors.

The major objection to this proposal comes from a consideration of the Franck-Condon factors involved in the electron transfer leading directly to ion pair formation. Increasing polarity would be expected to stabilize the ion pair state with respect to that of the initial species leading, in fact, to a decrease in the importance of (i) relative to (ii) with increasing polarity.

An altogether more feasible explanation may be gained from the work of Petrov et al. [6] who studied the effect of static magnetic fields on exciplex fluorescence quantum yield arising from pyrene-dimethylaniline (Py/DMA) systems in a range of alcohol solvents. In this case Py acts as an electron acceptor, DMA a donor giving rise to a ($Py^{\cdot -}$ $DMA^{\cdot +}$) radical ion pair.

Steady-state experiments clearly demonstrated that the exciplex emission could be modulated by low magnetic fields, suggesting that the effect on radical pair ISC was being communicated to the exciplex. The proposal was that a back-reaction step existed,

$$^{1}(\,^{2}A^{-}\;^{2}D^{+}\,) \longrightarrow {}^{1}(\,A^{\delta+}...D^{\delta-}),$$

linking exciplex fluorescence yield and lifetime to an ion recombination process, and simultaneously providing a field effect mechanism and accounting for the non-trivial fluorescence-quantum yield behaviour.

The clear implication is that exciplex systems have the potential to act as 'self-indicating' candidates for the study of radical pair processes; their fluorescence providing a monitor, albeit indirect, of the singlet pair state. In this sense there is a resemblance to the situation found in pulse radiolysis work conducted in non-polar hydrocarbon media wherein ion recombination is sufficiently energetic to populate excited monomer singlet states.

Prior to the work of Petrov et al. the py/DMA system had been the subject of experimental and theoretical field effect studies conducted by Schulten et al. [7,8]. Their work considered the effects of solvent polarity and viscosity on magnetic modulation of geminate triplet pyrene and free ion yields, complementary to the singlet recombination process. Ion yields showed small, positive field effects, enhanced by decreasing polarity as the total geminate reaction yield increased with increasing coulombic attraction between the pair members. Triplet yields showed larger, negative effects which were relatively insensitive to solvent properties. From the negative effect it may be deduced that the ion pair was generated in a singlet state whilst the solvent insensitivity expresses the fact that the fractional change in geminate triplet yield, on application of a magnetic field, is not critically sensitive to the geminate fraction of the total reaction. Taken together the triplet and free ion yield field effect observations imply that triplet ion recombination is favoured over that of singlet pairs. This, at first sight, unexpected observation can be rationalized on energetic grounds already discussed in that the triplet state of pyrene lies at an energy intermediate between S_0 and S_1, and closer to the ion pair state. Better F-C factors between initial and final states are therefore offered for the triplet reaction. The relationship $k_S < k_T$ is to be expected for a wide range of ion pair electron-transfer recombinations.

A further point to be gleaned from the work of Schulten et al. is the variation in field effect as a function of the species being detected. Careful consideration should therefore be given to this point when planning a field effect experiment.

In summary, the evidence suggests that the quenching of π-system fluorescence by interaction with ground state π-systems of differing electron acceptor/donor properties, involves the formation of excited charge transfer complexes exhibiting red-shifted fluorescence. Given solvents of sufficient polarity, the complexes can undergo reversible dissociation to radical ion pair states, the reactions of which are susceptible to magnetic field modulation.

4.2 The Pyrene-Dicyanobenzene System

4.2.1 Introduction

As an attempt to check the generality of the observations made for the Py/DMA system, and to test the fundamental implications of radical pair theory, a study was undertaken of pyrene fluorecence quenching by three substitution isomers of dicyanobenzene, each giving rise to radicals with characteristic magnetic properties.

The possible fates of species present in the photochemical system and an approximate indication of their relative energies (increasing vertically) for a polar solvent are presented in figure 4.2. Only processes of direct importance to the present study are included. A direct electron transfer pathway to the ion pair state (k_{qe}) has been shown in the figure although, as discussed, this might be expected to be of lesser significance, at high solvent polarity, than the alternative bimolecular association to an exciplex. In both cases the geminate ion pair is produced in a singlet state which can undergo interconversion with states of triplet spin configuration by the radical pair mechanisms outlined in chapter 2. Other possibilities are that the ion pair members overcome mutual electrostatic forces, escaping into the bulk solution, or they can react to give molecules in the corresponding spin configuration. The singlet pair has available to it, in addition, the important association channel (k_{ie}) forming an exciplex.

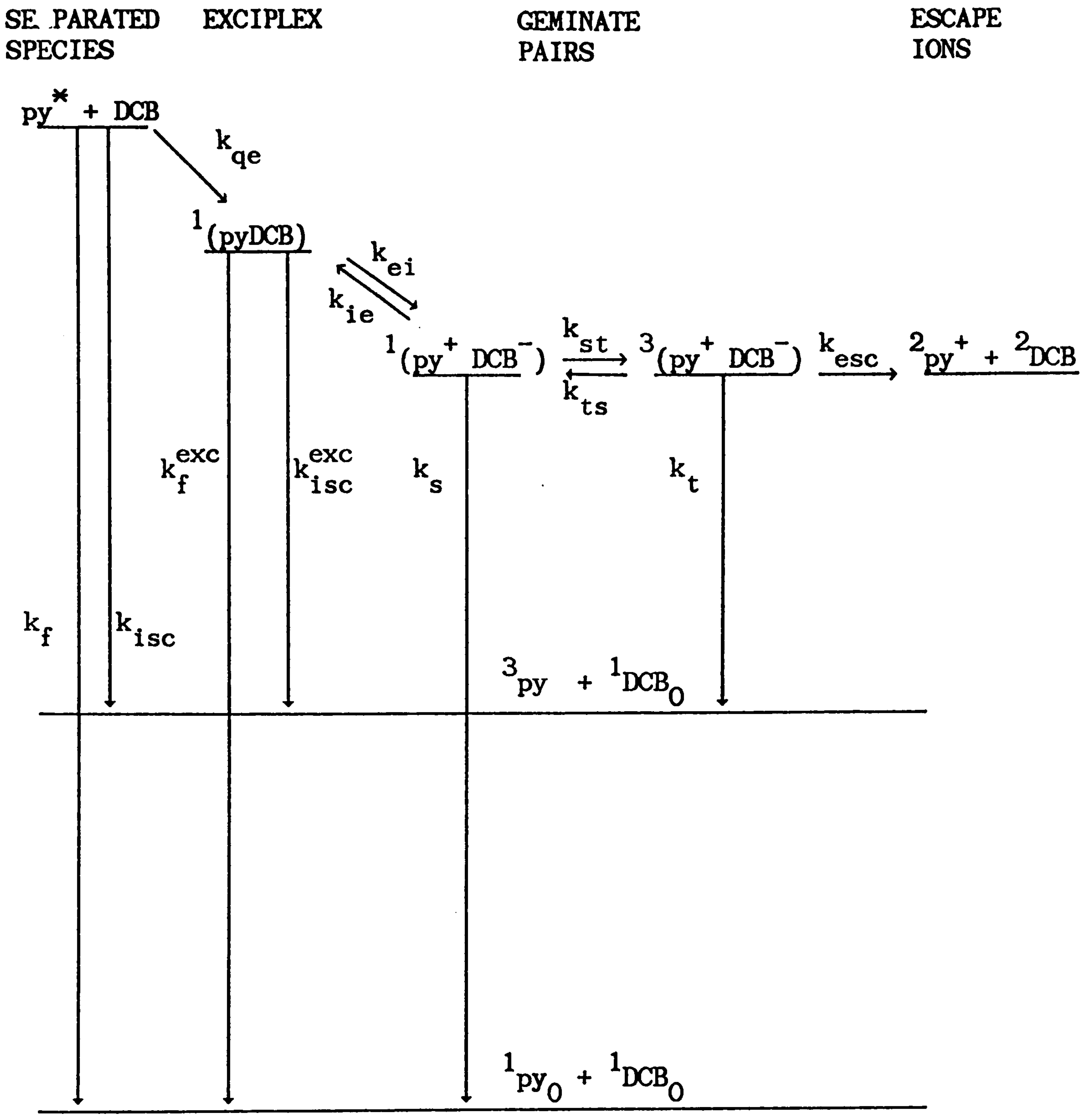

Figure 4.2. Schematic representation of the pyrene - dicyanobenzene system in a polar solvent, indicating relative energies of chemical species.

The relative energies shown in the figure 4.2 are those to be expected at polarities representative of the solvents used in the study. Of importance to the present work is the relationship between the exciplex and ion pair states which has been discussed by Weller in the context of photoinduced electron transfer reactions [1.9]. From a consideration of the Gibbs function for ion pair and exciplex formation, he concluded that, for the equilibrium

$$\text{ion pair} \rightleftharpoons \text{exciplex},$$

the Gibbs function change is independent of the redox parameters of the constituent species and can be approximated by

$$\Delta G_{ie} \quad = \quad -\frac{\mu^2}{\rho^3}\left[\frac{\epsilon - 1}{2\epsilon + 1} - 0.19\right] - \frac{2.6}{\epsilon}\,(\text{eV}) \quad + \; 0.15 \;\; \text{eV} \quad (1)$$

for charge transfer exciplexes, where μ an ρ are respectively the exciplex dipole moment and effective spherical radius, and ϵ is the solvent dielectric constant. (μ^2/ρ^3) relates exciplex solvation energy to the solvent polarity, and for a typical case has a value of ~0.75 eV [1], enabling the following table to be drawn up:

ϵ	2	4.3	7	12	>30
ΔG_{ie} (eV)	-0.8	-0.21	0.0	0.11	0.21
ΔG_{ie} / kT_{298}	-31	-8.0	0.0	4.0	8.0

showing that, on thermodynamic grounds, exciplex dissociation is favoured a $\epsilon \lesssim 7$. It has been assumed that the exciplex exists at a separation of 3 Å (molecular plane) and the ion pair at 7 Å.

Weller et al. [1] have also treated the problem of exciplex/ion pair distinguishability on theoretical grounds, showing that exciplex structure is relatively insensitive to solvent polarity and that an energy barrier is maintained between the two states. At $\epsilon \sim 30$ the barrier has been estimated to be ~ 0.1 eV and confirmed experimentally by temperature dependence studies on Py/DMA [10].

The situation in a polar solvent may be summarized by the potential curves of figure 4.3. As the free ion separation is reduced, coulombic and Heisenberg spin exchange interactions come into effect, giving rise to the formation of a contact ion pair which, at smaller separations, will have a significant singlet-triplet energy splitting. Further reduction in the separation leads to the potential barrier at the reaction radius and finally to exciplex states with singlet-triplet separations of a magnitude sufficient to prevent modulation of exciplex ISC by low magnetic fields. Ion pair and exciplex initial formation are taken to occur at the separations indicated in the figure.

It now remains to bring together the above knowledge into a model describing the behaviour in the target Py/DCB system. A phenomenological first order kinetic treatment will be applied with rate constants being estimated where necessary to give an approximation to the observations expected from experiment.

4.2.2 Kinetic Analysis

For the purposes of discussing the influence of a magnetic field upon exciplex fluorescence, the pertinent elements of figure 4.2 may be

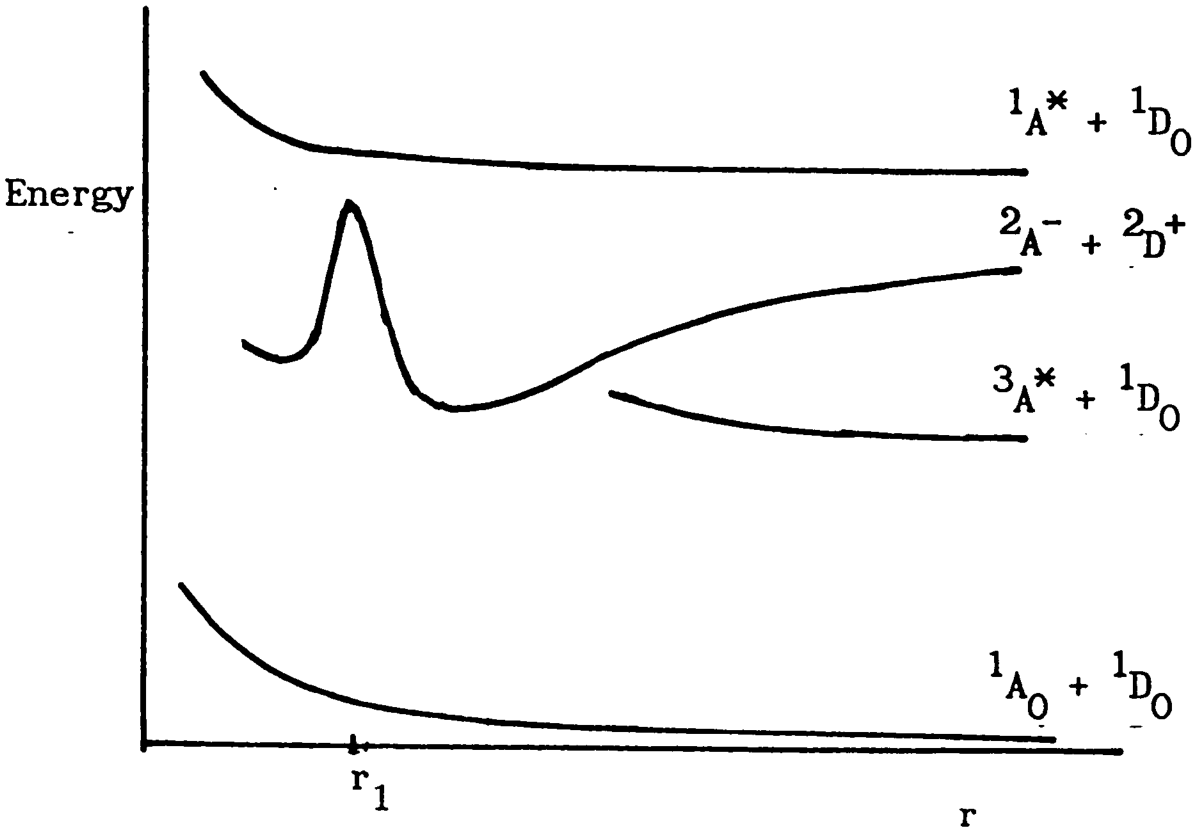

Figure 4.3. Representation of the potential energy of a donor - acceptor system as a function of separation, r. Recombination to form an exciplex occurs at r_1.

summarized by the kinetic scheme:

$$\begin{tikzcd} E \arrow[r, shift left, "k_{12}"] \arrow[d, "k_1"'] & S \arrow[l, shift left, "k_{21}"] \arrow[d, "k_2(B)"] \\ {} & {} \end{tikzcd} ,$$

accounting for the all-important coupling processes, with first-order rate constants k_{12} and k_{21} linking exciplex, E, and singlet, S, states. Additionally an independent loss process is included for each kinetic species. With regard to figure 4.2, the following assignments may be made:

$$\begin{aligned} k_1 &= k_f^{exc} + k_{isc}^{exc} , \\ k_2(B) &= k_s + k_{esc} + k_{st}(B) , \\ k_{12} &= k_{ei} , \\ k_{21} &= k_{ie} . \end{aligned} \qquad (2)$$

The rate constant k_{ts} has been deliberately excluded from the field-sensitive k_2 as it is expected that the triplet ion pair recombination process will be fast, leading to a negligible probability of a crossing back to a singlet radical pair state.

On the assumption that there will be a dominant contribution to ion pair formation by, either the direct pathway, or by that involving the intermediacy of an exciplex, analysis of the simplified scheme may be treated from a standpoint of δ-function generation of an initial singlet ion pair or of an initial exciplex. Extension to the overall scheme of figure 4.2 is then achieved by convolving the analytical response, obtained from the model, with a pyrene quenching function. Such a procedure will not affect the exciplex fluorescence-yield response to a magnetic field but may have an observable effect on the temporal profile of the emission.

The two coupled differential equations describing the model system may be solved by recourse to a rate coefficient matrix method, or by differentiation and solution of the resulting second order problem. The solutions for exciplex concentration-time dependence are:

applying initial conditions $E(0) = E_0$, $S(0) = 0$,

$$E(t) = \frac{(a - \lambda_+)\exp(\lambda_- t) - (a - \lambda_-)\exp(\lambda_+ t)}{(\lambda_- - \lambda_+)} E_0 \quad (3)$$

and for initial conditions $E(0) = 0$, $S(0) = S_0$,

$$E(t) = b\,\frac{\exp(\lambda_- t) - \exp(\lambda_+ t)}{(\lambda_- - \lambda_+)} S_0 \quad (4)$$

where the eigenvalues λ_+, λ_- are given by

$$\begin{aligned}\lambda_+, \lambda_- = & -\tfrac{1}{2}(k_1 + k_{12} + k_{21} + k_2) \\ & \pm \tfrac{1}{2}\{[(k_1 + k_{12}) - (k_2 + k_{21})]^2 - 4k_{12}k_{21}\}^{\frac{1}{2}},\end{aligned}$$

and $a = -(k_1 + k_{12})$, $b = k_{12}$.

Certain deductions may be made as to the relative magnitudes of the rate constants, purely on the basis that E(t) must represent a realistic decay and must not, at any time, become negative. Thus,

$$\left.\begin{array}{l}\lambda_+ \\ \lambda_-\end{array}\right\} \leq 0,$$

$$|\lambda_-| > |\lambda_+|,$$

$$(a - \lambda_+) \geq 0, \tag{5}$$

$$(a - \lambda_-) \geq 0,$$

$$|\lambda_+|,\ |\lambda_-| \geq k_1 + k_{12},$$

and the rising edge of E(t) will be dominated by λ_-, whilst the fall will be governed by λ_+. For the initial exciplex model (3), the slower λ_+ term will have the larger coefficient. Further consideration reveals that λ_+ contains a greater contribution from the field sensitive rate constant $k_2(B)$ and so the falling edge of E(t) is expected to show a field modulation greater than that of the rising edge.

If the magnetic field effect upon exciplex emission yield is defined as

$$FE = \frac{\int_0^\infty ([E(t)]_B - [E(t)]_0)\, dt}{\int_0^\infty [E(t)]_0\, dt}, \tag{6}$$

expressions for the two limiting cases may be derived (after substitution for k_1 and k_2),

$$FE_e = \frac{k_{12}\, k_{21}}{(k_1 + k_{12})} \cdot \frac{[k_{isc}(0) - k_{isc}(B)]}{[k_{21} + k_{esc} + k_{isc}(0)]\,[k_{isc}(B) + k_{esc} + k_1 k_{21}/(k_1 + k_{12})]}, \tag{7}$$

assuming an initial exciplex, and

$$FE_s = \frac{[k_{isc}(0) - k_{isc}(B)]}{[k_{isc}(B) + k_{esc} + k_1 k_{21}/(k_1 + k_{12})]} , \tag{8}$$

assuming an initial singlet ion pair. Considering solely the field effect on the radical pair ISC rate we have,

$$FE_{isc} = \frac{[k_{isc}(0) - k_{isc}(B)]}{k_{isc}(0)} . \tag{9}$$

It is apparent that the limiting cases will show detailed differences in their response to a magnetic field but both will bear some similarity to the sigmoidal behaviour predicted for the effect upon k_{isc} alone. The expectation is that in both cases the observed $B_{½}$ values will be greater than obtained from the ISC expression alone, unless

$$\frac{k_1\ k_{21}}{(k_1 + k_{12})} + k_{esc} \quad >> \quad k_{isc} \quad . \tag{10}$$

On comparing the magnitudes of the field effects it may be seen that $FE_e < FE_s$, confirming the notion that greater modulation depth may be obtained in the absence of a background signal which, in this case, is exciplex fluorescence not derived from a radical reaction process.

To make further inferences on the model system it is necessary to estimate the relative magnitudes of the component rate constants. If any field effect is observed k_{esc} should be comparable to, or less than, k_{isc} giving expected values, for both, of $10^8 - 10^9\ s^{-1}$. k_1 has been measured as $\sim 10^6$ s^{-1} whilst $k_{12} \sim k_{21} \sim 10^6 - 10^7$ s^{-1} [11]. Thus k_{esc} and k_{isc} terms will be dominant.

We are now in a position to assess solvent effects on the system with respect to polarity and viscosity. These are expected to be evidenced in k_{12}, k_{21} and k_{esc} with polarity responsible for the major changes in the former two rate constants as a result of their dependence on the exciplex-ion pair relative energies. Additionally, variation in k_{isc}, with these same variables, is conceivable due to its intrinsic dependence upon spin-evolution sampling time. As a first approximation, however, such an effect will be ignored.

FE_s (8) will show a monotonic decrease with increasing polarity and viscosity, the fractional term in the denominator being insignificant. The initial exciplex model (7), however, requires more careful consideration. The additional factor may be approximated as

$$\frac{k_{12}\, k_{21}}{[k_1 + k_{12}][k_{esc} + k^{(0)}_{isc}]} , \qquad (11)$$

or further as

$$\frac{k_{21}}{[k_{esc} + k^{(0)}_{isc}]} . (1 - k_1/k_{21}) , \qquad (12)$$

assuming $k_{21} >> k_1$. Increasing solvent dielectric constant leads to a lowering of the potential barrier between exciplex and ion pair, and a lowering of the ion pair state energy with respect to the exciplex. The latter change is predicted to be the more dramatic [1] and so it is satisfactory to assume k_{12} is an increasing function of polarity, whilst

k_{21} shows a decreasing trend. The overall dependence of FE_e upon ϵ would be expected to show a maximum brought about by a product of rising and falling functions.

Similarly temperature coefficients of the field effects are expected to arise from the activated processes k_{12}, k_{21}, k_{esc}. FE_s is predicted to fall with increasing temperature, through $k_{esc}(T)$, whilst the behaviour of FE_e is less clear with the possibility of $k_{21}(T)$ compensating $k_{esc}(T)$.

Summarizing, the two proposed limiting case of the model system, involving initial exciplex and singlet generation, should be distinguishable on the grounds of field effect magnitude, temperature coefficient and solvent dependence. The sensitivity to each of these factors is, however, dependent upon the absolute magnitudes of the rate constants involved.

4.3 Experimental Characterization

Having established a kinetic model for the behaviour of the pyrene-dicyanobenzene system based upon the evidence available in the literature, mainly with regard to pyrene-DMA, a range of experiments were designed to test the theoretical predictions for kinetic and magnetic field response. To this end, a series of ten solvent systems were devised to provide reaction media exhibiting a gradation in viscosity and dielectric properties. It was, unfortunately, not possible to choose systems which allowed independent variation of the two properties but by selecting three components, of which two had approximately equal dielectric constants, it was possible to prepare a series of binary mixtures showing identical e at different η.

Table 4.1 shows the values for viscosity and dielectric constant for each of the solvent systems used. Dielectric constants were calculated assuming ideal mixture behaviour as difficulties were experienced in the determination of ϵ by audio capacitance measurements. These were attributed to the high dielectric loss exhibited by such highly polar media. Viscosities were determined by the use of an Ostwald viscometer with reference to acetonitrile, though this did introduce some capillarity error for the high viscosity mixtures.

4.3.1 Steady State Response

As a preliminary to applying MARY and RYDMR techniques to the py/DCB system, certain characterization experiments were performed. Figure 4.4a shows the absorption spectrum of ground state pyrene in a hexane solvent. Steady-state excitation of py/DCB in a 5:3 v/v cyclohexanol : DMF mixed solvent at a wavelength of 337nm, close to the S_0-S_2 extinction maximum, leads to emission from pyrene monomer and py-DCB exciplex species. In this region DCB is essentially transparent. A comparison of the corresponding emission spectra recorded in the presence and absence of DCB is presented in figure 4.4b in which the traces have been normalized with respect to the peak intensity; in reality total emission yield is much reduced by the quenching action of DCB. Clearly exciplex and monomer emission are present, with maximum discrimination in the long-wavelength tail. As expected in a polar solvent mixture, exciplex fluorescence intensity is low. Both spectra were obtained from deaerated samples kept under a nitrogen atmosphere.

Table 4.1

Properties of Solvent Mixtures

Composition Cyclohexanol : X (v/v)	η (cP)		ϵ^{*}_{calc}
	X = DMF	X = ACN	
3 : 1	7.0	3.4	21
5 : 3	3.1	1.2	24
1 : 1	2.2	0.9	26
3 : 5	1.8	0.7	29
1 : 3	1.1	0.5	32

* Ideal binary mixture assumed,
Cyclohexanol : $\epsilon = 15.0$,
DMF and ACN : $\epsilon = 37.6$.

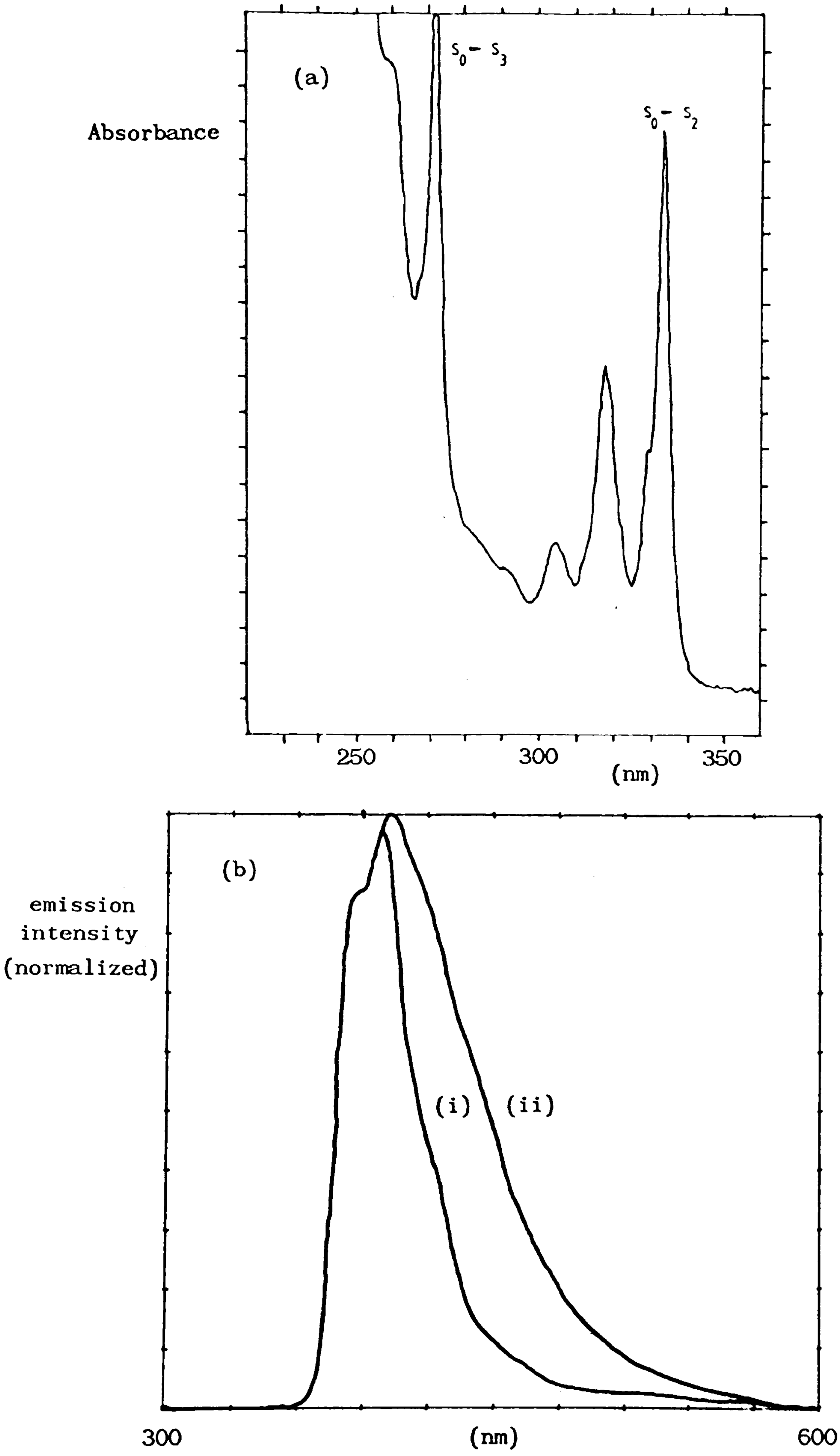

Figure 4.4. Optical spectrum characteristics of the py - dicyanobenzene system.

(a) U.V./visible absorption spectrum of 7.5 x 10^{-5} M pyrene in hexane.

(b) Emission observed upon excitation at 337 nm from a 7.5 x 10^{-5} M pyrene solution in 5:3 cyclohexanol:DMF (i), and in the presence of 0.25 M 1,2 dicyanobenzene (ii).

4.3.2 Temporal Response

The availability of recording equipment capable of operating on timescales of a few nanoseconds opens up the possibility of using time-domain information as a means of distinguishing short-lived fluorescent species. To gain maximum benefit from this dimension, however, it is necessary to approach δ-function fluorescence excitation. Of the equipment available, the N_2 laser provided the closest approximation to this condition with its gaussian profile output at 6 ns FWHM and wavelength of 337 nm, ideally suited to pyrene excitation.

A series of wavelength-time resolved emission experiments performed on py/DCB in a range of solvent media clearly showed the change from essentially single exponential decay at short wavelength to multi-exponential rise and fall kinetics at longer wavelengths; the crossover occuring in the region above 500 nm in all cases. Figure 4.5 shows effective lifetimes as a function of wavelength for two very different solvent mixtures. Results were obtained by fitting a single exponential to the trailing edge of fluorescence transients.

The signal observed at 500 nm in all solvents is identical in all solvents to that at shorter wavelengths and is characteristic of the quenching of Py^*. Assuming time-invariant DCB concentration, an effective second-order quenching rate constant, k_q, was estimated. The results are displayed in figure 4.5, together with the corresponding

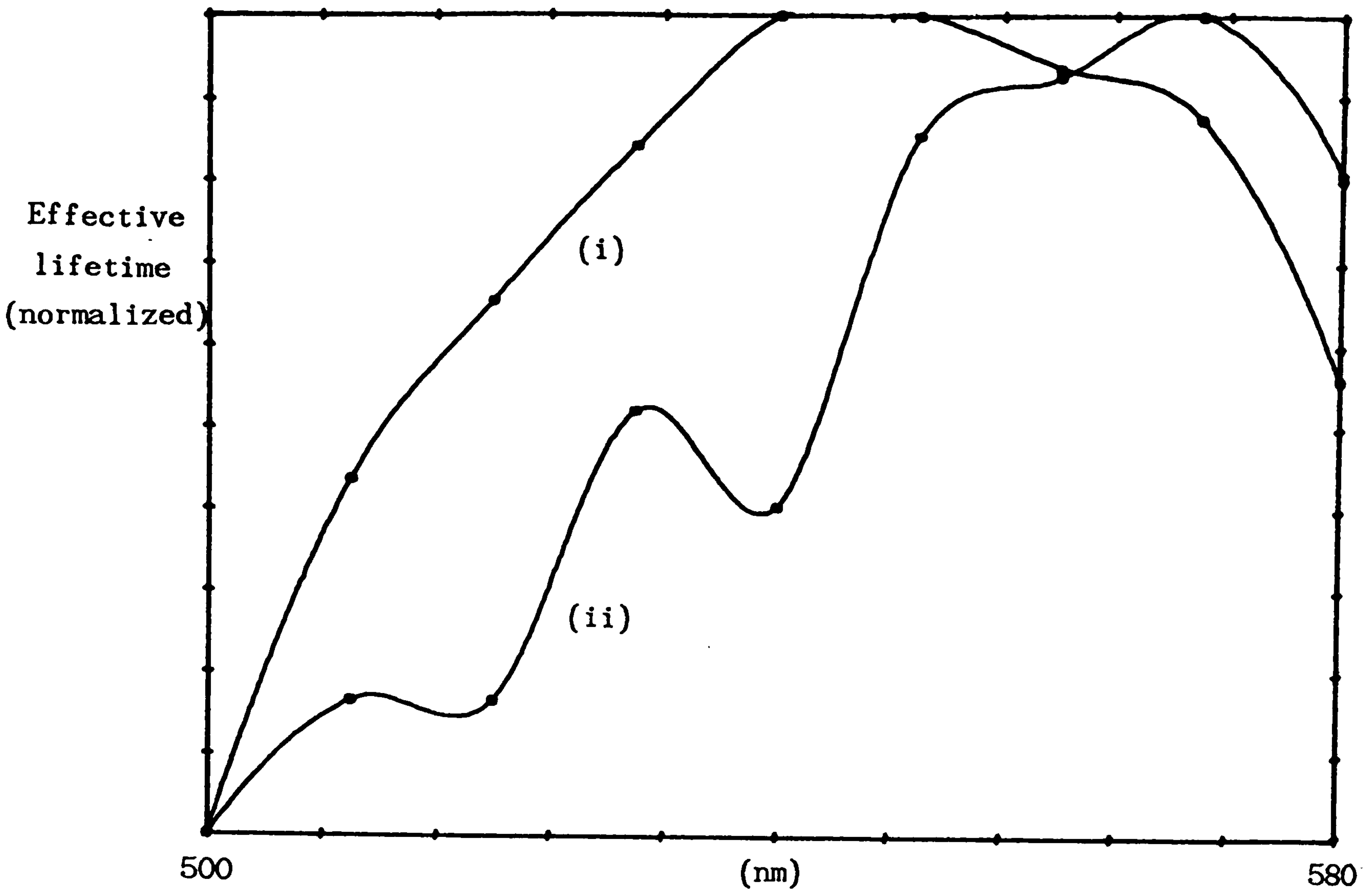

composition cyclohexanol : DMF	η (cP)	ϵ	$k_q^{obs\ a}$ $mol^{-1}dm^3s^{-1}$	k_{diff}^{b} $mol^{-1}dm^3s^{-1}$
5 : 3 (i)	3.1	24	3.0×10^9	2.2×10^9
1 : 3 (ii)	1.1	32	5.7×10^9	5.8×10^9

a [py] = 7.4×10^{-5} M.
[DCB] = 3×10^{-2} M.
b Calculated from equation (13).

Figure 4.5. Effective lifetime of emission from pyrene - dicyanobenzene in two solvent systems as a function of wavelength. Also indicated are corresponding pyrene-quenching rate constants determined from emission at 500 nm.

diffusion-limited constants calculated from the expression

$$k_{diff} = \frac{8RT}{3\eta} . \qquad (13)$$

applicable to reaction between neutral species in a medium of viscosity η. Close agreement between observed and calculated results exists, despite the lack of any attempt to allow for the finite lifetime of the excitation signal. This would be expected to be particularly significant for the short lifetime obtained in the low viscosity solution and an experimental result below the value calculated could be indicative of its effect. Results higher than k_{diff} might well be expected as a result of a contribution by first order quasi-static quenching in the presence of high DCB concentration local to Py^*.

It is also apparent that the timescales of Py^* and exciplex emission do not differ greatly. From the theoretical treatment of the kinetic model discussed earlier, the temporal dependence of Py^* emission will be present in the exciplex signal via a convolution relationship. Furthermore, additional complications may arise from significant spectral overlap between the two emissions. To aid in the clarification of the matter, the system variables of quencher concentration, solvent viscosity and polarity may be employed.

Increasing quencher concentration would obviously reduce Py^* lifetime by affecting the only second-order rate processes included in the kinetic model. There may, however, be additional pathways showing [DCB]-dependence and leading to the quenching of exciplex fluorescence, which would negate such attempts at separating the two luminescnce timescales.

Figure 4.6 compares short wavelength Py^* emission with that at 550 nm where, for the particular system in question, maximum discrimination in favour of the exciplex is expected. Results were obtained at three DCB concentrations and the exciplex emission profile deconvoluted using that of Py^* to give, according to the kinetic model, the exciplex fluorescence time profile.

The deconvolution method adopted was the Fourier transform technique, described in chapter 3, with a reconvolution procedure to suppress noise. In this case the latter was performed with a gaussian function. Lifetimes were obtained by fitting a single exponential to the trailing edge of the deconvoluted response in an attempt to extract the slow component, λ_+, of the biexponential exciplex kinetics.

The results show that DCB concentration does indeed have a bearing on exciplex lifetime, assuming insignificant spectral overlap (see below). Too much emphasis, however, must not be placed on the functional form of the dependence as this will be distorted by the reconvolution process. Reasons for the change in lifetime may be a bimolecular quenching process or a change in the micro-polarity sensed by the exciplex, leading to a change in k_{12}/k_{21}. The relative importance of the two possibilities is not apparent from the data obtained and the matter remains rather speculative.

The variables of viscosity and dielectric constant are linked for all solvents systems utilized. Thus increasing η leads to decreasing ϵ. The former trend is the most important for Py^* lifetime as evidenced by the $(k_q(\eta) - k_{diff}(\eta))$ relationship observed. Dielectric constant, on literature evidence (above), will have the dominant effect on exciplex

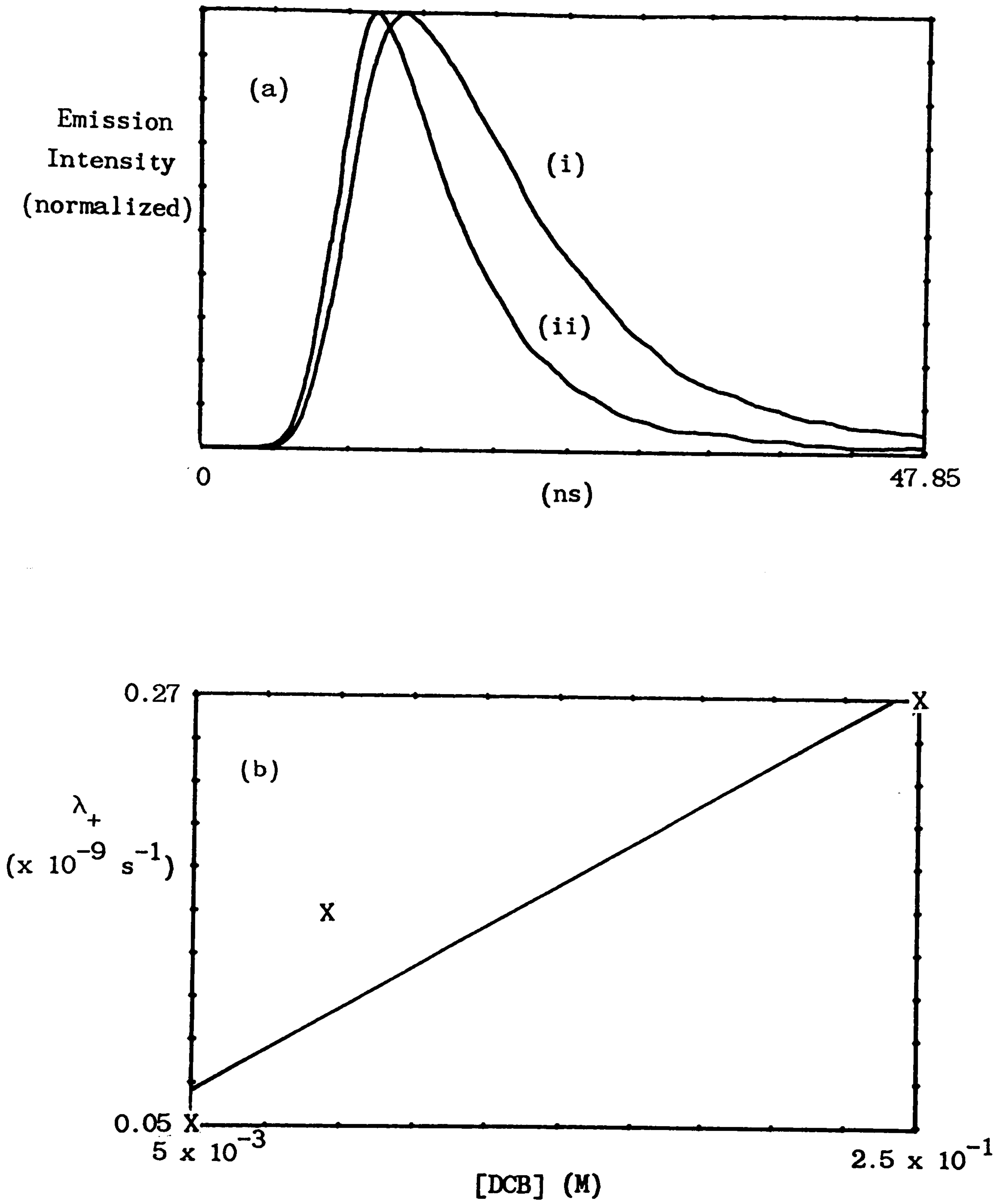

Figure 4.6. Evolution of pyrene - 1,2 dicyanobenzene emission in a 5:3 cyclohexanol:DMF solvent system.
(a) Comparison of emission at 500 nm (i) to that at 550 nm (ii).
(b) Effective exciplex-loss rate constant (λ_+) as a function of 1,2 dicyanobenzene concentration, obtained from deconvoluted emission at 550 nm. Excitation was at 337 nm.

lifetime, at the high dielectric constants involved. Taken together, similar trends in the lifetimes of both species are expected on changing the solvent system and indeed figure 4.5 bears this out. The figure also shows a change in the wavelength of maximum exciplex-monomer emission discrimination which is not inconsistent with the dependence on dielectric constant expected for a polar to neutral state transition; literature data would put the red shift at ~10 nm [1]. The possibility of an underlying Py^* component is, however, suggested by the fall off in τ at longer wavelengths.

4.3.3 Magnetic Field Response

The aim, first and foremost, in studying the Py/DCB system was as a candidate for exploring MARY and RYDMR techniques, the preliminary photophysical work being necessary to reach a level of understanding of the system sufficient to optimize its magnetic field response. As a system not requiring any analyzing or excitation input, other than at the initial photolysis stage, it was potentially extremely useful in the difficult geometry imposed by RYDMR experimental requirements.

Initial experiments focussed on the change in fluorescence transient profile as a function of magnetic field. They were performed in the MARY apparatus discussed in chapter 3. The pulsed magnetic field was activated prior to sample photolysis to ensure it had reached a steady state before the generation of Py^*. Return to zero (terrestrial) field conditions was not enabled until ~1 ms after photolysis. Figure 4.7 shows an example of the changes resulting in exciplex emission on moving from 0 to 220 G. As predicted by the kinetic model, the effect of a magnetic field is to enhance exciplex lifetime with the greatest

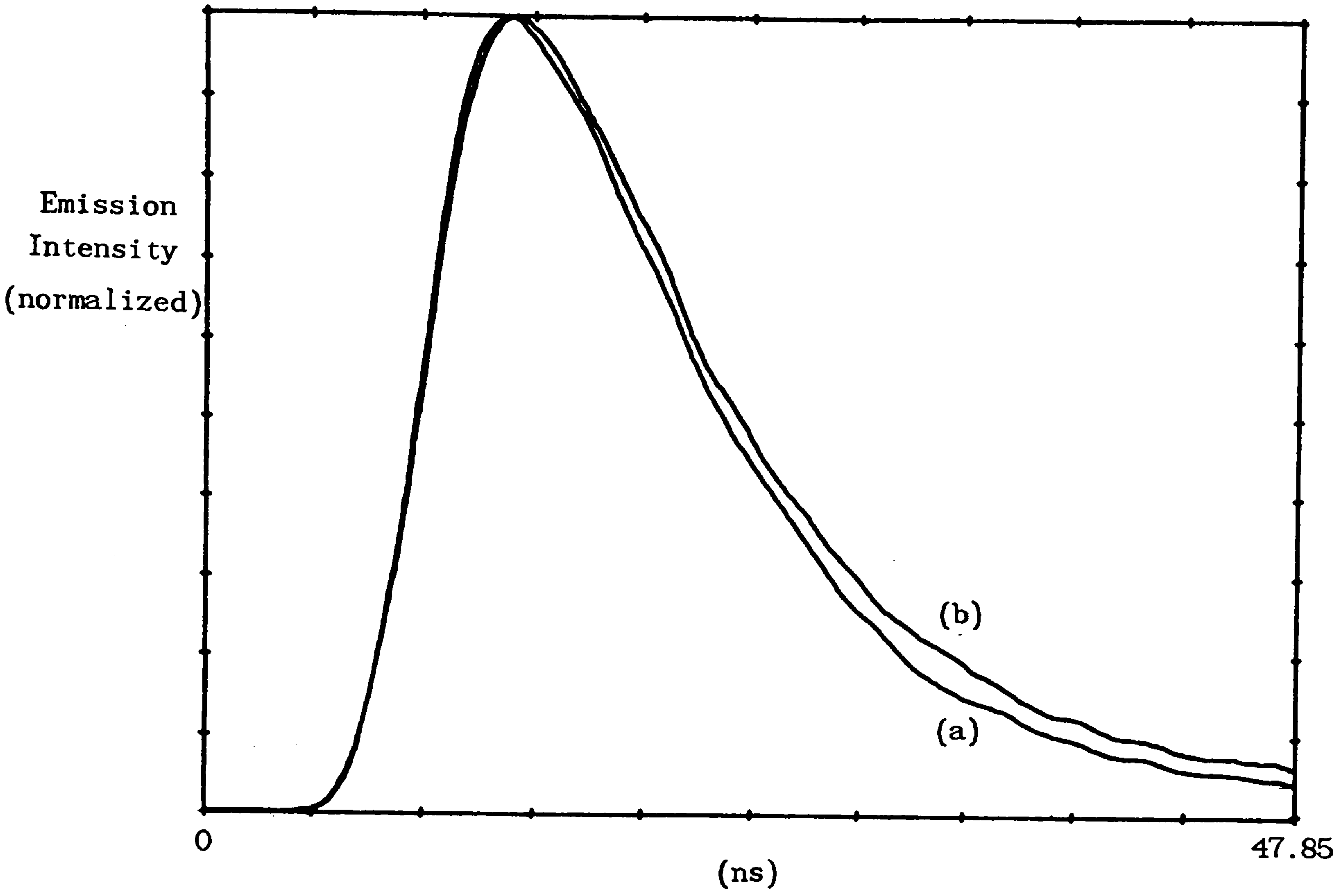

Figure 4.7. Evolution of pyrene - dicyanobenzene emission in a 5:3 cyclohexanol:DMF solvent system in the absence (a) and in the presence (b) of a 100 G magnetic field. Observation was at 550 nm and excitation at 337 nm.

influence on the trailing edge. This is expected on consideration of the reduction in k_2 (via k_{ISC}) which has its greater bearing on λ_+ as compared to λ_-.

Identical experiments performed in the short wavelength region showed no change in the temporal profile, confirming that the quenching process is magnetic field-independent and that no significant contribution to Py^* emission comes from radical ion recombination. They also indicated the absence of spurious instrumental effects.

Extraction of λ_+ and λ_-, defined by the kinetic model, in a biexponential curve-fitting exercise is complicated by convolution with excitation and quenching responses. A reasonable approximation to λ_+, however, should be achieved by fitting a single exponential curve to the tail of an exciplex emission profile. Effective λ_+ values, obtained in this way, as a function of field are depicted in figure 4.8 providing a MARY spectrum. A saturated field effect of 10 is evident for this system involving the 1,2 isomer of DCB. The value of the field at which the effect reaches half this value, $B_{½}$, may be determined as $\simeq$ 22 G.

Further comment is most usefully reserved until additional MARY spectra have been presented.

4.3.4 Automation of the MARY Technique

The process of recording transient information, and performing curve fits, is obviously a laborious task and not suitable for routine automated determination of MARY spectra. Significant simplification of the procedure was achieved by replacing measurement of the fundamental

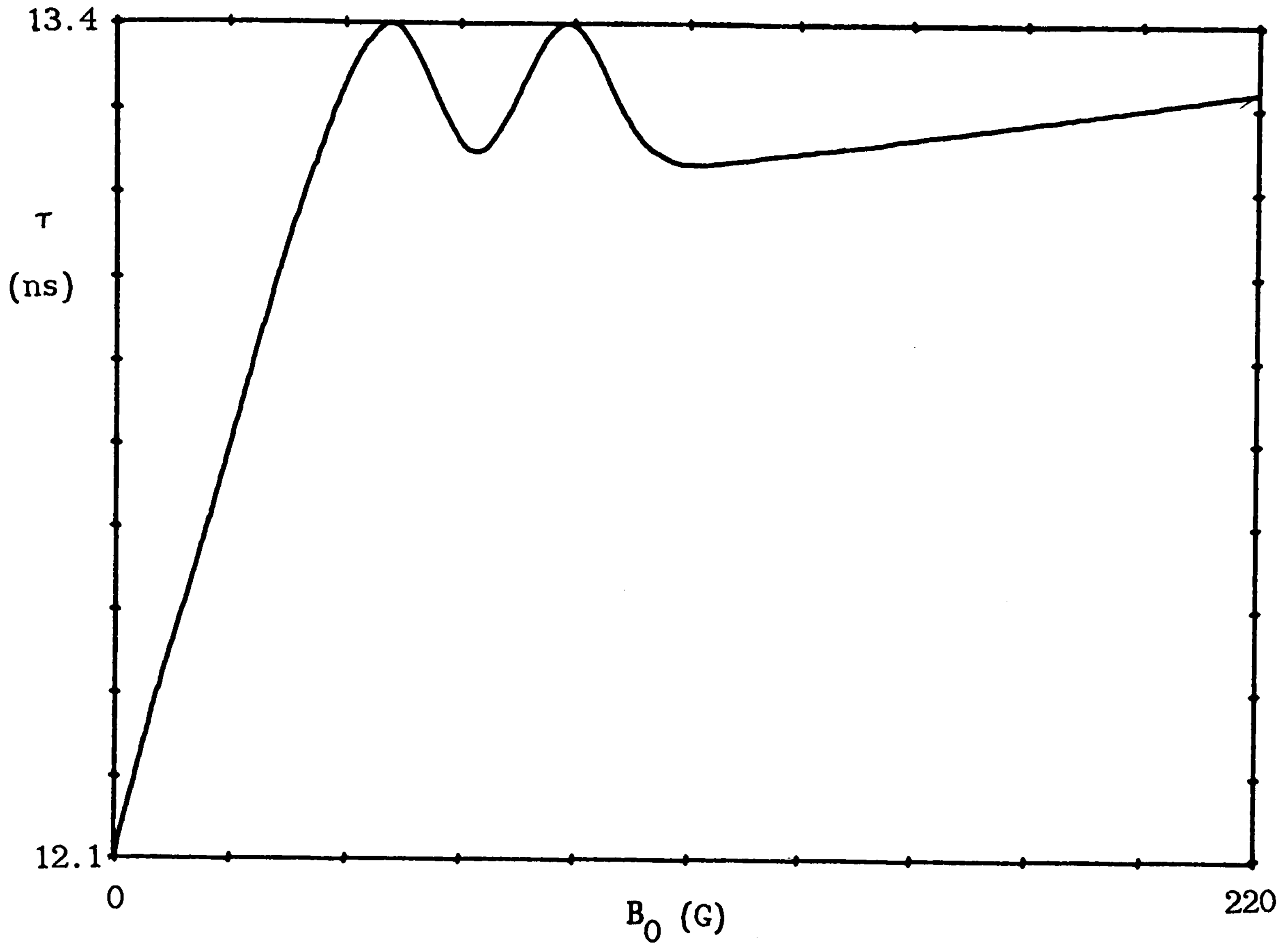

Figure 4.8. Effective lifetime of emission at 550 nm from pyrene - 1,2 dicyanobenzene in 5:3 cyclohexanol:DMF as a function of applied magnetic field, B_0.

system kinetic response with monitoring of the secondary effect on exciplex fluorescence yield as given by the integrated emission-time profile. Further benefits ensue from this approach in that field effect observations become independent of kinetic detail, important when the field response is required as a function of other variables affecting kinetic parameters, and, from an experimental point of view, S/N is enhanced by combining many individual time samples (reduction of signal bandwidth). In detail the mode of operation can best be described by reference to the schematic of figure 4.9 showing control signal relationships. Measurements were made under a repetitive signal-averaging regime with consecutive fluorescent emission profiles recorded alternately in the presence and absence of a magnetic field pulse with programmed amplitude. Signal integrals were represented by digital summations performed over time windows determined interactively with reference to the signal being recorded and prior to commencement of a signal-averaging sequence. Similarly chosen was an interval over which a mean baseline was calculated and which provided a reference level for the digital integral. After each pair of field on/off integrals (Σ_B, Σ_0) had been obtained, the associated field induced change ($\Sigma_B/\Sigma_0 - 1$) was calculated and accumulated with the results of previous pairwise averaging cycles (mode 2b of chapter 3). Simultaneously, a running variance of the results was maintained and displayed, together with the mean field effect and its standard error to date. Optimization of the averaging procedure to a required significance was thus facilitated, though some earlier results were not obtained in this manner and will be presented without statistical information.

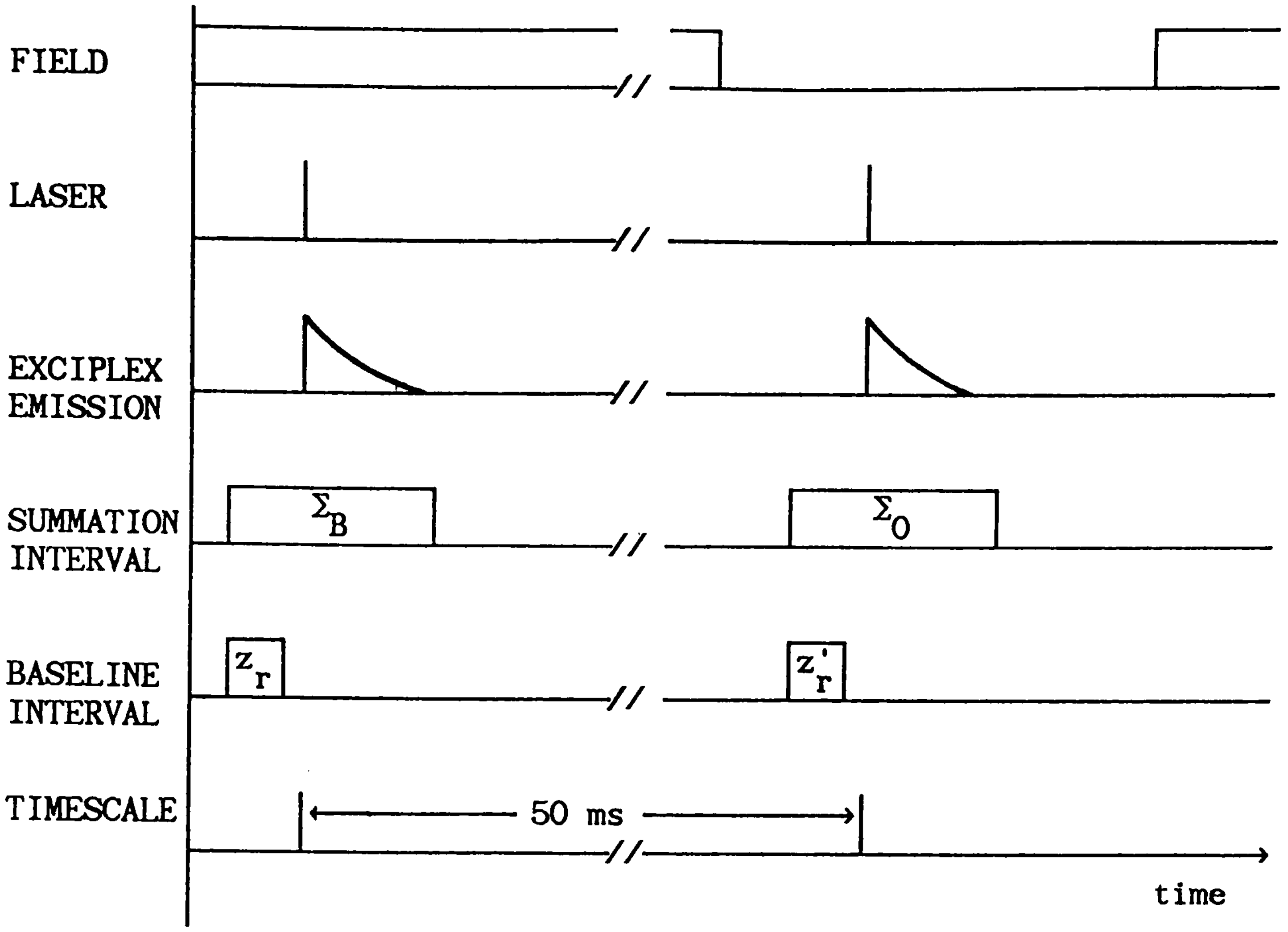

Figure 4.9. Timing relationships for the MARY experiment applied to the pyrene - dicyanobenzene system. The field effect is given by $\{(\Sigma_B - z_r)/(\Sigma_0 - z'_r) - 1\}$.

4.4 MARY as an Investigative Tool

The work to be described was carried out with a twofold purpose in mind. On the one hand it was desired to demonstrate the validity of the theoretical description of MARY, given in chapter 2, whilst on the other there was the notion of employing magnetic fields to reveal system-specific information which was not available to more conventional techniques.

Convenient presentation of the work may be achieved under a series of headings relating to the parameters varied while measuring magnetic field response.

4.4.1 Emission Wavelength Dependence

The effect of a fixed-strength magnetic field was observed at a range of wavelengths close to the region expected to show a maximum exciplex/Py^* emission intensity ratio. The results for two solvent systems are shown in figure 4.10. Such a procedure may be seen as an aid to spectral assignment, capable of distinguishing a field-modulated component which, in this case, is the exciplex fluorescence.

The position of the maximum field effect varies with solvent in a manner consistent with the conclusion drawn from the time-resolved data of figure 4.5. Additionally, comparison with figure 4.4b reveals the clarity with which field modulation extracts the exciplex spectrum from the pyrene monomer emission.

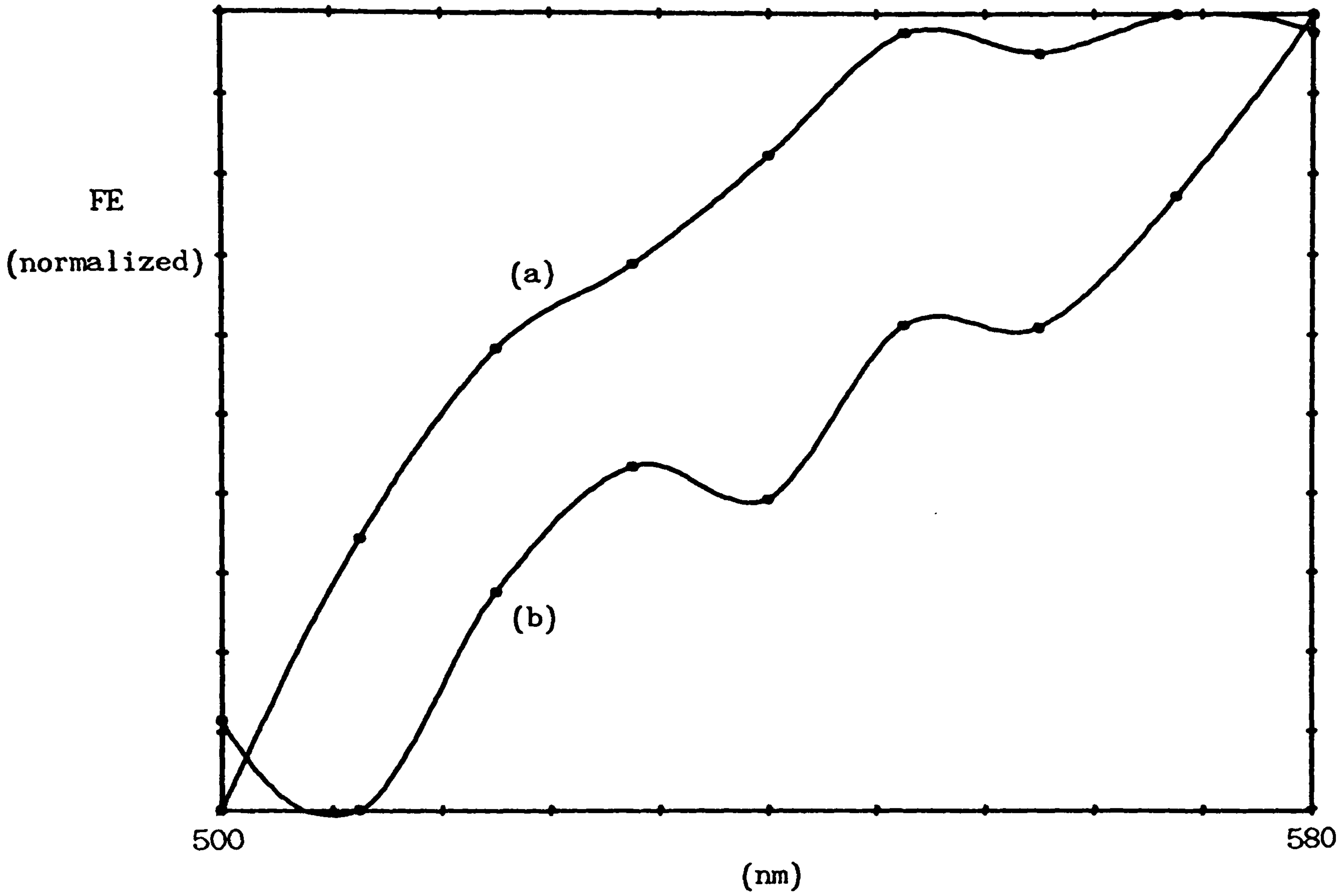

Figure 4.10. Wavelength dependence of observed field effect upon emission yield from pyrene - 1,2 dicyanobenzene in 5:3 cyclohexanol:DMF (a) and 1:3 cyclohexanol:DMF (b) solvent systems.

4.4.2 MARY Spectra

Studying the magnitude of response as a function of applied field strength provides a MARY spectrum which can be characterized by the two parameters of $B_{1/2}$ and saturation amplitude. These were measured as a function of a range of system variables to be detailed below after a description of the basic spectra.

The three substitution isomers of the dicyanobenzene radical anion exhibit different hyperfine couplings to the ring protons and substituent nitrogen nuclei [12]. These are set out in table 4.2 together with the proton coupling constants for the pyrene radical cation. Also included are the $B_{1/2}$ values calculated for a $^2py^{\cdot +}$- $^2DCB^{\cdot -}$ radical pair using the expression given in chapter 2. For comparison the experimentally-determined parameters, from the MARY spectra of figure 4.11, are also included.

It is clear that the experimental spectra have the form expected but are broader than theoretical $B_{1/2}$ values would predict, as expected from the pyrene/DCB kinetic model, and a distinction exists between the (1,3) and the (1,2), (1,4) isomers. Both factors confirm the hyperfine mechanism as responsible for the field response and from a practical point of view, the results demonstrate that MARY spectra can indeed be used as indicators of radical pair identity.

There is no evidence of distortion to the sigmoidal response at very low field indicating the absence of S - T_- or T_+ resonances and the insignificance of any Heisenberg exchange interaction between the spins, when averaged over all trajectories of the members of the radical pair ensemble, a factor in common with pyrene - DMA systems [8].

Table 4.2

Hyperfine Coupling Data for the Pyrene - Dicyanobenzene System

Radical **Coupling Constant ($\frac{a}{g\beta}$ Gauss) [12]**

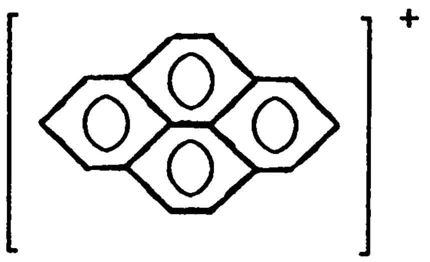

$H_{1,3,6,8}$ = 5.38
$H_{2,7}$ = 1.18
$H_{4,5,9,10}$ = 2.12

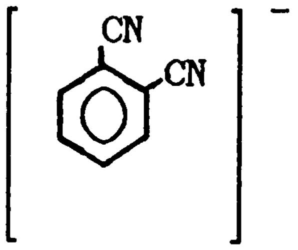

$N_{1,2}$ = 1.75
$H_{3,6}$ = 0.42
$H_{4,5}$ = 4.13

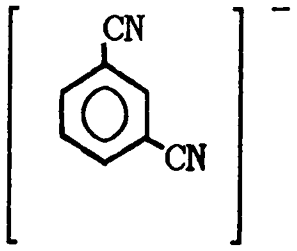

$N_{1,3}$ = 1.02
H_2 = 1.44
$H_{4,6}$ = 8.29
H_5 = 0.08

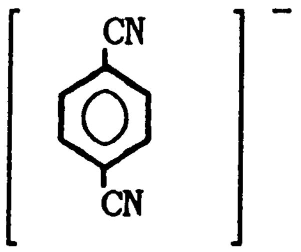

$N_{1,4}$ = 1.18

$H_{2,3,5,6}$ = 1.59

Radical 1	Radical 2	B_1*	B_2*	$B_{½}$*	$B_{½}$ x	FE_{sat} +
Pyrene$^+$	1,2 DCB$^-$	10.3	6.2	17.7	25.5	0.054
	1,3 DCB$^-$		10.4	20.8	33.3	0.123
	1,4 DCB$^-$		3.6	17.7	25.8	0.029

* In Gauss. Calculated from expressions (29 - 30), chapter 2.
x In Gauss. Determined from data of figure 4.11.
\+ Saturated value of field effect observed at 200 G in a 5:3 cyclohexanol : DMF solvent mixture.

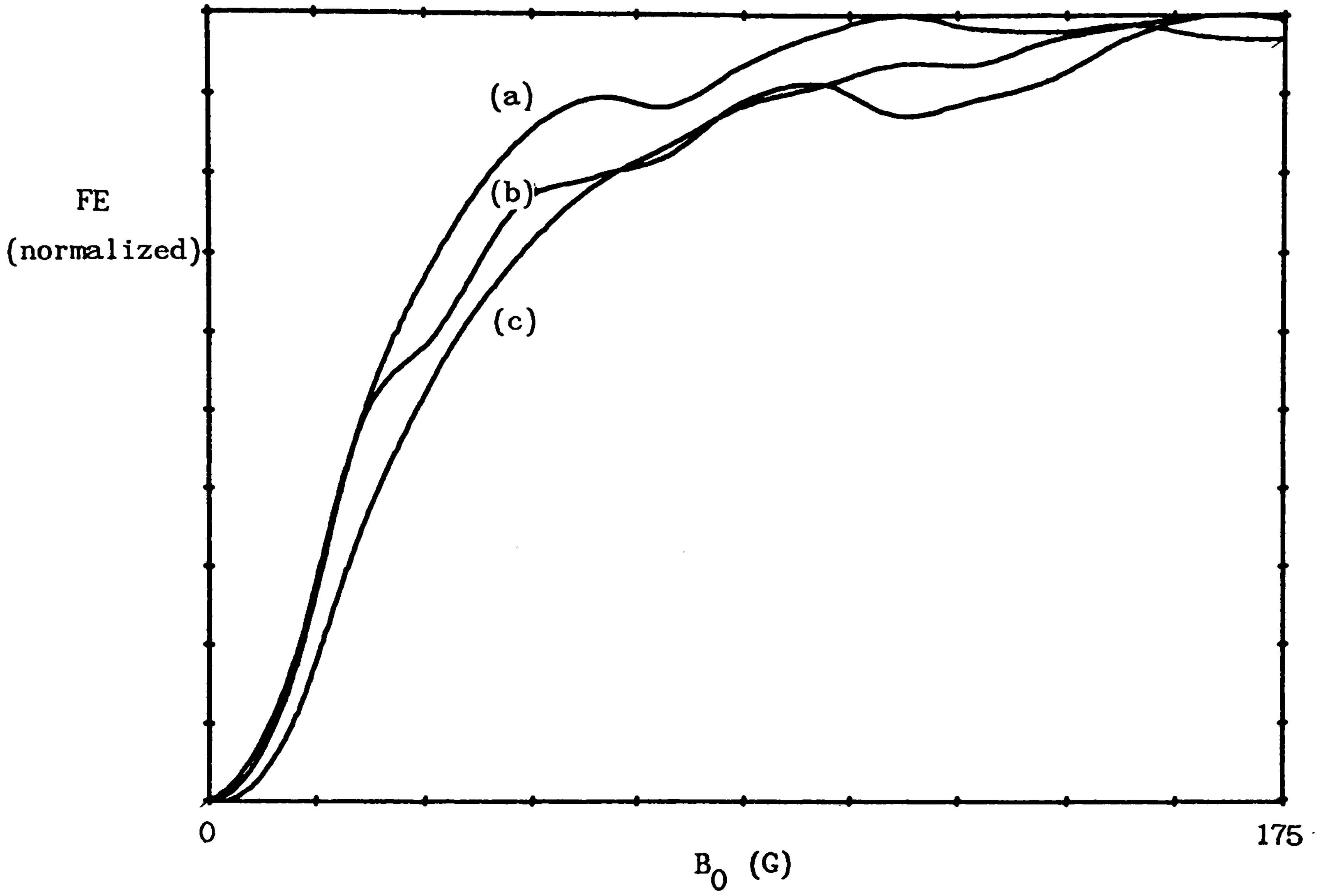

Figure 4.11. B_0 dependence of the field effect upon emission yield, as observed at 550 nm. 1,2 (a), 1,3 (b) and 1,4 (c) dicyanobenzenes were employed at 10^{-3} M in 5:3 cyclohexanol:DMF.

The positive sign of the effect is consistent with exciplex emission arising as a result of recombination from the initial radical pair state, assumed to be a singlet.

Values of saturated field effects are also given in table 4.2 for each of the DCB isomers. The position of the (1,3) isomer relative to the others is in agreement with its higher $B_{1/2}$, and correspondingly higher k_{isc}, but the magnitude of the difference cannot be explained on a first-order kinetic basis by only a 17% increase in $B_{1/2}$ for this isomer. In addition, if $B_{1/2}$ was the sole factor determining the saturated effect, results for the remaining isomers would be predicted as identical and not to differ by a factor of two, as found experimentally.

Turning aside from the phenomenological first-order rate treatment of hyperfine-induced ISC an explanation might be sought in the presence of a dominant high frequency component when considering the detailed spin evolution behaviour. The effect would be seen as a higher field modulation at short sampling times provided by a sufficiently reduced radical pair lifetime. Such a dominant coupling exists for the (1,3) and (1,2) isomers but this predicts a saturated-effect ordering of (1,2) and (1,4) isomers which is the reverse of that actually observed. Further investigation would require the calculation of the specific form of spin evolution for each of the possible radical pairs.

Alternative explanations might be sought in the effects of k_{12} and k_{21} on the pair lifetime and consequently spin motion sampling period. Activation energies for recombination and exciplex dissociation may well differ for each of the isomers as a result of differing charge distribution in the appropriate activated complexes. Indeed the variation in coupling constants through the series demonstrates differing spin electron density distributions in the radicals. Such considerations do, however, seem to be too remote from the available experimental data to be considered anything more than speculation.

4.4.3 DCB Concentration Dependence

As discussed in chapter 2, the value of $B_{1/2}$ is expected to be sensitive to degenerate electron hopping processes in which diamagnetic - paramagnetic exchange occurs between a radical pair member and a corresponding precursor molecule. Such processes have been found to increase $B_{1/2}$ and are of increasing importance at higher solute concentrations [2.3]. The effect may be considered one of lifetime broadening, the hopping process decreasing the lifetime of a radical in a particular nuclear configuration.

Experiments were performed over a DCB concentration range covering two orders of magnitude between .25 M and 5 x 10^{-3} M and, to within experimental error, no change in saturated field effect was observed. Similarly $B_{1/2}$ values were determined at DCB concentrations from 0.6 x 10^{-2} M to 6 x 10^{-2} M and again no effect observed.

The conclusion drawn is that processes of the type

$$\mathrm{DCB}^{\cdot -} + \mathrm{DCB} \longrightarrow \mathrm{DCB} + \mathrm{DCB}^{\cdot -}$$

are too slow to be significant within the concentration range investigated. Furthermore, as the quencher concentration would be expected to change the relative proportions of Py^* and exciplex fluorescence, the absence of any significant change in field effect may be taken as indicative of insignificant spectral overlap and also of the unimportance to the results of any possible bimolecular exciplex quenching process (see above).

4.4.4 Solvent Dependence

The role of the solvent was investigated with respect to the parameters of viscosity and dielectric constant. From the kinetic treatment already discussed, these system variables are predicted to have significant effects through their influence on $k_{esc}(\eta,\epsilon)$, $k_{12}(\epsilon)$ and $k_{21}(\epsilon)$.

Results were obtained in the ten binary solvent systems previously described and the values of $B_{½}$ and saturated field effect determined. They are listed in table 4.3.

From a comparison of the DMF and ACN systems it is evident that saturated field effects depend most strongly on solvent dielectric constant, esentially showing no difference for a factor of two change in viscosity. The inference is that k_{esc}, expected to show the greatest viscosity dependence, is not dominant in determining the field effect, though there is an anomaly at high η and low ϵ. The full bearing of this observation is best assessed by considering in detail the dependence of k_{esc} upon viscosity and dielectric constant. Considering k_{esc} to have activation contributions from viscous and electrostatic forces, we may write

$$k_{esc} \quad \alpha \quad \frac{T}{\eta} \exp(-E_c/RT) \; , \qquad (14)$$

Table 4.3

Solvent Effects on MARY Parameters

Effect on $B_{1/2}$*

Solvent System Cyclohexanol : X (v/v)	X = DMF		X = ACN		ϵ
	η (cP)	$B_{1/2}$ (G)	η (cP)	$B_{1/2}$ (G)	
3 : 1	7.0	26.0	3.4	26.9	21
5 : 3	3.1	25.5	1.2	25.5	24
1 : 1	2.2	26.3	0.9	31.2	26
3 : 5	1.8	25.1	0.7	31.3	29
1 : 3	1.1	24.0	0.5	30.2	32

Effect on Saturated Field Effect*

Solvent System Cyclohexanol : X (v/v)	X = DMF		X = ACN		ϵ
	η (cP)	FE_{sat}	η (cP)	FE_{sat}	
3 : 1	7.0	0.039	3.4	0.060	21
5 : 3	3.1	0.054	1.2	0.053	24
1 : 1	2.2	0.046	0.9	0.044	26
3 : 5	1.8	0.023	0.7	0.028	29
1 : 3	1.1	0.019	0.5	0.021	32

* Observed via exciplex fluorescence yield of 1,2 DCB - Py system.

At $\epsilon = 21$, E_c is expected to be less than 0.1 eV [9] and so, using this an upper limit, the expected change in k_{esc} as a function of ϵ may be estimated. Choosing two points at differing ϵ, for which there is minimal variation in η, it may be determined that the changes in k_{esc} due to ϵ will be less than the factor of two already demonstrated to be insignificant for the field effect.

Having established that the observed field-effect dependence upon solvent cannot be ascribed to k_{esc}, it becomes possible to eliminate any major contribution from a kinetic model assuming an initial singlet ion pair.

Turning to the initial exciplex limit of the model (7), at high ϵ, where $k_1 << k_{12}$, the observed solvent dependence is predicted to arise through k_{21}, describing the ion pair - exciplex recombination channel. Furthermore, if we assume that at $\epsilon \sim 30$ variation in k_{21} with ϵ comes about as a result of the depression in energy of the ion pair states relative to that of the exciplex, a clear prediction of the dependence is possible. Referring to the expression, due to Weller, for the appropriate energy difference, ΔG_{ie}, and discussed above (1), it is apparent that the ϵ dependence can be assigned to the terms representing exciplex solvation and inter-ion electrostatic forces. The former is close to saturation at $\epsilon \sim 30$ and so in this region

$$k_{21}(\epsilon) \quad \alpha \quad \exp(2.6/\epsilon RT)\exp(-E'/RT) \qquad (15)$$

where E' includes the non-ϵ dependent terms of the ion pair - exciplex activation energy. As the kinetic model predicts FE α $k_{21}(\epsilon)$, a plot of $\ln(FE_{sat})$ vs. $1/\epsilon$ will be linear in the high ϵ limit and have slope

2.6/RT (eV). Figure 4.12 shows such a plot, with slope confirming the above predictions and pointing to the validity of the initial exciplex model.

The observed fall-off in slope at low ϵ is expected, even within the bounds of this crude model, as the exciplex solvation term increases in importance in this region. Additionally, k_{12} is expected to assume greater significance, falling as ϵ decreases and eventually leading to a reversal in the dependence of field effect upon dielectric constant.

Both the ACN and DMF systems studied are in accord with this prediction if it is assumed there is a deviation from the ϵ values calculated on the basis of ideal behaviour of the binary solvent mixtures. The implication is that the ACN system shows specific solvation effects differing from those of DMF and maintaining ϵ at a higher level than expected from an extrapolation of the high ϵ data. The possibility of specific solvation effects in ACN systems has been recognized by other workers [6] in the context of pyrene - DMA systems, though the idea must remain somewhat speculative in the present case in view of the approximations involved in the first-order kinetic treatment, notably the assignment of a rate constant k_{isc}.

Table 4.3 also shows the dependence of $B_{1/2}$ on solvent properties. From the discussion above, the assumption $k_{isc} << k_{esc}$ is not valid and so the observed field-dependence is expected to show broadening compared to that predicted from the coupling constants. Other more fundamental reasons for enhanced $B_{1/2}$ values lie in their sensitivity to radical pair lifetime, increasing as the mean spin evolution sampling time is reduced. In the present case the sampling time is governed by the two

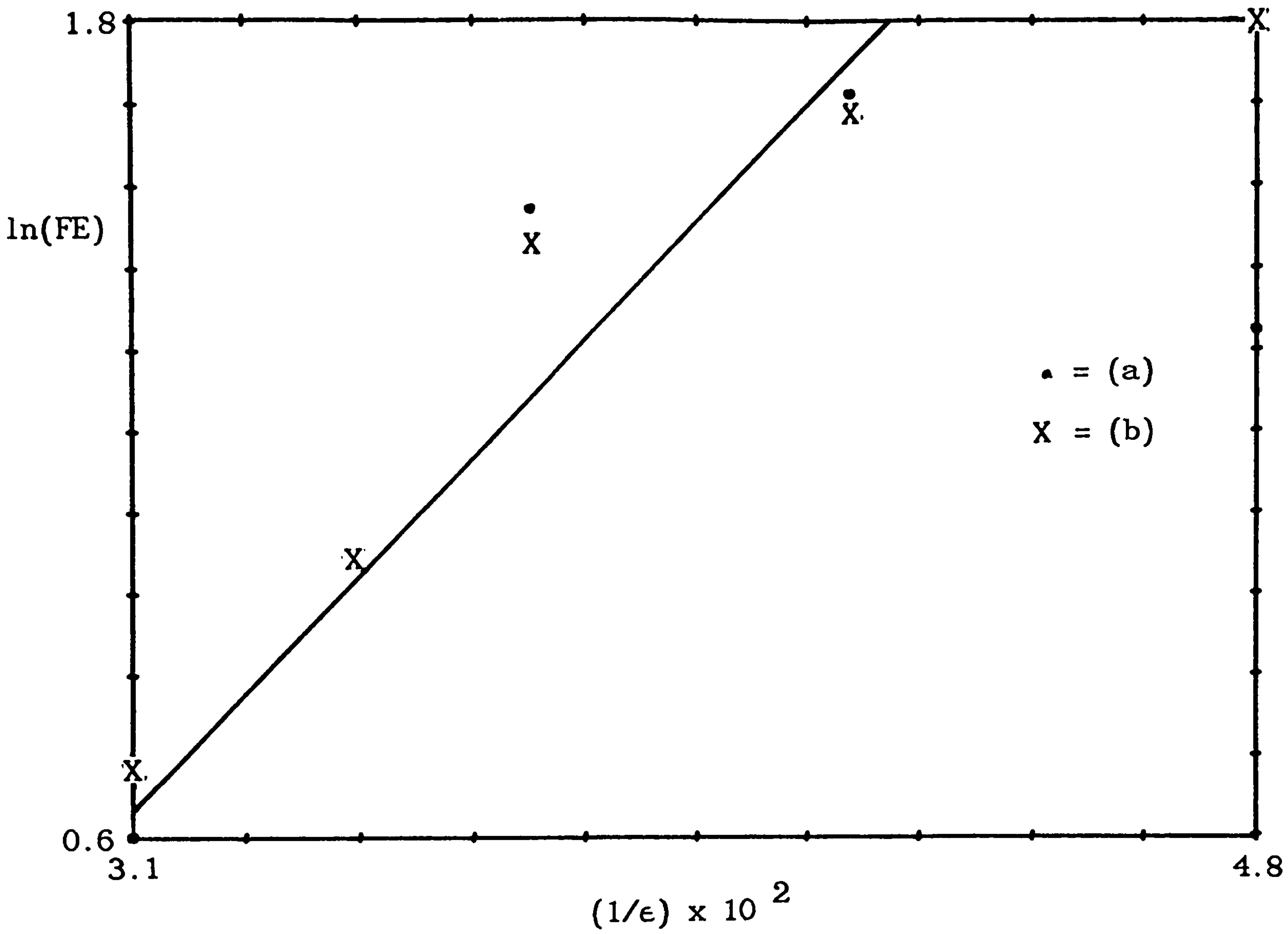

Figure 4.12. Dielectric dependence of the field effect on 550 nm emission yield for DMF (a) and ACN (b) solvent systems.

singlet loss pathways (showing opposing rate trends as a function of η and ϵ for the mixtures employed) of recombination and diffusional escape, whose rate constant has already been shown not to exceed k_{isc}. It would therefore seem as if the long time limit of spin evolution would be reached. An essentially constant $B_{½}$ in the DMF may then be considered to be indicative of such long lifetime behaviour, however a broadening in the MARY spectrum is clearly evident in the data obtained from the lower viscosity ACN system. The step nature of the transition to higher $B_{½}$ is somewhat indicative of a systematic error in the data but none was found, and reproducibility could be achieved. Theoretical support for such a change in $B_{½}$ may be found by noting that its occurence is at combinations of moderate dielectric constant and low viscosity not found in the DMF system; just the conditions which would favour high k_2 and k_{esc}, and so a shorter spin evolution sampling time.

4.4.5 Temperature Dependence

In an attempt to investigate the influence of k_{21} on the saturated field effect, and throw more light on activation parameters involved, a temperature dependence study was undertaken. Surprisingly no temperature effect was observed over a 289 K - 333 K range despite the use of a 3:1 DMF:cyclohexanol solvent mixture in which the activation energy for k_{21} is expected to be high, giving a corresponding strong temperature dependence. On the basis of $\Delta G_{ie} \sim 0.2$ eV an approximate twofold increase is predicted.

The results suggest a temperature effect opposing that on k_{21} is operative. Bearing in mind the previous discussion, a reduction in $(k_{isc}(0) - k_{isc}(B))$ seems the most likely candidate. This could be brought about by a reduction in the spin sampling time through a rise in k_{21} and k_{esc} but unfortunately data on $B_{½}$ as a function of temperature is not available to support or contradict this proposal.

4.5 RYDMR Studies

Having established the existence of observable static field effects in the 'self-indicating' Py/DCB system, attention turned to obtaining RYDMR spectra under the same range of experimental conditions. Averaging and control procedures were identical to those already described for MARY experiments except that a microwave pulse replaced that of the static field, the whole experiment being conducted in the appropriate apparatus described in chapter 3.

Spectral searches were undertaken in the field - frequency region around that of g = 2 expected to give resonances for carbon - centred radicals. No effects on exciplex were observed above a noise level of ~ 0.1%, for a range of microwave amplitudes.

A comparison of MARY and 'on resonance' B_1 RYDMR spectra described in chapter 2 leads to the conclusion that the magnitude of field effects should be comparable (assuming a narrow RYDMR spectrum). It is therefore not too surprising that at $B_1 \lesssim 13$ G effects are less than 0.1%, given MARY results of ~ 0.05% at the same field strengths.

At such low signal levels it was not considered that the Py/DCB system was a suitable candidate for the application of RYDMR techniques, although extensive averaging could depress the noise floor far below the 0.1% figure quoted.

4.6 Concluding Remarks

The participation of ion pair geminate recombination in exciplex fluorescence was clearly confirmed by magnetic field studies and the intermediacy of an exciplex indicated in electron transfer quenching reactions, even at high polarity. These conclusions were made possible by the ability of a magnetic field kinetic modulation experiments to isolate and focus attention on a particular part of a complex reaction system.

MARY spectra obtained were of the form expected, but hopes for employing the Py/DCB system as an example of an ideal class for the study of MARY/RYDMR phenomena were largely unfounded. Several factors contributed to this failure, the major ones being the presence of a large field-insensitive background fluorescent emission, arising from initial exciplex formation, and the involvement of kinetic processes other than radical pair ISC in determining the field effect. Additionally field modulation is observed by monitoring a process dependent upon the pair state (singlet) in which radicals are initially formed and so the field-insensitive signal component is enhanced.

CHAPTER 5

COMPARTMENTALIZED REACTION

A

B

C

5.1 Reaction Media

This section is intended to provide an overview of the media employed to achieve compartmentalized reaction and to indicate how microreactor environment may be characterized.

5.1.1 Surfactant Aggregates

Surface active molecules, possessing both solvophobic and solvophilic moieties, generally exhibit complex phase behaviour in certain polar and non-polar solvents. The former group comprises liquids with a tendency to form three dimensional H-bonded networks, water being by far the most commonly encountered example. For many surfactants, or amphiphiles, the surface activity, present at very low concentrations, gives way to a cooperative formation of aggregates within the solvent bulk at higher concentrations [1]. Such changes were first recognised by discontinuities, or at least marked deviation, in the behaviour of colligative properties as a function of concentration. Indeed the position of rapid change in slope came to be termed the critical micelle concentration (cmc) and indicates an almost temperature-independent region separating a lower concentration phase in which the solute exists essentially as monomeric units, from one which contains mainly surfactant aggregate units termed micelles. Values of cmc vary hugely between surfactant types but, in general, they all reveal micelle formation as a low concentration phenomenon. At higher surfactant fractions the tendency is to form structurally more complicated phases [1].

Crudely, the shapes and sizes of micelles result from a subtle balance of the solvqphobic tendency to increase aggregation to an extent that solvent and surfactant phases separate, and the solvophilic drive to maintain discrete monomer units. The exact nature of the interactions varies according to the specific type of surfactant involved.

The geometrical form of the micellar structures has been the subject of many investigations covering the physical techniques of coherent [2] and incoherent [3] light scattering, neutron [4] and low angle X-ray [5] diffraction, and chemical techniques [6] which rely on the influence of the micelle upon the properties of probe molecules situated within it. Results indicate that, close to the cmc, micelles are approximately spherical, though the structure is in dynamic equilibrium, exchanging monomer units with the bulk solution. The volume is approximately that expected from radial packing of a number of extended surfactant molecules equivalent to the mean aggregation value determined from experiment (see below). Often there is, however, a certain degree of polydispersity associated with the latter quantity [2].

At concentrations above the cmc, variations in aggregation number and shape show a marked dependence on particular surfactant. This renders further generalization fruitless and so we will now concentrate on the systems of direct relevance to the present work.

5.1.2 SDS - an Ionic Surfactant

Sodium Dodecyl Sulphate is perhaps the most thoroughly investigated of all micelle-forming surfactants. A member of the ionic amphiphile group, it gains its hydrophilic properties from a negatively charged sulphate head group, and its hydrophobic nature from a straight chain hydrocarbon tail. In aqueous systems the polar head groups are outermost in the micelles; a so-called normal micelle.

At the cmc of 8×10^{-3}M [7] aggregation numbers have been quoted in the range 30 - 60 [2,6] for pure water-SDS system, in the main probably indicative of the difficulties encountered in performing micellar investigations; slight contamination can significantly distort results; samples of SDS usually contain varying amounts of higher alcohols (dodecanol) [2] whose effects will be described below. The more recent measurements seem to settle for values at the lower end of the range and give a hydrodynamic spherical radius of 18 Å [2], but one must be aware of polydispersity.

For such ionic surfactants the values of the mean aggregation number $\bar{n}$, and the shape, are believed to be determined by a counterbalance of hydrophobic and electrostatic interactions. The former, for a nearly spherical micelle, favours growth, reducing the hydrocarbon-water contact area. The latter, however, resists growth as it is accompanied by a reduction in the available surface area per head group and so leads to an increase in electrostatic repulsion. Serving to reduce head group repulsion, of course, is solvation and the binding of counterions at the micelle-solvent interface forming a Stern layer. Manipulation of one, or both, of these factors would therefore be expected to affect significantly micelle size and/or shape. Merely increasing total surfactant concentration has been found to have little effect on micelle characteristics, except at concentrations approaching 1 M [7].

Several quantitative studies on the effect of solution ionic strength, with regard to micelle formation, have been conducted [2,8]. Added electrolyte, in the form of NaCl or $MgCl_2$, had several significant influences as a result of reducing head group repulsion. One was to increase the mean aggregation number, rendering it sensitive to total surfactant concentration. Above 0.4M it was found that the relationship $\bar{n} \propto [SDS]^{1/2}$ applied. The shape was deduced to be a prolate ellipsoid (rod-like), elongating dramatically at high electrolyte and surfactant concentrations. As an example, at 0.6M NaCl, 0.6 x 10^{-2}M SDS the semiminor axis was estimated at 25 Å, essentially unchanged on salt addition, whilst the semimajor axis had grown to 675 Å.

The second major change on salt addition arose from a depression in cmc and monomer solubility which, taken together, were responsible for a rise in the critical micellization temperature (cmt) at which point the monomer solubility is equal to the cmc. Below this point micellar systems become metastable and solid surfactant hydrate separates from the solution. Furthermore, added salt also rendered micelle form and $\bar{n}$ sensitive functions of temperature, all solutions tending towards near spherical shape and $\bar{n} \sim 60$ at higher temperature. The requirement for careful temperature control, when working with added electrolytes, is obvious.

Studies have also been performed on the addition of long chain alcohols to aqueous SDS systems [8]. Here the effects are not as clear cut for all surfactant concentrations.

Long chain alcohols are classed as surfactants in their own right, albeit rather poor examples, and distribute themselves between aqueous and micellar phases, becoming accomodated to large part in the palisade layer of the latter. Here they increase the degree of micellar ionization and enhance, not only intramicellar head group repulsion, but also that between individual micelles. At low surfactant or alcohol concentrations intermicellar effects are of lesser significance and the micelles tend to break up, forming smaller units. On approaching higher concentration, however, the tendency is to increase $\bar{n}$ in order that intermicellar repulsion is minimized.

From the point of view of shape, addition of alcohol cosurfactant seems to favour an oblate spheroid (disk-like) form. Rationalization of this behaviour has been attempted on the basis that the presence of long chain alcohols in the micelle has the effect of reducing the ratio of surface area per head group to the volume of the micelle; a factor considered to be of major importance in determining the shape [9].

With the existence of the above literature data covering the nature of SDS micellar systems, and providing the means to vary the micelle dimensions, they were the obvious starting point for any experiments intending to exploit surfactant aggregates as reaction media.

5.1.3 Microemulsion Media

The concept of a microreactor of variable dimensions may be approached more closely by extension of the ternary SDS-alcohol-water systems with the addition of one more, purely hydrocarbon, component which is taken up in the interior of the micelles. Typically about 10 vol. % (in terms of total system volume) of the added hydrocarbon (aromatic or aliphatic) can be accomodated, the presence of the alcohol cosurfactant being necessary to enable high uptake. Such quaternary systems are known as microemulsions, the example described above being an oil in water (o/w) type. Unlike macroemulsions, the systems are indefinitely stable to coagulation, a consideration which serves to distinguish the two.

The majority of characterization investigations have been directed towards water in oil (w/o) microemulsions inappropriate for the particular work to be described in this chapter. Information available on the SDS-alcohol-water based o/w systems comes from chemical probe studies [8] (see below) and not the less equivocal, non-invasive physical techniques. Results with 10 vol. % toluene as the oil component indicate spherical aggregates with typical radii of 45 Å and a central oil core of some 30 Å containing in the region of 700 toluene molecules (n_{SDS} ~ 200). By lowering the oil volume fraction it seems possible to produce a concomitant gradation in oil core radii.

From the microreactor standpoint, microemulsions would appear to offer advantages over pure micellar systems in that the central hydrocarbon core is easily varied in volume whilst maintaining a spherical form, and provides a non-polar reaction medium of greater uniformity.

5.1.4 Other Surfactant Systems

There are several reasons why systems other than those based upon SDS (or closely related surfactants) would be desirable for use as stable reaction media. For reactions involving ions, the charged surface of ionic micelles represents a major influence which may not always be required, and for all reactant species a greater volume range would be an advantage. In addition a polar, non-aqueous support solvent would aid some studies (see below). The problem to be faced, however, is the lack of detailed literature information om many systems under the conditions of interest.

Non-ionic surfactants such as the polyoxyethylenes would certainly seem to satisfy the first requirements at least, but in practice their phase behaviour appears more complex. Their cmc values are typically 2 orders of magnitude lower than the ionics and aggregation is not only heavily dependent on surfactant concentration, but severeley perturbed by solubilized material [10].

One interesting possibility for tackling the reactor size problem comes from the behaviour of the so-called polysoaps and the wider field of polyelectrolytes. Polysoaps may be exemplified by partially N-alkylated poly-4-vinylpyridine. Above about 10 mole percent dodecylation viscosity and light scattering experiments provide evidence for intramolecular micelle formation and their solubilization of hydrocarbons [11]. The analogy with tertiary structure of biological systems is clear.

The formation of normal (polar groups on the exterior) micelles in polar non-aqueous systems is possible [12], but little studied. The evidence suggests that solvophobic interaction is weaker and requires a solvent capable of forming three dimensional H-bonded networks, similar to the case with water. Such observations point towards the 'structure-breaking' entropic origin of the solvophobic interaction and also indicate little possibility of departing from protic solvents.

5.1.5 Solubilization

The important property of micellar aggregates, with respect to their ability to act as microreactors, is the solubilization of a wide range of hydrophobic molecules. The actual site of solute location can, in principle, vary widely in microviscosity and polarity from the inner core to the outer solvent interface. Attempts have been made to determine solute local environment by means of its effect upon certain probe molecules [6,8,13], though the dynamic nature of the problem should not be overlooked.

Probe studies have centred around luminescence studies on pyrene, or its derivatives, and have thrown light on aggregate size, shape, polarity, viscosity and dynamics of micelle-type systems. They may be categorized as stationary or time-resolved studies.

Steady-state observation of the intensity ratio of certain peaks (I_1/I_3) in pyrene fluorescence spectra have revealed it to be a sensitive measure of local environment polarity. When applied to micelles a certain insight may be gained into the pyrene solubilization site [12] but the validity of extrapolation to other molecules is not clear. Other probes can be criticized on the same grounds.

Time dependent studies of the intramolecular excimer formation rate in dipyrenylpropane have been employed to indicate microviscosity [8], but once again implications for other molecules are uncertain. Less equivocal are determinations of mean aggregation numbers from observation of pyrene intermolecular excimer formation kinetics [6]. This technique will be described in more detail below, together with its application to microemulsion systems.

The distribution of solute molecules over individual aggregates in a micellar-type medium may be most simply described statistically by a Poisson-Boltzmann function where the probability p_n of finding n solute molecules in a given 'compartment' can be written

$$p_n = \frac{m^n e^{-m}}{n!} , \qquad (1)$$

where m is a mean occupation number expressed as number of solute molecules per micelle. The calculation of m requires knowledge of micelle concentration and this can be obtained from

$$[\text{micelle}] = \frac{[\text{surfactant}] - \text{cmc}}{\bar{n}} , \qquad (2)$$

assuming a constant equilibrium monomer concentration above the cmc.

As a result of the spread in occupation probabilities, the fluorescence decay kinetics of a probe molecule will show contributions from micelles containing more than one solute molecule. If a pyrene probe is employed the result will reflect quenching behaviour arising from intermolecular excimer formation between molecules within a single micelle. The situation has been analyzed, using a Poisson-Boltzmann distribution, to predict the following time dependence of fluorescence at monomer emmision wavelengths [6] :

$$I = I_0 \exp\{-k_0 t + m[\exp(-k_e t) - 1]\} , \qquad (3)$$

where k_e and k_0 are respectively the effective first-order intermolecular excimer formation and the free monomer fluorescence decay rate constants. Under conditions of low occupation number, m, the decay reduces to that observed in the absence of excimer formation.

Fitting of the above expression (3) to pyrene probe fluorescence decays can thus reveal the aggregate concentration via m, the probe concentration being known. In addition, the concentration of micellized surfactant can be determined, as above, with knowledge of the cmc amd so a mean aggregation number can be estimated:

$$\bar{n} = \left[\frac{[\text{surfactant}] - \text{cmc}}{[\text{py}]} \right] m \, . \qquad (4)$$

This technique has previously been applied to microemulsions with a toluene oil core and a 1-pentanol cosurfactant, as descrbed above [8], and was used by the author as a convenient microreactor characterization technique for systems not detailed in the literature.

5.1.6 A Probe Study of SDS/1-pentanol Microemulsions

Table 5.1 lists results obtained by fitting the analytic expression for fluorescence decay, in the presence of excimer formation (3), to experimental data obtained from a series of SDS/1-pentanol microemulsions. Oil components were toluene and benzene, the former being used to provide a comparison with existing literature data (in parentheses) [6]. Additionally a typical experimental decay, after coherent background subtraction is also shown.

Table 5.1

Microemulsion Characteristics

Oil Component	Volume Fraction (%)	Fit Parameters			$\bar{n}$	r_m [a] x10nm	r_o [b] x10nm	η (cP)
		$10^{-6}\ k_0\ s^{-1}$	$10^{-7}k_e\ s^{-1}$	m				
Toluene	2	2.6 (2.49)	4.1 (4.57)	0.31	62 (86)	26 (27)	14 (16)	7.5
	6	2.4 (2.47)	4.5 (3.38)	0.57	114 (242)	35 (43)	25 (32)	4.0
Benzene	2	2.7	3.0	0.32	64	26	14	-
	4	2.6	4.5	0.38	76	76	29	-
	6	2.6	4.7	0.59	118	118	35	-

Values in parentheses are from ref. [6].

a Calculated using equation (5).

b Calculated using equation (6).

c Measured with dipyrenylpropane probe [6].

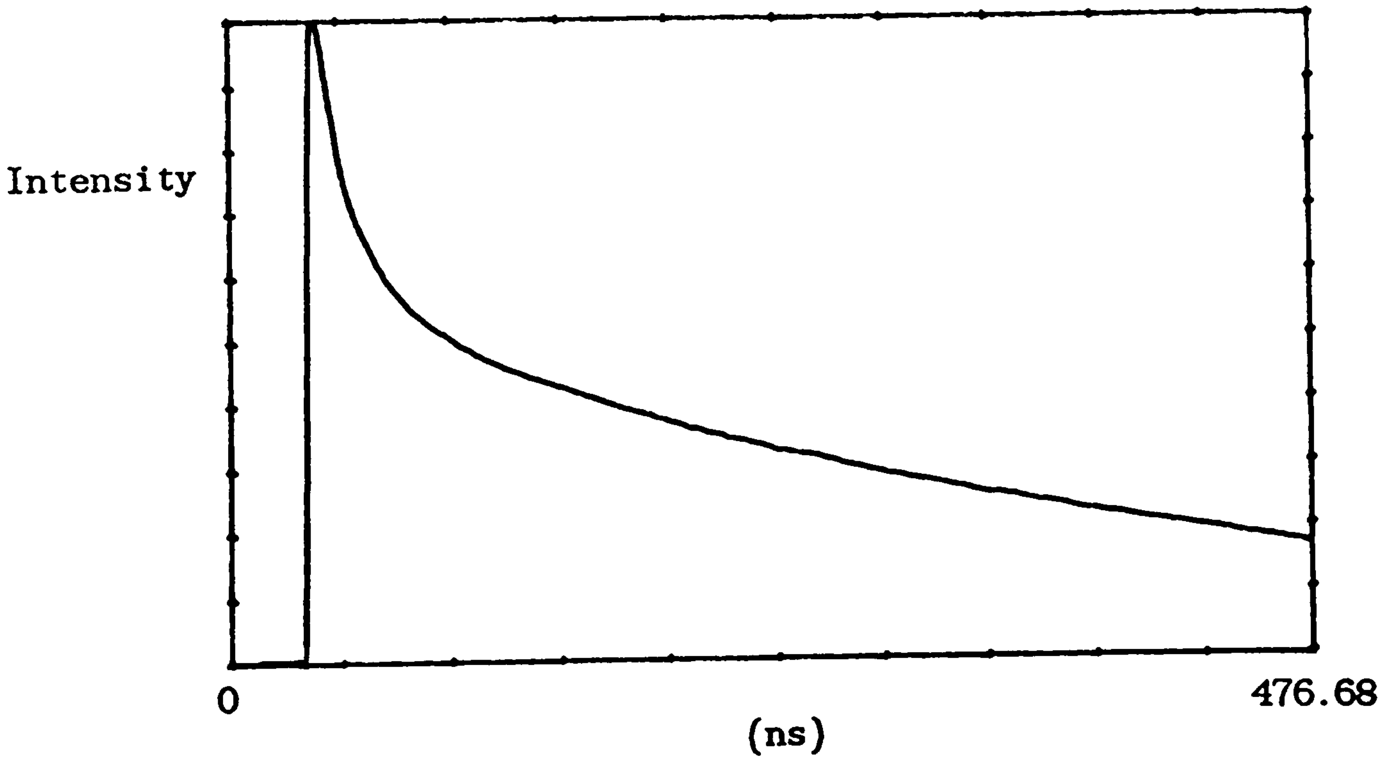

All measurements were made on carefully de-aerated (Ar saturation) static samples under N_2 (337 nm) laser excitation. Timescales were such that no significant error was introduced by finite excitation time or by recording equipment bandwidth limitations. In practice purity of sample and satisfactory removal of dissolved oxygen was taken to be indicated by a pyrene unquenched monomer lifetime ($1/k_0$) close to 400 ns and invariant with respect to further Ar saturation.

Results indicate almost identical behaviour for the toluene and benzene microemulsions. A divergence from the results of reference [6] is apparent at high oil volume fraction suggesting a systematic difference in the determination of this quantity. This is not supported, howevever, by further measurements which indicated agreement on the solubility limit for the oil component.

Having calculated the mean aggregation number, $\bar{n}$, it becomes possible to estimate aggregate dimensions. Assuming a spherical form [6], the aggregate radius may be calculated from

$$r_m = 0.74\{(\bar{n}/[\mathrm{SDS}])(246[\mathrm{SDS}] + 106[\mathrm{pentanol}] + 10^3\varphi)\}^{1/3}(\text{Å}), \quad (5)$$

where the partial molar volumes of micellized SDS and pentanol are respectively 246 cm^3/mol^{-1} and 106 cm^3/mol^{-1}. φ represents volume fraction of the oil component, implicitly assumed to be taken up entirely by the aggregates. If it is further assumed that the core is composed purely of oil, volume arguments can again be applied to furnish its radius,

$$r_o = 7.4(\bar{n}\varphi/[\mathrm{SDS}])^{1/3} (\text{Å}). \quad (6)$$

The appropriate calculations have been performed and the radii are listed in table 5.1, as are microviscosity results for the toluene system from reference [6].

An estimate of the radial length of the surfactant shell is given by $(r_m - r_o)$. Its value decreases from 12 Å at 2 vol. % oil to 10 Å at 6 vol. % and, in both cases, is considerably shorter than the 21 Å of an extended SDS molecule. Several explanations for these observations may be proposed. It cannot be assumed that SDS chains will be radially oriented or fully elongated and the notion of no inter-penetration of the component layers seems to be unreasonable. Indeed, the trend on increasing the oil fraction suggests greater overlap of the oil core and surfactant shell.

At this point a comment on the trend observed in k_e seems appropriate. It is clear that the rate of intermolecular excimer formation within the aggregate rises with volume. Solution of a spherically symmetric diffusion equation subject to an absorbing boundary (sink) at a reaction radius, a, and a reflecting boundary at a distance r_m, reveals that pseudo first-order kinetics are to be expected for a freely moving pair of species undergoing diffusion-controlled reaction [27]. The effective rate constant may be approximated by

$$k^m_{eff} \approx \frac{3Da}{r_m^3} , \qquad (7)$$

where D is the relative diffusion coefficient and $r_0 > a$. If D is related to viscosity by the Stokes-Einstein equation we have

$$k^{m}_{eff} \approx \frac{2kT}{\pi\eta r^{3}_{m}} \quad . \tag{8}$$

It is interesting to note that the equivalent result may be obtained by assuming bulk diffusion-limited kinetics at a concentration of one molecule per compartment volume.

The prediction for the (spin independent) rate of intermolecular excimer formation is an inverse variation with reactor volume (α r^{-3}) and microviscosity. Absolute k_e values are in agreement, within a factor of two, with the data of table 5.1 (where η values are available), but relative values do not show the expected trends. The latter point is probably indicative of the failure of the crude homogeneous spherical compartment model. In view of the paucity of data, further analysis appears fruitless, though the goal of characterizing the microemulsion media with respect to volume and viscosity have been achieved.

Further aspects of micellar kinetics will be discussed in a later section with regard to specific experimental systems utilized in MARY and RYDMR experiments.

5.1.7 Summary - Reaction Media

In summary, two reasonably well characterized categories of surfactant aggregate systems have been established for use as microreactor media. Additionally, techniques for routine assessment of the media have been described and demonstrated, enabling the utilization of system variants not described in the literature and providing a standardization test, at the molecular level, for repeated preparation of the many-component mixtures.

One major limitation is evident, however, in that the available microreactor volume range falls very short of that which would be desired. Especially welcome would be the capability to increase volume to a point at which approximation to bulk, homogeneous kinetics was apparent. Clearly further systems, probably microemulsion types, need to be evaluated.

5.2 Reactants

It now remains for the particular reactants to be described. In the present work certain qualities are required of the chemical species and these will be made clear in the following sections.

5.3.1 Radical Pair Probes

Having established the means to modify geminate radical pair behaviour, it now remains to provide techniques for convenient, quantitative monitoring of the effects in a time-resolved manner. In this particular work attention will be focussed on fluorescence-probe species offering very high S/N in detection (see chapter 3) and participating as members of primary radical pairs. In this way many ambiguities as to the relationship of the property measured to that desired, may be removed. A certain similarity to aromatic scintillator probes, utilized in pulse radiolysis work, is noted [24].

In recent years several doublet species have been reported to exhibit fluorescence emission in room temperature liquid solution [14-18]. Many of them have very low fluorescence efficiencies, often as a result of chemical quenching, and so intense excitation is needed. Despite this, radical fluorescence was seen as of major significance in the search for MARY/RYDMR detection possibilities and consequently several of the reported examples were investigated for this purpose, as discussed under the appropriate headings.

5.2.2 The Diphenylketyl Radical

The photochemistry of benzophenone (BP) is essentially that of its $^3(n\pi^*)$ lowest triplet state formed by very rapid intersystem crossing and internal conversion from its initially populated $^1(n\pi^*)$ singlet state [19]. Frequently the carbonyl $^3(n\pi^*)$ state is considered to have biradical character with electrophilic oxygen, its behaviour found to be analogous to that of alkoxy radicals [20]. Often reaction, with a wide range of substrates, leads to the formation of radical pairs containing diphenylketyl via a nominal H-atom abstraction. Whether the mechanism is direct abstraction, or initial electron transfer followed by further reaction to give the ketyl species, seems to be substrate-dependent [21]. Magnetic data for several species relevant to subsequent discussion is given in table 5.2.

The uv/visible absorption spectrum of the ketyl in cyclohexane has been obtained from flash photolytic studies and closely resembles that of the precursor triplet state. It exhibits extinction maxima at 355 nm ($D_0 \rightarrow D_2$) and 532 nm ($D_0 \rightarrow D_1$), the former being the strongest ($\epsilon_{355} \sim 2.7 \times 10^4\ M^{-1}cm^{-1}$, $\epsilon_{532} \sim 5.5 \times 10^3\ M^{-1}cm^{-1}$) [22]. Excitation at either of

Table 5.2

Magnetic Data [4.12]

Radical		Coupling Constants) ($\frac{a}{g\beta}$ Gauss)	
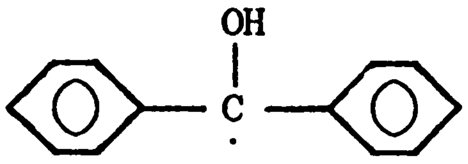 Diphenylketyl	g = 2.003	4 H (o)	3.21
		4 H (m)	1.23
		2 H (p)	3.64
		H (OH)	2.91
 Cyclohexadienyl	g = 2.0023 (assumed)	2 H(1,CH_2)	47.85
		2 H(2,6)	9.04
		2 H(3,5)	2.77
		H(4)	13.25
 Phenyl	g = 2.0024	2 H(2,6)	17.4
		2 H(3,5)	6.5
		H(4)	1.9
$-CH_2-\dot{C}H-CH_2-$ Secondary Alkyl	g = 2.0026	H(α)	21.0
		4 H(β)	25.0
$CH_3-\dot{C}H-CH_2-$ Secondary Alkyl	g = 2.0026	H(α)	21.9
		3 H(β)	24.6
		2 H(β)	27.2
$\dot{C}H_2-CH_2-$ Primary Alkyl	g = 2.0026	2 H(α)	20.8
		2 H(β)	25.8

these transitions results in a mirror-image fluorescence spectrum peaked at 580 nm with a very short solvent dependent lifetime of the order of a few nanoseconds [22]. Figure 5.1 shows an emission spectrum obtained from a benzophenone in methanol system at room temperature. Excitation was achieved in a two colour pulsed experiment, employing 308 nm radiation to initiate ketyl formation and 337 nm radiation to excite the observed fluorescence spectrum at a delay of ~ 100 ns. Low intensity structured emission at shorter wavelengths can be assigned to ^3BP phosphorescence. Discrimination between the two types of system luminescence is clear, both in terms of wavelength and intensity.

Monitoring of the emission elicited by a single 337 nm excitation pulse was also found to give a ketyl component in solvents capable of rapid triplet → ketyl quenching. Generation of significant concentrations of the radical within the 10 ns of the laser pulse enables the absorption of a second photon to give a ketyl emission signal which has a quadratic intensity dependence on the laser intensity. As a result, when performing two step experiments, intensities of the second probe excitation were reduced to a level such that two photon processes did not contribute to the signal. With this precaution, probe fluorescence provided an accurate measure of ketyl concentration resulting from the primary synthesis pulse.

As already indicated, the major limitation on using induced radical fluorescence as a concentration probe comes in the form of low quantum yields. The fluorescence radiative lifetime of diphenylketyl D_1 has been estimated to be 110 ns from the measured absorption and emission spectra, giving quantum efficiencies of less than 5% in toluene [14]. At first sight explanation of such a low figure might be sought in the

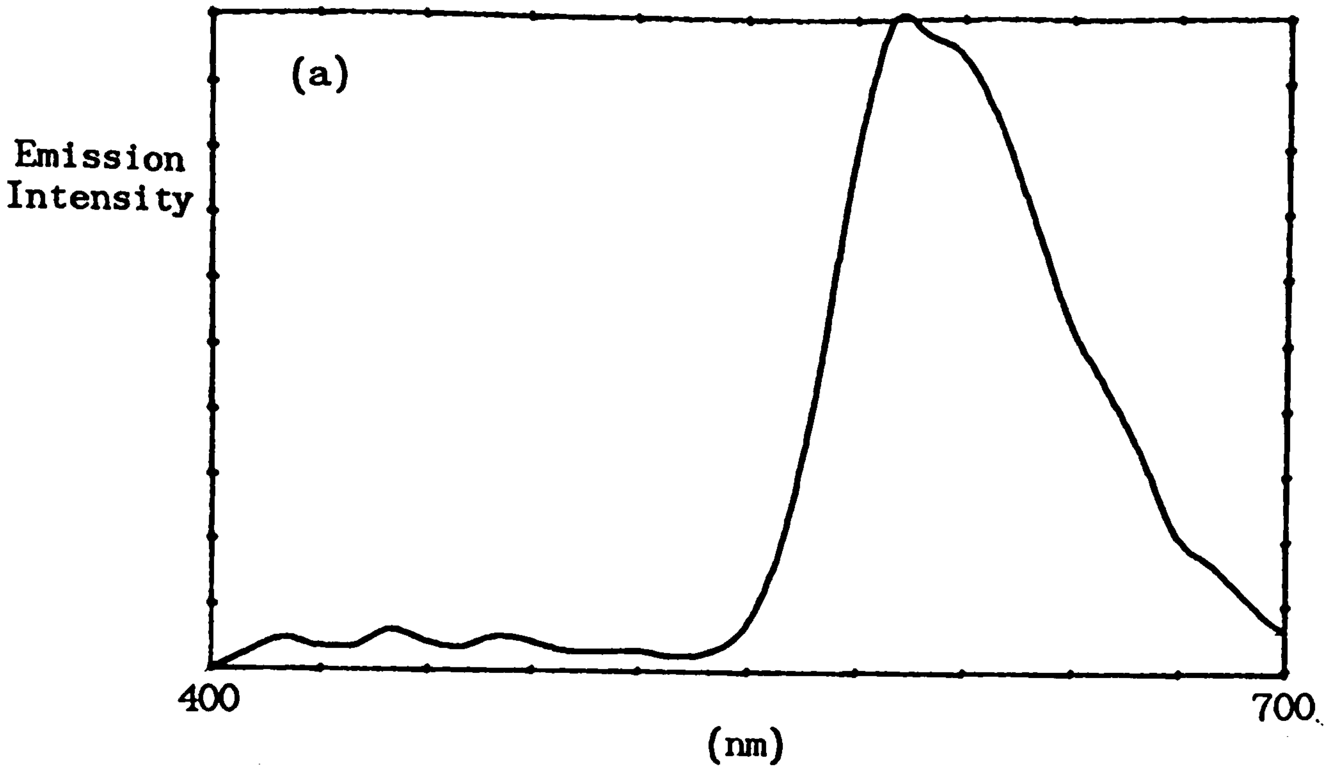

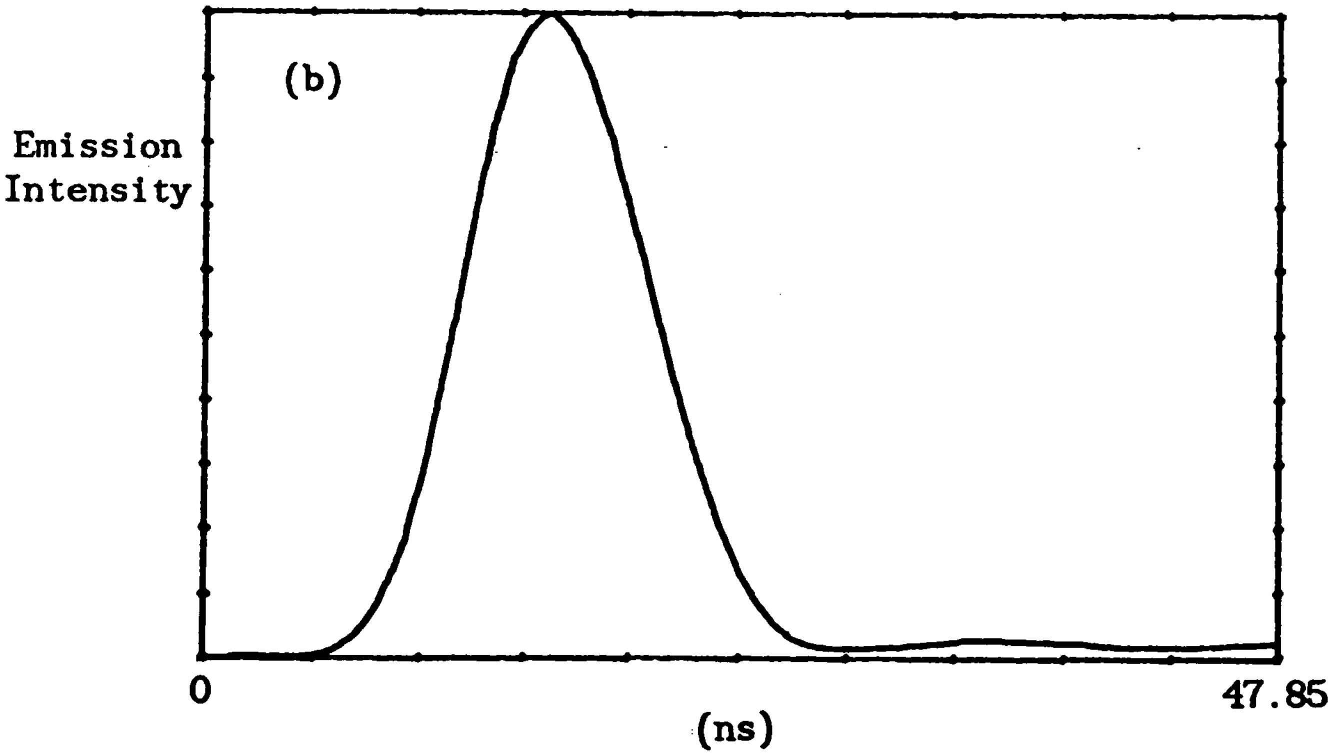

Figure 5.1. Laser induced emission from diphenylketyl generated in micellar aqueous SDS solution.

(a) Wavelength dependence of emission elicited by excitation at 337 nm (L2) following 308 nm photolysis (L1). The prominent feature is due to emission from D_1 of diphenylketyl.

(b) Temporal dependence of emission at 600 nm. Emission essentially follows the excitation-laser pulse profile.

existence of very efficient molecular ISC, especially in view of the behaviour known for the parent benzophenone molecule. There is, however, no evidence of a quartet state lying at energies lower than D_1, negating the ISC explanation [22]. Moreover, investigation has shown that lifetimes in toluene are affected by deuterium substitution at the ketyl hydroxylic position. The existence of such an isotope effect suggests that H atom transfer from this position plays an important role in the deactivation of D_1, though there is evidence for other decay pathways, including a very efficient process which is active in the presence of water [23]. The latter point is of particular significance for the reactions in aqueous surfactant media to be described in later sections.

On a more positive note, a beneficial aspect of very short ketyl fluorescence lifetimes is that time resolution, associated with concentration measurement, continues to be determined by probe laser width (6 ns FWHM); a point used to advantage in experiments to be described. It would, however, be preferable for fluorescence lifetime to be determined by high radiative rates, rather than competing non-radiative loss processes.

5.3.3 Other Radical Probes

The reactivity of the benzophenone triplet state provided much scope for MARY/RYDMR applications but nonetheless a series of other radicals were investigated for their usefulness as radical pair probes. Unfortunately, in comparison to diphenylketyl, they were found lacking in the blend of qualities required for their utilization and so all results to be presented centre on BP.

Two species had potential advantages over diphenylketyl and are worthy of note, The tri-t-butylphenoxyl radical has been reported, from stationary methods, to fluoresce at a peak of 430 nm and absorb strongly at 337 nm [18]. It may be derived from H-atom transfer from the parent phenol to many substrates [25] and so would provide complementary behaviour to that of the BP ketyl. Unfortunately, attempts at its photolytic generation by its quenching action on BP and acetophenone triplets did not show any 430 nm fluorescence with intensity dependent on the primary synthesis radiation. This may have been due to obscuring effects of luminescence arising from the precursor molecules or from the sample cell; the latter was found to be a particular problem in the short wavelength region.

On a slightly different note, the p-aminothiyl radical, generated by photolytic S-S bond cleavage of 4-aminophenyldisulphide, shows strong emission at a highly solvent dependent wavelength in the region of 650 nm upon excitation at 337 nm. Indeed this species has provided the first example of a doublet lasing medium [16]. Two step synthesis/probe experiments revealed the characteristic red fluorescence in toluene, THF and acetonitrile solvents. The presence of water (a few % in THF and ACN), however, was found to completely quench the emission. In this respect there is a similarity to diphenylketyl. Attempts at observing the doublet emission in toluene microemulsion media (described above) also failed, possibly providing an indicator to a significant degree of water penetration within the emulsion droplet. The application of RYDMR, to a sulphur species expected to have a high transverse relaxation rate, rendering it unobservable by conventional esr, may well have proved interesting but the failure only serves to emphasize the subtle balance of properties necessary for the intended magnetic resonance work.

5.3 Apparatus Modes

As already indicated, the crux of the experimental procedure was a two colour combination of synthesis and probe laser pulses. When included together with the appropriate magnetic field pulse, we see there is scope for a range of non-conventional experiments. These will be detailed here to provide the necessary background for interpretation of the range of results on compartmentalized systems presented in the forthcoming sections.

The various modes may be differentiated by the status and relative timing of the excitation and field pulses on each averaging cycle, be it single shot or pairwise. The situation is most easily described with reference to the following schematic:

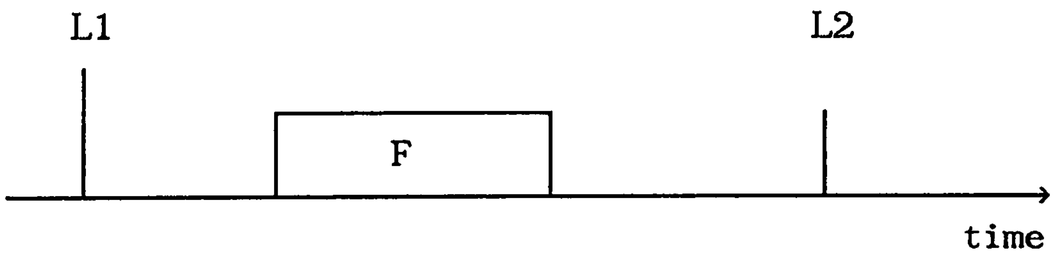

,

where L1, L2 represent laser excitation and F, the magnetic field (r.f. or static). L1 always remains fixed in time and provides a temporal reference point. Variation in time of a given signal will be indicated thus,

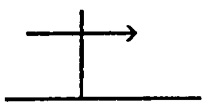

.

The width of field pulse will be given above F in the figure schematics.

5.3.1 Elucidation of Radical Pair Time Dependence

Radical pair temporal behaviour may be determined in two complementary experiments, both of which provide access to the hitherto uninvestigated technique of microwave kinetic spectroscopy.

By recording L2 induced fluorescence as a function of delay with respect to L1, the radical probe transient behaviour is established, subject to the condition of a short L2 pulse. This may be performed with optional static or r.f magnetic fields covering all or part of the L1-L2 delay range. Simple kinetic analysis can provide insight as to the transient behaviour expected from microreactor sytems.

Reactions to be considered are those of a triplet initial radical pair. At zero or high field internal conversion and intersystem crossing within the pair (zeroth-order S, T_0, $T_\pm$ model) may be considered fast (10^{-8}s) compared with diffusion-limited processes within the microreactor (10^{-6} - 10^{-7}s) and so the reaction rate constant may be approximated by (chapter 2),

$$k_{rec}(B_0, B_1) = \bar{p}_S \, k^m_{eff} \ , \qquad (9)$$

where k^m_{eff} has been defined above (8). The triplet state is not expected to lead to reaction products for neutral species.

Relaxing the notion of completely compartmentalized reaction, we introduce a field-independent process which removes the possibility of radical pair reaction (on the timescale of interest) but does not destroy the pair members. This is assigned a rate constant k_{esc}

indicating that it derives from a microreactor escape type process. The scheme we have is,

$$E \xleftarrow{k_{esc}} {}^{3}RP \xrightarrow{k_{rec}} {}^{1}P \;,$$

where E, RP and ${}^{1}P$ represent respectively escape radicals, geminate radical pairs and singlet products. Hence

$$[RP](t) = [RP](0)\,\exp\{-(k_{rec} + k_{esc})t\}\;, \qquad (10)$$

$$[E](t) = [RP](0)\,\frac{k_{esc}}{k_{rec} + k_{esc}}\,[1 - \exp\{-(k_{rec} + k_{esc})t\}]. \qquad (11)$$

L2 induces essentially indistiguishable fluorescence from both classes of radical probe and so the observed signal $S(t) = [RP](t) + [E](t)$ is given by

$$S(t) = [RP](0)\,\frac{k_{esc}}{k_{rec} + k_{esc}}\left[\,1 + \frac{k_{rec}}{k_{esc}}\exp\{-(k_{rec} + k_{esc})t\}\,\right]. \qquad (12)$$

At intermediate field, $S,T_0-T_\pm$ interconversion will become comparable to $(k_{rec} + k_{esc})$ leading to an essentially biexponential S(t) with fast $S-T_0$ and slow $S,T_0-T_\pm$ components, at least within the approximation of a first order ISC treatment. Kinetically the situation resembles the treatment proposed to account for the effects of relaxation as a 'slow' spin flip mechanism [28].

In the present case, the data to be presented is not of sufficient quality to sustain a biexponential analysis and, in view of the approximations inherent in the model, attention will be restricted to that of a single exponential (12). Clearly curve fitting can yield k_{esc} and k_{rec}, irrespective of global scaling.

The second experimental possibility has the L1-L2 delay at a value of $\geq 5 \times (k_{esc} + k_{rec})^{-1}$ such that geminate kinetics are essentially complete. Field-induced changes in L2 fluorescence are then observed, at a fixed static field, as a function of L1-F delay, where F represents a resonant microwave pulse of width τ. Analysis of the effects upon S(t) then reveal the observed signal will be described by

$$\begin{aligned} FE(T) &= \frac{S(B_1, \infty)}{S(0, \infty)} \\ &= \frac{k_{rec}(B_0, 0 - k_{rec}(B_0, B_1)}{k_{eff}(B_0, B_1)} \times \qquad (13) \\ & [RP](0)\,[1 - \exp\{-k_{eff}(B_0, B_1)\tau\}]\,\exp\{-k_{eff}(B_0)T\} , \end{aligned}$$

where F is applied at time T and $k_{eff}(B_0, B_1) = k_{rec}(B_0, B_1) + k_{esc}$. B_1 has been assumed to be of sufficient amplitude to establish a quasi-equilibrium spin state within the radical pair system (i.e. the fast ISC approximation is still valid).

For a fixed τ we see that the signal corresponds to the decay of the radical pair under B_1-free conditions, whilst if τ is varied at fixed T the decay rate constant with $B_1 \neq 0$ may be obtained. It is to be noted that signal magnitude is determined respectively by τ and T for the above two procedures.

A key point is that time resolution is no longer determined by the monitoring procedure but by the precision achieved in the setting of F, upon its risetime and the speed of response of the quantum system. Additionally, the monitoring of a quantity linearly related to the escape radical concentration will also reveal the effective radical pair decay rate constant.

5.3.2 Optical Spectrum Acquisition

Emission yield spectra obtained with L2 alone, or a combination of L1 and L2, comprise the simplest time-resolved spectral mode of operation. Difference spectra can be utilized to characterize and discriminate fluorescence from radical pair species and photoproducts.

5.3.3 Magnetic Resonance Spectrum Acquisition

This, the second time resolved submode, is the most important. Signal averaging is always conducted in a pairwise manner to maximize S/N.

MARY spectra are obtained when F represents a static magnetic field pulse which covers the entire geminate timescale, as dictated by the slow response time of the Helmholtz coil arrangement. Any time resolution requirement must be met by the relative delay L2-L1. Variation in detection wavelength can aid fluorescence spectral assignment (c.f. chapter 4).

RYDMR spectra can be obtained when F represents a microwave pulse and the experiment is conducted in a static field. All variants described in chapter 2 are possible and, in contrast to the MARY experiment, with time resolution capability down to a limit of ~ 50 ns set by the minimum microwave pulsewidth. Again a detection wavelength-resolved mode is possible.

Some RYDMR B_0 spectra presented in forthcoming sections were obtained in conjunction with a background correction procedure which entailed the specification of an initial static field reference point. Periodic evaluation of the spectral value at this position throughout a B_0 scan then permitted assessment and subtraction of a possibly varying background fluorescence signal. In several cases this was found necessary in order to generate symmetrical spectra.

5.4 Experimental Data

Experimental data will be categorized by the type of microreactor medium utilized and presented with reference to the apparatus modes (above). Interpretation and discussion will then follow.

A

5.4.A.1 Pure Micellar Systems

Experiments were performed with 0.1 M aqueous SDS providing a micellar aggregate concentration of ~ 2.5×10^{-3} M. Solubilization of 10^{-2} M benzophenone then leads to a mean occupation number of 4. If an absorption of 20% - 30% of laser excitation is assumed, it becomes apparent that ^{3}BP mean occupancy was approximatel y one molecule per micelle. Such a figure is rather higher than would have been desired for it indicates a significant degree of multi-occupancy. Lower concentrations of precursor benzophenone were, however, found to be accompanied by unacceptable degradation in final S/N.

Ketyl Time Dependence

In the absence of added H-donors, ^{3}BP abstracts a hydrogen atom from micellar surfactant, generating a linear-chain alkyl radical. A secondary species is assumed to be the major product.

Figure 5.2 shows the time evolution of induced ketyl fluorescence following 308nm synthesis excitation and in the presence of a 3420 G magnetic field. The ketyl signal risetime is in accord with a triplet decay rate constant of 3×10^6 s^{-1} quoted from optical absorption studies [29]. Although the ketyl decay is convoluted with a slow formation function, its lifetime may be judged to be in the region of 1 μs. Measurement of yield at times over 2 μs would therefore be expected to show steady-state behaviour from escape radicals, provided encroachment upon millisecond-timescale second-order events is avoided.

MARY Spectra

Figure 5.3 displays low field MARY spectra as revealed by sampling ketyl fluorescence yield at 2.5 μs after synthesis. The approximately 200 G scan of figure 5.3a was expanded in the 0-30 G region and forms figure 5.3b.

Although static magnetic field effects on the BP/SDS system have been observed many times [30], efforts were focussed on the coarse behaviour up to several kilogauss and so the data presented here represent the first such observations.

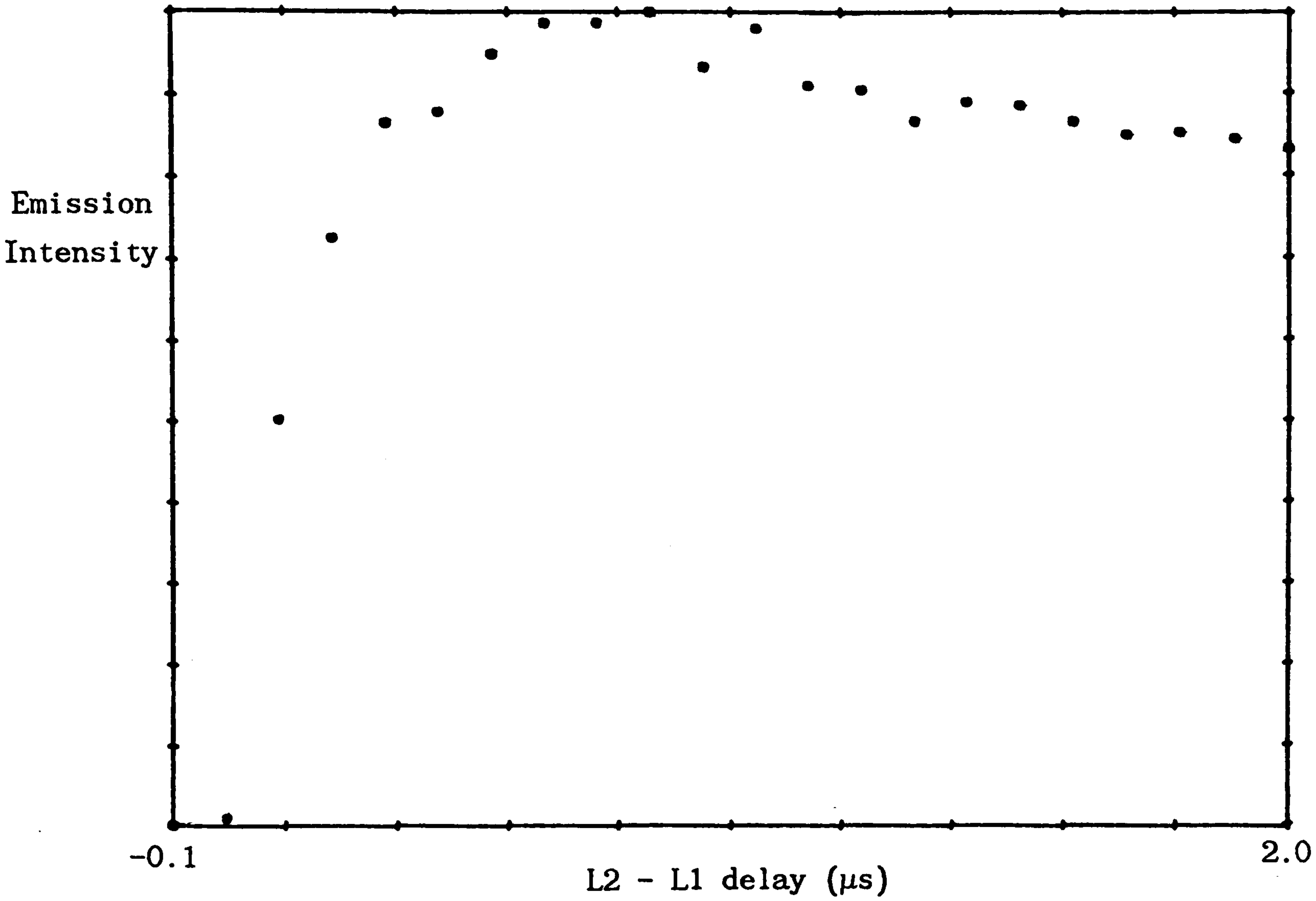

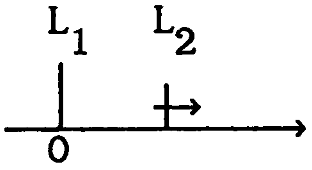

Figure 5.2. Temporal dependence of diphenylketyl in micellar aqueous SDS, measured by varying L2 - L1 delay.

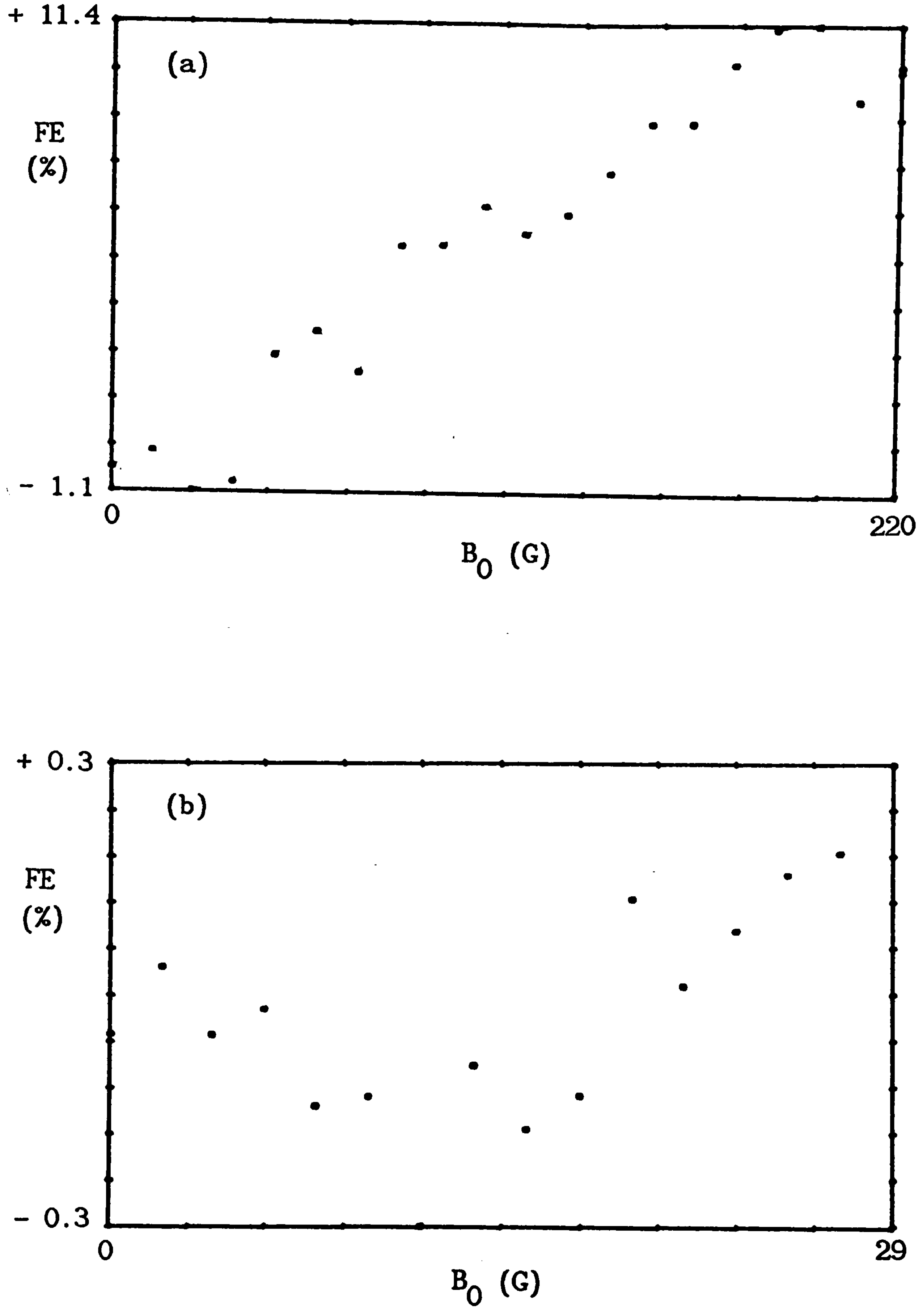

Figure 5.3. MARY B_0 dependence as observed via escape ketyl yield in benzophenone - micellar SDS system. The very low field part of (a) is displayed to greater resolution in (b).

Three major points are to be gleaned from the MARY data, in terms of sign and spectral form. The effect is positive at ~ 200 G, indicating an enhancement of ketyl yield upon application of a magnetic field. This is in accord with an expected initial triplet radical pair and singlet reaction. The form of the spectra is, however, not that expected from a simple view of hfi radical pair ISC. In contrast with the data of chapter 4, saturation of the field dependence is not observed in the region below 200 G. With a calculated $B_{½}$ of 70 G this is perhaps not too surprising, but high field work indicates saturation is not reached until ~ 5 kG [30]; a non-hfi mechanism is clearly inferred.

The final point, however, is of the greatest importance to the present work. It is clear from figure 5.3b that a very low field maximum exists and shows a MARY sign opposite to that at 200 G, corresponding to a field induced enhancement in ISC. From chapter 2 such a distortion of the MARY spectrum is expected to arise in the presence of a spin-spin interaction between the members of a radical pair. The effect is to introduce an S-T_0 separation at zero field. Although familiar in biradicals [31], this is the first reported observation of the MARY distortion exhibited by an unlinked radical pair. The phenomenon has also been observed, by the author, in micellar radical ion pair systems [32].

It might be argued that the presence of stray fields could also produce such an effect, provided that their sense was opposite to that being applied for the purpose of gathering the spectrum. This possibility was eliminated by the observation of identical results upon reversing the latter field.

RYDMR B_0 Spectra

Figure 5.4 shows a coarse (5 G intervals) B_0 swept RYDMR spectrum obtained at ~ 9.6 GHz with a microwave sampling pulse of 200 ns duration and centred at 200 ns after ^{3}BP generation. Such an interaction window represents an equivalent bandwidth of 5 MHz or 1.8 G, well within the 100 MHz cavity bandwidth and less than the microwave field amplitude which was set at the maximum achievable value, estimated at 13 G (chapter 3).

Also shown in the figure is a first order δ-function esr spectrum calculated assuming radical pairs consisting of benzophenone ketyl and secondary alkyl radicals as indicated. For the purposes of clarity, the contribution of each radical to the pair spectrum has been normalized to unit oscillator strength for the electron transition. Comparison reveals that the broad central RYDMR feature may be assigned to the ketyl radical, whilst structure in the RYDMR wings clearly matches the SDS-derived component in the simulation. This confirms the point, covered in chapter 2, that to a first approximation RYDMR resonances are expected to occur at field positions corresponding to those of the individual radicals predicted by a first-order esr treatment. In this respect the results are in agreement with those obtained from pulse radiolysis work [33].

The sign of the spectrum (negative) indicates a resonant increase in radical pair ISC, contrary to the static field (MARY) case and in accord the expectations of a simple theory in which the action of the microwave field is to induce $T_{\pm} - T_0$ transitions, recoupling states separated by the static field. From the perturbational lineshape considerations of a

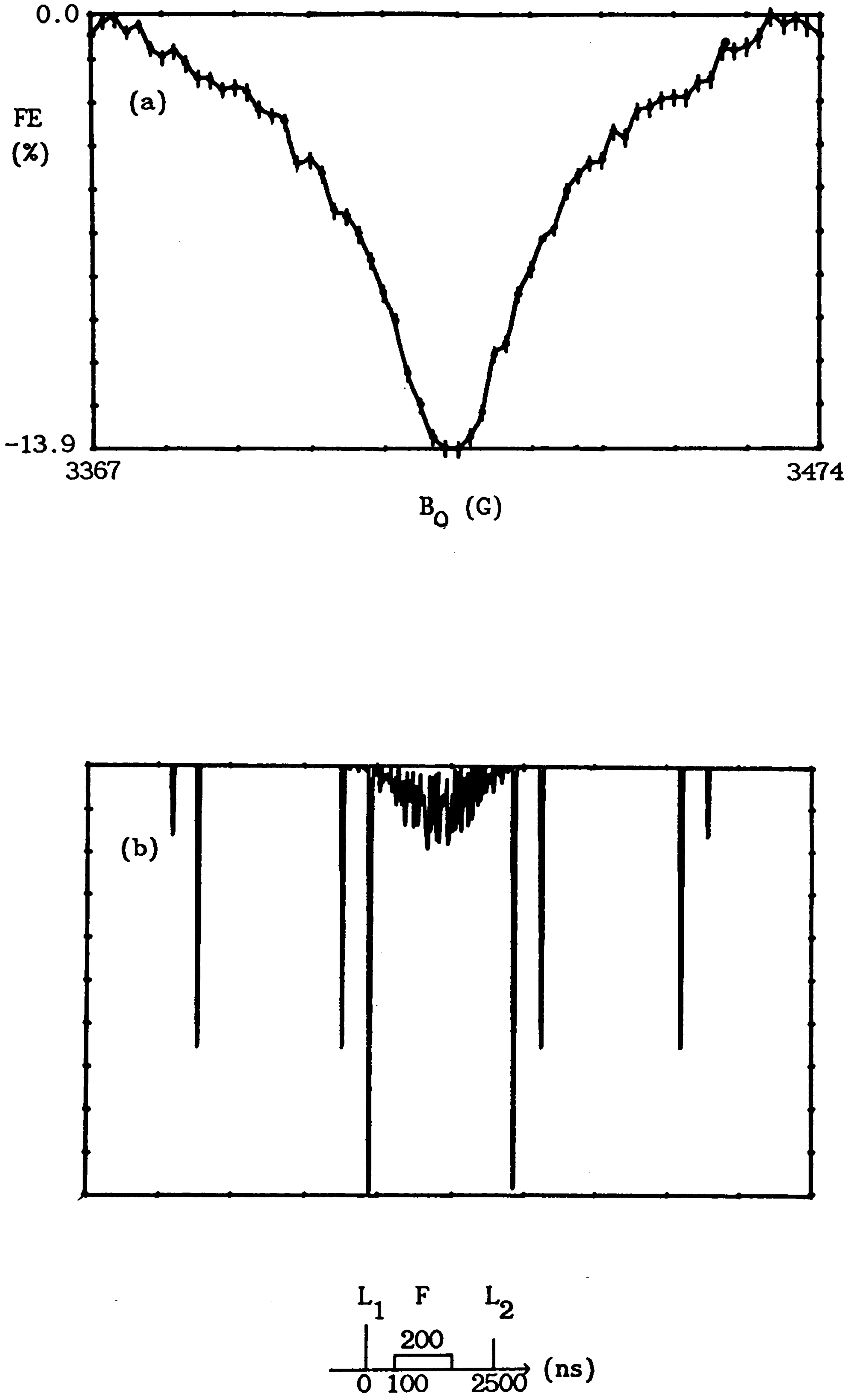

Figure 5.4. RYDMR B_0 spectrum obtained from a benzophenone - micellar SDS system.

(a) Spectrum observed via relative change in induced-fluorescence yield of escape ketyl radical. R.f. frequency = 9.5827 GHz, B_1 = 13 G.

(b) First-order esr simulation for a diphenylketyl - SDS radical pair (mid-chain secondary alkyl species - table 5.2) with parameters chosen to correspond to the above spectrum. Intensity for each pair member has been normalized to unit oscillator strength.

single member of a radical pair ensemble, given in chapter 2, this behaviour is only to be expected if there is spin-spin interaction of an energy in excess of that of the microwave field interaction. We thus seem to have further support to the conclusion already drawn from MARY spectra. There are, however, no resolved structural features that may be assigned to electron spin-spin coupling, though this is not too surprising in such a low resolution, broadened spectrum.

A further prediction from the simple perturbational treatment is the possibility of a so-called 'power narrowing' effect in the presence of significant inter-spin coupling (chapter 2). Figure 5.5 displays RYDMR B_0 spectra obtained at five values of B_1. They in fact clearly exhibit power broadening and are all in one phase.

RYDMR B_1 Spectra

Continuing the theme of spectral B_1 dependence, figure 5.6 shows the central portion of the RYDMR B_0 spectrum as a function of B_1. The results are plotted linearly with respect to B_1 (α $\{\text{power}\}^{1/2}$). Up to the maximum estimated B_1 of 13 G, there is no trend reversal as predicted to occur when $g\beta B_1$ is comparable to the S-T_0 separation (chapter 2). The effect is one of ISC enhancement at all B_1 values, though saturation is apparent at maximum B_1.

RYDMR Time Dependence

The dependence of RYDMR B_0 spectrum intensity upon microwave sampling interval delay, with respect to the synthesis laser excitation, is shown in figure 5.7. Results were obtained at maximum B_1 amplitude. Comparison

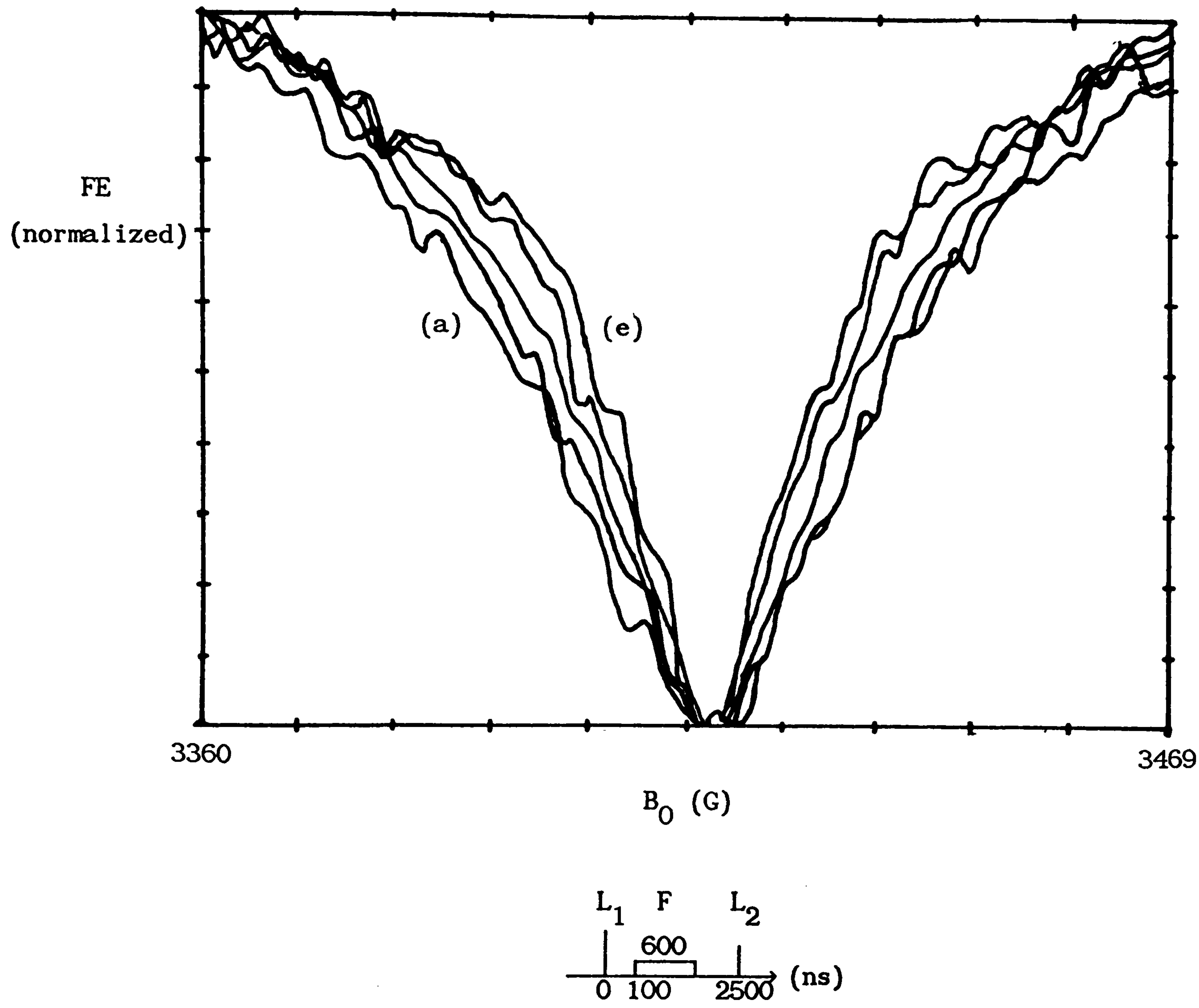

Figure 5.5. The B_1 dependence of RYDMR B_0 spectra from the benzophenone - SDS micellar radical pair system at 9.5827 GHz. (a) B_1 = 13 G, (b) B_1 = 9.2 G, (c) B_1 = 6.5 G, (d) B_1 = 4.6 G, (e) B_1 = 3.25 G.

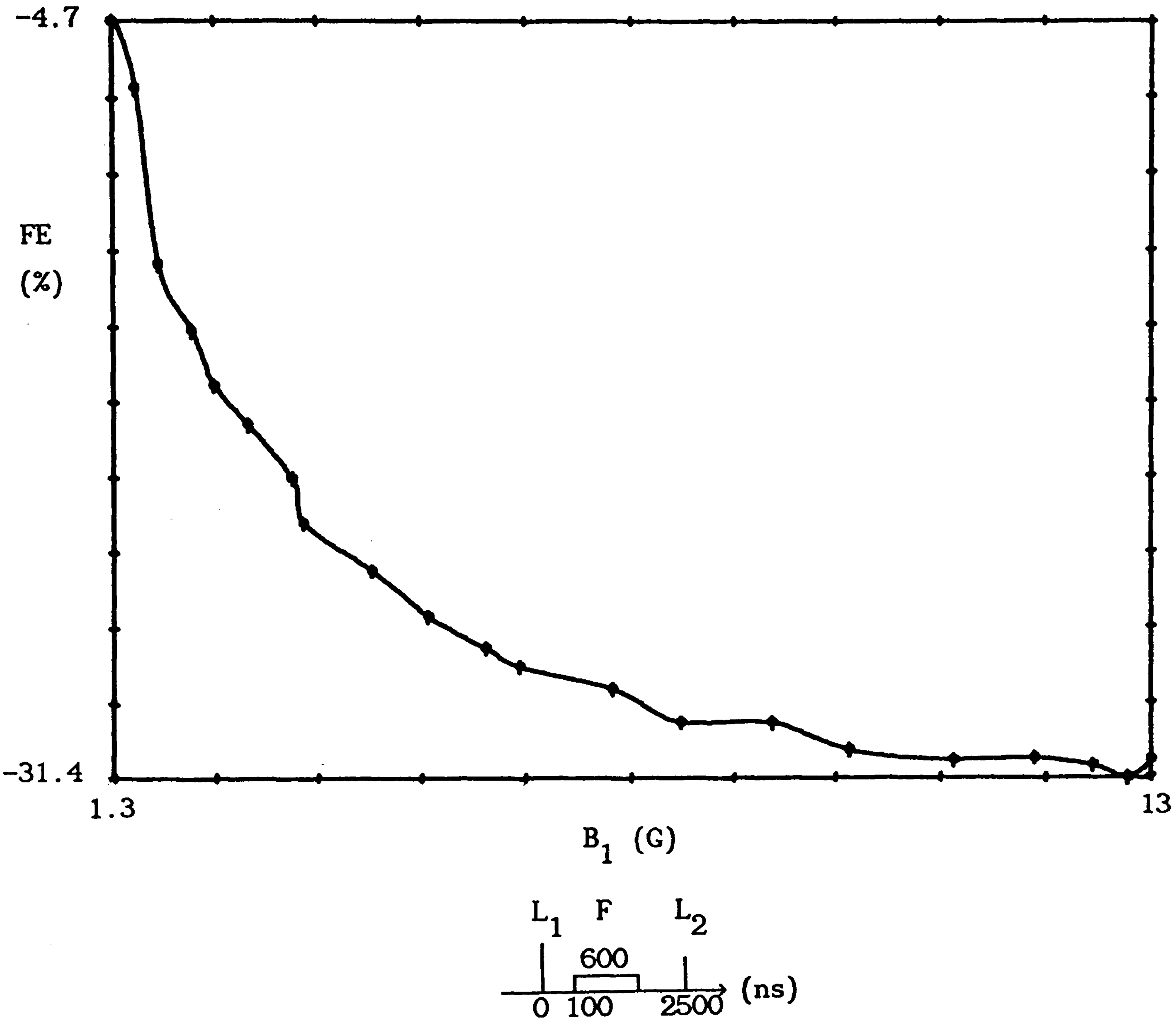

Figure 5.6. RYDMR B_1 spectrum for the benzophenone - micellar SDS system obtained at B_0 = 3418 G and r.f. frequency of 9.5827 GHz.

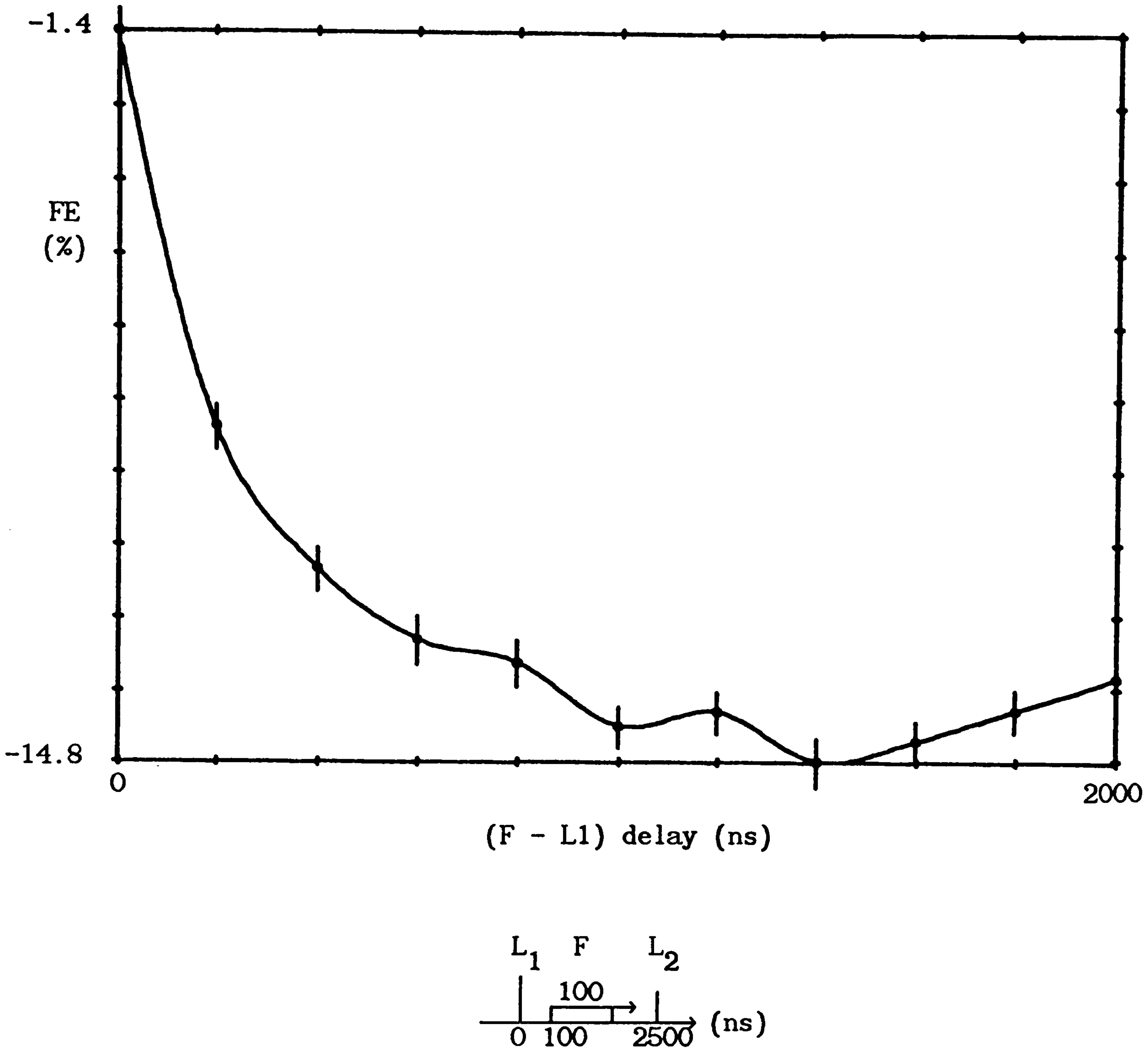

Figure 5.7. Time dependence of benzophenone - micellar SDS RYDMR intensity at B_0 = 3420 G and r.f frequency of 9.5827 GHz. B_1 = 13 G.

should be made with figure 5.2 revealing that, as expected, the RYDMR signal follows the time evolution of the ketyl radical at high field.

Dependence Upon Monitoring Wavelength

If the central RYDMR peak is recorded as a function of induced fluorescence wavelength, the results of figure 5.8 are obtained. There is clearly a changeover from a resonantly depleted fluorescence component to an enhanced fraction at shorter wavelengths. The latter contribution may be sensibly assigned to radical pair reaction products which most probably result from attack at a ketyl ring position and retain a high degree of conjugation in the product [29]. The observation also serves to illustrate that fluorescence detection of magnetic field induced effects is not solely restricted to emission from transient radical species, though the long term accumulation of photoproducts will obviously degrade the field-modulated signal amplitude.

5.4.A.2 Added Electrolytes

Increasing the ionic strength of the host aqueous environment is expected to increase surfactant aggregation and generate ellipsoidal micelles (see above). $MgCl_2$ was employed at 5×10^{-2} M and NaCl at 0.6 M, the latter requiring temperature stabilization at ~ 30°C to maintain the system above the cmt.

Ketyl Time Dependence

High field ketyl time evolution was found to be essentially identical to that observed in the absence of added electrolytes.

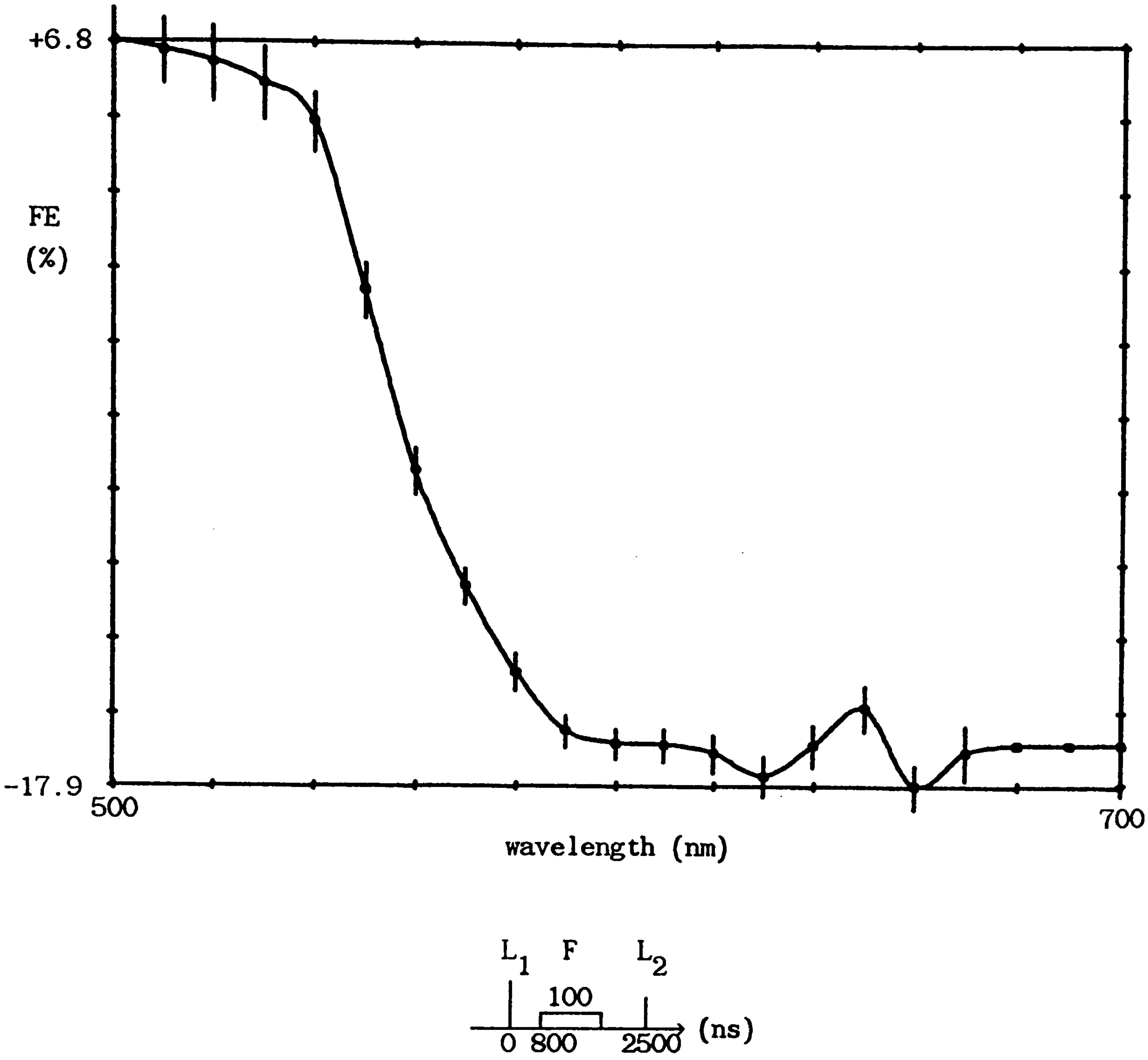

Figure 5.8. Dependence of induced-fluorescence detected RYDMR upon wavelength for the benzophenone - micellar SDS system. B_0 = 3420 G, B_1 = 13 G.

RYDMR B_0 Spectra

B_0 sweeps were performed in the presence of NaCl in an attempt to observe an inversion of the spectrum concomitant with a reduction in spin-spin interaction arising from the larger micelle environment. As evidenced in figure 5.9 no such change was apparent, though the RYDMR signal intensity was diminished in comparison to the pure SDS systems.

RYDMR B_1 Spectra

Further investigations were confined to the microwave field strength dependence of the central RYDMR B_0 peak. Results are illustrated in figure 5.10 for the addition of NaCl and $MgCl_2$. The pure SDS result is also reproduced for convenience of reference. There appears to be essentially no difference in the lineshape on comparison of all three results, but it is noticeable that the low concentration of $MgCl_2$ gives a saturated magnitude intermediate between that of a pure SDS system and that of the high concentration NaCl variant. It would seem that added electrolyte reduces the amplitude of field modulation, the above results apparently ruling out an effect upon ISC and pointing to kinetic factors, though no change is observed in the ketyl time profile. The trend, with added salts, is consistent with unpublished work concerning MARY signal amplitudes, performed by the author.

5.4.A.3 Added H-donors

Continuing the theme of a microreactor system, the micellar solubilization of a second radical precursor species, in addition to benzophenone, was attempted. 1,4 cyclohexadiene has two 'double allylic'

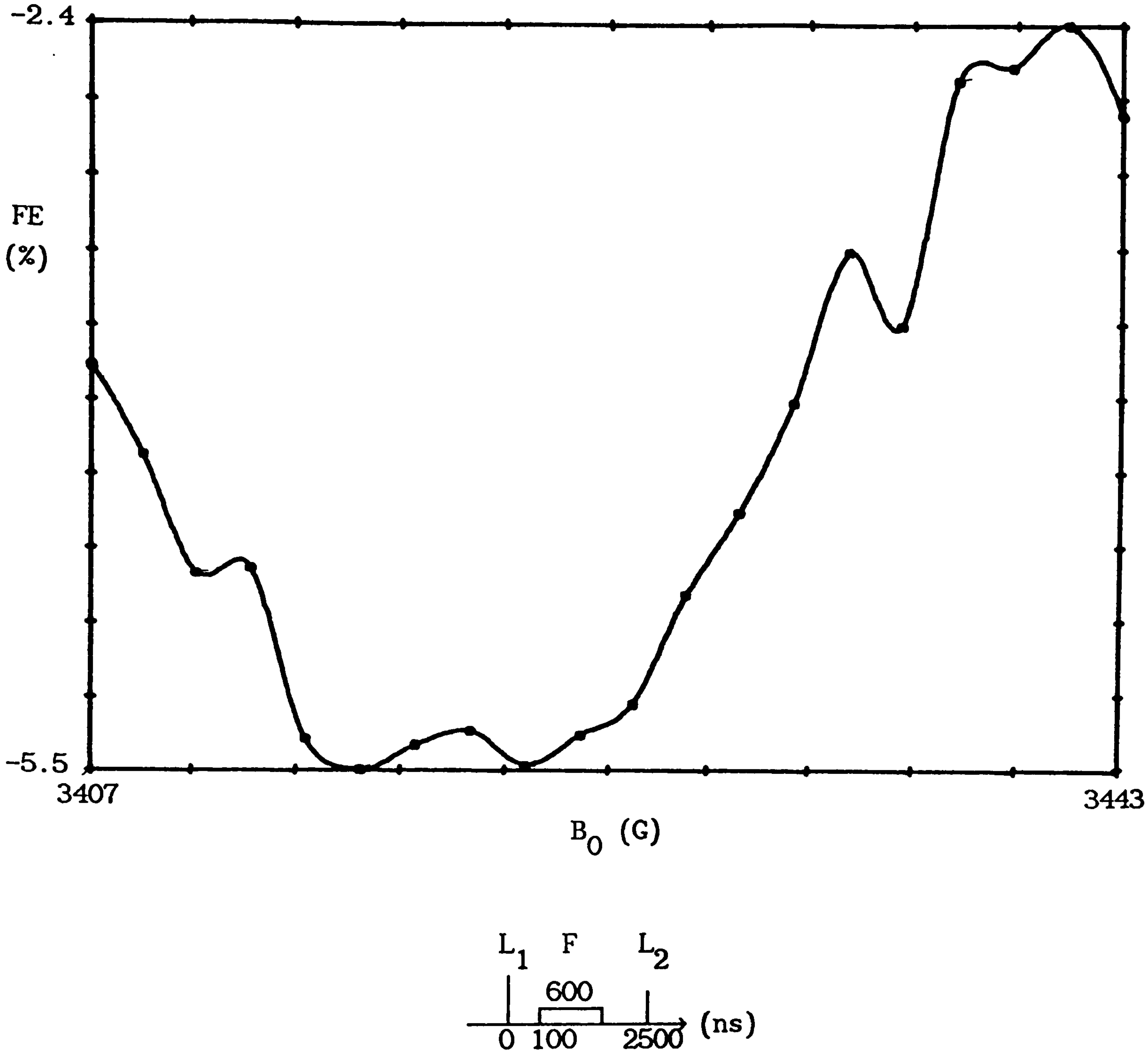

Figure 5.9. Central portion of RYDMR B_0 spectrum obtained from the benzophenone - micellar SDS system with added NaCl (0.6 M). R.f. frequency = 9.5827 GHz, B_1 = 13 G.

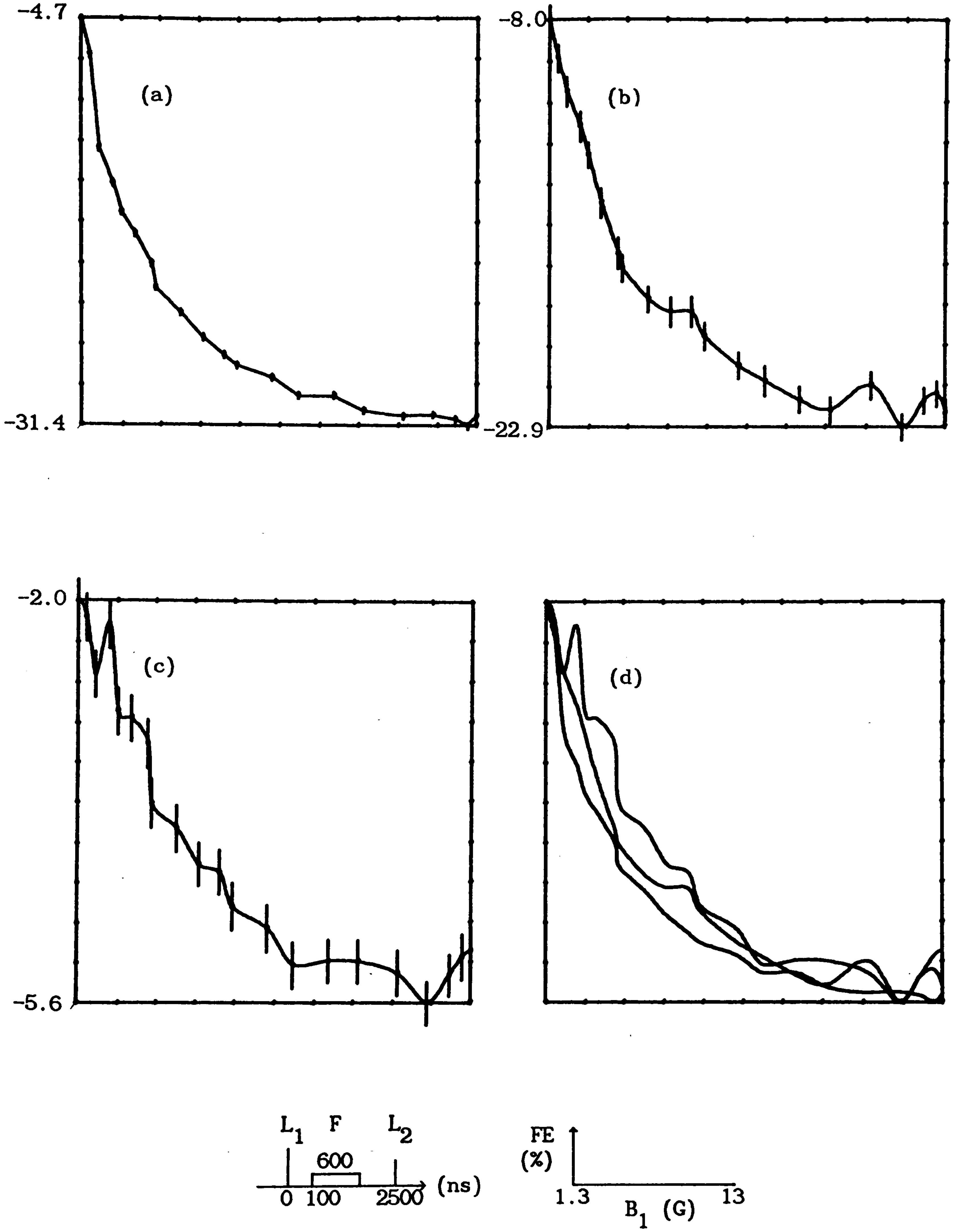

Figure 5.10. Comparison of RYDMR B_1 spectra for the benzophenone - micellar SDS system in the presence of different electrolytes. All were obtained at B_0 = 3420 G, and 9.5827 GHz.

(a) No added electrolyte.
(b) + 0.05 M $MgCl_2$.
(c) + 0.6 M NaCl.
(d) Comparison of (a), (b), (c).

positions from which an H atom may be abstracted. Earlier work had confirmed its ability to compete efectively with the high local SDS concentration within the micelle and to almost quantitatively generate diphenylmethylketyl from ^{3}BP [29]. At an occupancy ratio of 2:1 1,4 cyclohexadiene:benzopheneone, the author found that ketyl generation was completed almost within the timescale of the synthesis laser pulse, greatly simplifying subsequent kinetic analysis. Unfortunately photoproducts formed, again presumably ring coupled species, precipitated from the micellar phase and presented an unacceptable background fluorescence accumulation within the flow system employed. Nevertheless useful data were obtained.

RYDMR B_0 Spectra

Figure 5.11 shows RYDMR B_0 spectra obtained from benzophenone/1,4 cyclohexadiene combinations in a micellar system immediately after L1 excitation and after a delay of 1 μs. The effect of high β proton couplings in the cyclohexadienyl species is to separate high and low field resonance groups away from the central ketyl contribution. This effect may be seen in the first order simulation, also displayed in the figure, and is readily discerned in the both RYDMR spectra. Indeed, within the limits of experimental error, the latter are identical, confirming the rapid generation of the cyclohexadienyl radical species.

Having obtained a system in which major spectral features could be 'removed' from the overlapping diphenylmethylketyl resonances (deuterated benzophenone would have been useful in this context), experiments were performed in an attempt to assess the resolution capabilities of the RYDMR experiments. Attention was focussed on the low

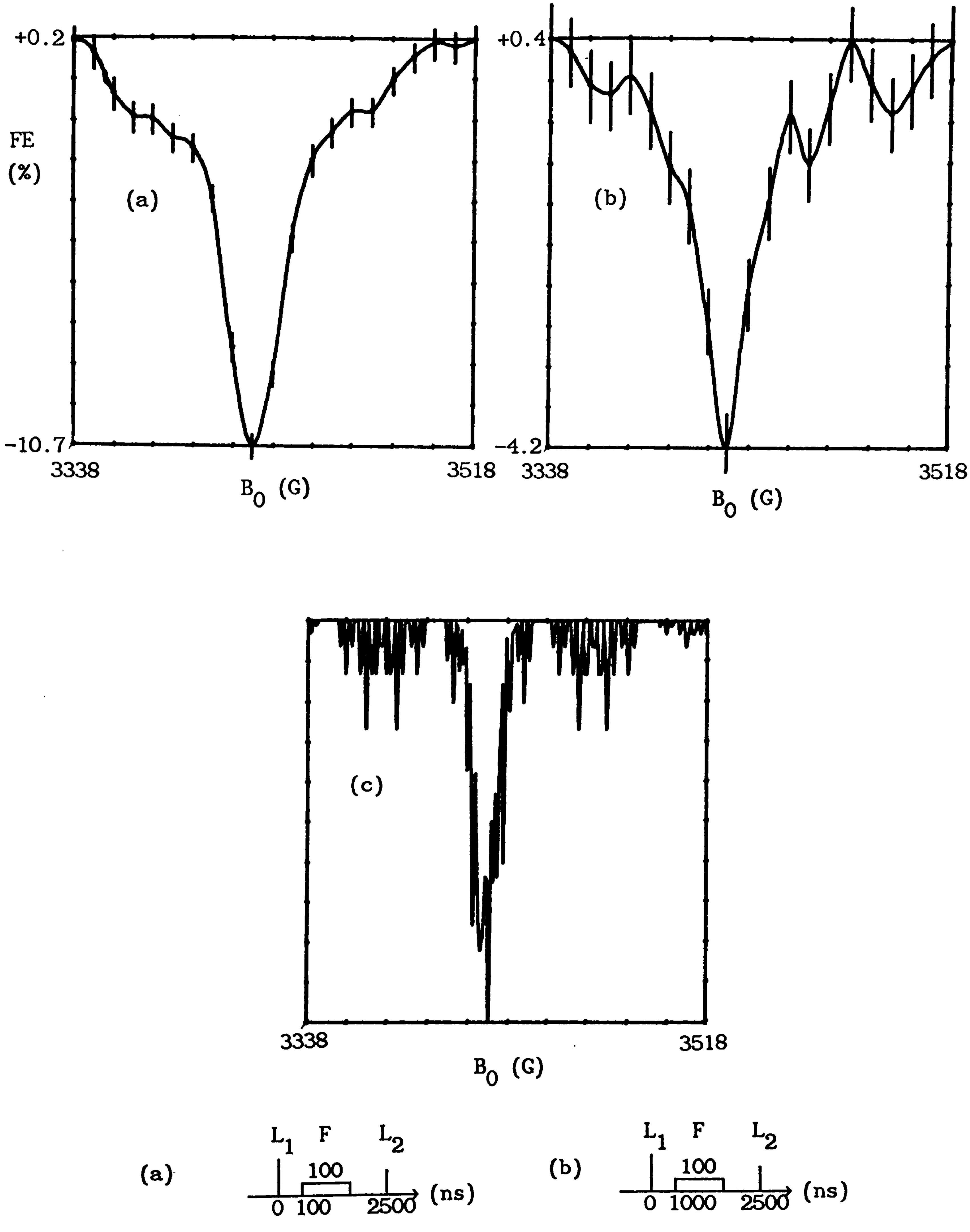

Figure 5.11. RYDMR B_0 spectra obtained from a benzophenone - 1,4 cyclohexadiene - micellar SDS system at 9.5827 GHz. B_1 = 13 G.

(a) Spectrum recorded 100 ns after L1.
(b) Spectrum recorded 1000 ns after L1.
(c) First-order esr simulation of the above spectra using a diphenylketyl - cyclohexadienyl radical pair (table 5.2). Intensity for each pair member has been normalized to unit oscillator strength.

field wing which, according to the simulation, comprises essentially regularly spaced resonances at intervals of approximately 5 G. Unfortunately RYDMR intensity in this region corresponded to a 'long time' change in ketyl yield of only a few per cent (see figure). Statistically significant results could only be obtained at high B_1 values, which have already been shown to generate considerable line broadening.

Figure 5.12 shows examples of B_0 spectra collected at 'early' and 'late' times after radical generation. The field sweeps were performed approximately about the centre of the low field feature. Comparison with the relevant simulation (figure 5,12c) reveals a correspondence in the form of a major line splitting at 13 G, but only in the spectrum sampled at 800 ns (figure 5.12b). Also in evidence is a B_0 field offset of some 5 G between the simulation and the experimental data. Most probably the greater part of this discrepancy may be assigned to field stability problems, though at such a magnitude it is greater than that typically experienced during spectral data gathering (chapter 3). Furthering this point, it is noticeable that figures 5.12a,b, programmed nominally as identical scans, do in fact differ in the observed sweep width and position. With this in mind, the absence of a major doublet component in the 'early time' spectrum may be taken as an illustration of experimental difficulty encountered rather than of any greater fundamental significance.

Once again the absence of any significant line splitting arising from spin-spin interaction is noted, though the statement must be qualified by referring to the lack of resolution.

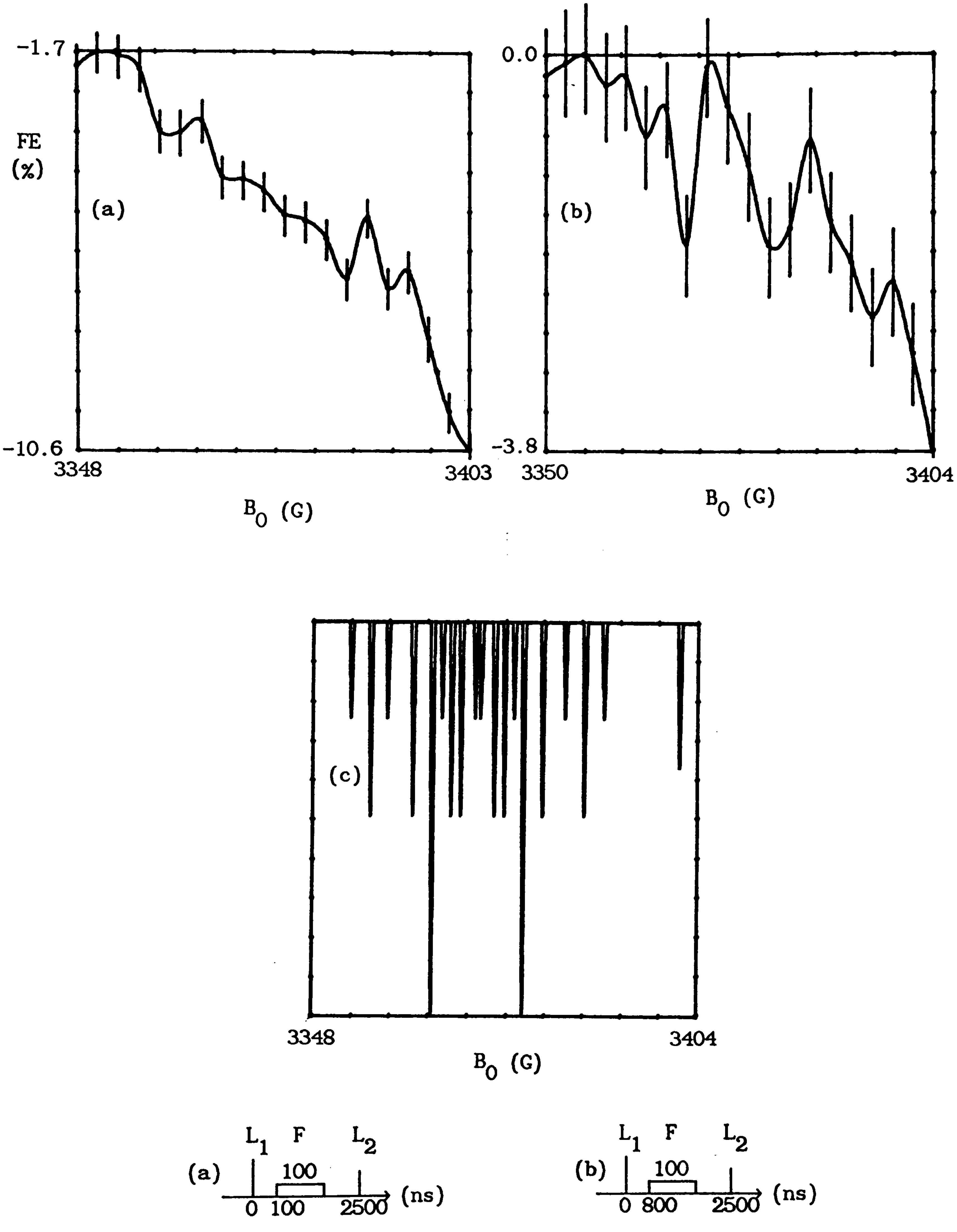

Figure 5.12. RYDMR B_0 spectra covering low field wing of benzophenone - 1,4 cyclohexadiene - micellar SDS system. R.f. frequency = 9.5827 GHz, B_1 = 13 G.

(a) Spectrum recorded 100 ns after L1.
(b) Spectrum recorded 800 ns after L1.
(c) First-order esr simulation of the above spectra.

RYDMR Time Dependence

The kinetic effect of 1,4 cyclohexadiene addition upon radical pair time evolution is well demonstrated by figure 5.13 which shows the time dependence of the RYDMR B_0 central intensity. The contrast with figure 5.7 is remarkable, the slow radical generation being replaced by an effective δ-formation function.

B

5.4.B.1 Microemulsion Systems

Benzene microemulsion systems, as discussed and characterized above, were employed as variable-size microreactor media. They were capable of readily solubilizing a range of hydrophobic materials and in this respect proved considerably more convenient in use.

All experiments were performed by solubilizing benzophenone at a overall concentration of 10^{-2} M in 0.2 M aqueous SDS - 0.6 M 1-pentanol - benzene quaternary systems. The benzene component was present variously at a range of volume fractions from 0 % - 6 %. From the probe studies described above, it may be concluded that benzophenone occupation numbers ranged from 2-8. Again, as with the pure micellar systems, it is apparent that there was a significant probability of generating an excess of one ^{3}BP molecule per microreactor compartment. S/N optimization was again the reason for the choice of this situation, although it was noticeable that ketyl fluorescence signals were considerably enhanced with respect to pure aqueous SDS. This effect is most probably attributable to the solubilization of the ketyl in the central oil core and the accompanying high degree of isolation from the bulk aqueous solvent.

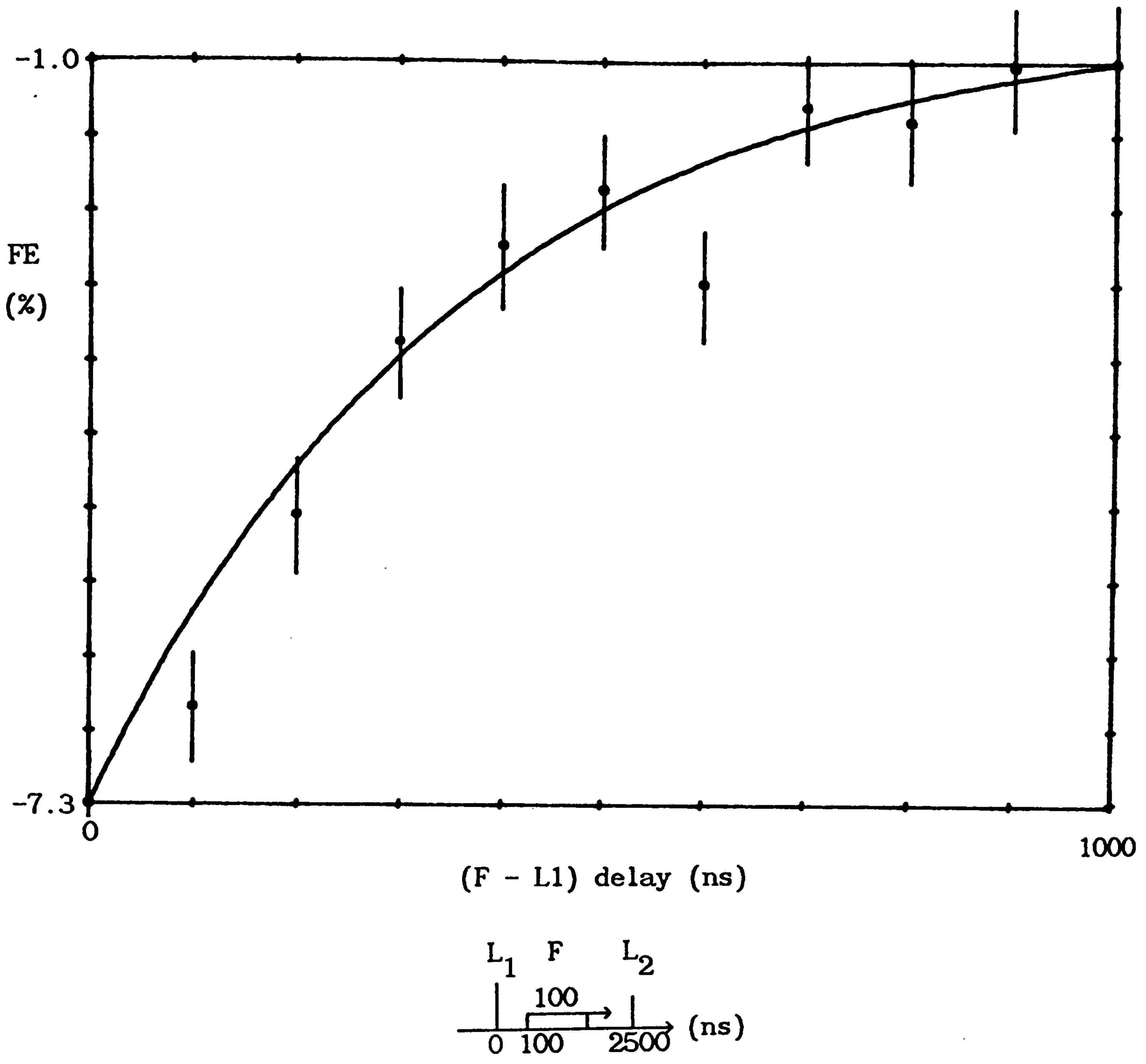

Figure 5.13. Time dependence of RYDMR intensity for a benzophenone - 1,4 cyclohexadiene - micellar SDS system at 3428 G, 9.5827 GHz and B_1 = 13 G. The data has been fitted to a single exponential function of time constant 354 ns.

Ketyl Time Dependence

Time resolved L2 fluorescence yield, recorded over the range 0-2 μs in a static field of 3420 G, revealed no difference in the ketyl time evolution on comparison with 0.1 M aqueous SDS systems; at least within experimental error. In addition, this time range produced no observable dependence upon the expected change in microreactor core size with volume fraction of oil component.

The hydrogen abstraction from benzene solvent by ^{3}BP is known to proceed with a pseudo first-order rate constant of 1.6×10^4 s^{-1} [34] which leads to a ketyl formation time greater than that observed by two orders of magnitude. It must be concluded, therefore, that the major route to to ketyl generation is H abstraction from the SDS-pentanol interfacial layer. On this point a degree of oil core-surfactant overlap was indicated by probe studies (above) and similarly reaction timescales are not inconsistent with diffusional migration throughout the microreactor volume.

In terms of radical pair members, the expectation is that the major components will be surfactant-derived species. Pentanol is present in greater concentration, but it may be argued to be more inaccessible if it is located in the aqueous interface and ^{3}BP in the oil core. The major radical species derived from both pentanol and SDS would, however, be expected to show similar esr structures and so the matter is unlikely to be easily resolved.

RYDMR B_0 Spectra

In an attempt to confirm or deny the absence of significant phenyl radical concentrations, a high resolution (in comparison with those previously presented) RYDMR B_0 spectrum was recorded from the products arising at 100 ns after the photoinitiated reaction of ^3BP in a 6 % benzene microemulsion. Figure 5.14 presents the results obtained with a B_0 sampling interval of 0.5 G which marks the limit of field stability expected during data gathering at a single field position. The figure is drawn in continuous form, without error indicators, for the purposes of clarity. The standard deviations were observed to be ~ 1/20 th. full scale. First-order esr line positions for a range of possible alkyl radical species derived from the surfactant molecules are shown in a composite simulation (figure 5.14b). Examination reveals there are indeed correspondences with the RYDMR spectrum, apparently indicating resolution of a few Gauss even at B_1 ~ 13 G. Further confidence in the latter spectrum is gained by noting the symmetrical nature of much of the structure about the centre position. The existence of a phenyl species (simulation figure 5.14c) clearly cannot be decided from the RYDMR spectrum.

As found with pure micellar systems, the sign of the RYDMR signal is negative. RYDMR intensities are not directly comparable, with respect to magnetic evolution, as a result of differing kinetics and microwave sampling intervals.

The effect of varying oil droplet size is presented in figure 5.15. Spectra were obtained at benzene compositions ranging from 6 % (solubility limit) to 0 % by volume. Other conditions were as stated in

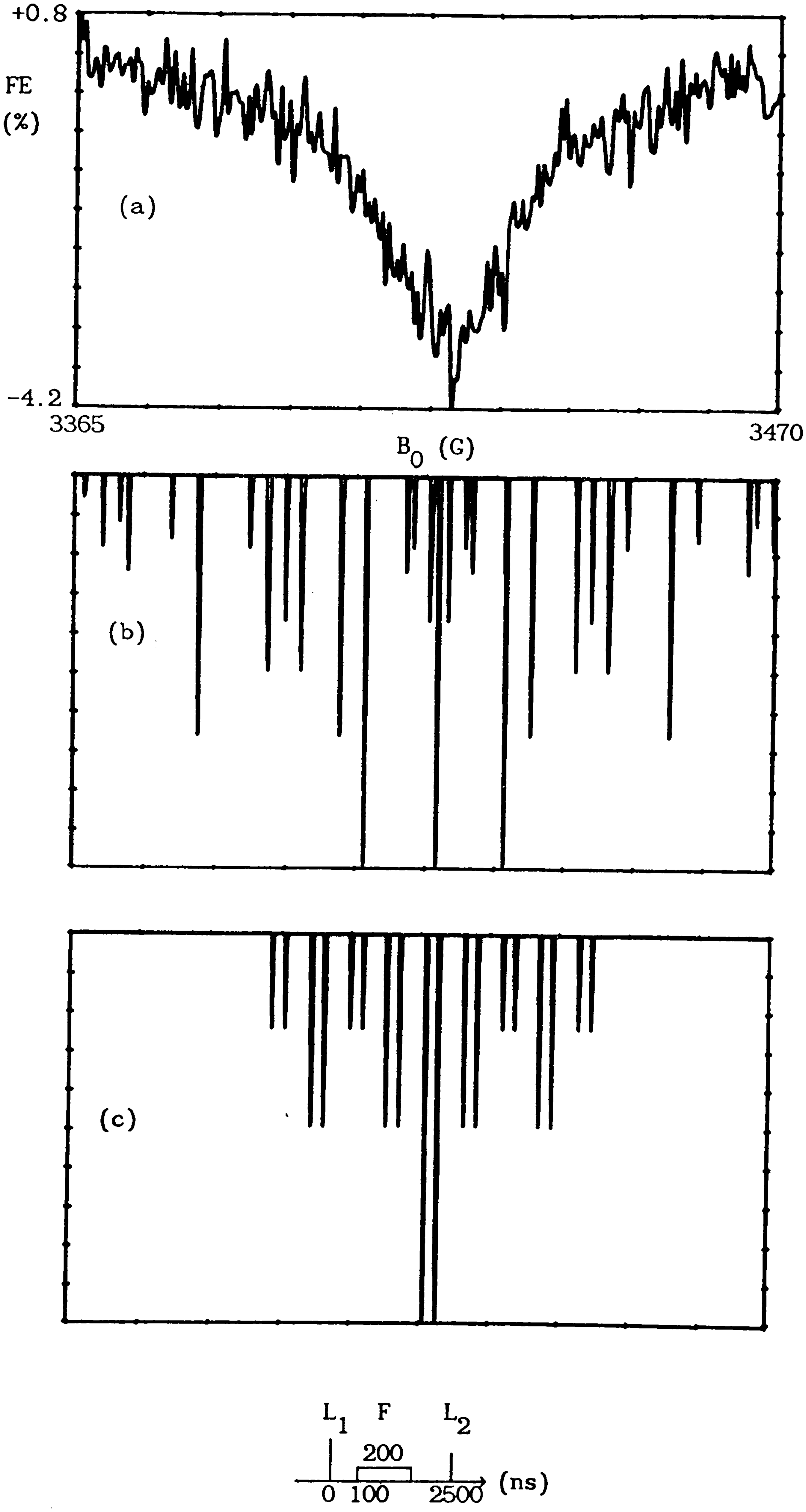

Figure 5.14. RYDMR from microemulsion media.

(a) RYDMR B_0 spectrum obtained from a benzophenone - 6 vol. % benzene microemulsion system via induced fluorescence of escape ketyl species. R.f. frequency = 9.5827 GHz, B_1 = 13 G.

(b) First-order esr simulation of the spectrum expected for all three alkyl species of table 5.2 under the conditions of (a).

(c) First-order esr simulation for a phenyl radical under the conditions of (a).

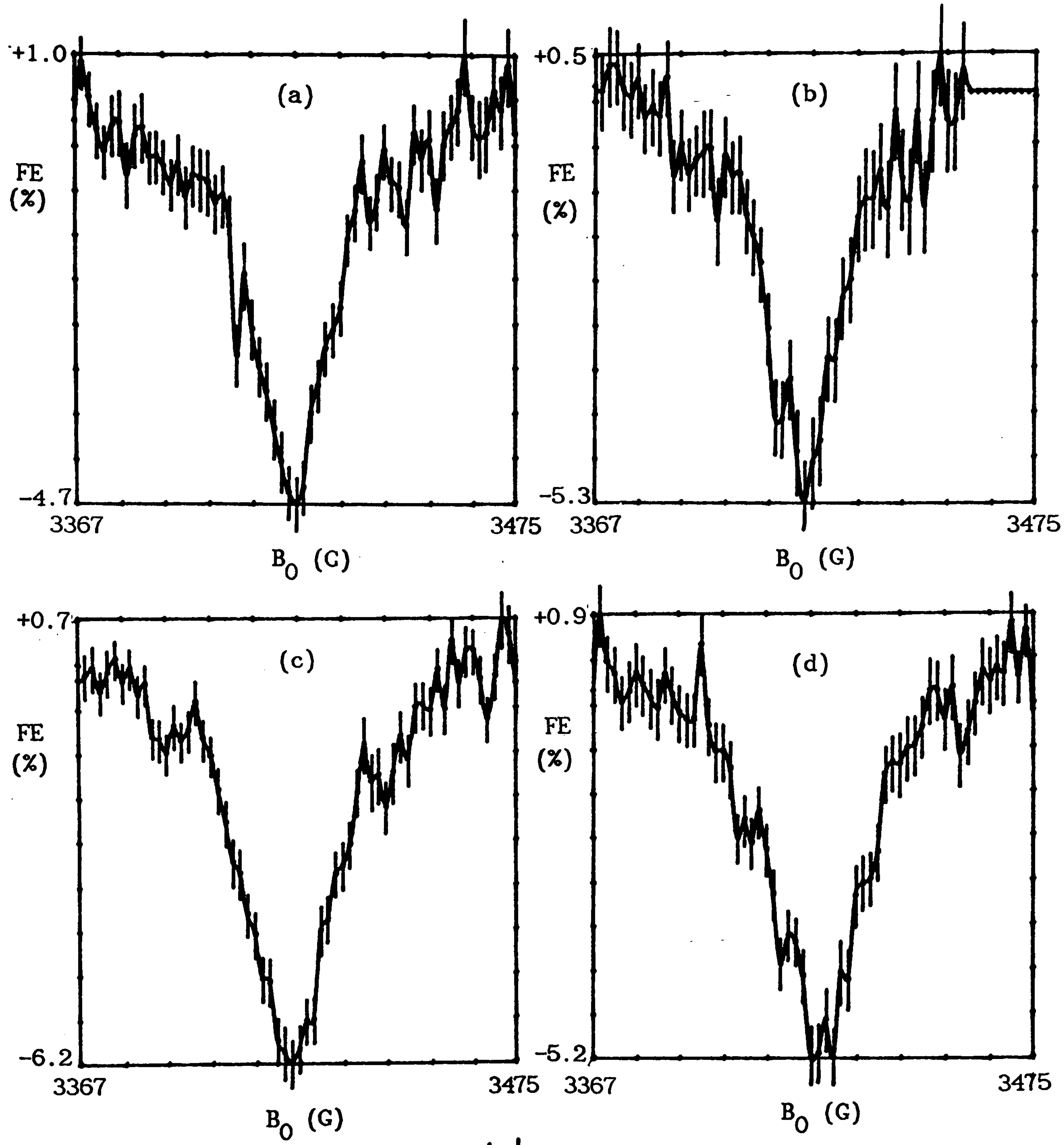

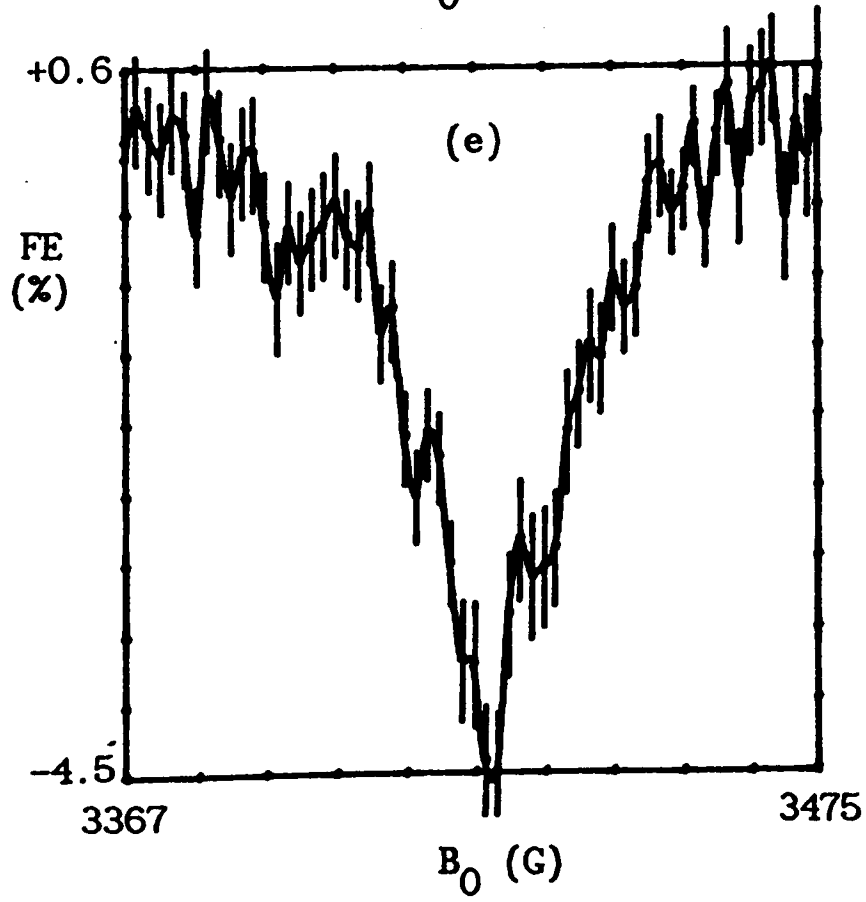

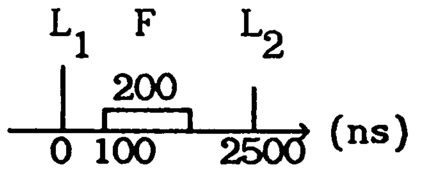

Figure 5.15. Benzophenone in benzene microemulsions: the effect of reactor volume on RYDMR B_0 spectra observed via escape ketyl fluorescence. R.F. frequency = 9.5827 GHz, B_1 = 13 G.

(a) 6 vol. % benzene oil component.
(b) 4 vol. % benzene oil component.
(c) 2 vol. % benzene oil component.
(d) 1 vol. % benzene oil component.
(e) 0 vol. % benzene oil component.

the figure. Coarse sampling at ~ 1.5 G intervals was employed as interest was focussed on the effect of reactor volume upon the RYDMR spectral envelope. Within the limits of experimental error, no changes are discernible. In particular the width of the central feature remains constant and there is no phase inversion of the spectrum.

Confirmation of the variation in oil core volume was provided by pyrene probe studies (above).

5.4.B.2 Added H-donor

As with pure micellar media, addition of 1,4 cyclohexadiene at a mole ratio of 2:1 to benzophenone was found to be efficient in the generation of the ketyl species and simplification of the kinetic profile.

Ketyl Time Dependence

Results presented in figure 5.16 show ketyl time evolution under RYDMR resonant, static field only and zero (terrestrial) field conditions for a 2 % benzene microemulsion medium. First-order rate constants were evaluated by a least squares fitting to the functional form of S(t) described above (12), and are given in table 5.3 for 2 % and 6 % benzene media.

It is to be noted that k_{esc} does not show field independence as required by the proposed model. This is indicative of the importance of biexponential behaviour, briefly acknowledged above, but it is difficult to proceed with the analysis along these lines in view of the data quality. The original intention behind its gathering was the

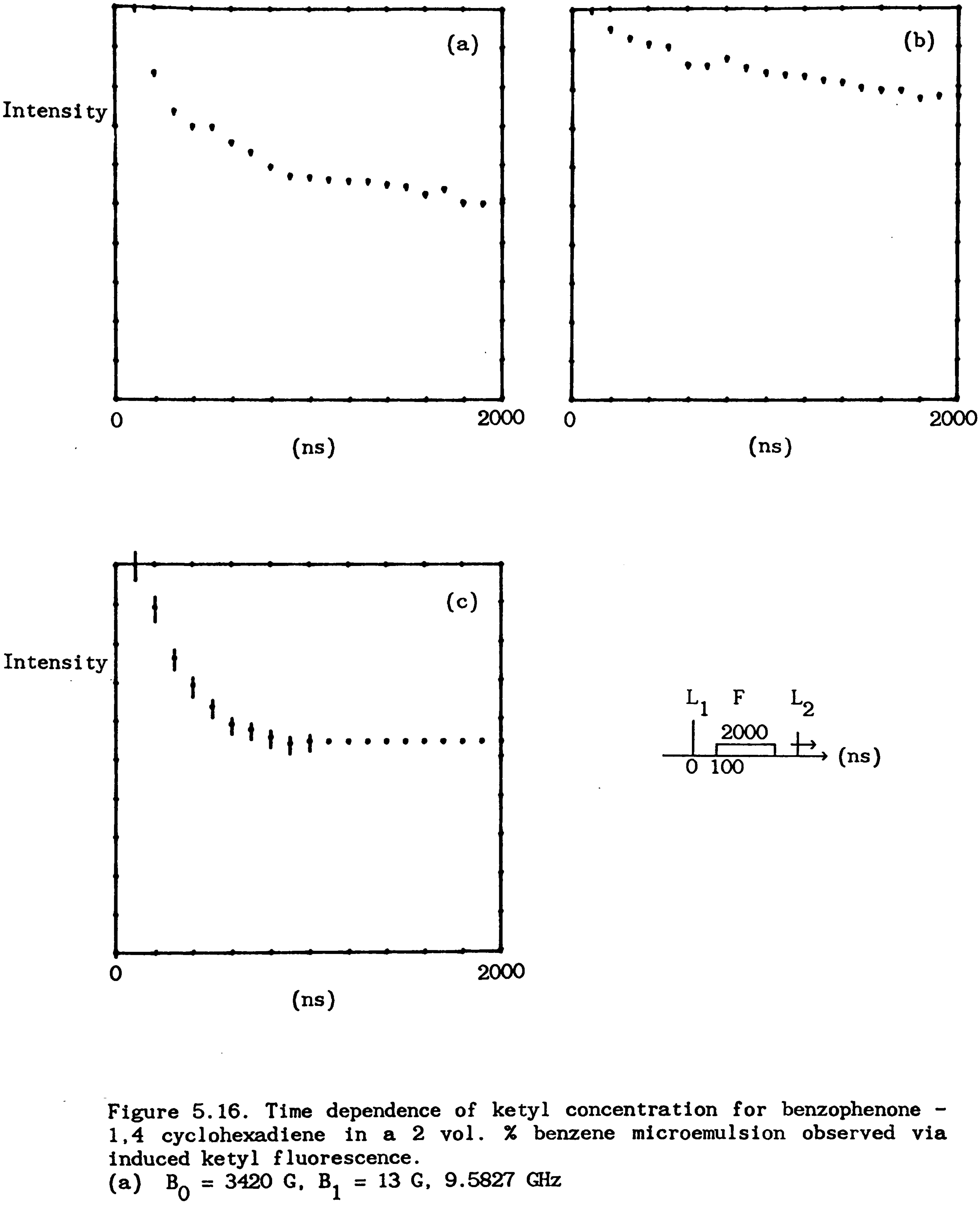

Figure 5.16. Time dependence of ketyl concentration for benzophenone - 1,4 cyclohexadiene in a 2 vol. % benzene microemulsion observed via induced ketyl fluorescence.

(a) B_0 = 3420 G, B_1 = 13 G, 9.5827 GHz

(b) B_0 = 3420 G, B_1 = 0 G.

(c) Terrestrial field only.

Table 5.3

Kinetic Field Effects [a]

6 % (v/v) Benzene

B_0(G)	B_1(G) [b]	$10^{-6} k_{rec} s^{-1}$	$10^{-7} k_{esc} s^{-1}$	$k_{rec}(B_0,B_1)/k_{rec}(0)$
3420	13	2.7	1.0	0.9
3420	0	0.8	1.2	0.3
0	0	3.0	3.0	1.0

2 % (v/v/) Benzene

B_0(G)	B_1(G) [a]	$10^{-6} k_{rec} s^{-1}$	$10^{-7} k_{esc} s^{-1}$	$k_{rec}(B_0,B_1)/k_{rec}(0)$
3420	13	1.2	1.5	0.6
3420	0	0.3	0.9	0.2
0	0	2.0	2.1	1.0

[a] Parameters from fitting of equation (12)

[b]

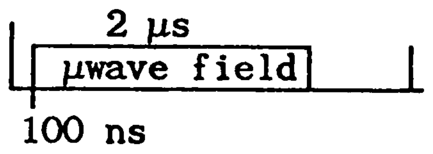

illustration of the kinetic effects of r.f. and static fields. Despite this, useful conclusions may still be drawn.

On the basis of a purely hyperfine-dependent model of radical pair ISC, the effective recombination rate constant within the microreactor volume is given by,

$$\begin{aligned} k_{rec}(B_0). &= \bar{p}_s(B_0)\, k^m_{eff} = 0.5k^m_{eff} \,, \\ k_{rec}(0) &= \bar{p}_s(0)\, k^m_{eff} = 0.25k^m_{eff} \,. \end{aligned} \qquad (14)$$

We thus should observe a factor of two increase in the ketyl recombination rate constant upon moving from zero field to a high field regime. If, however, the possibility of $T_\pm \rightarrow T_0$, S processes at high field, induced for example by relaxational effects, is acknowledged then the resulting biexponential decay would include the expected rate constant ($k_{eff}/2$) in a component with a weighting of only one third (T_0 born pairs only) [28]. In this manner the detection of the dominant slow component is explicable and the unexpected trend in rate constant accounted for by a change in the ISC process being monitored.

The inclusion of a resonant microwave field adds complexity as witnessed by the subtle dependence of RYDMR lineshape upon the system parameters. In simple terms, however, if the effect is to enhance singlet probability over its value at high static field only (as will be evident from RYDMR spectra to be presented) then, at a sufficiently high B_1, we would expect a change in recombination rate constants towards that observed at zero field. This conclusion is in agreement with the results of table 5.3, though added complications arise as a result of part of the ensemble being 'off resonance'.

The magnitudes of k_{rec} at zero field, where a single exponential model is presumed valid, may be compared with the prediction of $0.25k^{m}_{eff}$. Employing the rate constants for the diffusion-limited, spin-independent intermolecular excimer formation determined from pyrene probe studies, it may be seen that the observed k_{rec} values are somewhat low, but by a comparable factor for both types of microemulsion. This would suggest a singlet recombination probability of only 0.25 from the assumed diffusion-controlled ring coupling of ketyl and cyclohexadienyl radicals. The error associated with this figure is expected to be large due to the paucity of data (21 time samples per ketyl transient), but encouragement may be gained from the agreement between the two microemulsion systems. It must also be recognized that application of pyrene probe data to the intraemulsion behaviour of a polar ketyl molecule is to be regarded with some caution.

MARY Spectra

MARY spectra were obtained from the ketyl/cyclohexadienyl radical pair distributed in microemulsions of 2 % and 6 % benzene volume fraction. Figure 5.17 shows approximately 200 G sweeps for each of the media, with expansions of the very low field region. Long term drift, mainly arising from fluorescent photoproduct background deposition within the sample cell, may be judged by the final data point in each 200 G scan which was recorded at zero field. The reference-field background correction procedure was not followed in the collection of these results.

As found in pure micellar analogues, no saturation is observed within the field range, a distortion is present at very low field and, at 200 G, the spectrum corresponds to an enhanced ketyl escape fraction.

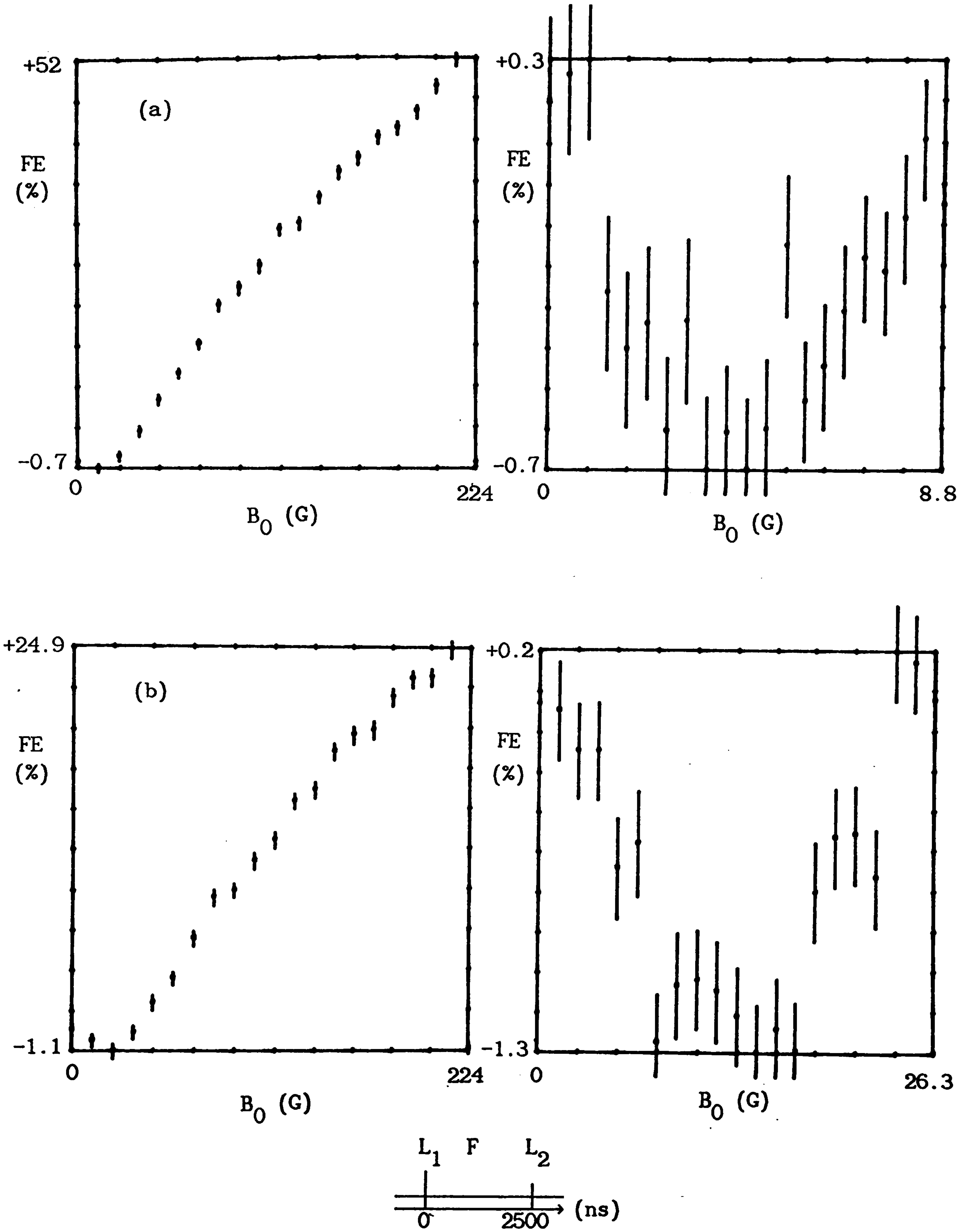

Figure 5.17. MARY spectra observed from benzophenone - 1,4 cycohexadiene in benzene microemulsion systems via induced fluorescence of escape ketyl.

(a) 6 vol. % benzene.

(b) 2 vol. % benzene

The very low field negative excursions are centred at ~ 4 G and ~ 13 G respectively for 6 % and 2 % benzene volume fractions.

It is also apparent that the spectral intensity at 200 G is considerably greater in the 6 % benzene variant. If the low field negative extrema are taken to be indicative of spin - spin interaction leading to S - T_0 separation at zero field, the order of field effect magnitudes at $B_0 \gg \epsilon_{S-T_0}/g\beta$ would indeed be expected to follow that observed; a correspondingly lower singlet fraction at zero field would be obtained in the system exhibiting the larger S - T_0 separation. This statement must, however, be qualified by the results presented in table 5.3 which show that a greater ratio k_{esc}/k_{rec} in the low-volume oil droplet, suggesting that kinetic factors are also important.

RYDMR B_0 Spectra

Having clearly demonstrated a change in magnetic behaviour with microreactor volume, attention was turned to RYDMR B_0 spectra. Data recorded immediately after ketyl generation, and 2 μs later, confirmed the presence of the ketyl/cyclohexadienyl radical pair throughout this timescale (figure 5.18) and so further spectra were recorded under 2 μs microwave sampling conditions in order to optimize S/N. The benefits of this procedure are evident in the spectra of figure 5.19 which compares results from 2 % and 6 % benzene media under otherwise identical conditions. A slight broadening of the small volume spectrum is visible, in comparison with its 6 % benzene counterpart, but there is no evidence of the dramatic changes predicted by the perturbational treatment (chapter 2).

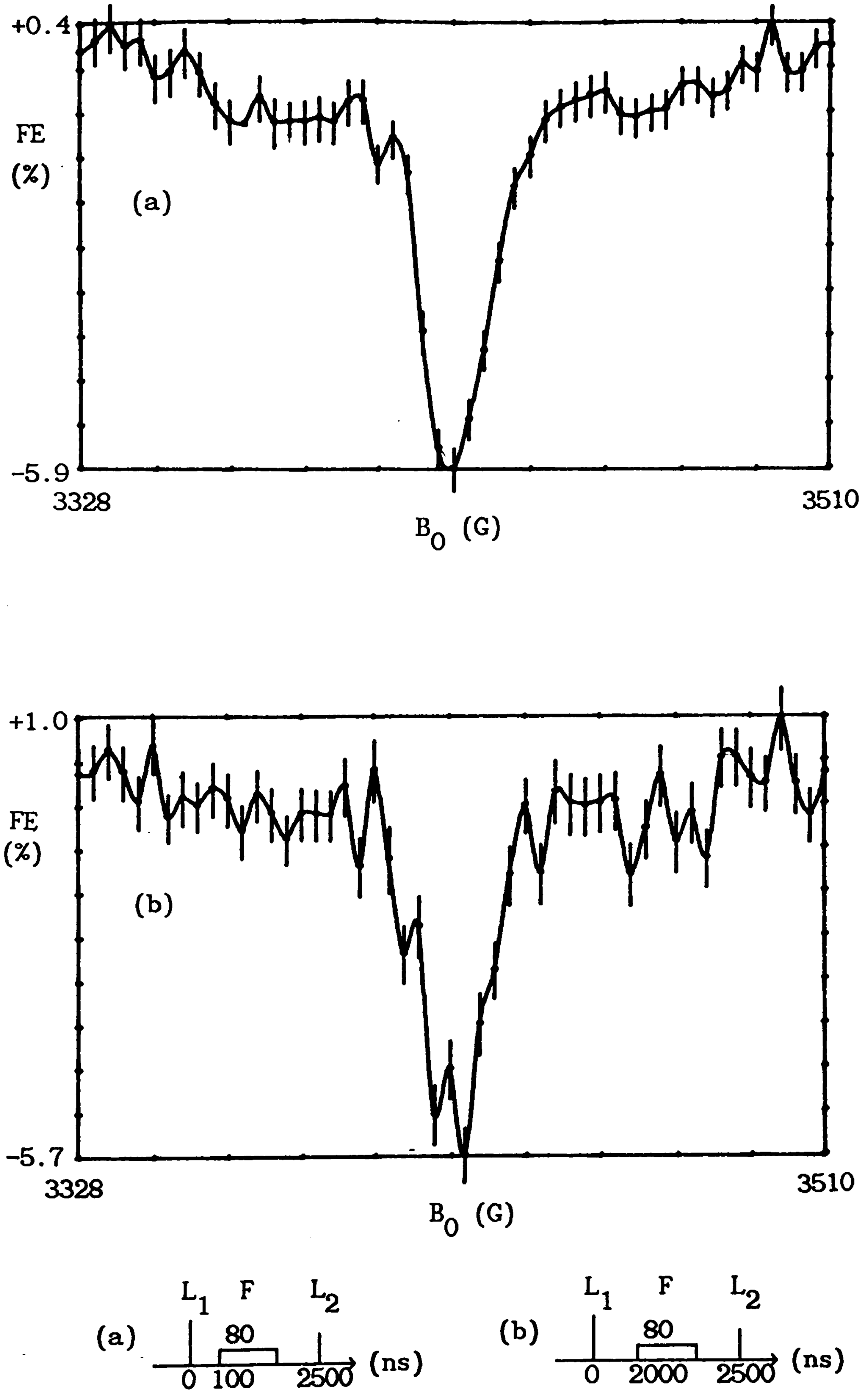

Figure 5.18. RYDMR B_0 spectra from benzophenone - 1,4 cyclohexadiene in a 6 vol. % benzene microemulsion system at B_1 = 13 G, 9.5827 GHz.

(a) Recorded 100 ns after L1.
(b) Recorded 2000 ns after L1.

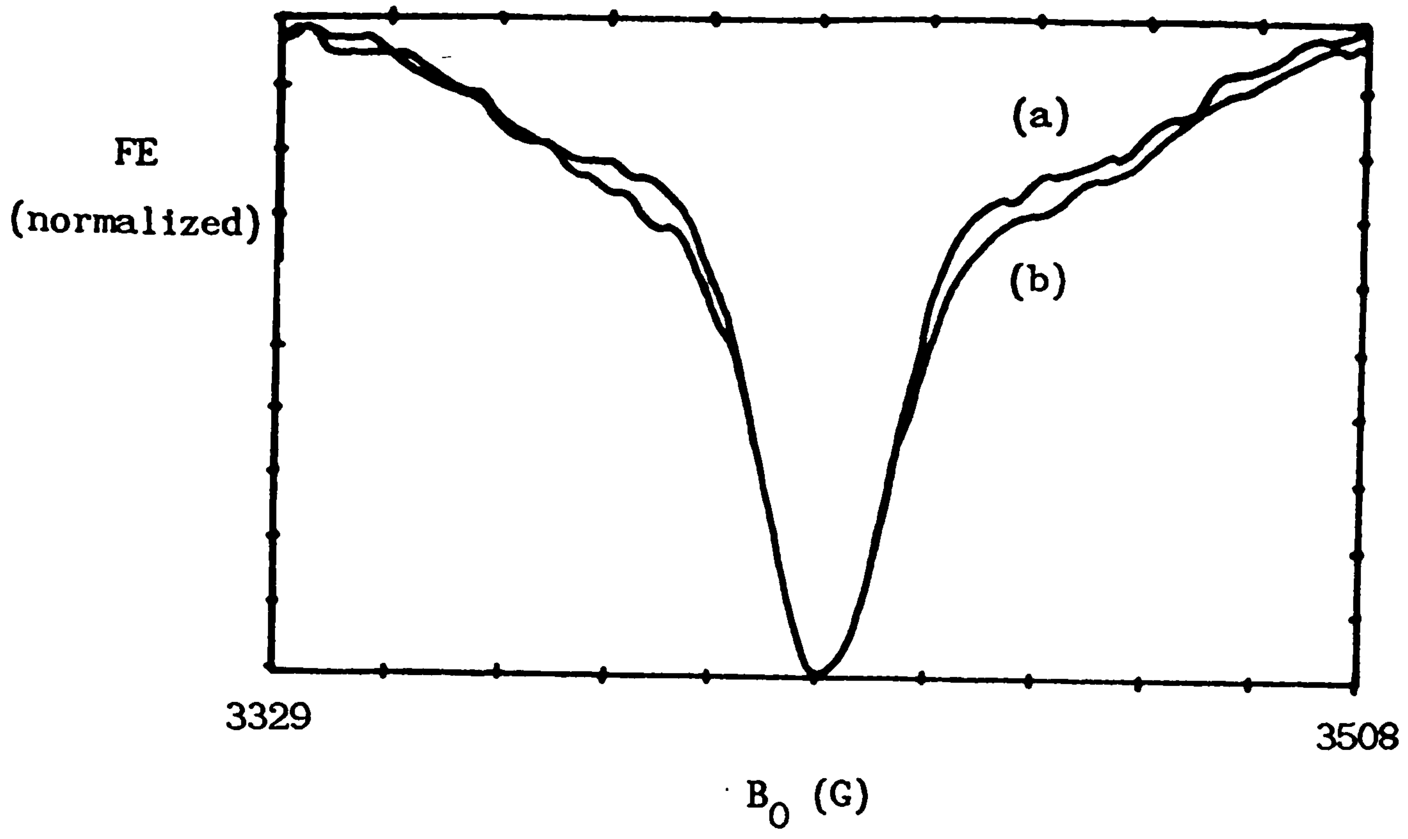

Figure 5.19. Effect of reactor volume on RYDMR B_0 spectra of benzophenone - 1,4 cyclohexadiene in benzene microemulsion media. R.f. frequency 9.5827 GHz, B_1 = 13 G. Observation via induced fluorescence of escape ketyl radical.

(a) 6 vol. % benzene oil component.

(b) 2 vol. % benzene oil component.

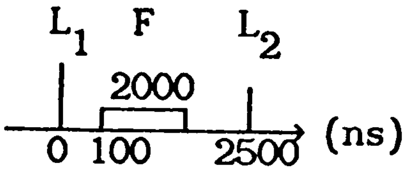

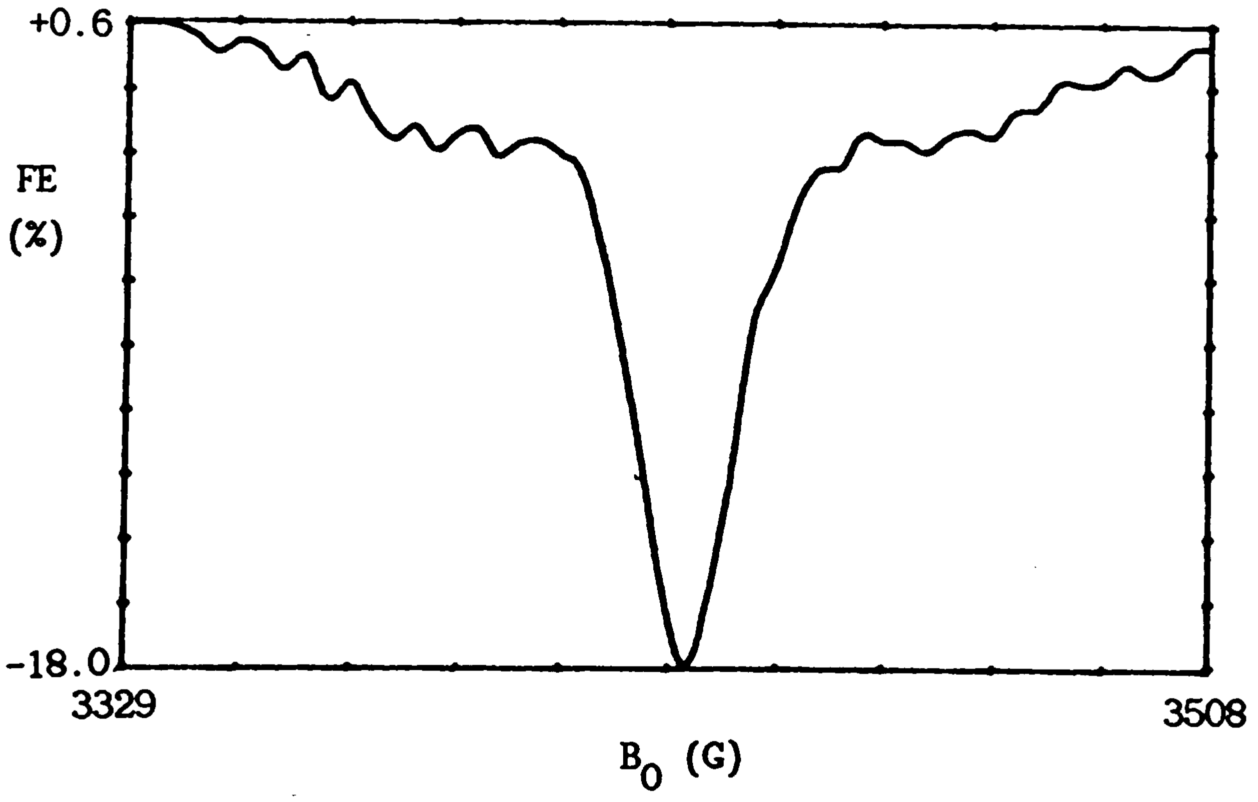

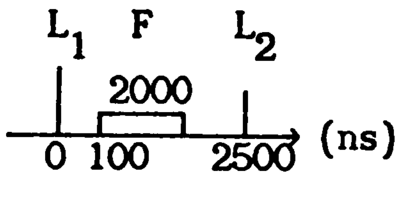

Figure 5.20. Effect of B_1 on RYDMR B_0 spectra from benzophenone - 1,4 cyclohexadiene in 2 vol. % benzene microemulsion media. R.f. frequency 9.5827 GHz, B_1 = 4.1 G. Observation via induced fluorescence of escape ketyl radical. Comparison is to be made with figure 5.19 (b), recorded at B_1 = 13 G.

Confirmation of power broadening effects is provided by figure 5.20, showing the 2 % benzene result at a lower B_1.

In agreement with the MARY findings, RYDMR intensity is considerably enhanced for the large volume microemulsion.

RYDMR B_1 Spectra

Further investigation of the importance of microemulsion volume proceeded with the recording of peak intensity B_1 spectra at two media volumes. With a sampling r.f field pulse of 2 μs duration, commencing at 100 ns after L1, the results of figure 5.21a were obtained. A more rapid increase in RYDMR intensity and noticeable saturation with increasing B_1 may be seen in the 6 % benzene system. This is consistent with a lower electron spin-spin interaction exhibited by radical pairs in the larger volume microreactor. Straightforward interpretation in terms of the homogeneous lineshape description of chapter 2 must, however, be tempered by considering contributions from the full radical pair ensemble.

Sampling the spin motion by means of a 200 ns r.f field centred at 200 ns after L1, produces quite different spectral behaviour (figure 5.21b). All droplet sizes give indistinguishable lineshapes and no high B_1 saturation. A new feature, in the form of a degree of B_1 insensitivity at very low field, is also apparent. In view of the state broadening of ~ 2 G expected on sampling the system at 200 ns, and with a similar field interaction time, such effects are perhaps not too surprising. Recording of spectra at 2 μs delay with respect to L1 appeared to show similar behaviour if a 200 ns r.f. pulse was employed, but S/N was considerably degraded.

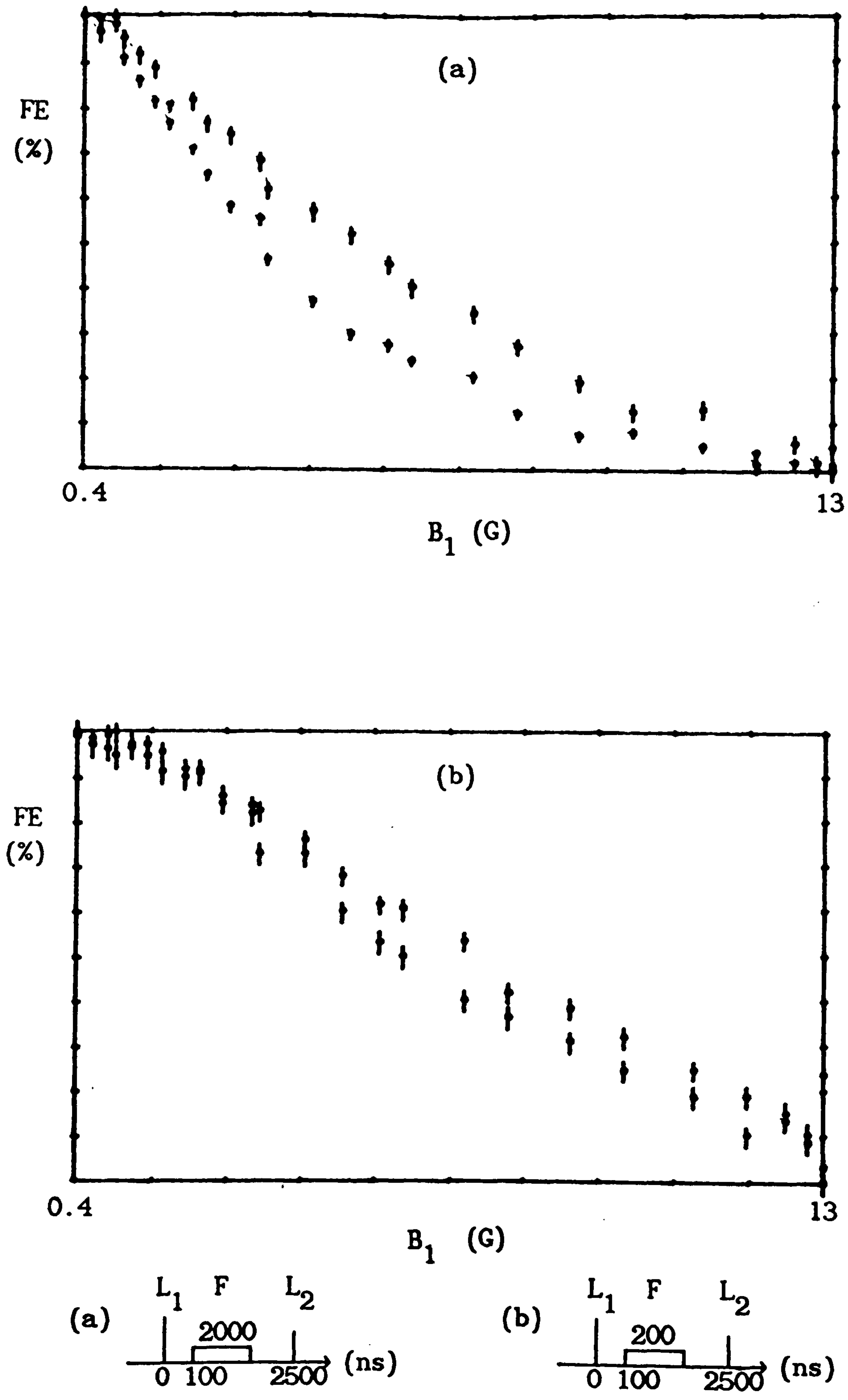

Figure 5.21. Effect of reactor volume and spin sampling time on RYDMR B_1 spectra from benzophenone - 1,4 cyclohexadiene in benzene microemulsion media. R.f. frequency 9.5827 GHz, B_0 = 3420 G. Observation via induced fluorescence of escape ketyl radical. (i) 6 vol. % benzene oil component, (ii) 2 vol. % benzene oil component.
(a) 2000 ns sampling time.
(b) 200 ns sampling time.

C

5.4.C Discussion

Several features of the magnetic modulation experiment, not seen in the homogeneous solution work of chapter 4, are evident from the above data. They may be sumarized as:

(1) large field effect (MARY/RYDMR intensity),

(2) non-saturation of MARY spectra at 200 G,

(3) kinetic behaviour inconsistent with hfi ISC,

(4) indication of resolvable electron spin-spin coupling.

In accounting for these phenomena the effects of microreactor media will be artificially separated into those of radical pair lifetime, reactor microenvironment and volume of enclosure.

The action of compartmentalizing a radical pair may be visualized as a replacement of the random encounter phase of reaction, which forms the major fraction in homogeneous solution, with an extended geminate phase, the timescale of which is determined by the enclosure volume and microenvironment. The rapid initial reaction, forming the geminate phase in homogeneous media, still occurs within the microreactor, the presence of a compartment boundary being unimportant after only a few diffusional steps, each characterized by τ_D (chapter 2). It will, however, be insignificant with regard to magnetic modulation in microreactor systems as it forms only a small fraction of the total reaction period of the initial pair.

By extending the mean timescale over which a geminate pair reacts, spin motion is able to attain long-time asymptotic values which will, in the absence of oscillatory behaviour arising from dominant hyperfine components, exhibit maximum achievable depth of field modulation. In addition, unavoidable state broadening, due to limited field - spin system interaction times, is eliminated. Thus, for example, the observation of very low field MARY phenomena is made possible.

A secondary aspect, but one of very great importance in the present work, comes from the increase in the fraction of geminate reaction. When field effects are monitored by via unreacted, escape species, the reduction in effective k_{esc}/k_{rec} leads to a much greater field effect, as observed.

As well as enhancing magnetic field effects, the extension of geminate timescale brings with it added complexity by encroaching on the μs region in which relaxational effects are important for C-centred radicals. This is demonstrated by the non-saturation of MARY spectra at field values well above $B_{½}$, and by the unexpected kinetic behaviour of k_{rec}.

To investigate fully the effects of stochastic relaxational processes, attention must be turned to the effective microenvironment experienced by radical species solubilized in surfactant aggregates. In particular the important quantity is the correlation time, τ_c, characterizing the fluctuating interaction responsible for relaxation. Values may be estimated from the Debye formula for a spherical molecule,

$$\tau_c = \frac{4\pi\eta a^3}{3kT} , \qquad (15)$$

where a is the assumed spherical radius.

For radical pairs in which one component is surfactant-derived, the τ_c characterizing electron dipolar effects is best considered to be that of the whole surfactant aggregate. In other situations, and for g and hyperfine anisotropy effects, the correlation time of interest is that of the solubilized radical species at the effective viscosity experienced within the microreactor. The latter is indicated to be in the region of 15 cP in pure SDS micellar media (fluorescence depolarisation study [35]), whilst for the microemulsions a range of 4 - 7 cP has already been quoted and found to be consistent with kinetic studies. We thus arrive at figures of $\sim 10^{-10}$ s and $\sim 10^{-8}$ s for correlation times of radical species and surfactant aggregates respectively, assuming radii of 3 Å and 25 Å. Such values predict longitudinal relaxation times (T_1) of ~ 1 μs, consistent with a significant contribution to the field dependence and non-saturation of MARY spectra [28].

Having obtained the bounds of correlation times in the relevant media, it is now possible to qualify an earlier assumption made while establishing a spin Hamiltonian to describe radical pair systems (chapter 2).

All anisotropic interactions described by traceless tensors are rotationally averaged to zero if the relevant correlation time is much less than the inverse of their characteristic mean energy (in frequency units). Thus a correlation time of 10^{-10} s will be sufficient to eliminate contributions of a few thousand Gauss (g = 2), whilst a value of 10^{-8} s will only be effective for small interactions of a few tens of Gauss.

The latter figure indicates that dipolar electron spin - spin features may be important for the benzophenone - SDS system but as evidence from the present work suggests S - T_0 zero field splittings of only a few Gauss, it would appear such effects can be dismissed. Electron spin - spin coupling features will thus be assigned to a scalar Heisenberg exchange interaction as proposed in chapter 2.

Clearly the existence of exchange coupling is dependent upon inter-radical separation. The exact distance dependence is not known but for a spherically symmetric model, an exponential dependence, calculated for two hydrogen atoms, is often assumed [36],

$$J = J_0 \exp(-\alpha r) \quad , \qquad (16)$$

typically with $J_0 = -6.25 \times 10^6$ G and $\alpha = 1.32$ Å^{-1}.

To apply such a relationship we clearly have to recognize the S - T_0 splitting observed in MARY and RYDMR expriments as a mean quantity averaged over a spatial distribution of compartmentalized radical pairs and the period of spin motion probing. It is here that the effect of a compartment boundary becomes important in providing an upper limit to radical separation, and so a minimum J.

With respect to averaging over the duration and time of field application, we must consider the timescale relative to that characterizing the motion of radicals within the enclosure. At the microviscosities quoted, a period of 10 - 20 ns is expected to be typical for movement across the microvolume. Thus for observation times (RYDMR) of 200 ns, and at ~ 200 ns after generation, a given radical pair might be expected to sample the full range of separations. In essence an ensemble spatial distribution can be considered established by 200 ns and maintained throughout the observation period. The problem is to determine the distribution and employ it in arriving at a J distribution for the radical pair ensemble.

Qualitatively, after many diffusional steps, a uniform spherical distribution of radical separations in the range 0 - r_m would be expected, giving rise to a radial probability growing as r^2 up to the barrier at r_m. Consideration of the effects of reaction at approximately zero separation, and a 'leaky' reflecting outer boundary, will distort this form but nevertheless its usefulness as a qualitative picture is not damaged. A more quantitative approach, such as via solutions of the relevant diffusion equations [27], is not considered justified in view of the many approximations involved in modelling of the system.

The rapid attainment and maintainance of a given distribution is supported by the essentially single exponential decay predicted and observed for compartmentalized reaction.

Averaging an exponentially falling J over a rising r^2 function will produce a mean J greater than $J(r_m)$ and a distribution considerably broadened to high J values. At 10 Å the above expression gives J ~ 11 G, whilst at 20 Å J ~ 10^{-5} G. In this light the observed range 4 - 12 G, for the very low field extrema of MARY spectra, appears reasonable. In view of the steeply rising J interaction, their widths of 10 - 20 G do appear surprisingly low. This point has been noted previously in connection with biradical CIDNP [37] and micellar esr [38], it being attributed to motional narrowing. At these low values of J, and effective viscosities of only a few cP, such a dynamic effect must surely be present.

It is noteworthy that the width and peak of the MARY minimum for benzophenone - SDS are comparable to the relevant parameters extracted from the esr results of reference [38], and that in the present work, microemulsion and pure SDS media of equivalent volume exhibit similar J values.

Furthering the dynamical point, structure corresponding to preferred radical pair configurations is not expected and indeed the structure observed in MARY spectra is within the recorded error limits and was not reproducible. Similarly B_1 spectra recorded at 200 ns differed from those averaged over 2 μs but the effect is assigned to an interaction-time broadening rather than an evolution of radical spatial distribution.

Having established a minimum J of ~ 4 G and maximum B_1 ~ 13 G, the lack of expected RYDMR B_0 spectral inversion at high microwave fields, or the absence of J splitting, may well be accounted for by the inhomogeneity of the RYDMR linewidth; the presence of overlapping resonances masking the effects predicted for a homogeneous lineshape. At sufficiently high B_1, or low J, inversion would still be expected.

The existence of a non-inverted RYDMR signal and absence of J resonances, have been addressed by workers in the photosynthetic field [39] and variously attributed to high electron dipolar interaction and extensive lifetime broadening as a result of fast recombination. Both of these factors may be eliminated from the present work.

Additionally, in the present case we are dealing with initial triplet pairs and the effects of non-uniform T-state populations (ignoring thermal polarization) should be considered (chapter 2). Such effects are important at high molecular triplet quenching rates when radicals are generated before the triplet is fully relaxed and so would only be expected to influence the results obtained in the presence of added H-donors. A re-examination of the data in this light does not however reveal any distortions to the spectral symmetry, but this is perhaps not too surprising in view of the failure to resolve other features predicted from a simple lineshape treatment.

CHAPTER 6

CONCLUDING REMARKS

6.1 Assessment of MARY and RYDMR

Techniques and interpretation have been developed sufficiently to obtain basic physico-chemical information from radical pair magnetic resonance techniques applied to certain trial systems, but the goal of routinely extracting MARY and RYDMR spectra from generalized radical pair systems has not been achieved. Indeed, in order to obtain acceptable S/N the scope of the techniques was drastically reduced by restriction to systems exhibiting modified diffusional characteristics, notably those of compartmentalized reaction media. Additionally further specialization came in the employment of fluorescence detection, abandoning the more general absorption option.

As an illustration of the magnitude of the S/N problem consider the recording of a 100 G-wide RYDMR spectrum to a field step resolution of 0.5 G by the induced fluorescence method of chapter 5. In favourable cases the definition of single point RYDMR intensity of ≃ 2 % field effect to an error level of 20 % typically required 500 pairwise averages and a recording time of approximately one minute at 15 - 20 Hz. Thus a full spectrum could be recorded in ≃ 3½ hrs. This is to be compared with a time approaching 25 minutes per field point required in preliminary micellar escape yield experiments utilizing absorption detection (not presented here). Obviously on the latter timescale, defining a full RYDMR spectrum to any degree of significance is not practicable, although the situation could be improved considerably, S/N would not surpass that of the fluorescence technique (chapter 3).

The major source of error found for the fluorescence-detected results of chapters 4 and 5 appeared to arise from difficulty in maintaining a constant sample composition, compounded by the high photolysis and probe energies necessary to generate a detectable signal. Allied to this were varying photoproduct background fluorescence signals.

One solution to the above problems would be to accept a poor single-shot S/N and improve the maximum achievable averaging rate currently set by laser repetition frequency limits. Ideally, however, the need is for at least an order of magnitude rate enhancement. This is clearly not a minor adjustment to the current apparatus design.

Almost divorced from S/N difficulties, more fundamental problems may be seen for radical pair magnetic resonance techniques. The simulations of chapter 2 suggest that, in the general case, spectra are not as readily interpretable as more conventional low time resolution spectroscopic techniques. This arises through the involvement of significant lifetime and radiation field terms. The situation is further complicated when full consideration is given to the interaction between spin and spatial dynamics. Conversely, of course, the sensitivity to so many parameters may be seen as a bonus in that the information content of a given spectrum is considerably increased. In order to make use of this fact, however, extensive system modelling and, crucially, excellent S/N are demanded.

In summary, the present 'state of the art' as regards radical pair magnetic resonance fails to yield anything more than semi-quantitative insight into rather specialized systems, and its extension to a wider subject range appears not to be a simple task, although it is theoretically possible. Encouragement may be gained from the observation, by the author, of fluorescence-detected static field effects (at $\simeq 200$ G) in the region of 0.5 % for a benzophenone cyclohexane system, corresponding to the condition of free diffusion in a low viscosity solvent. Furthermore, effects of a similar magnitude have been recorded by absorption in the much more viscous benzophenone - octan-2-ol system.

References - Chapter 1

1. For a review of early literature see P.W. Atkins and T.P. Lambert, Ann. Rep. Chem. Soc., 72A, 67, (1975).

2. B. Brocklehurst, Nature, 221, 921, (1969).

3. R. Kaptein and L.J. Oosterhoff, Chem. Phys. Letts., 90, 402, (1969).

4. E.P. Wigner, Z. Phys. Chem., 23B, 28, (1933).

5. B.A. Rushin and E.L. Frankevich, Phys. Stat. Sol., 33, 885, (1969).

6. B. Brocklehurst, R.S. Dixon, E.M. Gardy, V.J. Lopata, M.J. Quinn, A. Singh and F.P. Sargent, Chem. Phys. Letts., 28, 361, (1974).

7. R.G. Lawler and G.T. Evans, Ind. Chim. Belge., 36, 1087, (1971).

8a. T. Schmidt and I. Solomon, Compt. Rend. Acad. Sci., (Paris), 236B, 169, (1966).

b. Y. Ruedin, P.A. Shegg, L.C. Jaceard and M. Aegeter, Phys. Stat. Sol., 54, 565, (1972).

9. S.I. Kubarev and E.A. Pschenichnov, Chem. Phys. Letts., 28, 66, (1974).

10a. O.A. Anisimov, V.M. Grigoryants, V.K. Molchanov and Yu.N. Molin, Chem. Phys. Letts., 66, 265, (1979).

b. A.D. Trifunac and J.P. Smith, Chem. Phys. Letts., 73, 94, (1980).

11a N.J. Turro, B. Kraeutler and D.R. Anderson, J. Amer. Chem. Soc., 101, 7435, (1979).

b. Y. Sakaguchi, H. Hayashi and S. Nagakura, J. Phys. Chem., 86, 3177, (1982).

12. W. Lersch and M.E. Michel-Beyerle, Chem. Phys., 78, 115, (1983).

References - Chapter 2

1. P.W. Atkins, Chem. Phys. Letts., 66, 403, (1979).

2. H, Fischer, Chem. Phys. Letts., 100, 255, (1983).

3. K. Schulten and P.G. Wolynes, J. Chem. Phys., 68, 3292, (1978).

4(a). R. Haberkorn, Chem. Phys., 19, 165, (1977).

(b). R. Haberkorn, Chem. Phys., 24, 111, (1977).

(c). R. Haberkorn, Chem. Phys., 26, 35, (1977).

5. B. Brocklehurst, J. Chem. Soc. Faraday Trans. II, 72, 1869, (1976).

6. Y. Sakaguchi, S. Nagakura, A. Minoh and H. Hayashi, Chem. Phys. Letts., 82, 213, (1981).

7. H.-J. Werner, Z. Schulten and K. Schulten, J. Chem. Phys., 67, 646, (1977).

8. R.M. Noyes, J. Chem. Phys., 22, 1349, (1954).

9. R.Z. Sagdeev, K.M. Salikhov and Yu.N. Molin, Russ. Chem. Rev., 46, 297, (1977).

10. M.D. Hatlee, J.J. Kozak, G. Rothenberger, P.P. Infelta and M. Grätzel, J. Phys. Chem., 84, 1508, (1980).

11. Y. Sakaguchi, H. Hayashi and S. Nagakura, J. Phys. Chem., 86, 3177, (1982).

12(a). W. Schlenker, T. Ulrich and U.E. Steiner, Chem. Phys. Letts., 103, 118, (1982).

(b). T. Ulrich, U.E. Steiner, Chem. Phys. Letts., 112, 365, (1984).

13. A. Weller, F. Nolting and H. Staerk, Chem. Phys. Letts., 96, 24, (1983).

14. W. Lersch and M.E. Michel-Beyerle, Chem. Phys., 78, 115, (1985).

15(a). G.L. Closs, M.D.E. Forbes and J. R. Norris, Jr., J. Phys. Chem., 91, 3592, (1987).

(b) C.D. Buckley, D.A. Hunter, P.J. Hore and K.A. McLauchlan, Chem. Phys. Letts., 135, 307, (1987).

16. A.S. Davydov, *Quantum Mechanics*, (ed. D. ter Haar), Pergamon, Oxford, (1965).

17. D.A. Hunter, A.J. Hoff and P.J. Hore, Chem. Phys. Letts., 134, 6, (1987).

18. W. Lersch and M.E. Michel-Beyerle, Chem. Phys. Letts., 136, 346, (1987).

19. S.K. Wong, D.A. Hutchinson and J.K.S. Wan, J. Chem. Phys., 58, 985, (1973).

References - Chapter 3

1. M.K. Bowman, D.E. Budil, G.L. Closs, A.G. Kostka, C.A. Wraight and J.R. Norris, Proc. Natl. Acad. Sci. US, 78, 3305, (1981).

2. P.W Atkins and G.T. Evans, Adv. Chem. Phys., 35, 1, (1976).

3. A. Carrington and A.D. McLachlan, *Introduction to Magnetic Resonance*, Chapman and Hall, London, (1979).

4. M.C. Thurnauer and J.R. Norris, Chem. Phys. Letts., 76, 557, (1980).

5(a). A.B. Doktorov, O.A. Anisimov, A.J. Burshtein and Yu.N. Molin, Chem. Phys., 71, 1, (1982).

(b). A.D. Trifunac and J.P. Smith, Chem. Phys. Letts., 73, 94, (1980).

6. S. Basu, K.A. McLauchlan and G.R. Sealy, Mol. Phys.,11, 1, (1984).

7. G. Beck, Rev. Sci. Instrum., 47, 537, (1976).

8. C.P. Poole, *Electron Spin Resonance*, Wiley, New York, (1967).

9. R. Gallay and J.J. Van der Klink, J. Phys. E. Sci. Instrum., 19, 226, (1986).

10. U.P. Wild, A.R. Holzwarth and H.P. Good, Rev. Sci. Instrum., 48, 1621, (1977).

11. W.R Ware, L.J. Doemy and T.L. Nemzek, J. Phys. Chem, 77, 2039, (1973).

12. P. R. Bevington, *Data Reduction and Error Analysis for the Physical Sciences*, Mc. Graw-Hill, New York, (1969).

13. J.P. Gordon, Rev. Sci. Instrum., 32, 658, (1961).

References - Chapter 4

1. H. Beens and A. Weller in *Organic Molecular Photophysics*, (J.B. Birks, ed.), Vol II, Wiley, London, 159, (1975)
2. M. Ottolenghi, Acc. Chem. Res., 6, 153, (1973).
3. N, Mataga, T. Okada and N. Yamamoto, Chem. Phys. Letts., 1, 119, (1967).
4. H. Leonhardt and A. Weller, Ber. Bunsenges. Phys. Chem., 67, 791, (1963).
5. Y, Taniguchi and N. Mataga, Chem. Phys. Letts., 13, 596, (1972).
6. N. K. Petrov, E.Ya. Fedotova and E.L. Frankevich, Khim. Vys. Energ., 14, 345, (1980).
7. Z. Schulten and K. Schulten, J. Chem. Phys., 66, 4616, (1977).
8. K. Schulten, H. Staerk, A. Weller, H.-J. Werner and B. Nickel, Z. Phys. Chem., NF 101, 371, (1976).
9. A. Weller, Z. Phys. Chem., 133, 93, (1982).
10. H. Schomberg, H. Staerk, A. Weller and H.-J. Werner, Chem. Phys. Letts., 56, 399, (1978).
11. A. Weller, Z. Phys. Chem., 130, 129, (1982).
12. Landolt-Börnstein, *Structural Data and Functional Relationships in Science and Technology*, New Series, Group II: Vol. 9(b).

References - Chapter 5

1. *Micellization, Micelles and Microemulsions*, (ed. K.L Mittal), Plenum Press, New.York. (1977).

2. A. Rohde and E. Sackmann, J. Phys. Chem., 84, 1598, (1980).

3. N.A. Mazer, G.B. Benedek, M.C. Carey, J. Phys. Chem., 80, 1075, (1976).

4. K.J. Mysels and L.H. Princen, J. Phys. Chem., 63, 1686, (1959).

4. M. Dvolaitzky, M. Guyot, M. Lagues, J.P. le Pesant, R. Ober, C. Sauterey and C. Taupin, J. Chem. Phys., 69, 3279, (1978).

5. F. Reiss-Husson and V. Luzzati, J. Phys. Chem., 68, 3504, (1964).

6. S. Atik, M. Nam and L. Singer, Chem. Phys. Letts., 67, 75, (1979).

7. P. Mukerjee and K. Mysels, Natl. Stnd. Ref. Data. Ser., NBS 36, (1971).

8. P. Lianos, J. Lang, C. Strazielle and R. Zana, J. Phys. Chem., 86, 1019, (1982).

9. H. Wennerstrom, J. Colloid Interface Sci., 68, 589, (1979).

10. H. Saito and K. Shinoda, J. Colloid Interface Sci., 24, 10, (1967).

11. U.P. Strauss and N.L. Gershfeld, J. Phys. Chem., 58, 747, (1954).

12. A. Ray, Nature, 231, 313, (1971).

13. J.K. Thomas, Chem. Rev., 80, 283, (1980).

14. M.R. Topp, Chem. Phys. Letts., 39, 423, (1976).

15. L.J. Johnston and J.C. Sciano, J. Amer. Chem. Soc., 107, 6368, (1985).

16. G.H. Morine and R.R. Kuntz, Chem. Phys. Letts., 67, 552, (1979).

17. A. Bromberg, K.H. Schmidt and D. Meisel, J. Amer. Chem. Soc., 107, 83, (1985).

18. T. Okamura and R.W. Yip, Bull. Chem. Soc. Jpn., 51, 937, (1978).

19. A. Beckett and G. Porter, Trans. Farad. Soc., 59, 3038, (1963).

20. A. Padwa, Tetrahedron Letts., 3465, (1964).

21. J.C. Scaiano, J. Photochem., 2, 81, (1973/74).

22. V. Nagrajan and R.W. Fessenden, Chem. Phys. Letts., 112, 207, (1984).

23. L.J. Johnston, D.J. Lougnot and J.C. Sciano, Chem. Phys. Letts., 129, 205,(1986).

24. S.M. Lefkowitz and A.D. Trifunac, J. Phys. Chem., 88, 77, (1984).

25. N.J. Turro and R. Engel, J. Amer. Chem. Soc., 91, 7113, (1969).

26. T. Ulrich and U.E. Steiner, Chem. Phys. Letts., 112, 365, (1984).

27. M.D. Hatlee, J.J. Kozak, G. Rothenberger, P.P. Infelta and M. Gratzel, J. Phys. Chem., 84, 1508, (1980).

28. H. Hayashi and S. Nagakura, Bull. Chem. Soc. Jpn., 57, 322, (1984).

29. J.C. Scaiano, E.B. Abuin and L.C. Stewart, J. Amer. Chem. Soc., 104, 5673, (1982).

30. Y. Sakaguchi, H. Hayashi and S. Nagakura, J. Phys. Chem., 86, 3177, (1982).

31. A. Weller, H. Staerk and R. Treichel, Faraday. Discuss. Chem. Soc., 78, 271, (1984).

32. S.R. Nattrass, Part II Thesis, Oxford, (1984).

33. as [24].

34. A.V. Buettner and J.V. Dedinas, J. Phys. Chem., 75, 187, (1971).

35. M. Grätzel and K. Thomas, J. Amer. Chem. Soc., 95, 6885, (1973).

36. F.J.J. de Kanter, R. Kaptein and R.A. van Sauten, Chem. Phys. Letts., 45, 13, (1977).

37. F.J.J. de Kanter, J.A. den Hollander, A. Huizer and R. Kaptein, Mol. Phys., 34, 857, (1977).

38. G.L. Closs, M.D.E. Forbes and J.R. Norris, J. Phys. Chem., 91, 3592, (1987).

39. W. Lersch and M.E. Michel-Beyerle, Chem. Phys., 78, 115, (1983).

Optically Detected Magnetic Resonance of Radical Pairs

A thesis submitted for the degree of Doctor of Philosophy

by

Stephen R. Nattrass

Wolfson College, Oxford. Michaelmas 1987.

Abstract

Current theories of the effects of static and resonant high frequency magnetic fields on radical pair reaction are presented with a view to establishing how they can form the basis of the high time resolution liquid phase magnetic resonance techniques of MARY and RYDMR. Approximate calculations are performed to reveal RYDMR spectral details for the case of an initial triplet radical pair.

The design of unique apparatus to explore the capabilities of the techniques, and routinely collect quantitative data to test theoretical predictions, is described. This includes the development of an ultra-fast waveform scan-digitizing facility which can attain effective sampling rates of up to 20 GHz.

The apparatus is employed to provide the first demonstration of recombination exciplex fluorescence from pyrene - dicyanobenzene radical-ion pairs. It is also applied in the dimensional characterization of micellar and microemulsion media prior to their use in enhancing MARY and RYDMR signal intensities from solubilized radical pairs.

By means of a laser induced radical fluorescence technique and compartmentalized reaction media, first observations are reported of optically detected RYDMR spectra from neutral radical pairs, the existence of very low field MARY spectral structure and the kinetic effect of a resonant microwave field. The MARY structure is attributed to Heisenberg exchange interaction and shown to be sensitive to microreactor volume.